Multimass Modelling of Milky Way Globular Clusters and Implications on Their Dark Remnant Content and Stellar Initial Mass Function

by

Nolan Dickson

A Thesis Submitted to Saint Mary's University, Halifax, Nova Scotia in Partial Fulfillment of the Requirements for the Degree of Master of Science in Astronomy (Department of Astronomy and Physics)

August 2022 Halifax, Nova Scotia

Approved: Dr. Vincent Hénault-Brunet
Supervisor

Approved: Dr. Marcin Sawicki
Examiner

Approved: Dr. Rob Thacker
Examiner

Date: AUGUST 25, 2022

Acknowledgements

Firstly, I must acknowledge the tireless guidance and support of my supervisor, Dr. Vincent Hénault-Brunet, whose enthusiasm and advice I am eternally thankful for, and without which this research would not have been possible. I extend my thanks to Dr. Holger Baumgardt, for providing the HST mass function data so necessary for this work, and Dr. Mark Gieles, for the LIMEPY models used here, and for their respective helpful advice and direction. I am also greatly appreciative of the aid and camaraderie that has been provided throughout the course of this work by the clusters group, and by all the astronomy graduate students, at SMU.

I am grateful to my entire family, and most especially to my parents, whose unceasing encouragement and unquestioning assistance, not only during the recent, unprecedented years, but over my entire life, has made all of this possible.

Finally, I am forever and most of all indebted to my amazing partner, Alison, for all the love, patience and support in the Universe, and for being my constant reminder of the rest of the wonderful world that exists outside these pages.

Table of Contents

List of Figures

List of Tables

Abstract

Multimass Modelling of Milky Way Globular Clusters and Implications on Their Dark Remnant Content and Stellar Initial Mass Function

by

Nolan Dickson

The distribution of stars and stellar remnants within globular clusters holds clues about their formation and long-term evolution. In this work, we infer best-fitting multimass models for a number of Milky Way globular clusters, which are compared to various datasets. These models allow us to explore in detail the stellar (initial) mass functions and remnant populations of a large sample of Milky Way GCs. Examination of the low-mass mass function of the clusters suggests an IMF which is considerably flatter and depleted in low mass stars than canonical IMFs, while the high-mass IMF is consistent with a Salpeter IMF. New constraints on the number and mass in black holes for each cluster are inferred from our models, and comparisons to various studies predicting the black hole population in GCs are performed, finding generally good agreement, and in most cases no need for large populations of BHs to explain the data.

August 25, 2022

Chapter 1

Introduction

Globular clusters, among the most massive and dense of all stellar clusters, present a rich laboratory for the study of numerous astrophysical concepts. However, a large number of these processes cannot be directly observed or measured, as certain stellar populations are hidden from view, either by their nature or the extreme density of the system. They must instead be inferred from accurate dynamical models. In order to best explore a real cluster these models must fit strictly to its observables and account for the various astrophysical and dynamical mechanisms present in globular clusters.

In this thesis we will fit dynamical models to a number of Milky Way globular clusters of various metallicities, in order to explore the relationships between cluster parameters, their initial distribution of mass and their populations of dark remnants.

1.1 Globular Clusters

In contrast to the looser open clusters, globular clusters (GCs) are considerably more massive ($M \sim 10^5 \mathrm{M}_\odot$), dense ($r_h \sim 5\,\mathrm{pc}$) and bright ($M_V \sim -7$) (Harris, 1996;

Baumgardt & Hilker, 2018). Substantial gravitational wells tightly bind their stellar members into their namesake roughly spherical shapes, which are mostly free of gas and dust.

This extra gas and dust is thought to have all been converted into stars or expelled from the system, as globular clusters are among the oldest galactic objects (age $\sim$ 12.5 Gyr) (VandenBerg et al., 2013) and remain relatively isolated from external material, residing mostly in the halo of their host galaxies.

1.1.1 Stellar Populations

Given that all of their stars are formed during the same star formation event and from the same cloud of gas, globular clusters exhibit a *Single Stellar Population* (to first approximation, save for some light-element abundance spreads; see Bastian & Lardo 2018). While the exact mechanisms of this initial stellar formation are not completely understood (Krause et al., 2020), for dynamical purposes a cluster's initial stellar population is distributed by mass based on an initial stellar mass function (IMF). As all stars in the system are of roughly the same age, this mass spread is the determining factor of stellar evolution, as the stars progress along the cluster's Hertzsprung-Russell diagram. The system's stellar isochrones are defined by its age and metallicity, and the very well-defined sub-giant branch of a globular cluster allows for a precise identification of its *turnoff point* (Binney & Merrifield, 1998).

The clusters, in addition to the main sequence and giant branch stars, are also home to a considerable population of stellar remnants: white dwarfs, neutron stars and black holes. Due to the old ages of globular clusters, white dwarfs can make up a significant portion of a cluster's mass. The dense nature of globular clusters means they can also play host to some exotic classes of stars, such as blue stragglers, X-ray

binaries and millisecond pulsars (Binney & Merrifield, 1998). Many of these objects are part of the clusters binary population, which although depleted due to dynamical interactions, play an important part in the dynamical evolution of the system (e.g. Heggie & Hut, 2003; Ivanova et al., 2005; Cournoyer-Cloutier et al., 2021)

1.1.2 Mass Segregation

The spectrum of stellar masses in a cluster also gives rise over time to important long-term dynamical effects. Mass segregation is the process wherein stars are stratified radially by mass. This mechanism is driven by the trend towards kinetic energy equipartition, which induces a decrease in the velocity of massive stars, and a corresponding increase in that of lighter stars, overall. The faster, lighter stars are then able to rise further from the centre of the cluster's gravitational potential well. The result is that by the time a cluster is "relaxed", i.e. has experienced enough encounters for stars to have lost all memory of their initial configuration and reached equilibrium, the most massive stars will tend to have "sunk" towards the core of the cluster, and the stellar populations will be arranged largely by mass (Spitzer, 1969; Spitzer, 1987).

This process is both driven by, and has a strong effect on, the cluster's dynamical evolution. Sinking massive objects can greatly increase the density at the core of the system, leading to more frequent and stronger interactions. Towards the outer edges, mass segregation inflates the size of the cluster halo, and leads to increased "evaporation" of light, fast-moving stars over the tidal boundary. Together these effects can also hasten the core-collapse of the cluster. Mass segregation has a strong effect on the overall profiles of density, velocity dispersion and mass, and understanding it is vital to understanding the dynamical evolution of a system (Spitzer, 1987).

As this operation is dependent on mass, it can also be "disrupted" by heavy

remnants, such as black holes. The massive, invisible objects will be stratified to the core, and push the larger stars out, towards their lighter counterparts. A cluster core of remnants is able to suppress the *visible* mass segregation and increase the velocities of brighter stars (Mackey et al., 2008; Gill et al., 2008; Alessandrini et al., 2016).

1.2 Initial Mass Functions

The distribution of individual stellar masses present directly after the initial burst of formation of a population of stars is governed by a probability distribution function; the *initial mass function* (IMF).

The IMF is a function of stellar mass, and defines the starting masses of stars in a single population. In typically isolated, single-population systems such as globular clusters, this means the IMF plays a very important role in the cluster's evolution. The distribution of masses of stars in a cluster controls how mass segregation proceeds in the cluster; its timescale and degree (Fregeau et al., 2002). The initial mass of a star also dictates how it will evolve over time. The post-main-sequence evolution of a star and what type of object it will form at the end of its lifetime, is controlled primarily by its initial mass. Therefore the IMF controls the shape of the present-day mass function (PDMF) and the population of a cluster's stellar remnants (Binney & Tremaine, 2008).

The IMF is typically inferred from observations of the PDMF and models of stellar and cluster evolution. The transformation from PDMF to IMF is not always trivial. As seen in Figure 1.1, more massive stars will have evolved into remnants and not be present in PDMFs inferred from the simple counting of stars (e.g. Elmegreen & Scalo, 2006), while lower mass stars will have been preferentially lost through evaporation

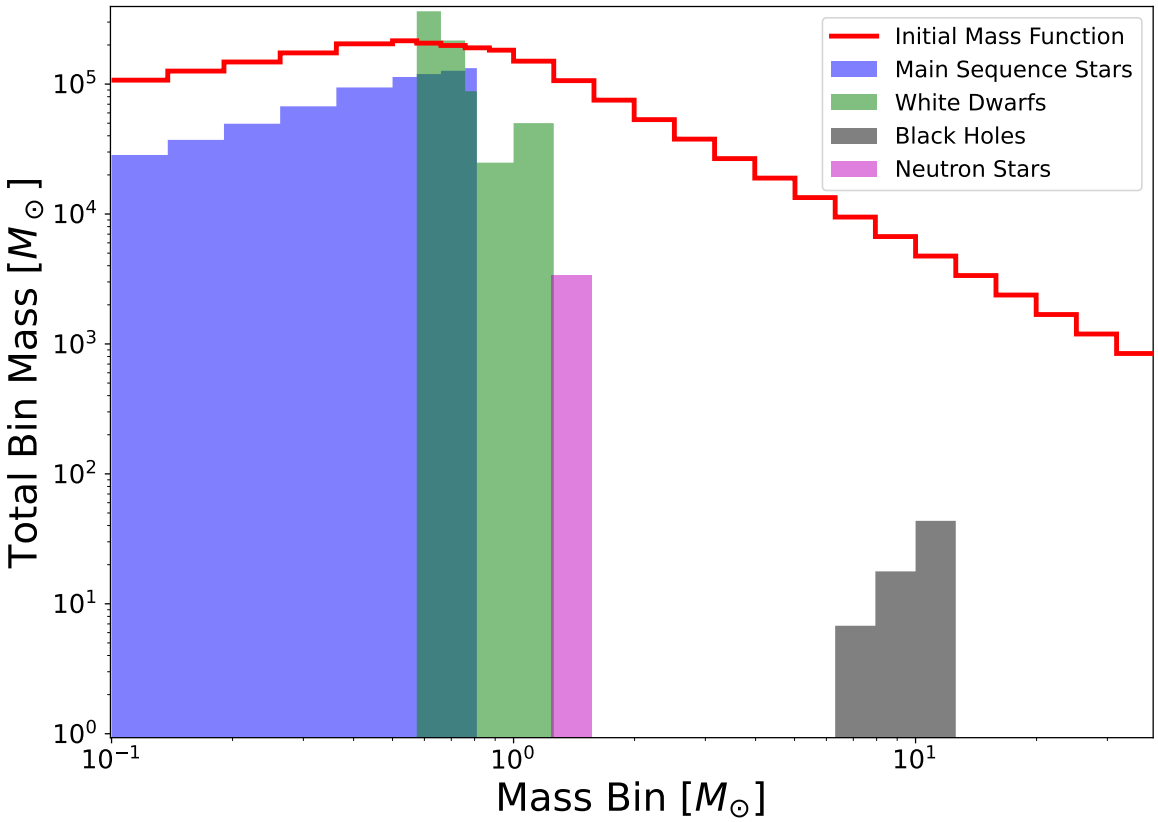

Figure 1.1: Example of the evolution of the mass function of a GC from IMF to present day (12.5 Gyr), including remnant formation, dynamical ejections and the preferential escape of low-mass stars.

over the cluster tidal boundary. PDMFs may also be influenced by the region of the cluster observed, where certain populations may be deficient, due to mass segregation.

Salpeter (1955) approximated the IMF, based on stars in the solar neighbourhood, as a single component power law with exponent $\alpha = 2.35$:

$$\xi(m) \propto m^{-2.35} \tag{1.1}$$

where $\xi(m)\Delta m$ is the number of stars with masses within the range $m + \Delta m$.

This formulation remains a good estimate of the distribution at higher masses, but overpredicts the number of stars at the low-mass end.

More recently, Kroupa (2001) utilized observations of low-mass solar-neighbourhood and high-mass cluster and OB-association stars to expand the Salpeter power law for lower mass stars, breaking the expression into three power-law components:

$$\xi(m) \propto \begin{cases} m^{-0.3} & m \leq 0.08\mathrm{M}_{\odot}, \\ m^{-1.3} & 0.08\mathrm{M}_{\odot} < m \leq 0.5\mathrm{M}_{\odot}, \\ m^{-2.3} & m > 0.5\mathrm{M}_{\odot}, \end{cases} \tag{1.2}$$

In similar fashion, Chabrier (2003) extended the low mass regime in the form of a log-normal distribution, with a mean stellar mass of 0.079 and standard deviation of 0.69:

$$\xi(m) \propto \begin{cases} \exp\left[-\dfrac{(\log(m) - \log(0.079))^2}{(2 \times 0.69^2)}\right] & m < 1\mathrm{M}_{\odot}, \\ m^{-2.3} & m > 1\mathrm{M}_{\odot}, \end{cases} \tag{1.3}$$

Typically one of these "canonical" IMF formulations is assumed to initialize cluster simulations. Figure 1.2 illustrates the shape of these various canonical IMFs, and how they behave similarly at high masses.

1.2.1 IMF Variations

The universality of the initial mass function is a debated topic. While the majority of observational determinations of the IMF seem to demonstrate that the function is universal among star-forming systems (Bastian et al., 2010), this is counter to most theories of star formation, which dictate that initial distributions should vary according to star formation conditions. Namely, at lower metallicities, less efficient cooling should in theory require a larger Jeans Mass for the collapse of molecular clouds and thus on average produce more massive stars and a top-heavy IMF (Larson,

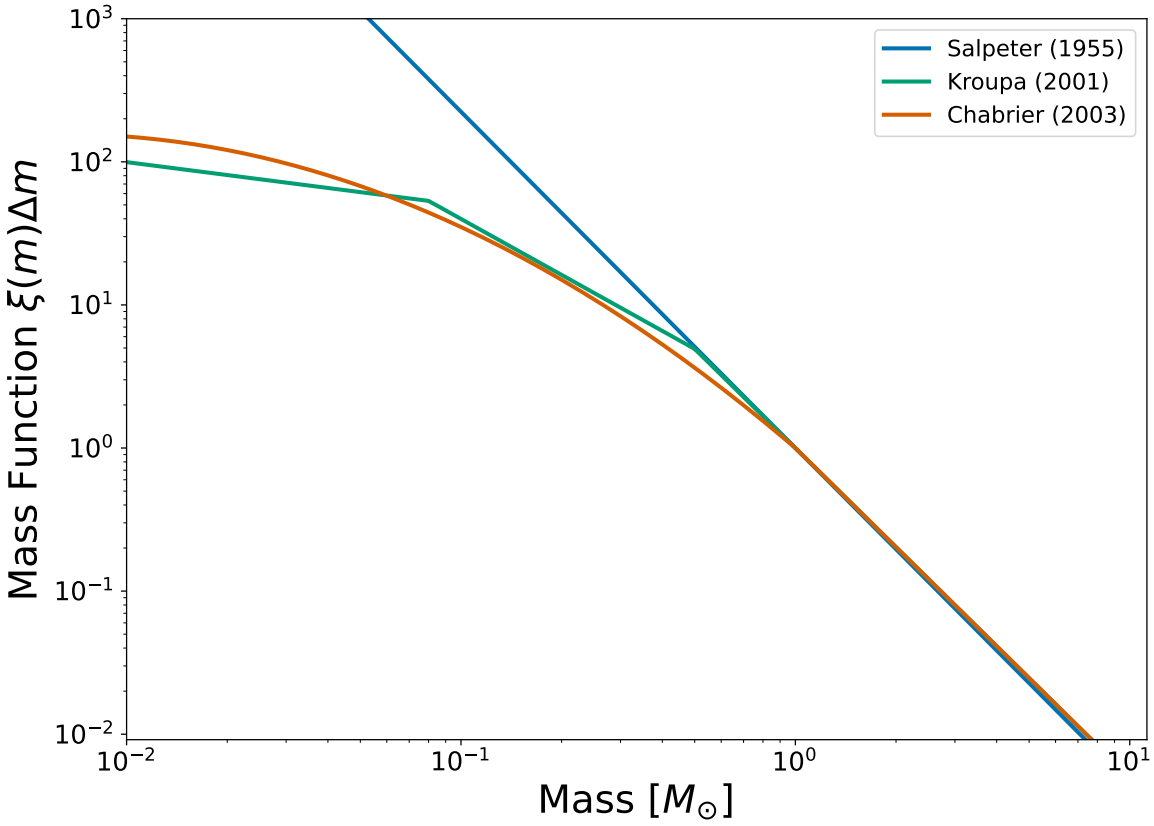

Figure 1.2: The canonical initial mass functions of Salpeter (1955); Kroupa (2001) and Chabrier (2003).

1998). Various fundamental planes relating the massive portion of a cluster's IMF with metallicity and initial cloud density have been postulated (e.g. Marks et al., 2012).

Possible Evidence of Non-Canonical IMFs

A number of recent observational works have showcased cluster trends which could be explained by a non-canonical IMF, however these observations are also typically explainable without the need to invoke a variable IMF.

Strader et al. (2011) demonstrated that dynamical mass measurements of 200 M31 globular clusters showed a decreasing trend in the dynamical mass-to-light ratio,

as a function of cluster metallicity. This result is opposite to what standard stellar population models would predict, while assuming a canonical IMF. Haghi et al. (2017) showed that these results could be explained by introducing a non-canonical, metallicity-dependent IMF, with an increasing level of top-heaviness for low metallicity clusters. The greater amount of massive luminous stars in these clusters would in turn lower the mass-to-light ratios, as seen in M31. However Baumgardt et al. (2020), while observing Milky Way globular clusters, also noted that such a discrepancy in the mass-to-light ratios could be accounted for once the low-mass depleted PDMF of the metal-rich clusters, caused only by evolution within the galactic tidal field and exacerbated in metal-rich clusters which typically reside closer to the galactic centre (van den Bergh, 2011), was taken into consideration. Metallicity-dependent stellar evolution models were also able to account for the difference in the metal-poor clusters. Shanahan & Gieles (2015) also demonstrated that not accounting for mass segregation introduces a bias in the inferred dynamical mass, dependent on metallicity as metal-rich clusters exhibit higher turn-off masses and lowered central concentrations of non-luminous remnants, and showed that there is no need for variations in the IMF to explain the Strader et al. observations.

De Marchi et al. (2007) examined 20 Milky Way globular clusters and found that the PDMF of low-density clusters is deficient in low-mass stars. As dynamical interactions would tend to eject lower-mass stars from the cluster, we would expect the opposite; for low-density clusters to be less bottom-light, if only driven by dynamical evolution. Another possibility is that these clusters were formed with a bottom-light IMF. However Ebrahimi et al. (2020) investigated correlations between a number of cluster parameters and their present-day mass functions, and found that the relation between PDMF slope and concentration of De Marchi et al. (2007) was not significant.

Effects of Top-Heavy IMFs in GCs

Varying the IMF would have a drastic effect on almost all characteristics of a globular cluster. Examined in particular here is the case of the "top-heavy" IMF, which displays a flatter slope at higher masses ($\geq 1M_{\odot}$) and necessarily produces a larger number of massive objects; giant stars, white dwarfs, black holes, neutron stars. Recently, the possibility of top-heavy IMFs in metal-poor GCs has been considered in the literature, however it has not been conclusively established.

Typically, the slow loss of mass over the lifetime of globular clusters is driven by stellar winds, until such time as the shrinking gravitational potential well allows the mass-segregated cluster halo to swell with faster, lighter stars. From here the mass loss is dominated by tidal evaporation, in which these lighter halo stars are lost beyond the tidal boundary to the host galaxies potential well.

Weatherford et al. (2021) demonstrated that, in clusters with a top-heavy IMF, the larger massive object population leads to increased stellar winds, but also, to a much higher degree, significant mass loss from supernovae and their corresponding natal kicks during the heightened period of remnant formation. This considerable mass loss, combined with amplified two-body dynamical interactions between massive and light objects leads the cluster halo to expand greatly, on much shorter timescales than in clusters with a canonical IMF. This swelled halo results in similarly increased losses to tidal evaporation.

Both of these mass loss processes can be nearly catastrophic; remnant formation may cause the cluster to lose close to half its original mass in the first tens of Myrs. Haghi et al. (2020) showed that clusters with a top-heavy IMF, due to this enhanced mass loss, may struggle to survive to late ages. A cluster formed with the most top-heavy IMF typically considered ($\alpha \sim 1.6$) was shown to require an initial cluster mass

upwards of $\sim 7 \times 10^5\,\mathrm{M}_\odot$ in order to have survived to the present day.

1.3 Dark Remnant Populations

Globular clusters host, alongside their visible stars, significant populations of stellar remnants, as the stars initially formed from the IMF evolve and die over time, forging new compact objects; white dwarfs, neutron stars and black holes. Given the age of the Milky Way GCs, a large portion of the most massive stars will have evolved into these dark remnants by the present day, and thus they may represent a sizable fraction of the total cluster mass. These massive objects play a vital role in the dynamical evolution and present-day structure of the GCs.

1.3.1 Black Holes

Black holes form from the most massive stars in the cluster. However, natal kicks received from their initial supernova explosion and ejections from highly-energetic dynamical encounters over the course of the clusters lifetime will expel most of the formed black holes. It was thought for a long time that any initially retained BHs would, after segregating rapidly to the core of the host cluster, quickly be ejected within a few gigayears. It has been shown, however, in recent years that at least a small number of these BHs must be able to be retained in GCs, as BH candidates in binaries have been detected in a small number of Milky Way GCs via X-ray and radio observations (Strader et al., 2012; Miller-Jones et al., 2015) and companion radial velocity variations (Giesers et al., 2018, 2019). This observational evidence has also been complemented by more recent dynamical models, which have demonstrated that realistic clusters can retain thousands of BHs to the present-day, by delaying the

rapid and total segregation of BHs to the core through three-body interactions (e.g. Morscher et al., 2015; Rodriguez et al., 2016).

The presence of massive black holes plays a large role in the dynamical evolution of globular clusters, and shapes their present-day structures, as a population of black holes will serve to quench mass segregation among the visible stars, increase the central velocity dispersion, inflate the cluster cores and support against core-collapse (Gill et al., 2008; Peuten et al., 2016; Heggie et al., 2007; Zocchi et al., 2019; Kremer et al., 2020b). The formation of BH binaries in the dense cluster cores has also been proposed as one of the main formation channels for gravitational wave sources (e.g. Abbott et al., 2016; Rodriguez et al., 2016).

Intermediate Mass Black Holes

The elusive intermediate mass black hole (IMBH) is a class of BHs with masses significantly larger than typical stellar-mass BHs, but less than a supermassive black hole ($\sim 10^2 - 10^5$ $M_\odot$). It has been theorized that IMBHs may form in the dense cores of GCs, and various claims of IMBHs in Milky Way GCs have been presented, based on indirect dynamical inferences (e.g. Noyola et al., 2008; McNamara et al., 2012; Kızıltan et al., 2017; Perera et al., 2017a). However, all of these candidates have been controversial, and in many cases have been rebutted, either by the introduction of improved data, or by other, more plausible, physical interpretations of the data (e.g. van der Marel & Anderson, 2010; Zocchi et al., 2017). This search is complicated further due to the fact that a partial degeneracy exists between the dynamical effects of a central IMBH and a central concentration of stellar-mass BHs (e.g. Lützgendorf et al., 2013).

1.4 Star Cluster Models

While the evolution of globular clusters is driven by a number of stellar and dynamical processes, the relative simplicity of a collisional (dominated by two-body stellar encounters, as cluster relaxation time is shorter than their age) gravitational system of similar, discrete particles allows their present-day properties to be well captured by relatively straightforward dynamical models (Heggie & Hut, 2003).

Dynamical models which aim to describe the internal kinematics and structures of clusters are grouped in two main categories: equilibrium and evolutionary models (e.g. Hénault-Brunet et al., 2019). The first contains static analytical methods such as distribution function models and Jeans models, whereas the second contains approaches such as N-body and Monte Carlo models.

1.4.1 Distribution Function Models

The phase-space distribution (positions and velocities) of stars in a cluster can be described by *distribution-function (DF) models*.

DF models are equilibrium models built around a distribution function f which describes the particle density of stars and satisfies the collisionless-Boltzmann equation (which is derived from the conservation of particles):

$$\frac{\partial f}{\partial t} + \mathbf{v} \cdot \frac{\partial f}{\partial \mathbf{x}} - \frac{\partial \Phi}{\partial \mathbf{x}} \cdot \frac{\partial f}{\partial \mathbf{v}} = 0 \tag{1.4}$$

This distribution function is formulated based on a number of key assumptions about the structure and dynamics of globular clusters. First it must be assumed that the discrete impact of objects in the cluster can be ignored in favour of a continuous

gravitational potential field. Further, in order to allow for simple analytical DFs, it is often assumed that the potential, the DF and all cluster properties are time-independent and the system is entirely spherically symmetrical (Spitzer, 1987).

This DF is used to self-consistently solve for the system's potential $\phi(r)$ using Poisson's equation:

$$\frac{1}{r^2}\frac{\mathrm{d}}{\mathrm{d}r}\left[r^2\frac{\mathrm{d}\phi(r)}{\mathrm{d}r}\right] = 4\pi G\rho \tag{1.5}$$

where the density is found by integrating the DF over the velocity distribution:

$$\rho(r) = \int f(\mathbf{r},\mathbf{v})d^3v \tag{1.6}$$

A variety of quantities can be derived from the DF which can be used to describe a globular cluster, including the velocity dispersion (the second velocity moment), the projected surface density, the total mass, the potential energy and the system entropy, and observational data can be used to compare and constrain the models (Spitzer, 1987; Gieles & Zocchi, 2015).

Historical Development

Various classes of DF models have been proposed and used extensively to model clusters over the years, with varying levels of complexity added to the logical starting point of a simple isothermal (constant temperature) sphere, as described by Chandrasekhar (1960, 1967), which characterizes the inner core of clusters well, but is infinite in extent and mass, and thus cannot be used to represent real systems.

Woolley (1954) first addressed the issue of the infinite spatial and mass bounds of ideal isothermal models by relaxing the assumption of the Maxwell-Boltzmann distribution of velocities in these models through the introduction of a constant energy-

lowering term $\phi(r_t)$:

$$f_{\text{Woolley}}(E) = \begin{cases} A \exp\left(-\dfrac{E-\phi(r_t)}{s^2}\right) & E < \phi(r_t) \\ 0 & E > \phi(r_t) \end{cases} \tag{1.7}$$

Reducing the mechanical energy E by the specific potential at the truncation radius $\phi(r_t)$, with a velocity scaling s, mimics the escaping of stars, which attain a velocity high enough to exceed the clusters tidal boundary r_t, to the host galaxy.

These models are finite in both mass and extent, but introduce a new discontinuity at $E = \phi(r_t)$, and show a rather abrupt boundary cutoff.

In order to relieve this cutoff, King (1966) introduced a new subtracted constant, allowing the models to be continuous at the truncation radius and resulting in a gentler decline in density near the truncation radius, in comparison to the Woolley models.

$$f_{\text{king}}(E) = \begin{cases} A\left[\exp\left(-\dfrac{E-\phi(r_t)}{s^2}\right) - 1\right] & E \leq \phi(r_t) \\ 0 & E > \phi(r_t) \end{cases} \tag{1.8}$$

Wilson (1975) introduced another subtractive term, in this case linear with respect to the energy E, which renders both the distribution and its derivative continuous. Wilson's model was created for the modelling of elliptical galaxies with rotational symmetry, but the non-rotating, spherical case applies just as well to globular clusters.

$$f_{\text{wilson}}(E) = \begin{cases} A\left[\exp\left(-\dfrac{E-\phi(r_t)}{s^2}\right) - 1 + \dfrac{E-\phi(r_t)}{s^2}\right] & E \leq \phi(r_t) \\ 0 & E > \phi(r_t) \end{cases} \tag{1.9}$$

The problem of radial velocity dispersion anisotropy, that is, an increase in the radial component of the velocity dispersion over the tangential component, which can be seen at the outer edges of clusters (Spitzer, 1987) was first approached by Michie (1963), by proposing a separable DF; the product of the isotropic King (Equation (1.8)) models and an exponential angular momentum term, which adds a measure of radial anisotropy.

$$f_{\text{michie}}(E, J^2) = \begin{cases} A \exp\left(-\frac{J^2}{2r_a^2 s^2}\right)\left[\exp\left(-\frac{E-\phi(r_t)}{s^2}\right) - 1\right] & E \leq \phi(r_t) \\ 0 & E > \phi(r_t) \end{cases} \tag{1.10}$$

The resulting model, often referred to as Michie-King models, displays approximate isotropy in the core of globular clusters, where the shorter relaxation time dominates, and becomes increasingly anisotropic further from the centre. At the edge of the cluster, the energy truncation term again brings the cluster to isotropy.

More recently, Gomez-Leyton & Velazquez (2014) generalized the Woolley and King isotropic models by consolidating the truncation schemes of the exponential function into a single energy series E_n:

$$f_{\text{GV}}(E, n) = AE_n(x) = \begin{cases} A\left[\exp(x) - \sum_{k=0}^{n-1} \frac{x^k}{k!}\right] & x > 0 \\ 0 & x \leq 0 \end{cases} \tag{1.11}$$

where x is the truncated energy term from before $x = (E - \phi(r_t))/s^2$.

For values of $n = 0$ and $n = 1$, this formulation (hereafter referred to as GV models) retrieves the isotropic Woolley and King DFs, respectively, and can be simplified

and extended to any non-negative real number g in terms of the gamma functions:

$$f_{\rm GV}(E, g) = AE_g(x) = A\exp(x)\frac{\gamma(g, x)}{\Gamma(g)} \tag{1.12}$$

LIMEPY Models

Gieles & Zocchi (2015) extended the GV models by allowing for radial anisotropy in similar fashion to the general Michie-King models, defining a DF as the product of an exponential angular momentum term with a slightly modified GV energy term:

$$f_{\rm LIMEPY}(E, J^2, g) = A\exp\left(-\frac{J^2}{2r_a^2 s^2}\right) E_g\left(x\right) = A\exp\left(-\frac{J^2}{2r_a^2 s^2}\right) \begin{cases} \exp(x) & g = 0 \\ \exp(x)\dfrac{\gamma(g, x)}{\Gamma(g)} & g > 0 \end{cases} \tag{1.13}$$

where x is as before; $x = (E - \phi(r_t))/s^2$.

This expression is dictated by a few structural and scaling parameters; the *truncation parameter* (g), which controls the smoothness of the model around the truncation radius, the *anisotropy radius* (r_a), determining the amount of anisotropy in the system, as a proxy of the distance from the core where isotropy begins to break down, and the *velocity scale* (s), which define the scale of the phase-space density.

This extension of past formulations represents a superset of the other distribution functions, allowing, in isotropic cases (wherein LIMEPY matches the GV function), the Woolley, King and Wilson models to be recovered under integer values of $g = 0, 1, 2$, respectively, while the more general, anisotropic case of $g = 1$ recovers the Michie-King model. There are no models of finite extent above the case of $g = 3.5$ (Gomez-Leyton & Velazquez, 2014).

The above DFs, which typically assume a single, uniform stellar mass population,

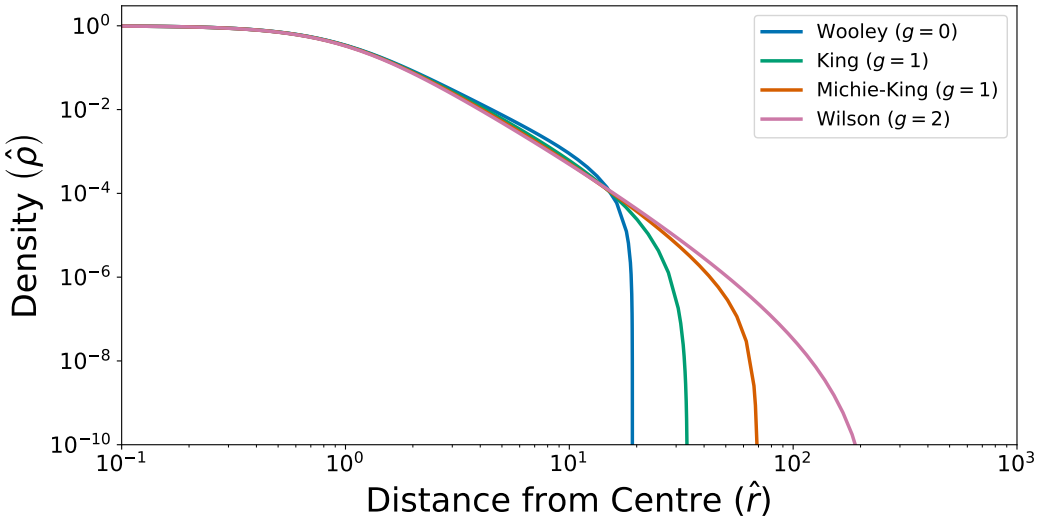

Figure 1.3: LIMEPY density behaviour under various truncation parameters (dimensionless model units).

can also be expanded to include a mass spectrum under the assumption of grouping stars into discrete mass classes or bins, which are each described by their own respective DF (Da Costa & Freeman, 1976).

The DF of LIMEPY multimass models is simply given by the sum of component DFs, each in the form of Equation (1.13), with mass-dependent velocity s_j and anisotropy radius $\hat{r}_{a,j}$ scales. It is this separate mass-dependent velocity scaling which allows for capturing the trend towards kinetic energy equipartition among masses, and thus mass segregation, as shown in Figure 1.4. These models can be solved self-consistently in much the same way as single-mass models, using a Poisson equation with the normalized sum of component densities.

Multimass models allow a more accurate description of real globular clusters, which are made up of a continuous spectrum of stellar masses. Multiple mass components are necessary in order to describe the distributions of different stellar populations within the system. This in turn enables the examination of both the process and effects of mass segregation, which could otherwise bias measures of radius and velocity

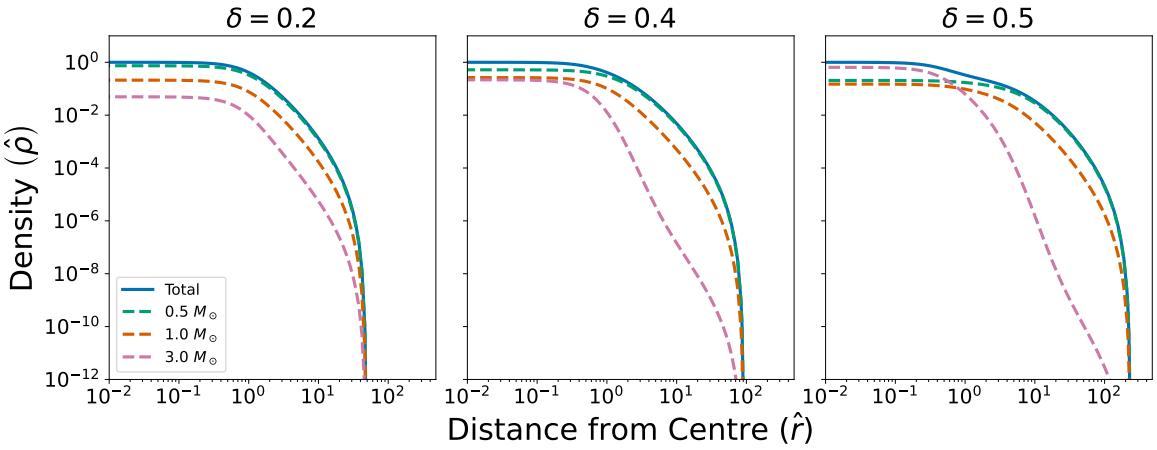

Figure 1.4: LIMEPY (multimass, $g = 1$, dimensionless model units) density behaviour of separate mass bins, under various mass-dependent velocity scales ($s_j \propto m_j^{-\delta}$). $\delta \sim 0.5$ is typically used to reproduce the degree of mass segregation present in GCs (Sollima et al., 2015).

dispersions, as well as the make-up of specific populations, such as turn-off stars and stellar remnants (Shanahan & Gieles, 2015; Sollima et al., 2015; Hénault-Brunet et al., 2019).

1.4.2 Jeans Models

Another group of equilibrium models, similar to DF models in that they revolve around the solutions to analytical equilibrium equations and provide static instantaneous descriptions of the clusters, are *Jeans Models* (e.g. Hénault-Brunet et al., 2019).

Jeans models rely on solving the spherical Jeans equation, which follows from the collisionless Boltzmann equation (Cappellari, 2008), in order to derive the cluster's mass profile, based on the velocity and anisotropy profiles of a tracer population (e.g. Sollima et al., 2016; Watkins et al., 2013):

$$-\frac{GM(r)}{r^2} = \frac{1}{\rho_j}\frac{\mathrm{d}(\rho_j \sigma_{r,j}^2)}{\mathrm{d}r} + 2\left(1 - \frac{\sigma_{t,j}}{2\sigma_{r,j}}\right)\frac{\sigma_{r,j}^2}{r} \tag{1.14}$$

where ρ_j and $\sigma_{x,j}$ are the mass density and velocity dispersion (radial and tangential) of a tracer population j.

This equation, although typically solved for one tracer population, produces a global gravitational potential which represents all mass components, even within a mass-segregated system (Sollima et al., 2016). This also means, however, that the models cannot directly infer the phase-space distribution of different individual mass components alone.

These models allow significant freedom in the structural profiles of mass and anisotropy, as they do not depend on a specific functional distribution, as the DF models, however this lack of constraint may also allow for unphysical results (Hénault-Brunet et al., 2019).

1.4.3 N-Body Models

The first and most, in principle, straightforward of evolutionary models are the family of *N-body models*.

A system of N particles which interact through gravity alone, at the scale of a star cluster, is driven simply by Newton's law between each particle, with an additional component of external potential (Heggie & Hut, 2003):

$$\vec{F_i} = -\sum_{j \neq i} G \frac{m_i m_j (\vec{r_i} - \vec{r_j})}{|\vec{r_i} - \vec{r_j}|^3} - \vec{\nabla} \cdot \phi_{ext}(\vec{r_i}) \tag{1.15}$$

The kinematic equations derived from this force and their corresponding solutions require numerical computation for all systems of $N \geq 3$. Direct methods, which introduce no physical approximations whatsoever to the solving of the equations of motion (excepting numerical discreteness), scale on the order of $\mathcal{O}(N^2)$, per time-step. Given

the timescale ($\tau \sim 12$ Gyr) and size ($N \sim 10^6$) of globular clusters, until only recently it was prohibitively expensive to directly simulate a complete cluster. Over time a number of optimizations, regularizations and schemes have been developed in order to improve the speed, accuracy and astrophysical complexity of these direct models (Aarseth, 1999, 2003), with, in recent years, the notable inclusion of GPU (graphics processing unit) powered parallelization greatly increasing the size of possible simulations (Wang et al., 2015). These models are still, however, very computationally expensive, and large grids of diverse full-scale models remain infeasible.

1.4.4 Monte Carlo Models

Monte Carlo cluster models, while still evolutionary by definition, cover more of an intermediate ground between equilibrium and N-body models, in an attempt to combine certain advantages of both.

Monte Carlo models attempt to improve on the performance costs of N-body models by exploiting the assumptions and peculiarities within large, spherical symmetrical, relaxed system like globular clusters, while also recognizing that the statistical conclusions of N-body models are much more important than the detailed, per-body results (Hénon, 1971a).

The simulation is split into two separate scales; a large-scale, smooth, mean gravitational-field, which represents the overall distribution of stellar subsystems within the cluster, and smaller-scale fluctuating fields which handle the interactions and evolution of constituent stars within the orbits of the mean field.

Within the small-scale field, rather than computing every step along each orbital time-step or the influence of every other star, Monte Carlo random selections of both are employed, and thus a smaller, random distribution of interactions are accounted

for, in comparison to N-body methods. This reduction in computations allows for much faster simulations, reducing the complexity of the complete model up to $\mathcal{O}(N)$ (Hénon, 1971b).

The models also permit the incorporation of various astrophysical processes, similar to N-body models and at both scales, such as stellar evolution, remnant formation, escaping objects and tidal truncation (Kremer et al., 2020a; Hypki & Giersz, 2013). They are also able to demonstrate mass segregation and its effects (Weatherford et al., 2020).

1.4.5 Model Comparisons

The various types of dynamical models differ in important practical details, and thus offer various advantages and disadvantages, and are well suited for different types of analysis.

Model Fitting

In order to make comparisons with and draw conclusions on real globular clusters, models must be fit to the observations of the system; velocity dispersions and anisotropy, surface density and brightness profiles, stellar mass functions, etc.

Despite their relative simplicity, DF models are often used for the fitting of observed profiles, due to their fast computation and the fact that they do not require knowledge of any difficult to constrain inputs such as orbits and tidal effects, yet are still able to capture basic physical ingredients such as two-body relaxation effects and tidal truncation (Zocchi et al., 2016). The models cost so little to compute that very fine grids can allow for very precise fits. The models are also easily extensible to

include, as in the case of LIMEPY, measures of multiple mass bins and anisotropy, which are important to represent clusters without bias.

Jean's models share many of the benefits found in the fitting of DF models, and can similarly be used on cluster observations, however the large amount of flexibility present in these models can also risk over-fitting the data, and can lead to noisy or unphysical results (Hénault-Brunet et al., 2019), while the lack of information on the distribution of individual mass components limits the the possible predictions which can be made of populations in mass segregated systems.

Equilibrium models are also fast enough to permit the practical application of various statistical fitting techniques, in order to attain a very precise fit to a number of datasets (e.g. Hénault-Brunet et al., 2020).

N-body models can be matched to various observables, however the high cost of computation means the feasible grid of models is relatively sparse, and thus the fit for any particular cluster may not be available, or match well. As $N = 10^6$ models are just becoming practical, many studies rely on the scaling of model runs of fewer particles, in order to make comparisons with observations (e.g. Baumgardt, 2017).

Monte Carlo models suffer from similar limitations to N-body models, although their decreased costs allow for somewhat finer grids and thus more variable initial conditions and easier matching to observations (e.g. Giersz et al., 2013; Rui et al., 2021b).

Stellar Populations

Equilibrium models, by definition, deal only with the distribution of instantaneous mass and velocity profiles. As such, the models themselves cannot account for many temporal astrophysical processes, such as stellar evolution. In order to account for

things such as the evolution of different mass populations in multimass models, additional outside algorithms are required in order to learn something about the initial population of stars (e.g. Balbinot & Gieles, 2018; Hénault-Brunet et al., 2019, 2020).

These models, for the same reasons, do not account for individual orbits and interactions. They are unable to provide a view of specific objects and could not follow the history of the cluster or any star, nor provide information on its interactions. This means that they cannot reveal direct information on processes such as BH mergers. Multimass DF and Jeans models instead produce continuous profiles of mass, which allow the models to, for example, infer the amount of dark mass in a cluster, without directly simulating any individual remnants (Hénault-Brunet et al., 2019). Jeans models, however, also possess the important caveat that, while allowing for the inference of the underlying gravitational potential and mass profile, they do not self-consistently model the effect of mass segregation and the distribution of different mass components.

Evolutionary models, on the other hand, are able to account for stellar evolution over the lifetime of their systems, incorporating existing prescriptions such as the popular "single star evolution" (`SSE`) and "binary star evolution" (`BSE`) libraries (e.g. Kremer et al., 2020a). These algorithms are able to account for remnant formation through various channels, and directly handle strong encounters such as BH mergers, and their effects. It is possible to use these models to examine the formation and evolution of several exotic object populations; millisecond pulsars, blue stragglers, cataclysmic variables, Type Ia supernovae, and merging compact binaries (Hypki & Giersz, 2013).

1.5 This Thesis: Exploring Globular Cluster IMFs and Dark Remnants

In this thesis we intend to model and study in detail the stellar (initial) mass functions and remnant populations of a large sample of Milky Way GCs.

In order to explore the stellar mass function in globular clusters, including its potential variability and relationship with metallicity, we will fit dynamical models of a number of Milky Way clusters to various observables, including proper motions, line-of-sight velocities, number densities and present-day mass functions. To ensure the most accurate fit of all model parameters, including the mass function exponents, to real globular clusters, multimass LIMEPY DF models are used. Their low computational cost allows for the application of statistical fitting techniques, ensuring both that the full range of possible parameter space is explored (rather than the small grid of values typical in evolutionary model studies), and that the most accurate models possible (as dictated by current observations) are attained. Utilizing multimass models allows for the probing of various stellar mass components, necessary for fitting the PDMF and constraining the IMF, and also for exploring the distribution of black holes and other dark remnants in the clusters. Inferring the presence and distribution of black holes within our clusters will allow us to better understand and constrain the initial massive populations and evolutionary history of Milky Way globular clusters.

1.5.1 Outline of Thesis

The structure of the remainder of this thesis is as follows. The multimass LIMEPY models and the mass function evolution algorithm is explained in more detail in Chapter 2. Chapter 3 describes the methods and sources used to obtain all observational

cluster data used to fit the models, as well as how the cluster sample was chosen. The model fitting process, including descriptions of all probabilities and Bayesian sampling techniques, is given in Chapter 4. The novel software library and fitting pipeline which was created to facilitate this fitting is also presented in this chapter. The results of the fitting of all clusters in our sample based on these methods are given in Chapter 5, along with some short analysis of the best-fitting parameter distributions. The (initial) mass function results for all clusters are presented and explored in more detail in Chapter 6. Chapter 7 examines the black hole and other remnant populations in all clusters, and takes a in-depth look at a handful of clusters of interest. Finally, we conclude in Chapter 8.

Chapter 2

Models

To model the mass distribution of the globular clusters analyzed in this work, we use the LIMEPY multimass distribution-function based models (Gieles & Zocchi, 2015), as described in Section 1.4.1 and characterized by the DF in Equation (1.13). These models compute the phase-space density and the moments of the velocity distribution as a function of distance from cluster centre for stars and remnants of different masses.

2.1 Model Parameters

The models are defined by 10 free parameters (listed in Table 2.1) which dictate the stellar mass evolution and physical solution of the LIMEPY DF.

The overall structure of these models is controlled by the (dimensionless) central potential parameter $\hat{\phi}_0$, which is used as a boundary condition for solving Poisson's equation and defines how centrally concentrated the model is. The cluster model is spherical out to the truncation radius of the system, where its energy is reduced, mimicking the effects of the host galaxy's tides, which reduce the escape velocity of

Parameter	Description
$\hat{\phi}_0$	Dimensionless central potential
M	Total system mass [10^6 $M_\odot$]
g	Truncation parameter
r_h	Half-mass radius
$\log(r_a)$	Anisotropy radius
δ	Velocity scale mass dependence
α_1	MF exponent (0.1 $M_\odot < m \leq 0.5$ $M_\odot$)
α_2	MF exponent (0.5 $M_\odot < m \leq 1$ $M_\odot$)
α_3	MF exponent (1 $M_\odot < m \leq 100$ $M_\odot$)
BH_{ret}	Black hole retention fraction [%]
F	Mass function nuisance parameter
s^2	Number density nuisance parameter
d	Heliocentric distance [kpc]

Table 2.1: List of free parameters and their descriptions. First six are structural LIMEPY parameters (Section 2.1), next four define the mass function (Section 2.2), and final three aid in comparing models to observations (Section 4.1).

stars, making it easier for them to escape. The sharpness of this energy truncation is defined by the truncation parameter g, as the models behave like polytropes near the truncation radius, with a polytropic index given by $n = g + 7/2$ (see Equation (20) in Gieles & Zocchi 2015). Lower g values result in a more abrupt energy truncation, increasing up to models with the maximum possible finite extent at $g = 3.5$, while finite models with realistic values of $\hat{\phi}_0$ are limited to $g \lesssim 2.5$ (Gieles & Zocchi, 2015).

The mass and size scales of the model can be expressed in any desired physical units by adopting corresponding values for the normalization constant A and the global velocity scale s in the LIMEPY DF (Equation (1.13)). We opt to scale the models to match observations using the parameters for total cluster mass M and 3D half-mass radius r_h as mass and size scales, which are used internally to compute the A and s scales.

LIMEPY models allow for velocity anisotropy through an exponential angular momentum term in the DF. With this term, the system is isotropic in the core, gains a degree of radial velocity anisotropy at intermediate distances from the centre, and then becomes isotropic once more near the truncation radius. This parametrization mimics how GCs naturally develop radially-biased velocity anisotropy throughout their evolution as a result of two-body relaxation and tides (Zocchi et al., 2016; Tiongco et al., 2016). The two-body relaxation process drives the core of clusters to isotropy, however scattering (on preferentially radial orbits) of stars outside the core acts to increase the radial component of the velocity dispersion. Finally, a combination of the tidal torque from the host galaxy, which induces a transfer of angular momentum near the Jacobi radius to stellar orbits in the tangential direction (Oh & Lin, 1992), and the preferential loss of stars on radial orbits (Tiongco et al., 2016), act to increase the tangentiality of the outer stars, damping the amount of radial anisotropy and leading to a return to isotropy near the immediate edge of the system. The anisotropy radius

parameter r_a dictates the amount of radial velocity anisotropy present in the models. The smaller the value of r_a, the more anisotropic the system. In the limit $r_a \to \infty$, the models become entirely isotropic. In practice, models with r_a greater than the truncation radius can be considered isotropic.

The exact meaning of both the $\hat{\phi}_0$ and r_a parameters depends on the definition of the mean mass (Peuten et al., 2017). In this work we adopt the global mean mass, that is, the mean mass of the entire cluster.

The multimass version of the LIMEPY DF is defined by the sum of similar component DFs for each mass bin j, with mass-dependent velocity (s_j) and anisotropy radius ($\hat{r}_{a,j}$) scales. The mass-dependent velocity scaling captures the trend towards kinetic energy equipartition among stars of different masses and models the effects of mass segregation. The velocity scale is defined based on the parameter δ, such that $s_j \propto s m_j^{-\delta}$, where s is defined above. The mass-dependent anisotropy radius is defined in a similar fashion, using a parameter η ($r_{a,j} \propto r_a m_j^{\eta}$). For the analysis presented in this thesis we have chosen to fix η to 0, defining the anisotropy to be identical among all mass bins, the default assumption in multimass DF-based models. Our observations do not contain the information that would allow us to constrain the mass-dependence of the velocity anisotropy (e.g. Peuten et al., 2017), and thus the η parameter.

Finally, the constituent discrete mass components which approximate the continuous mass spectrum of a GC are represented in the multimass LIMEPY models by the total (M_j) and mean (m_j) masses of each mass bin. These must be defined *a priori* by external methods, based on the mass function ($\alpha_1, \alpha_2, \alpha_3$) and black hole retention percentage (BH_{ret}) parameters. The algorithm, which takes into account stellar evolution to predict the mean and total mass in stellar remnant bins, is described in

detail in Section 2.2 below.

External to the LIMEPY models themselves, we also employ a few extra parameters to aid in the fitting of the models to observations. These parameters are explained in more detail in Section 4.1.

2.2 Mass Function Evolution

DF-based models, such as LIMEPY, compute the distribution of mass and velocity in a system in equilibrium. They are instantaneous "snapshot" models, and do not directly simulate any temporal astrophysical processes during their computation, including stellar evolution. As such, in order to determine the realistic mass populations for which the model will determine the phase-space distribution, we must incorporate a separate prescription for stellar evolution from an initial mass function, over the age of the cluster, to the present-day stellar and remnant mass functions.

In keeping with the formulation of canonical IMFs (e.g. Kroupa, 2001), we use a 3-component broken power law:

$$\xi(m) \propto \begin{cases} m^{-\alpha_1} & 0.1\ \mathrm{M}_\odot < m \leq 0.5\ \mathrm{M}_\odot, \\ m^{-\alpha_2} & 0.5\ \mathrm{M}_\odot < m \leq 1\ \mathrm{M}_\odot, \\ m^{-\alpha_3} & 1\ \mathrm{M}_\odot < m \leq 100\ \mathrm{M}_\odot, \end{cases} \tag{2.1}$$

where the α_i parameters define the exponential 'slope' of each component, and are allowed to vary freely during model fitting, and $\xi(m)\,\mathrm{d}m$ is the number of stars with masses within the interval $[m,\ m + \mathrm{d}m]$. It should be noted here that our choices of break masses (0.1, 0.5, 1, 100 $\mathrm{M}_\odot$) are different than that of Kroupa (2001), to allow for a more specific study of the high-mass ($m > 1\,\mathrm{M}_\odot$) regime.

To evolve the population of stars to the present day we follow the algorithm first described by Balbinot & Gieles (2018) and expanded upon in the `ssptools`[1] library. This method is summarized below.

To begin, the rate of change of the number of main-sequence stars in each mass bin over time is given by the equation:

$$\dot{N}(m_{to}) = -\left.\frac{\mathrm{d}N}{\mathrm{d}m}\right|_{m_{to}} \left|\frac{\mathrm{d}m_{to}}{\mathrm{d}t}\right| \tag{2.2}$$

where the amount of stars per unit mass (dN/dm) at the turn-off mass (m_{to}) is given by the IMF, and the rate of change of the turn-off mass can be derived by approximating the lifetime of main-sequence stars as a function of initial mass:

$$t_{ms} = a_0 \exp(a_1 m^{a_2}) \tag{2.3}$$

where the a_i coefficients are interpolated from the Dartmouth Stellar Evolution Program models (Dotter et al., 2007, 2008). This equation can then be inverted and differentiated to find the rate of change:

$$\frac{\mathrm{d}m_{to}}{\mathrm{d}t} = \frac{1}{a_1 a_2}\frac{1}{t}\left(\frac{\log(t/a_0)}{a_1}\right)^{1/a_2 - 1} \tag{2.4}$$

Equation (2.2) dictates the amount of stars which evolve off the main sequence at an age t. As these stars evolve, the stellar remnants they will form will depend (both in type and in mass) on their initial mass and metallicity, and a functional initial-final

[1] https://github.com/SMU-clusters/ssptools

mass relation (IFMR):

$$\frac{m_r}{\mathrm{M}_\odot} = \begin{cases} \sum_{j=0}^{10} b_j m_i^j & m_i < m_{\mathrm{WD,max}} \text{ (WD)}, \\ 1.4 & m_{\mathrm{WD,max}} \leq m_i < m_{\mathrm{BH,min}} \text{ (NS)}, \\ \sum_{j=0}^{1} c_j m_i^j & m_{\mathrm{BH,min}} \leq m_i < m_{\mathrm{BH,a}} \text{ (BH)}, \\ \sum_{j=0}^{1} d_j m_i^j & m_{\mathrm{BH,a}} \leq m_i < m_{\mathrm{BH,b}} \text{ (BH)}, \\ \sum_{j=0}^{6} e_j m_i^j & m_{\mathrm{BH,b}} \leq m_i \text{ (BH)}, \end{cases} \tag{2.5}$$

where m_i is the initial mass of the star, m_r is final mass of the formed remnant, and the coefficients (b_j, c_j, d_j, e_j) are constants defining the individual polynomials. The sources of this adopted IFMR are described below.

The maximum initial mass which will form a white dwarf (WD) is interpolated, based on the metallicity, from the MIST 2018 isochrones (Dotter, 2016; Choi et al., 2016). The WD IFMR is computed as a 10th order polynomial, with coefficients similarly extracted from the MIST models. The minimum mass required to form a black hole (BH) is taken in the same fashion from the stellar evolution library (SSE) used in the NBODY6 models (Hurley et al., 2000; Aarseth, 2003). The BH IFMR is approximated by three separate polynomials, within three different mass ranges, and is also dependent on metallicity. These relations are shown in Figure 2.1. All stars with initial masses between the WD and BH precursor masses are assumed to form neutron stars (NS). For simplicity, their final mass is always assumed to be $1.4\mathrm{M}_\odot$, regardless of the initial mass.

The amount and final mass of these remnants (as dictated by Equation (2.2))

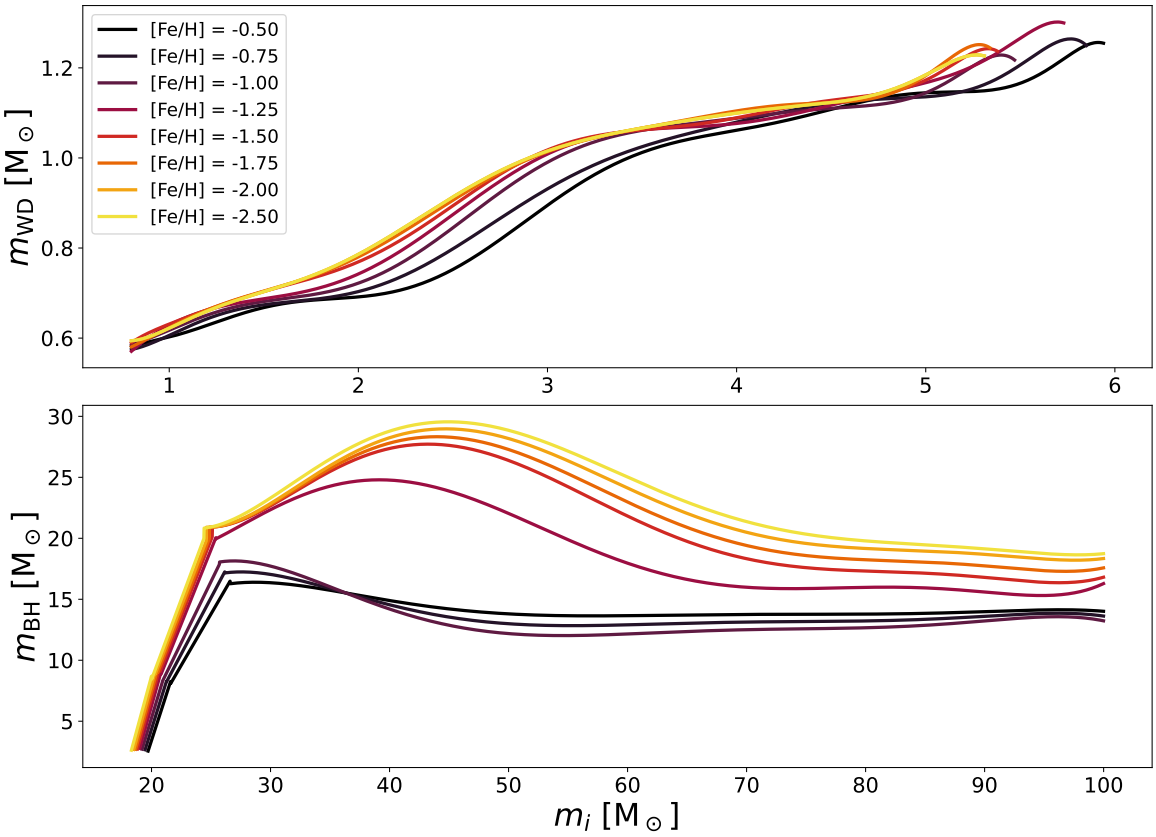

Figure 2.1: Adopted metallicity-dependent initial-final mass relations for white dwarf and black hole formation. Lower metallicities generally result in higher final remnant masses.

must then be scaled downwards by an "initial retention fraction" $f_{\rm ret}$, in order to mimic the loss of newly formed remnants due to natal kicks. For WDs this is always equal to 1. In this analysis, we assume a NS retention fraction of 10%, as is common (e.g. Pfahl et al., 2002), however as shown in Hénault-Brunet et al. (2020) our results are insensitive to this exact value. The mass function evolution algorithm includes two more specific prescriptions for the loss of black holes, accounting for dynamical ejections on top of the typical natal kicks.

Firstly the ejection of, primarily low-mass, BHs through natal kicks is simulated. We begin by assuming that the kick velocity is drawn from a Maxwellian distribution with a dispersion of $265\,{\rm km\,s^{-1}}$, as has been found for neutron stars (Hobbs et al.,

2005). This velocity is then scaled down linearly by the "fallback fraction" f_b, the fraction of the precursor stellar envelope which falls back onto the BH after the initial supernova explosion. This fraction is interpolated from a grid of SSE models based on the BH precursor's initial mass and metallicity (Banerjee et al., 2020). The fraction of black holes retained in each mass bin is then found by integrating the Maxwellian kick velocity distribution from 0 to the system escape velocity. The initial system escape velocity of each cluster was estimated by assuming that about half of the initial cluster mass was lost through stellar evolution, while adiabatically expanding the cluster to a present-day half-mass radius a factor of two larger than the initial value, resulting in an initial escape velocity twice as large as the present-day value. A set of preliminary models were computed for all clusters, and the initial escape velocity was computed based on the best-fitting central density as $v_{\rm esc} = 2\sqrt{2\phi_0}$.

Black holes are also ejected over time from the core of GCs due to dynamical interactions with one another (e.g. Breen & Heggie, 2013a,b). This process is simulated through the removal of BHs, beginning with the heaviest mean-mass bins (with larger gravitational interaction cross-sections) through to the lightest (Morscher et al., 2015). This is carried out iteratively until the combination of mass lost through both the natal kicks and these dynamical ejections equals the fraction of BHs specified by the black hole retention fraction parameter ($\rm BH_{\it ret}$).

The final avenue for cluster mass loss is through the escape of stars and remnants driven by two-body relaxation and lost to the host galaxy. Such losses, in a mass segregated cluster, are dominated by the escape of low-mass objects from the outer regions of the cluster. Determining the overall losses through this process is a complicated task, dependent on the dynamical history and orbital evolution of the cluster, which we do not attempt to model here. We thus opt to ignore this preferential loss of low-mass stars and do not further model the escape of any stars, apart from

through the processes described above. This means that the low-mass α exponents determined here may, in most cases, describe most accurately the PDMF rather than the low-mass IMF of our clusters. This is discussed in more detail in Chapter 6.

Chapter 3

Cluster Data

In this work we determine best-fitting model parameters for a large number of Milky Way globular clusters through the comparison of the phase-space distribution of stars in the LIMEPY models to analogous observations of GC structure and kinematics.

3.1 Cluster Selection

The clusters analyzed in this work were selected from the population of Milky Way GCs in order to best study the possible relationship of the mass function with metallicity. To do so, we choose clusters over a range of metallicities, with most clusters in our sample being metal-poor ([Fe/H] $\lesssim -1.0$). The greatest discerning factor used in cluster selection was the quantity and quality of data available. We searched for clusters with a combination of adequate mass function depth and radial coverage from HST photometry, and sufficient kinematic data to constrain the models. These selection criteria lead to the choice of 40 final clusters, listed in Table 3.1.

Cluster	[Fe/H]	Mass [10^6 $M_\odot$]	Cluster	[Fe/H]	Mass [10^6 $M_\odot$]
NGC 104	−0.72	0.85	NGC 6218	−1.37	0.11
NGC 288	−1.32	0.10	NGC 6254	−1.56	0.21
NGC 362	−1.26	0.28	NGC 6266	−1.18	0.60
NGC 1261	−1.27	0.18	NGC 6341	−2.31	0.33
NGC 1851	−1.18	0.35	NGC 6352	−0.64	0.07
NGC 2808	−1.14	0.88	NGC 6362	−0.99	0.13
NGC 3201	−1.59	0.16	NGC 6366	−0.59	0.04
NGC 4372	−2.17	0.20	NGC 6397	−2.02	0.10
NGC 4590	−2.23	0.13	NGC 6541	−1.81	0.30
NGC 4833	−1.85	0.20	NGC 6624	−0.44	0.16
NGC 5024	−2.10	0.46	NGC 6656	−1.70	0.51
NGC 5139	−1.53	3.94	NGC 6681	−1.62	0.13
NGC 5272	−1.50	0.40	NGC 6723	−1.10	0.18
NGC 5904	−1.29	0.40	NGC 6752	−1.54	0.27
NGC 5927	−0.49	0.28	NGC 6779	−1.98	0.19
NGC 5986	−1.59	0.34	NGC 6809	−1.94	0.19
NGC 6093	−1.75	0.31	NGC 6981	−1.42	0.07
NGC 6121	−1.16	0.09	NGC 7078	−2.37	0.61
NGC 6171	−1.02	0.08	NGC 7089	−1.65	0.64
NGC 6205	−1.53	0.54	NGC 7099	−2.27	0.14

Table 3.1: The names (NGC identifications), metallicity (Harris, 1996) and mass (Baumgardt & Hilker, 2018) of all 40 initially selected clusters.

3.2 Observations

Models are fit to all chosen GCs through comparison with a variety of observational datasets, which help directly constrain the phase-space distribution of visible cluster stars. This, in turn, provides indirect constraints on the amount and distribution of dark mass (in both faint low-mass stars and dark remnants) as, together with mass segregation, the possible distribution of cluster mass among different components has limited flexibility.

We utilize a large number of observables from various sources, while aiming to provide as much homogeneity between clusters as possible. Where multiple data sources exist for the same observable, we attempt to bring them into agreement with one another. Data sources specific to each cluster can be seen in the figures shown in Appendix A.

3.2.1 Proper Motions

Proper motions (PM), the astrometric measure of an object's apparent velocity, can be observed, in the simplest sense, through the repeated measurements of an object's changing position at different epochs.

Radial profiles of the dispersion of proper motions of cluster stars are used to constrain the cluster velocity dispersion profiles, and in turn the total cluster mass and its distribution. By incorporating the kinematics in both the radial and tangential directions in the plane of the sky, we are also able to constrain the amount of velocity anisotropy in the system. We define these components, on the sky, such that the radial component is positive outwards from the cluster centre, and the tangential component is positive in the counterclockwise rotational direction on the sky. Given the proper

motions of a star in a cluster-centred orthographic projection (e.g. equation (2) in Gaia Collaboration et al. 2018), the radial (μ_R) and tangential (μ_T) components are defined as:

$$\mu_R \equiv \frac{(x\mu_x + y\mu_y)}{R} \tag{3.1}$$

$$\mu_T \equiv \frac{(y\mu_x - x\mu_y)}{R} \tag{3.2}$$

where x, y, μ_x and μ_y are the orthographic positions and proper motions and $R = \sqrt{x^2 + y^2}$ is the projected distance from the cluster centre, which is taken from Baumgardt (2017) [1].

We employ proper motion dispersion profiles, from various sources, in the fits of all clusters analyzed. These sources are described below.

Gaia EDR3

We extract PM dispersion profiles in both components from Gaia Early Data Release 3 (EDR3; Gaia Collaboration et al., 2021) proper motions for all clusters.

The catalogue of cluster stars, along with their membership probabilities, is taken from Vasiliev & Baumgardt (2021). We then follow similar methodology to Vasiliev (2019) and Vasiliev & Baumgardt (2021) to construct binned dispersion profiles in both directional components.

First we select only stars which pass the quality filters discussed in Vasiliev & Baumgardt (2021) and have 5-parameter astrometric solutions, then we cut all remaining stars with a membership probability below 90%. The right-ascension and declination components of proper motion provided by Gaia are first subtracted from the cluster mean computed by Vasiliev & Baumgardt (2021) and then transformed

[1] Cluster centres typically vary between different studies on the order of a few arcsec, and would have a negligible impact on these profiles.

Cluster	Member Stars	Stars per bin	Cluster	Member Stars	Stars per bin
NGC 104	39761	3600	NGC 6218	6123	595
NGC 288	4635	760	NGC 6254	7130	1735
NGC 362	3839	760	NGC 6266	682	165
NGC 1261	1160	545	NGC 6341	4297	1400
NGC 1851	2436	395	NGC 6352	1513	550
NGC 2808	4638	900	NGC 6362	5542	1385
NGC 3201	11391	875	NGC 6366	1630	265
NGC 4372	2487	600	NGC 6397	12308	1365
NGC 4590	3203	1035	NGC 6541	2292	515
NGC 4833	2316	365	NGC 6624	96	45
NGC 5024	3338	1080	NGC 6656	4328	430
NGC 5139	52854	4030	NGC 6681	648	300
NGC 5272	8941	1260	NGC 6723	2130	950
NGC 5904	9141	1820	NGC 6752	16155	2015
NGC 5927	658	100	NGC 6779	1533	500
NGC 5986	835	210	NGC 6809	7420	1830
NGC 6093	1046	290	NGC 6981	726	690
NGC 6121	5208	345	NGC 7078	4467	1110
NGC 6171	1625	385	NGC 7089	2957	935
NGC 6205	9537	1875	NGC 7099	2946	715

Table 3.2: The total number of stars in the Gaia EDR3 catalogue which pass our quality and membership criterion, and the number of stars per radial bin used to construct the Gaia proper motion dispersion profiles for each cluster.

to a cluster-centred orthographic projection (by equation (2) in Gaia Collaboration et al. (2018)) and finally to radial and tangential components using Equations (3.1) and (3.2).

The stars are then binned based on their radial distance from the cluster centre, with each bin containing an equal number of stars. The number of stars per bin (listed in Table 3.2) differs for each cluster, and was chosen to maximize the radial coverage while still providing a sufficient number of stars with which to calculate reliable dispersions in each bin.

Following the conclusions of Vasiliev & Baumgardt (2021), in order to account for underestimations in the statistical uncertainty of proper motions of Gaia sources in dense regions, we scale the PM uncertainties in each bin by a density-dependent

factor η:

$$\eta = \left(1 + \frac{\Sigma}{\Sigma_0}\right)^{\zeta} \tag{3.3}$$

where (from Table 1 in Vasiliev & Baumgardt, 2021) $\Sigma_0 = 10\,\mathrm{stars/arcmin}^2$ and $\zeta = 0.04$, and Σ is computed, assuming spherical symmetry, by counting the density of stars within the area of each radial bin.

We then fit a multivariate Gaussian distribution to the proper motions of all stars in each bin, following the likelihood:

$$\ln \mathcal{L} = -\frac{1}{2}\left[\ln(\det(\Sigma)) - (\mu - \mathbf{v})^T \mathbf{\Sigma}^{-1} (\mu - \mathbf{v})\right] \tag{3.4}$$

where μ is the mean of the distribution, $\mathbf{v}$ is the (flattened) vector of proper motions for all stars in both radial and tangential directions, and $\mathbf{\Sigma}$ is the corresponding covariance matrix.

The covariance matrix is constructed of two parts; $\mathbf{\Sigma} = \mathbf{\Sigma}_{\mathrm{stat}} + \mathbf{\Sigma}_{\mathrm{int}}$. Both constituent covariances are block-diagonals matrices containing N_{stars} two-by-two blocks along the diagonal:

$$\mathbf{\Sigma}_{\mathrm{stat}} \equiv \begin{pmatrix} E_1 & 0_{2\times2} & \cdots & 0_{2\times2} \\ 0_{2\times2} & E_2 & \cdots & 0_{2\times2} \\ \vdots & \vdots & \ddots & \vdots \\ 0_{2\times2} & 0_{2\times2} & \cdots & E_N \end{pmatrix}, \quad E_i \equiv \begin{pmatrix} \epsilon_{i,R}^2 & \rho_i \epsilon_{i,R} \epsilon_{i,T} \\ \rho_i \epsilon_{i,R} \epsilon_{i,T} & \epsilon_{i,T}^2 \end{pmatrix} \tag{3.5}$$

$$\mathbf{\Sigma}_{\mathrm{int}} \equiv \begin{pmatrix} S_1 & 0_{2\times2} & \cdots & 0_{2\times2} \\ 0_{2\times2} & S_2 & \cdots & 0_{2\times2} \\ \vdots & \vdots & \ddots & \vdots \\ 0_{2\times2} & 0_{2\times2} & \cdots & S_N \end{pmatrix}, \quad S_i \equiv \begin{pmatrix} \sigma_R^2 & 0 \\ 0 & \sigma_T^2 \end{pmatrix} \tag{3.6}$$

where $\epsilon_{i,R}, \epsilon_{i,T}$ are the PM uncertainties in both components of the i-th star, ρ_i is the correlation coefficient between the components, and σ_R, σ_T are the PM dispersions, for both components, of the bin.

Vasiliev (2019) also included a third component in the covariance matrix representing the systematic error present in the astrometry (related to the Gaia scanning law), however we find that the magnitude of this component is negligible compared to the (scaled) uncertainties and dispersions, and thus is neglected here.

This likelihood was then explored using nested sampling (see Section 4.2.1), with the mean and dispersion in both components allowed to vary freely.

The weighted mean and standard deviation of this dispersion was used, in each bin, to construct the PM dispersion profiles, with the radial position of each bin taken as the median of the positions of all constituent stars.

Supplementary Datasets

We supplement the Gaia proper motion datasets of specific clusters, where further PM studies are available from the Hubble Space Telescope (HST).

Watkins et al. (2015) presented profiles of proper motion dispersions in the central regions of 22 globular clusters, based on the HST catalogues of Bellini et al. (2014). The profiles consists only of catalogue stars brighter than 1 mag below the main-sequence turn off and are trimmed based on data quality and velocity sigma-clipping, in order to calculate the most accurate and unbiased kinematics possible. These brightness and quality filters leave between around 1000 to 15000 stars per cluster, save for NGC 7099 which has the smallest sample size in the study and only ~ 100 final stars.

These catalogues are binned radially and fit to a Gaussian likelihood using a Monte-Carlo technique, resulting in dispersion profiles for both radial and tangential components for all clusters, with typical uncertainties on the order of ~ 0.001 m arcsec/yr. Our analysis overlaps with this sample in 15 clusters (NGC 1851, NGC 2808, NGC 5139, NGC 5904, NGC 5927, NGC 6266, NGC 6341, NGC 6362, NGC 6397, NGC 6624, NGC 6656, NGC 6681, NGC 6752, NGC 7078 and NGC 7099), in which case we utilize the presented total dispersion $\sigma = \sqrt{(\sigma_T^2 + \sigma_R^2)/2}$ and anisotropy ratio σ_T/σ_R.

Libralato et al. (2019) provided an in-depth study of the internal kinematics of NGC 6352 as part of the Hubble Space Telescope "UV Legacy Survey of Galactic Globular Clusters" program. The proper motion profiles, extending out to ~ 1.5 core radii (75 arcsec), were extracted in similar fashion to Bellini et al. (2014).

Raso et al. (2020) compiled archival HST imaging of the central region of NGC 1261. Proper motion profiles, extending out to 90 arcsec, were extracted once again based on Bellini et al. (2014), and restricted by magnitude to only include bright stars near the turn off mass.

The quality of data and the resulting dispersion uncertainties for both of these supplementary analyses are similar to those of Watkins et al. (2015).

3.2.2 Line-of-Sight Velocities

The kinematic data is also supplemented by line-of-sight (LOS) velocity dispersion profiles, providing a 3-dimensional view of the cluster dynamics. The LOS velocities used to construct the dispersion profiles are determined from spectrography of each individual star, by comparing absorption lines in the stellar spectra to spectral

models[2].

The majority of the LOS dispersion profiles used come from compilations of different surveys and programs. Baumgardt (2017) gathered, from the literature, 95 publications with large enough (> 20 stars) LOS velocity datasets for 45 GCs (31 in common with our sample), amounting to $\sim 25\,500$ stars in total. Baumgardt & Hilker (2018) expanded on this catalogue by including additional ESO/Keck archival data of the LOS velocities of $\sim 15\,000$ stars in 90 GCs. The median uncertainty of the individual velocities in these two compilations is about $0.5\,\mathrm{km\,s^{-1}}$. In both cases, the different datasets were combined by scaling them to the cluster's mean radial velocity, and iteratively excluding all stars more than three standard deviations from the mean as binaries and background stars. The LOS dispersion profiles were then computed by maximizing a Gaussian likelihood function, resulting in average uncertainties on the dispersion at a given projected radial distance on the order of $\sim 0.5\,\mathrm{km\,s^{-1}}$, in the clusters which are a part of our survey.

Baumgardt et al. (2019a) derived the velocity dispersion profiles of 127 GCs (including our entire sample) using the Gaia DR2 radial velocity data. This catalogue of stars was matched to that of Baumgardt & Hilker (2018), and scaled to a common mean velocity. Similar outlier removal and maximum-likelihood approaches were then used to compute the LOS velocity dispersion profiles, out to projected distances from the centre of around 100-700 arcsec, depending on surrounding field densities.

Dalgleish et al. (2020) followed this work by considering a subset of 1622 stars in 59 GCs from the WAGGS survey, from the WiFeS integral field spectrograph. The chosen clusters were selected to complement the Baumgardt et al. (2019a) datasets and increase the sample sizes in the core (~ 20 arcsec) of the systems.

[2] All LOS velocity dispersion profiles used were retrieved from the catalogue at https://people.smp.uq.edu.au/HolgerBaumgardt/globular/.

These datasets are further complemented in the cores of some clusters by the LOS dispersion profiles presented by Kamann et al. (2018), who gathered data for some $\sim$ 200,000 stars within the half-light radius of 22 GCs (14 in common with our sample) using the MUSE integral-field-unit spectrograph on the VLT. Spectra were extracted for all stars within the field-of-view of each pointing, before cluster membership and signal-to-noise quality cuts were applied. LOS velocity dispersion profiles were then determined by maximizing a similar Gaussian likelihood through a Markov-Chain Monte-Carlo sampler, resulting in profiles with uncertainties on the same order as the above profiles ($\sim 0.5\,\mathrm{km\,s^{-1}}$).

3.2.3 Number Density Profiles

Radial profiles of the projected surface number density of stars in our GCs are vital in constraining the spatial structure and concentration of the clusters.

The projected number density profiles of most clusters are taken from de Boer et al. (2019), who utilized counts of member stars from Gaia DR2, binned radially, for 81 Milky Way clusters. Membership was determined, for stars up to a faint magnitude limit of $G = 20$, based on the Gaia proper motions. To aid with the coverage of the cluster centres, where Gaia is incomplete and struggles with crowding in all but the least dense GCs, the authors stitched the Gaia profiles together with profiles from HST photometry (Miocchi et al., 2013) and a collection of ground-based surface brightness profiles (Trager et al., 1995). These profiles from the literature were scaled to match the Gaia profiles in the regions where they overlap, with the final profile being constructed of Gaia counts in all regions with a density lower than 10^5 stars/deg^2 and literature profiles otherwise. de Boer et al. (2019) also computed a constant background contamination level for each cluster, computed as the average

stellar density between 1.5 and 2 Jacobi radii, which we subtract from the entire profile before fitting.

Three of our selected clusters (NGC 4372, NGC 4833 and NGC 5927) are not presented in the catalogue of de Boer et al. (2019), as they are either not present, or have insufficient coverage in the Trager et al. (1995) catalogue. NGC 5927, in particular, possesses an atypical central jump in its surface brightness profile, which may be the result of a few very bright stars. In future work, the number density profiles for these clusters may be constructed based on other HST sources (e.g. Sarajedini et al., 2007) and Gaia EDR3, however for this thesis we opt to remove these clusters from our sample.

3.2.4 Mass Functions

To provide constraints on the global present-day mass function of the clusters, the degree of mass segregation and the total mass in visible stars, we compare our models against measurements of the stellar mass function in radial annuli and mass bins obtained from deep HST photometry.

The mass function data for each cluster was derived from archival HST photometry by Baumgardt et al. (2022) and includes data from large-scale archival surveys (e.g. Sarajedini et al., 2007; Simioni et al., 2018). Stellar photometry and completeness correction of the data was done using `DOLPHOT` (Dolphin, 2000, 2016). Stellar number counts were then derived as a function of stellar magnitude and distance from the cluster centre and were then converted into stellar mass functions through isochrone fits. The compilation of images is made up of several HST fields for each cluster, at varying distances from the cluster centres. The observations typically cover stars within a mass range of $\sim 0.16 - 0.8\,\mathrm{M}_{\odot}$. The large radial and mass ranges covered

allow us to constrain the varying local stellar mass function as a function of distance from the cluster centre, and therefore the degree of mass segregation in the cluster.

Chapter 4

Model Fitting

The models described in Chapter 2 are constrained by the data described in Chapter 3 in order to provide distributions of the best-fitting model parameters that describe each cluster, which are determined through Bayesian parameter estimation techniques.

4.1 Probability Distributions

Given a model M, the probability associated with a given set of model parameters Θ, subject to some observed data $\mathcal{D}$ is given by the Bayesian posterior:

$$P(\Theta \mid \mathcal{D}, M) = \frac{P(\mathcal{D} \mid \Theta, M)P(\Theta \mid M)}{P(\mathcal{D} \mid M)} = \frac{\mathcal{L}(\Theta)\pi(\Theta)}{\mathcal{Z}} \tag{4.1}$$

where $\mathcal{L}$ is the likelihood, π is the prior and $\mathcal{Z}$ is the evidence.

4.1.1 Likelihood

In this work, the total log-likelihood function $\ln(\mathcal{L})$, for all data $\mathcal{D}$ considered for a certain cluster, is given simply by the summation of all log-likelihood functions for each individual dataset $\mathcal{D}_i$:

$$\ln(\mathcal{L}) = \sum_{i}^{\text{datasets}} \ln(P(\mathcal{D}_i \mid \Theta)) = \sum_{i} \ln(\mathcal{L}_i(\Theta))) \tag{4.2}$$

and each observational dataset, as described in Section 3.2, has its own component likelihood function $\ln(\mathcal{L}_i)$, detailed below.

In order to compare all observed quantities with model predictions, certain quantities, which involve angular units (radial distances, proper motions, cluster sizes, etc.) must be converted to the projected, linear model lengths. To do so, we introduce the heliocentric distance to the GC as a new free parameter d, and use the velocity and position conversions:

$$v_T = 4.74\ d\ \cdot \mu \tag{4.3}$$

$$r = 2\ d \cdot \tan\left(\frac{\theta}{2}\right) \tag{4.4}$$

where v_T is the plane-of-the-sky velocity in $\mathrm{km\,s^{-1}}$, μ is the observed proper motion in arcsec/yr, r is the projected length in pc, θ is the observed angular separation in rad.

Velocity Dispersion Profiles

The likelihood function used for all velocity dispersions (LOS and PM) is a Gaussian, over a number of dispersion measurements at different projected radial distances:

$$\ln(\mathcal{L}_i) = \frac{1}{2}\sum_j \left(\frac{(\sigma_{\rm obs}(r_j) - \sigma_{\rm model}(r_j))^2}{\delta\sigma^2_{\rm obs}(r_j)} - \ln\big(\delta\sigma^2_{\rm obs}(r_j)\big) \right) \tag{4.5}$$

where $\sigma(r_j)$ corresponds to the dispersion at a distance r_j from the cluster centre, with corresponding uncertainties $\delta\sigma(r_j)$. Dispersions with subscript *obs* correspond to the observed dispersions and uncertainties, while subscript *model* corresponds to the predicted model dispersions.

Number Density Profiles

The likelihood function used for the number density profile datasets is a modified Gaussian likelihood.

The translation between the surface brightness measurements and discrete star counts (both considered for the number density profiles, as discussed in Section 3.2.3), is difficult to quantify exactly. To compare star counts above a magnitude limit to the integrated light of a surface- brightness profile would require precise knowledge of the mass-to-light ratio for each mass bin, which is an uncertain quantity especially for evolved stars. To account for this in the fitting procedure, the model is actually fit on the *shape* of the number density profile, rather than on the absolute star counts. To accomplish this the number density profile of the model is scaled to have the same mean value as the observed and combined profiles. As in Hénault-Brunet et al. (2020),

the constant scaling factor K is chosen to minimize the chi-squared distance:

$$K = \frac{\sum_j \Sigma_{obs}(r_j)\Sigma_{model}(r_j)/\delta\Sigma^2(r_j)}{\sum_j \Sigma^2_{model}(r_j)/\delta\Sigma^2(r_j)} \tag{4.6}$$

where $\Sigma(r_j)_{model}$ and $\Sigma(r_j)_{obs}$ is the modelled and observed number density, respectively, at a distance r_j from the cluster centre.

We also account for the effects of background and foreground contaminant stars present near the outskirts of the cluster, which may not have been perfectly accounted by our background subtraction procedure. We thus introduce an extra "nuisance" parameter (s^2) to the fitting. This parameter is added in quadrature, as a constant error over the entire profile, to the observational uncertainties to give the overall error $\delta\Sigma$:

$$\delta\Sigma^2(r_j) = \delta\Sigma^2_{\rm obs}(r_j) + s^2 \tag{4.7}$$

The likelihood is then given in similar fashion to the dispersion profiles:

$$\ln(\mathcal{L}_i) = \frac{1}{2}\sum_j \left(\frac{(\Sigma_{\rm obs}(r_j) - K\Sigma_{\rm model}(r_j))^2}{\delta\Sigma^2(r_j)} - \ln\big(\delta\Sigma^2(r_j)\big) \right) \tag{4.8}$$

Mass Functions

To compare the models against the mass function datasets, the local stellar mass functions are extracted from the models within specific areas in order to match the observed MF data at different projected radial distances from the cluster centre within their respective HST fields.

To compute the stellar mass functions, the model surface density in a given mass bin $\Sigma_k(r)$ is integrated, using a Monte Carlo method, over the area A_j, which covers

a radial slice of the corresponding HST field from the projected distances r_j to r_{j+1}. This gives the count $N_{\mathrm{model},k,j}$ of stars within this footprint j in the mass bin k:

$$N_{\mathrm{model},k,j} = \int_{A_j} \Sigma_k(r) dA_j \tag{4.9}$$

This star count can then be used to compute the Gaussian likelihood:

$$\ln(\mathcal{L}_i) = \frac{1}{2} \sum_{k}^{\substack{\text{radial}\\ \text{bins}}} \sum_{j}^{\substack{\text{mass}\\ \text{bins}}} \left(\frac{(N_{\mathrm{obs},k,j} - N_{\mathrm{model},k,j})^2}{\delta N_{k,j}^2} - \ln\left(\delta N_{k,j}^2\right) \right) \tag{4.10}$$

which is computed separately for each HST program considered.

The error term $\delta N_{k,j}$ must also account for unknown and unaccounted for sources of error in the mass function counts, as well as the fact that our assumed parametrization of the global mass function (equation (2.1)) may not be a perfect representation of the data. Therefore we include another nuisance parameter (F) which scales up the uncertainties:

$$\delta N_{k,j} = \delta N_{\mathrm{obs,k,j}} \cdot F \tag{4.11}$$

This scaling boosts the errors by a constant factor, leading to larger relative errors in regions with lower counts.

4.1.2 Priors

The prior probability distribution π for our set of model parameters Θ is given by the product of individual, independent priors for each parameter in Θ:

$$\pi(\Theta) = \prod_{i}^{N_{\mathrm{params}}} \pi_i(\theta_i) \tag{4.12}$$

The priors for individual parameters can take a few possible forms.

Uniform, or flat, priors are used to provide an uninformative prior to most parameters. The uniform distribution is defined as constant between two bounds (L, U), with a total probability normalized to unity:

$$\pi_i(\theta_i) = \begin{cases} \frac{1}{U-L} & \text{for } \theta_i \in [L, U] \\ 0 & \text{otherwise} \end{cases} \tag{4.13}$$

The upper and lower bounds are chosen, for most parameters, to simply bound a large enough area of parameter space containing all valid parameter values, whereas for certain parameters the bounds are specifically set to disallow values outside a certain range.

The truncation parameter g is limited to values between 0 and 3.5 for all clusters, corresponding to the limit of models of finite extent, as discussed in Section 1.4.1.

The mass-dependant velocity scale δ is also given an upper limit of 0.5, corresponding to the typical value reached by fully mass segregated cluster (Peuten et al., 2017).

Finally the mass function exponents α_i are limited to reasonable regimes. The low and intermediate mass components α_1 and α_2 are given bounds between -1 and 2.35, confining the MF to remain shallower than the canonical high-mass IMF, and allowing for an increasing mass function with decreasing masses, which may best describe the most evolved clusters. The high-mass exponent α_3 is restricted to values between 1.6 and 4.0. The lower-bound of 1.6 is chosen as it has been shown that clusters this "top-heavy" are expected to have dissolved by the present day (Weatherford et al., 2021; Haghi et al., 2020). The upper limit of 4 is chosen as, above this value, lower-

mass globular clusters will contain very few heavy remnants and no neutron stars or black holes, in contradiction with observations of stellar remnants within clusters. All exponents are also required to decrease from the lower to the higher mass regimes, such that $\alpha_1 \leq \alpha_2 \leq \alpha_3$.

Gaussian priors are used for the parameters which are informed by previous and independent analyses, and take the form of a Gaussian distribution centred on the reported value μ with a width of corresponding to the reported uncertainty σ:

$$\pi_i(\theta_i) = \frac{1}{\sigma\sqrt{2\pi}} e^{-\frac{1}{2}\left(\frac{\theta_i - \mu}{\sigma}\right)^2} \tag{4.14}$$

In particular for this analysis, we adopt a Gaussian prior for the distance parameter d, with a mean and standard deviation taken from Baumgardt & Vasiliev (2021). This allows the distance to vary in order to accommodate other observational constraints used in this work, while still being strongly influenced by the robust value obtained through the averaging of a variety of distance determinations from different methods from by Baumgardt & Vasiliev (2021).

4.2 Samplers

The posterior probability distribution $P(\Theta \mid \mathcal{D}, M)$ of the parameter set Θ cannot be solved analytically, but must be estimated through numerical sampling techniques, which aim to generate a set of samples that can be used to approximate the posterior distribution. Numerous algorithms exist (see, e.g. Chopin & Ridgway, 2017) for generating this set.

A commonly used approach in astronomy today is Markov chain Monte Carlo (MCMC) (e.g. Foreman-Mackey et al., 2013). MCMC randomly generates samples

in a chain such that the final density distribution of the set in parameter space is proportional to the posterior probability. MCMC can however struggle to explore posteriors with multiple modes, especially in high-dimensional problems, and relies on arbitrarily chosen initial chain positions. Thus, in this work, we opt to utilize a different technique; nested sampling.

4.2.1 Nested Sampling

Nested sampling (Skilling, 2004; Skilling, 2006) is a Monte Carlo integration method, first proposed for estimating the Bayesian evidence integral $\mathcal{Z}$, which works by iteratively integrating the posterior over the shells of prior volume contained within nested, increasing iso-likelihood contours.

Samples are proposed randomly at each step, subject to a minimum likelihood constraint corresponding to the current likelihood contour. This sampling proceeds from the outer (low-likelihood) parameter space inwards, until the estimated remaining proportion of the evidence integral, which can be determined naturally, reaches a desiredly small percentage. This well-defined stopping criterion is a great advantage of nested sampling, as in most other sampling methods convergence can be difficult to ascertain.

The set of samples computed can also be used to directly estimate the posterior, alongside the evidence integral. This is possible as nested sampling directly incorporates the notion of the *typical set* into the estimation. The typical set is the region of parameter space which jointly maximizes the likelihood probability and the differential prior volume of a slice of a posterior distribution. This concept emerges naturally in nested sampling through the integrated shells of prior volume, and can be used to (importance) weight the samples to be directly proportional to the posterior.

Nested sampling has the benefit of flexibility, as the independently generated samples are able to probe complex posterior shapes, with little danger of falling into local minima, or of missing distant modes. It also does not depend, like many other sampling methods, on a choice of initial sampler positions, and will always cover the entire prior volume. In cases of well defined priors and smoothly transitioning posteriors, as is the case in this work, the sampling efficiency can exceed that of the typical MCMC samplers.

Dynamic nested sampling is an extension of the typical nested algorithm designed to retune the sampling to more efficiently estimate the posterior (Higson et al., 2019). This algorithm effectively functions by spending less time probing the "outer" sections of the prior volume which have little impact on the posterior. The sampler first samples the entire volume, in the same fashion as the typical, static nested sampling, but at a much lower "resolution". The specific areas of greatest "importance" to the posterior, based on the weights, are then iteratively re-sampled at a higher resolution until a sufficient measure of the distribution is obtained. This method essentially allows for a more efficient sampling of the posterior, at the expense of the evidence accuracy.

In this work, we have chosen to utilize dynamic nested sampling for its speed and efficiency, and to ensure that no separate, distant modes in the posterior are missed.

4.3 GCfit

All methodology in this work, from data collection to model fitting, is handled by the novel software library and fitting pipeline `GCfit` [1] (see Appendix B).

[1] https://github.com/nmdickson/GCfit

`GCfit` was created to facilitate the fitting of LIMEPY models to a number of observables through a parallelized sampling procedure. While `GCfit` allows for both MCMC and nested sampling, for the reasons mentioned in Section 4.2.1, we opt to use only the nested sampling in this work.

Nested sampling is handled by the `dynesty` software package (Speagle, 2020). The sampler is run, for all clusters, using the default (multi-ellipsoid bounded, random-walk) dynamic sampling (see Speagle 2020 for more details). The sampling is continued until it reaches an effective sample size (ESS; Kish, 1965) of at least 5000:

$$\mathrm{ESS} = \frac{\left(\sum_{i=1}^{n} w_i\right)^2}{\sum_{i=1}^{n} w_i^2} \tag{4.15}$$

where w_i is the importance weight of the sample i in the set of generated samples.

Chapter 5

Results

Presented in this chapter are the results of the fits based on the methodology of Chapter 4. First we will introduce the resulting posterior probability distributions of all model parameters, and the corresponding fits they give to the relevant data. We will then briefly discuss the distribution between clusters of some structural parameters of interest. The stellar mass functions of the clusters are explored in more detail in Chapter 6, and the distributions of black holes and other remnants are discussed further in Chapter 7.

5.1 Fitting Results

5.1.1 Parameter Distributions

The set of weighted samples retrieved from the nested sampler, after sampling until the stopping condition described in Section 4.3, are used to construct posterior probability distributions for all model parameters.

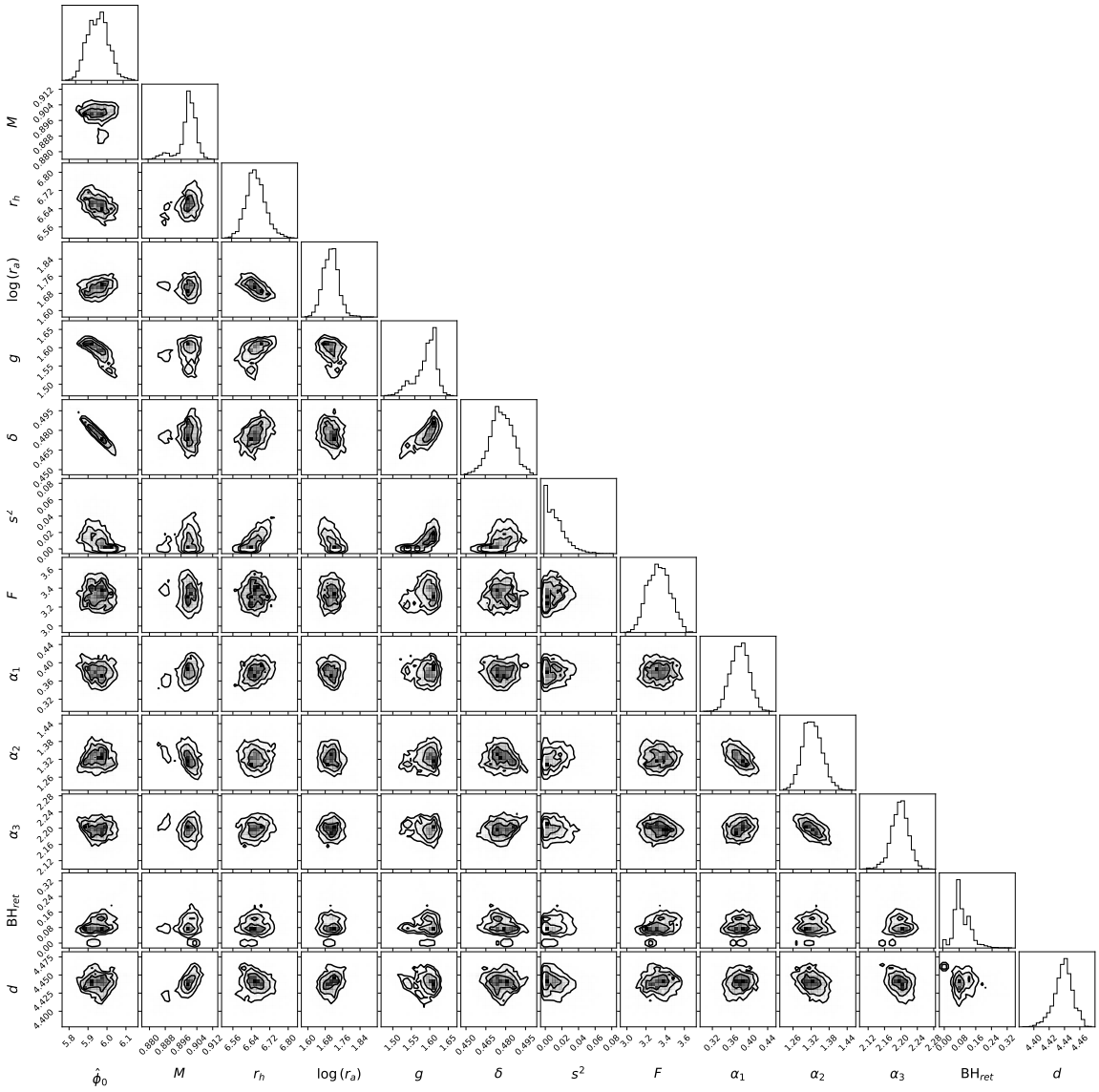

Figure 5.1: Marginalized and 2D projections of the posterior probability distributions of all model parameters for the fit to NGC 104. Contours indicate 1σ, 2σ and 3σ levels on the 2D posterior probability distributions.

Figure 5.1 shows an example of the resulting posterior distributions for the cluster NGC 104. The best-fitting parameter values for all clusters can be found in Table 5.1[1].

The vast majority of marginalized posterior distributions for the cluster parameters follow a unimodal and approximately Gaussian shape. The marginalized posterior probability distribution of some parameters are skewed towards or hitting the boundaries of the prior ranges, however, as indicated in Section 4.1.2, this is only allowed to occur for parameters with physically motivated prior boundaries.

Two parameters ($\log(r_a)$ and BH_{ret}) often have a much broader posterior probability distribution. The anisotropy radius may be unconstrained above a certain minimum value, illustrating the fact that all values of the anisotropy radius greater than the truncation radius effectively lead to an entirely isotropic cluster. The black hole retention fraction may be completely unconstrained in models with a very small number of black holes initially formed (e.g. due to a "top-light" mass function), in which case the fraction of black holes retained has a negligible effect on the models. Both of these parameters are examined in more detail below.

A fraction of our clusters are core-collapsed, and should not retain any significant populations of black holes (Giersz & Heggie, 2009). However, three such clusters (NGC 6266, NGC 6624, NGC 7078) do possess BHs, and may not be physical. In these cases, we recompute the models, this time with the amount of retained black holes at the present day fixed to 0 (by fixing the BH_{ret} parameter to 0%). These models are the ones used in the analysis presented in this chapter and Chapter 6. This is discussed in more detail in Section 7.1.

[1] All results, figures and tables from this thesis are also available for all clusters by download from https://github.com/nmdickson/GCfit-results

5.1.2 Best-Fitting Models

Figures 5.2 and 5.3 show an example (also for NGC 104) of the observables predicted by the best-fitting models, overlaid with the observational datasets used to constrain them. Similar plots for all clusters are shown in Appendix A.

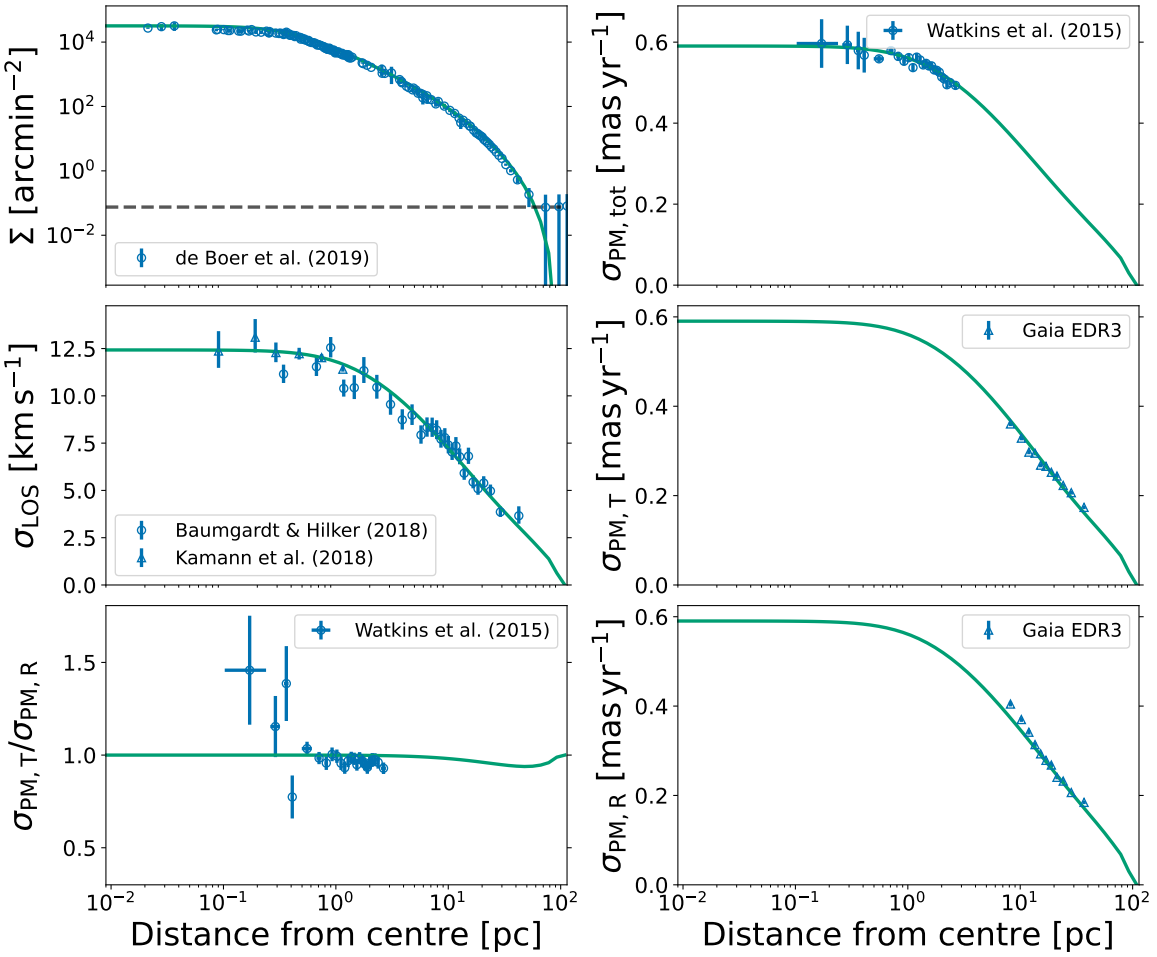

Figure 5.2: Model radial profiles (in green) of surface number density (Σ), line-of-sight velocity dispersions ($\sigma_{\rm LOS}$), total ($\sigma_{\rm PM,tot}$), radial ($\sigma_{\rm PM,R}$) and tangential ($\sigma_{\rm PM,T}$) proper motion velocity dispersions and proper motion anisotropy ratio ($\sigma_{\rm PM,T}/\sigma_{\rm PM,R}$), for the fit of NGC 104. The dark and light shaded regions represent the 1σ and 2σ credible intervals of the model fits, respectively. The observational datasets used to constrain the models are shown alongside their 1σ uncertainties by the blue points and errorbars. The background value subtracted from the number density profile is shown by the dashed line.

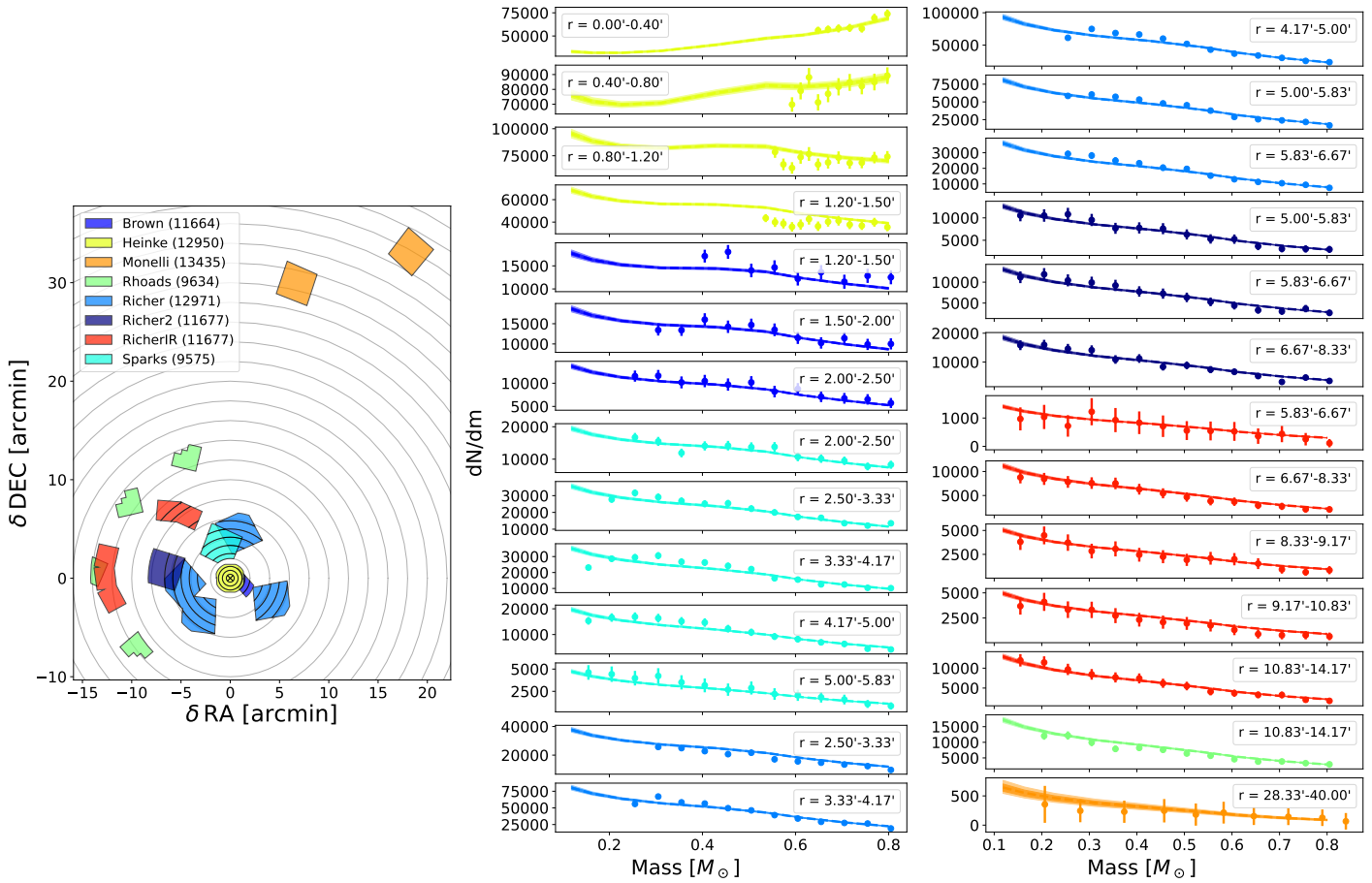

Figure 5.3: Model local stellar mass functions fit to the observations of NGC 104. Each panel in the centre and right columns show the number of stars per unit mass as a function of stellar mass, for different distance ranges from the cluster centre. The dark and light shaded regions represent the 1σ and 2σ credible intervals of the model fits, respectively. The measurements used to constrain the models are shown alongside their 1σ uncertainties by the points and errorbars. Each individual HST observing program is denoted by a separate colour, and the corresponding fields for each are shown on the left panel.

The best-fitting models for the majority of clusters match the given data extraordinarily well. There is, however, a small number of clusters, from our original sample of 40 clusters, where the fits do not reproduce certain datasets adequately. This tends to occur in systems with small amounts of proper motion and LOS velocity data. Having few kinematic datapoints, as compared to the mass function and number density datasets, means that these models are less able to constrain the non-visible mass and are prone to overfitting the mass functions, at the expense of the kinematics. As fitting both the visible and dark components well is vital to our analysis of the high-mass mass function and the remnant populations, we choose to remove these clusters from our sample going forward. Five such clusters (NGC 4590, NGC 5986, NGC 6352, NGC 6809, NGC 6981) were discarded due to their unsatisfactory fits, on top of the three discarded due to their number density profiles (see Section 3.2.3). The remaining 32 clusters have best-fitting models that are well matched to all datasets and will make up the set of clusters used in all further analysis in this thesis.

5.2 Cluster Parameters

Given this set of best-fitting models, we next examine the distribution and relationships of various model parameters to search for any correlations between clusters and compare with other results from the literature. The best-fitting model and mass function parameters for all clusters are shown in Table 5.1 and all nuisance parameters are shown in Table 5.2.

It must be noted here that all uncertainties presented for these parameters, in this entire analysis, are accounting solely for the statistical uncertainties on the parameter fits. Our fitting procedure operates under the assumption that our models are a good representation of the data, and as such may, in reality, be underestimating the true

errors.

Cluster	$\hat{\phi}_0$	M [10^6 $M_\odot$]	r_h [pc]	$\log_{10}(r_a$ [pc])	g	δ	α_1	α_2	α_3	BH$_{ret}$	d
NGC 104	$5.95^{+0.05}_{-0.05}$	$0.900^{+0.003}_{-0.002}$	$6.66^{+0.04}_{-0.04}$	$1.71^{+0.03}_{-0.03}$	$1.60^{+0.04}_{-0.02}$	$0.476^{+0.007}_{-0.008}$	$0.38^{+0.02}_{-0.02}$	$1.32^{+0.03}_{-0.03}$	$2.18^{+0.02}_{-0.02}$	$0.08^{+0.02}_{-0.05}$	$4.44^{+0.01}_{-0.01}$
NGC 288	$3.72^{+0.06}_{-0.07}$	$0.087^{+0.002}_{-0.002}$	$8.68^{+0.09}_{-0.09}$	2^{+1}_{-2}	$0.48^{+0.07}_{-0.07}$	$0.487^{+0.015}_{-0.008}$	$0.59^{+0.03}_{-0.03}$	$0.67^{+0.04}_{-0.05}$	$2.31^{+0.09}_{-0.09}$	$0.4^{+0.3}_{-0.4}$	$8.90^{+0.09}_{-0.09}$
NGC 362	$5.38^{+0.04}_{-0.05}$	$0.263^{+0.002}_{-0.002}$	$3.41^{+0.03}_{-0.04}$	$1.13^{+0.03}_{-0.04}$	$1.46^{+0.03}_{-0.04}$	$0.495^{+0.005}_{-0.003}$	$0.64^{+0.02}_{-0.02}$	$0.65^{+0.02}_{-0.02}$	$3.12^{+0.07}_{-0.09}$	$4.2^{+0.4}_{-0.5}$	$8.65^{+0.06}_{-0.05}$
NGC 1261	$3.67^{+0.09}_{-0.10}$	$0.176^{+0.002}_{-0.002}$	$4.81^{+0.04}_{-0.04}$	$0.84^{+0.08}_{-0.08}$	$1.99^{+0.08}_{-0.07}$	$0.489^{+0.013}_{-0.008}$	$0.83^{+0.06}_{-0.05}$	$0.94^{+0.05}_{-0.06}$	$2.54^{+0.05}_{-0.06}$	$1.9^{+0.6}_{-0.5}$	$15.9^{+0.1}_{-0.1}$
NGC 1851	$6.00^{+0.02}_{-0.07}$	$0.327^{+0.001}_{-0.000}$	$3.568^{+0.004}_{-0.002}$	$4.11^{+0.14}_{-0.04}$	$1.732^{+0.009}_{-0.002}$	$0.440^{+0.012}_{-0.005}$	$0.694^{+0.014}_{-0.003}$	$0.91^{+0.01}_{-0.02}$	$3.033^{+0.017}_{-0.004}$	$2.0^{+0.1}_{-0.2}$	$11.682^{+0.056}_{-0.006}$
NGC 2808	$5.10^{+0.03}_{-0.03}$	$0.928^{+0.004}_{-0.005}$	$3.84^{+0.02}_{-0.02}$	$1.32^{+0.05}_{-0.03}$	$1.72^{+0.03}_{-0.03}$	$0.442^{+0.005}_{-0.006}$	$0.41^{+0.02}_{-0.03}$	$1.46^{+0.05}_{-0.04}$	$2.99^{+0.04}_{-0.04}$	13^{+2}_{-1}	$10.14^{+0.02}_{-0.03}$
NGC 3201	$5.0^{+0.2}_{-0.2}$	$0.170^{+0.004}_{-0.004}$	$9.5^{+0.4}_{-0.4}$	$1.14^{+0.05}_{-0.06}$	$1.78^{+0.08}_{-0.08}$	$0.45^{+0.03}_{-0.03}$	$0.98^{+0.03}_{-0.04}$	$1.04^{+0.04}_{-0.04}$	$2.36^{+0.06}_{-0.06}$	$0.10^{+0.07}_{-0.13}$	$4.61^{+0.03}_{-0.02}$
NGC 5024	$5.0^{+0.1}_{-0.1}$	$0.48^{+0.02}_{-0.02}$	$10.6^{+0.3}_{-0.3}$	6^{+3}_{-3}	$2.3^{+0.1}_{-0.1}$	$0.311^{+0.008}_{-0.014}$	$0.96^{+0.04}_{-0.04}$	$1.90^{+0.06}_{-0.06}$	$2.7^{+0.2}_{-0.2}$	8^{+5}_{-7}	$18.5^{+0.2}_{-0.1}$
NGC 5139	$2.3^{+0.2}_{-0.2}$	$3.25^{+0.03}_{-0.05}$	$9.65^{+0.04}_{-0.04}$	$6.8^{+0.8}_{-0.5}$	$2.56^{+0.02}_{-0.02}$	$0.42^{+0.01}_{-0.01}$	$0.94^{+0.01}_{-0.02}$	$1.06^{+0.04}_{-0.02}$	$2.21^{+0.07}_{-0.03}$	20^{+4}_{-2}	$5.38^{+0.02}_{-0.03}$
NGC 5272	$5.30^{+0.10}_{-0.08}$	$0.46^{+0.01}_{-0.01}$	$6.68^{+0.09}_{-0.11}$	6^{+3}_{-2}	$2.12^{+0.06}_{-0.05}$	$0.313^{+0.009}_{-0.016}$	$1.22^{+0.01}_{-0.02}$	$1.26^{+0.02}_{-0.03}$	$2.5^{+0.1}_{-0.1}$	5^{+2}_{-3}	$10.04^{+0.09}_{-0.09}$
NGC 5904	$5.5^{+0.1}_{-0.1}$	$0.408^{+0.005}_{-0.004}$	$6.64^{+0.05}_{-0.04}$	$1.2^{+0.1}_{-0.2}$	$1.13^{+0.05}_{-0.05}$	$0.47^{+0.02}_{-0.02}$	$0.46^{+0.04}_{-0.04}$	$0.63^{+0.06}_{-0.06}$	$2.30^{+0.05}_{-0.05}$	$0.3^{+0.2}_{-0.2}$	$7.34^{+0.04}_{-0.03}$
NGC 6093	$5.64^{+0.09}_{-0.15}$	$0.308^{+0.004}_{-0.004}$	$2.41^{+0.03}_{-0.02}$	5^{+2}_{-2}	$1.41^{+0.06}_{-0.05}$	$0.48^{+0.04}_{-0.02}$	$-0.01^{+0.05}_{-0.05}$	$0.99^{+0.07}_{-0.08}$	$2.15^{+0.06}_{-0.06}$	$0.54^{+0.01}_{-0.13}$	$10.27^{+0.09}_{-0.08}$
NGC 6121	$6.8^{+0.4}_{-0.9}$	$0.090^{+0.001}_{-0.001}$	$4.09^{+0.07}_{-0.08}$	7^{+2}_{-2}	$0.7^{+0.1}_{-0.1}$	$0.43^{+0.06}_{-0.04}$	$-0.3^{+0.1}_{-0.1}$	$0.8^{+0.1}_{-0.1}$	$1.85^{+0.09}_{-0.09}$	$0.16^{+0.08}_{-0.10}$	$1.85^{+0.01}_{-0.01}$
NGC 6171	$5.56^{+0.05}_{-0.07}$	$0.063^{+0.002}_{-0.002}$	$3.91^{+0.06}_{-0.06}$	5^{+2}_{-2}	$0.31^{+0.09}_{-0.09}$	$0.487^{+0.015}_{-0.009}$	$-0.05^{+0.03}_{-0.03}$	$0.00^{+0.04}_{-0.04}$	$2.35^{+0.08}_{-0.08}$	$0.3^{+0.2}_{-0.4}$	$5.58^{+0.07}_{-0.07}$
NGC 6205	$4.41^{+0.05}_{-0.05}$	$0.465^{+0.007}_{-0.009}$	$5.19^{+0.08}_{-0.08}$	4^{+3}_{-3}	$1.54^{+0.06}_{-0.06}$	$0.490^{+0.009}_{-0.006}$	$0.51^{+0.03}_{-0.03}$	$0.55^{+0.03}_{-0.03}$	$2.8^{+0.1}_{-0.1}$	$0.7^{+0.5}_{-0.8}$	$7.15^{+0.04}_{-0.05}$
NGC 6218	$4.97^{+0.07}_{-0.07}$	$0.098^{+0.001}_{-0.001}$	$4.08^{+0.04}_{-0.05}$	$1.7^{+0.3}_{-1.8}$	$0.51^{+0.06}_{-0.05}$	$0.497^{+0.002}_{-0.001}$	$0.18^{+0.03}_{-0.03}$	$0.23^{+0.04}_{-0.04}$	$2.53^{+0.06}_{-0.06}$	$0.8^{+0.2}_{-0.3}$	$5.07^{+0.04}_{-0.02}$
NGC 6254	$5.5^{+0.1}_{-0.2}$	$0.212^{+0.004}_{-0.004}$	$5.25^{+0.08}_{-0.08}$	3^{+1}_{-1}	$0.94^{+0.09}_{-0.07}$	$0.44^{+0.03}_{-0.03}$	$0.47^{+0.04}_{-0.04}$	$0.65^{+0.08}_{-0.08}$	$2.40^{+0.07}_{-0.08}$	$0.4^{+0.3}_{-0.5}$	$5.09^{+0.05}_{-0.05}$
NGC 6266	$5.5^{+0.1}_{-0.1}$	$0.71^{+0.01}_{-0.01}$	$3.05^{+0.05}_{-0.05}$	$1.34^{+0.06}_{-0.09}$	$0.91^{+0.07}_{-0.07}$	$0.497^{+0.003}_{-0.001}$	$0.5^{+0.1}_{-0.1}$	$0.73^{+0.09}_{-0.10}$	$2.26^{+0.06}_{-0.06}$	—	$6.42^{+0.04}_{-0.04}$
NGC 6341	$5.2^{+0.2}_{-0.6}$	$0.315^{+0.004}_{-0.004}$	$4.34^{+0.06}_{-0.05}$	7^{+2}_{-2}	$1.66^{+0.04}_{-0.04}$	$0.48^{+0.03}_{-0.01}$	$0.83^{+0.03}_{-0.03}$	$1.27^{+0.05}_{-0.05}$	$2.03^{+0.05}_{-0.05}$	$0.28^{+0.11}_{-0.08}$	$8.47^{+0.05}_{-0.04}$
NGC 6362	$4.10^{+0.08}_{-0.11}$	$0.113^{+0.003}_{-0.003}$	$6.84^{+0.09}_{-0.10}$	4^{+2}_{-2}	$0.6^{+0.2}_{-0.2}$	$0.47^{+0.04}_{-0.02}$	$0.27^{+0.04}_{-0.04}$	$0.63^{+0.08}_{-0.08}$	$1.78^{+0.07}_{-0.08}$	$0.04^{+0.03}_{-0.05}$	$7.61^{+0.07}_{-0.06}$
NGC 6366	$3.9^{+0.2}_{-0.1}$	$0.031^{+0.001}_{-0.001}$	$4.6^{+0.1}_{-0.1}$	2^{+1}_{-2}	$0.9^{+0.3}_{-0.3}$	$0.48^{+0.02}_{-0.01}$	$-0.4^{+0.1}_{-0.1}$	$-0.1^{+0.1}_{-0.1}$	$3.1^{+0.2}_{-0.2}$	6^{+4}_{-7}	$3.39^{+0.04}_{-0.04}$
NGC 6397	$7.87^{+0.06}_{-0.07}$	$0.106^{+0.001}_{-0.001}$	$4.8^{+0.1}_{-0.1}$	$2.33^{+0.04}_{-0.05}$	$1.49^{+0.07}_{-0.08}$	$0.498^{+0.002}_{-0.001}$	$0.49^{+0.04}_{-0.04}$	$0.59^{+0.06}_{-0.06}$	$2.48^{+0.05}_{-0.04}$	$0.13^{+0.01}_{-0.02}$	$2.42^{+0.01}_{-0.01}$
NGC 6541	$5.96^{+0.03}_{-0.11}$	$0.240^{+0.000}_{-0.004}$	$4.02^{+0.02}_{-0.05}$	$1.234^{+0.009}_{-0.045}$	$0.68^{+0.02}_{-0.05}$	$0.499^{+0.001}_{-0.000}$	$0.38^{+0.04}_{-0.03}$	$0.95^{+0.01}_{-0.04}$	$2.34^{+0.05}_{-0.03}$	$0.34^{+0.07}_{-0.03}$	$7.61^{+0.04}_{-0.01}$
NGC 6624	$11.0^{+0.1}_{-0.2}$	$0.101^{+0.002}_{-0.002}$	$1.94^{+0.03}_{-0.04}$	5^{+2}_{-3}	$1.19^{+0.09}_{-0.09}$	$0.495^{+0.005}_{-0.003}$	$-0.47^{+0.11}_{-0.07}$	$-0.33^{+0.04}_{-0.05}$	$2.29^{+0.06}_{-0.05}$	—	$7.99^{+0.08}_{-0.07}$
NGC 6656	$5.53^{+0.06}_{-0.05}$	$0.447^{+0.007}_{-0.007}$	$5.11^{+0.07}_{-0.06}$	$1.16^{+0.06}_{-0.08}$	$1.09^{+0.08}_{-0.09}$	$0.35^{+0.01}_{-0.01}$	$0.23^{+0.06}_{-0.07}$	$0.8^{+0.1}_{-0.1}$	$2.59^{+0.05}_{-0.06}$	$2.4^{+0.7}_{-0.8}$	$3.23^{+0.02}_{-0.01}$
NGC 6681	$11.32^{+0.03}_{-0.09}$	$0.105^{+0.001}_{-0.001}$	$2.55^{+0.02}_{-0.02}$	$3.13^{+0.04}_{-0.03}$	$1.51^{+0.04}_{-0.04}$	$0.473^{+0.004}_{-0.005}$	$-0.24^{+0.03}_{-0.03}$	$-0.19^{+0.05}_{-0.04}$	$2.06^{+0.05}_{-0.04}$	$0.128^{+0.006}_{-0.013}$	$9.23^{+0.03}_{-0.04}$
NGC 6723	$4.14^{+0.10}_{-0.09}$	$0.143^{+0.005}_{-0.005}$	$5.14^{+0.06}_{-0.05}$	$0.61^{+0.07}_{-0.09}$	$1.4^{+0.1}_{-0.1}$	$0.48^{+0.02}_{-0.01}$	$0.04^{+0.05}_{-0.04}$	$0.22^{+0.06}_{-0.06}$	$3.2^{+0.2}_{-0.2}$	2^{+2}_{-3}	$8.17^{+0.07}_{-0.06}$
NGC 6752	$6.44^{+0.05}_{-0.05}$	$0.229^{+0.003}_{-0.003}$	$4.56^{+0.09}_{-0.09}$	$1.49^{+0.02}_{-0.02}$	$1.16^{+0.06}_{-0.06}$	$0.496^{+0.004}_{-0.002}$	$0.46^{+0.04}_{-0.04}$	$0.52^{+0.04}_{-0.04}$	$2.65^{+0.05}_{-0.05}$	$0.52^{+0.08}_{-0.06}$	$4.01^{+0.02}_{-0.02}$
NGC 6779	$5.82^{+0.07}_{-0.06}$	$0.158^{+0.004}_{-0.004}$	$5.64^{+0.08}_{-0.09}$	4^{+2}_{-2}	$0.66^{+0.06}_{-0.06}$	$0.35^{+0.02}_{-0.02}$	$0.27^{+0.03}_{-0.03}$	$1.19^{+0.07}_{-0.07}$	$2.21^{+0.08}_{-0.08}$	$1.5^{+0.5}_{-0.6}$	$10.4^{+0.1}_{-0.1}$
NGC 7078	$9.1^{+0.2}_{-0.1}$	$0.617^{+0.008}_{-0.006}$	$4.95^{+0.03}_{-0.04}$	$3.00^{+0.06}_{-0.07}$	$1.49^{+0.05}_{-0.04}$	$0.437^{+0.010}_{-0.009}$	$0.90^{+0.06}_{-0.05}$	$1.61^{+0.09}_{-0.04}$	$1.79^{+0.05}_{-0.05}$	—	$10.58^{+0.06}_{-0.04}$
NGC 7089	$4.9^{+0.2}_{-0.2}$	$0.612^{+0.005}_{-0.007}$	$4.69^{+0.06}_{-0.05}$	6^{+3}_{-4}	$1.89^{+0.06}_{-0.06}$	$0.35^{+0.02}_{-0.02}$	$1.13^{+0.03}_{-0.02}$	$1.22^{+0.04}_{-0.05}$	$2.48^{+0.05}_{-0.056}$	5^{+1}_{-1}	$11.56^{+0.11}_{-0.09}$
NGC 7099	$9.67^{+0.06}_{-0.06}$	$0.140^{+0.001}_{-0.002}$	$4.20^{+0.06}_{-0.05}$	$3.17^{+0.04}_{-0.03}$	$1.10^{+0.06}_{-0.06}$	$0.496^{+0.003}_{-0.002}$	$0.58^{+0.03}_{-0.03}$	$0.94^{+0.06}_{-0.06}$	$2.32^{+0.05}_{-0.04}$	$0.047^{+0.006}_{-0.009}$	$8.34^{+0.07}_{-0.07}$

Table 5.1: Median and 1σ uncertainties of all best-fitting model and mass function parameters, for all clusters. Empty dashes in the BH$_{ret}$ column represent the three core-collapsed clusters with a value fixed to 0.

5.2.1 Comparison with Literature

To begin, we can compare our best-fitting models with other comprehensive studies of Milky Way GCs in the literature. Namely, we consider in Figure 5.4 the distances determined by Vasiliev & Baumgardt (2021), and the total masses and half-mass radii inferred from the N-body model fits of Baumgardt et al. (2019a, 2022), where our results show good agreement. While the excellent agreement with the heliocentric distances of Vasiliev & Baumgardt (2021) is largely by design, given our use of a Gaussian centred on their values as the prior on the distance parameter (see Section 4.1.2), this does indicate that our models and observations are perfectly compatible with those distances. The excellent agreements between our models and the previous determinations of total cluster mass and half-mass radius are also reassuring, and any small deviations present are to be expected, given the large amount of additional freedom in the remnant mass function of our models.

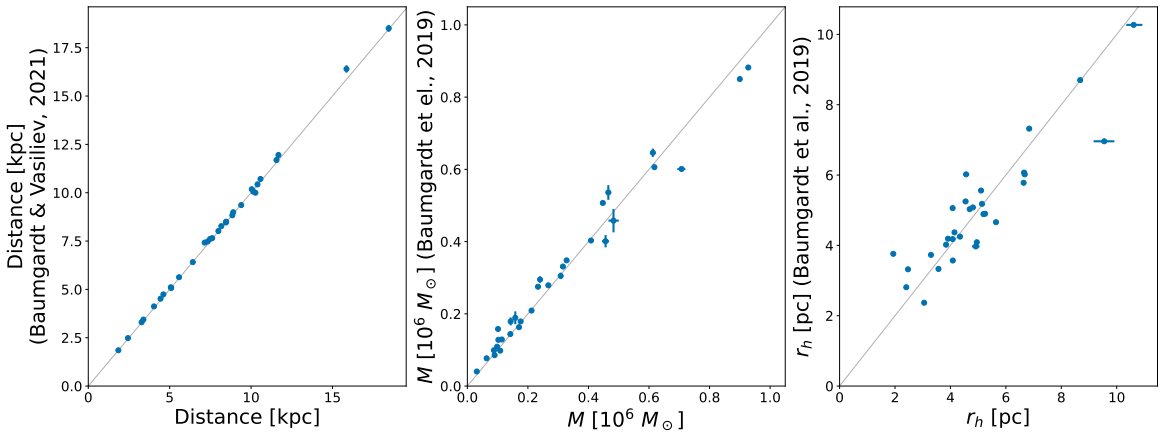

Figure 5.4: Comparison of heliocentric distances, total system mass, and half-mass radii of all cluster fits against the distances computed by Vasiliev & Baumgardt (2021) and the properties inferred from the N-body model fits of Baumgardt et al. (2019a). NGC 5139 is excluded from these figures due to its very large mass, but is discussed in more detail in Section 7.4.

Cluster	s^2	F
NGC 104	$0.011^{+0.009}_{-0.013}$	$3.3^{+0.1}_{-0.1}$
NGC 288	$0.04^{+0.04}_{-0.3}$	$1.47^{+0.07}_{-0.07}$
NGC 362	$0.00018^{+0.00008}_{-0.00007}$	$3.18^{+0.10}_{-0.09}$
NGC 1261	$0.000005^{+0.000005}_{-0.000003}$	$5.2^{+0.2}_{-0.2}$
NGC 1851	$4.13^{+0.02}_{-0.11}$	$3.53^{+0.02}_{-0.11}$
NGC 2808	$0.000020^{+0.000007}_{-0.000005}$	$4.8^{+0.1}_{-0.1}$
NGC 3201	$18.6^{+1.3}_{-1.0}$	$2.7^{+0.2}_{-0.2}$
NGC 5024	$0.001^{+0.000}_{-0.002}$	$3.7^{+0.2}_{-0.2}$
NGC 5139	$0.00035^{+0.00010}_{-0.00006}$	$8.4^{+0.1}_{-0.2}$
NGC 5272	$3.2^{+1.1}_{-1.3}$	$2.5^{+0.1}_{-0.1}$
NGC 5904	$0.007^{+0.005}_{-0.009}$	$6.2^{+0.3}_{-0.3}$
NGC 6093	$0.008^{+0.002}_{-0.002}$	$5.0^{+0.3}_{-0.3}$
NGC 6121	$0.00002^{+0.00009}_{-0.00001}$	$2.3^{+0.2}_{-0.2}$
NGC 6171	$0.004^{+0.001}_{-0.002}$	$1.52^{+0.09}_{-0.10}$
NGC 6205	11^{+3}_{-3}	$4.5^{+0.3}_{-0.3}$
NGC 6218	$0.00007^{+0.00010}_{-0.00005}$	$2.5^{+0.2}_{-0.2}$
NGC 6254	$0.0003^{+0.0002}_{-0.0002}$	$3.1^{+0.2}_{-0.2}$
NGC 6266	$0.24^{+0.02}_{-0.03}$	$5.8^{+0.5}_{-0.6}$
NGC 6341	$0.0002^{+0.0004}_{-0.0001}$	$3.1^{+0.1}_{-0.2}$
NGC 6362	15^{+5}_{-3}	$1.7^{+0.1}_{-0.1}$
NGC 6366	$0.001^{+0.001}_{-0.001}$	$1.5^{+0.1}_{-0.1}$
NGC 6397	$9.2^{+0.9}_{-0.6}$	$2.40^{+0.10}_{-0.11}$
NGC 6541	$14.8^{+0.9}_{-1.0}$	$2.35^{+0.09}_{-0.05}$
NGC 6624	$0.3^{+0.1}_{-0.1}$	$1.6^{+0.1}_{-0.2}$
NGC 6656	$0.000003^{+0.000011}_{-0.000002}$	$6.6^{+0.2}_{-0.2}$
NGC 6681	$0.054^{+0.006}_{-0.006}$	$3.97^{+0.08}_{-0.10}$
NGC 6723	$0.005^{+0.002}_{-0.004}$	$2.4^{+0.2}_{-0.2}$
NGC 6752	23^{+2}_{-1}	$5.2^{+0.3}_{-0.3}$
NGC 6779	$0.0002^{+0.0002}_{-0.0002}$	$2.9^{+0.2}_{-0.2}$
NGC 7078	$0.00006^{+0.00007}_{-0.00003}$	$7.5^{+0.2}_{-0.3}$
NGC 7089	$0.00008^{+0.00007}_{-0.00003}$	$5.3^{+0.4}_{-0.4}$
NGC 7099	$0.00005^{+0.00011}_{-0.00003}$	$3.2^{+0.1}_{-0.2}$

Table 5.2: Median and 1σ uncertainties of all best-fitting nuisance parameters, for all clusters.

5.2.2 Relationships Between Parameters

Figure 5.5 shows the relationships between the structural parameters of all clusters. As can be seen here, the central potential $\hat{\phi}_0$ is anti-correlated somewhat with the (log) half-mass radius. We also find, as would be expected, a clear correlation between the (log) truncation radius and the truncation parameter g, as well as between the truncation and half-mass radii themselves. These correlations match those found by de Boer et al. (2019) in their fits of single-mass LIMEPY models to Gaia DR2 density profiles. However, due to the large scatter at low central potentials, our results do not seem to indicate an anti-correlation between $\hat{\phi}_0$ and $\log(r_t)$, as seen in their fits. Similarly, while there may be a general linearly-decreasing trend between g and $\hat{\phi}_0$, the large scatter and outliers prevent us from finding a statistically-significant, clear correlation between the two, as found in their models.

5.2.3 Anisotropy

Figure 5.6 shows the distribution of the anisotropy radius parameter for all clusters. It is immediately clear from this plot that there are two populations of anisotropy results in our fits; distributions with a clear peak, constrained to a narrow range of best-fitting values, and very broad, flat distributions with no clear peak above a certain minimum value, extending up to the prior bounds. As described in Section 2.1, clusters where $\log(r_a)$ is more clearly peaked favour a certain amount of radial anisotropy, whereas clusters with broad posterior distributions are effectively isotropic, as all values of $\log(r_a)$ above the minima of the broad distributions (corresponding to approximately at or above the truncation radius) essentially lead to the same isotropic model. Values above this minimum therefore have a negligible effect on the computed model likelihoods. An example of both categories is shown in Figure 5.7.

It should be noted that the constraints we can place on velocity anisotropy come entirely from the Gaia (and HST, where covered by Watkins et al. (2015)) proper motion dispersion profiles. These datasets are quite limited in many clusters, and as such some of the clusters with broad distributions may not actually be entirely isotropic in reality, but simply cannot be sufficiently constrained by the data currently available. It is also important to note that our LIMEPY models are unable to reproduce any amount of tangential anisotropy (Gieles & Zocchi, 2015), and instead, when tangentially biased anisotropy is present in our data. the models will favour a mostly isotropic fit as a compromise between the radial and tangential regimes (Peuten et al., 2017).

It is clear, based on the wide range of $\log(r_a)$ values, that allowing the anisotropy radius to vary freely is necessary to best model the GCs. The degree of anisotropy in a cluster is important for understanding the central dark remnant populations, as there exists a degeneracy between the observational fingerprints of central dark mass and velocity anisotropy (e.g. Zocchi et al., 2017).

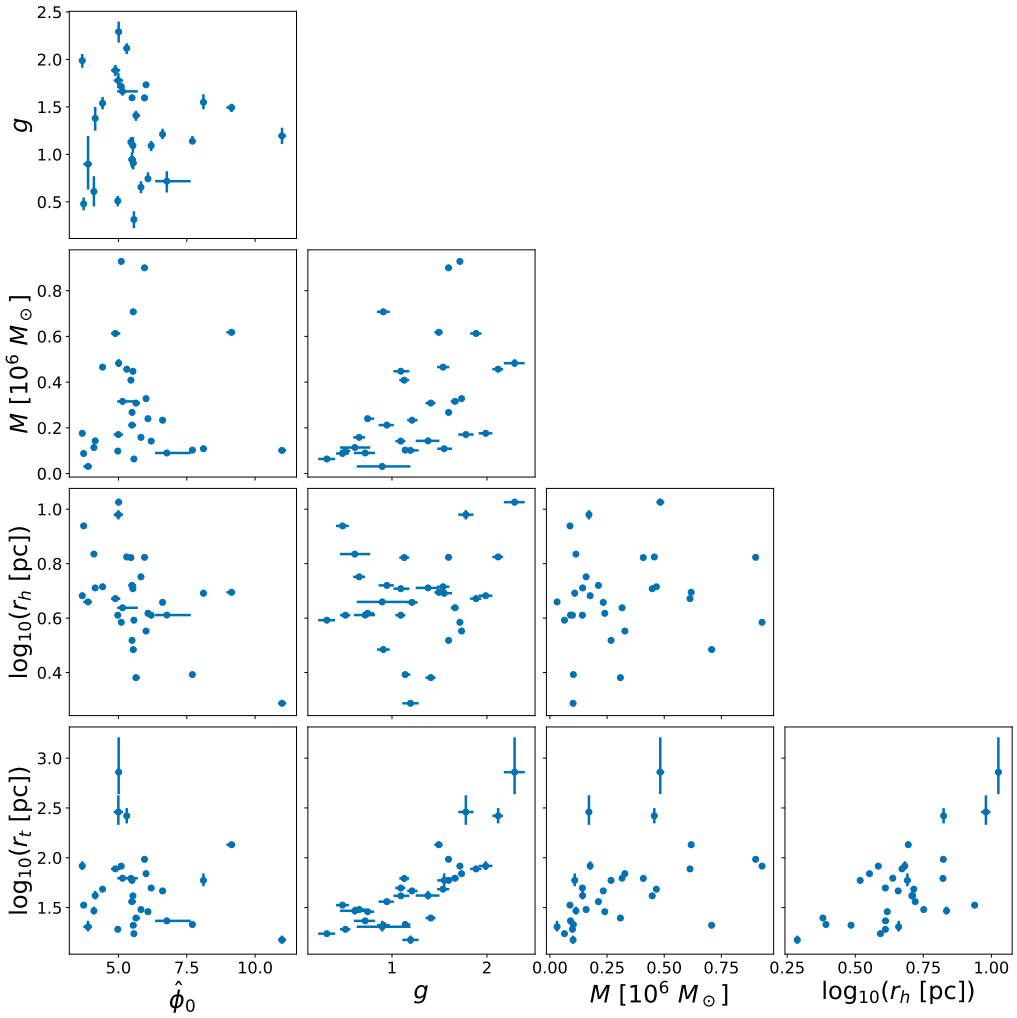

Figure 5.5: Relations between a variety of structural parameters; the dimensionless central potential $\hat{\phi}_0$, the truncation parameter g, the total cluster mass M, the (log) half-mass radius $\log(r_h)$ and the (log) truncation radius $\log(r_h)$. All but the truncation radius are free model parameters. NGC 5139 is excluded from these figures due to its very large mass and low central potential, but is discussed in more detail in Section 7.4.

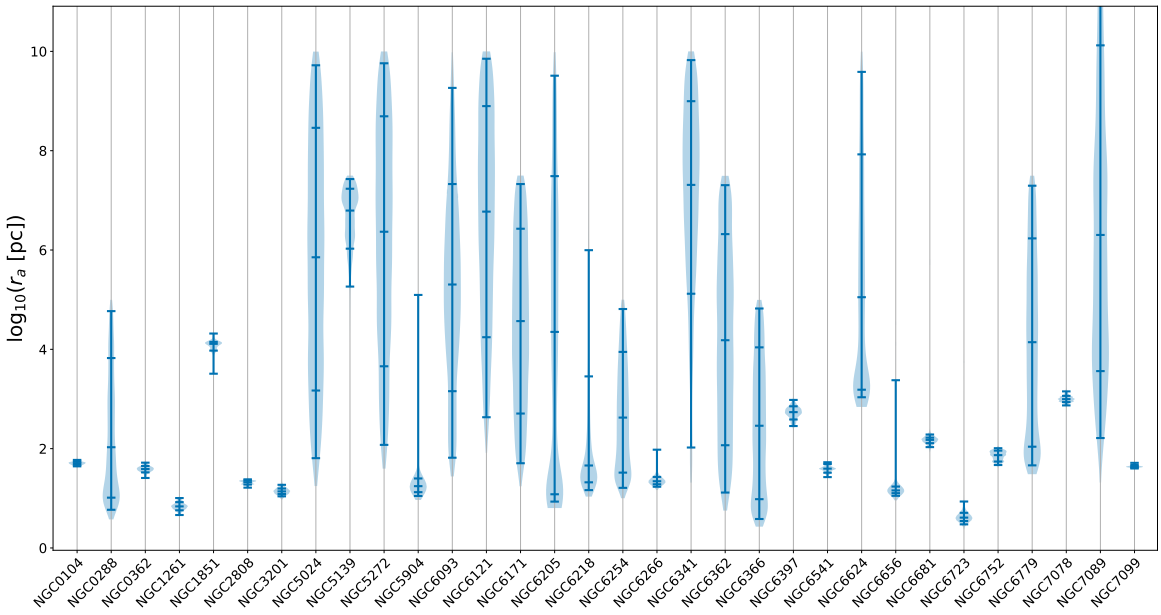

Figure 5.6: Violin plot of the (log) anisotropy radius $\log(r_a)$ parameter posterior distributions for all clusters. All clusters, except NGC 7089, were fit using a uniform prior with an upper bound at $\log(r_a) = 10$. The median, 1σ and 2σ values are denoted by the horizontal ticks on each distribution.

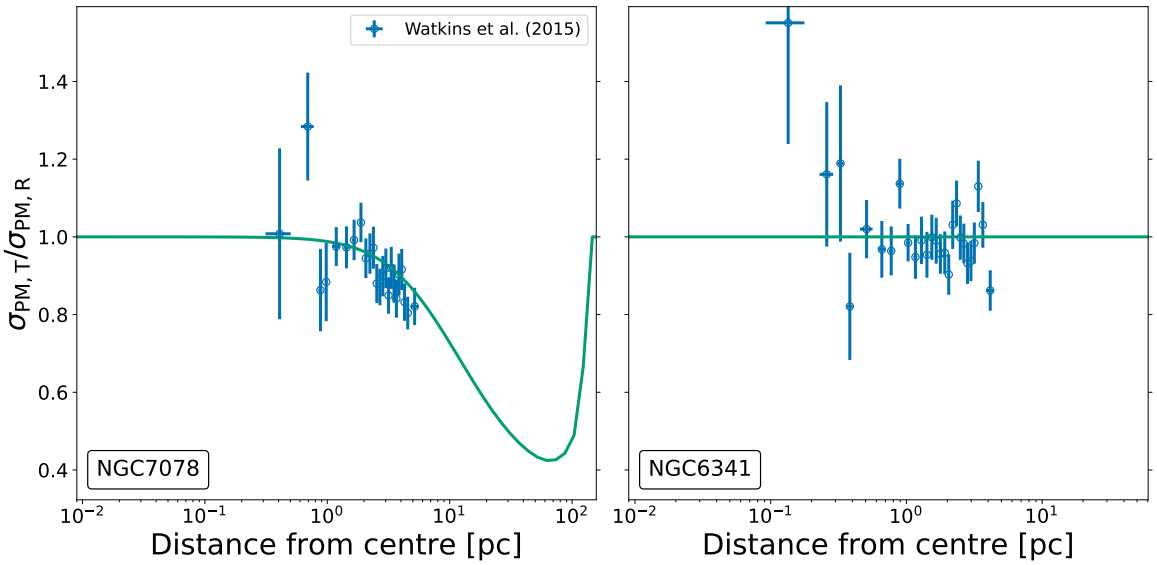

Figure 5.7: Model radial profiles (in green) of the proper motion anisotropy ratio ($\sigma_{\mathrm{PM,T}}/\sigma_{\mathrm{PM,R}}$), for an example of both an anisotropic model (NGC 7078, left panel) and isotropic model (NGC 6341, right panel). The dark and light shaded regions represent the 1σ and 2σ credible intervals of the model fits, respectively. The observational data from Watkins et al. (2015) used to constrain the models are shown alongside their 1σ uncertainties by the blue points and errorbars.

Chapter 6

Mass Functions

In this chapter, we explore the mass function exponents inferred from our model fits, in all mass regimes. We will examine the relationships between the MF exponents, discuss the connection between the global mass function probed by our models and the initial stellar mass function of GCs, and search for any possible correlations between the IMF and environment of globular clusters.

To begin, we examine the distribution of the α parameters between all clusters. Figure 6.1 shows the relationships between all three mass function slopes ($\alpha_1, \alpha_2, \alpha_3$). The high-mass α_3 is not clearly correlated to either of the other MF exponents, however a clear relation can be seen between α_1 and α_2. While it should be noted that, by design, the priors used here disallow $\alpha_1 < \alpha_2$ (as shown by the shaded regions in Figure 6.1), which may introduce a bias to this trend, it is clear that, in general, clusters with a more depleted low-mass mass function also have a correspondingly depleted intermediate-mass mass function, as might be expected due to dynamical evolution.

The relation between α_1 and α_2 also showcases another important phenomenon;

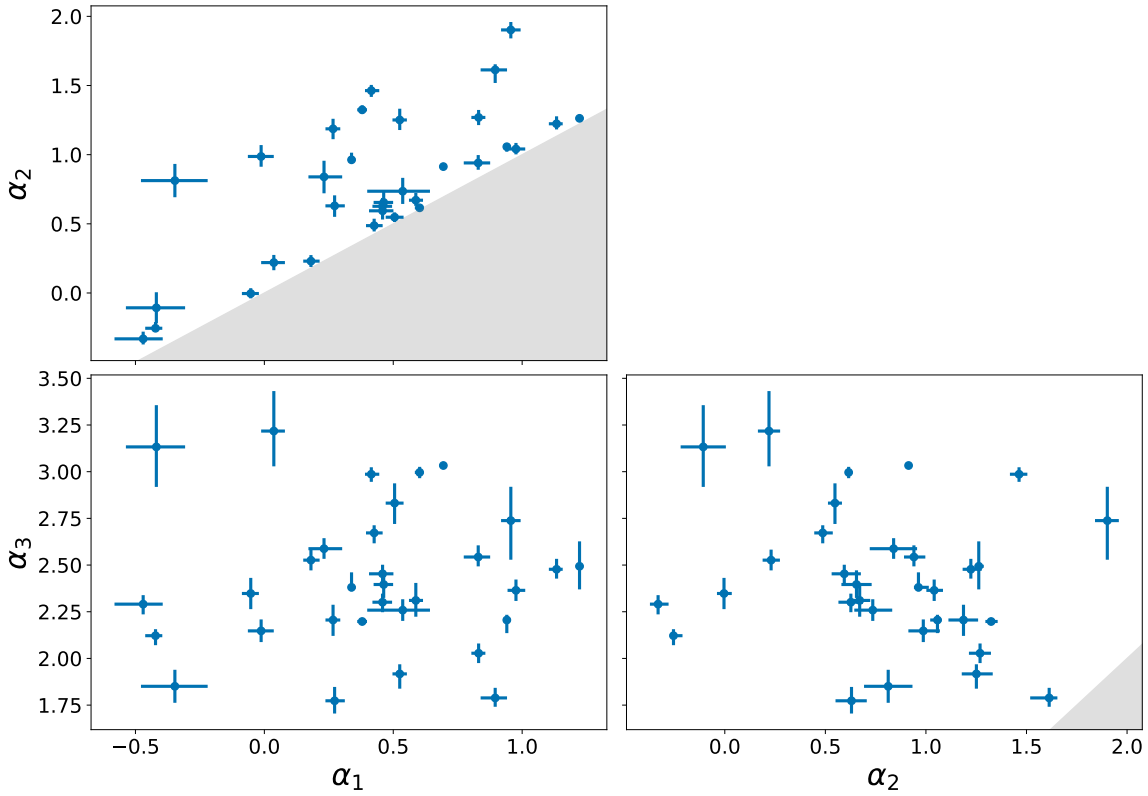

Figure 6.1: Relations between all three mass function exponent parameters. Gray shaded areas represent the parameter space which is disallowed by the priors on the mass function slopes.

a large number of clusters do not fall on or near the $\alpha_1 = \alpha_2$ line, but are instead steeper in the intermediate-mass regime than the low-mass regime. This suggests that a two-component power law is necessary to describe the global mass function below $1\,M_\odot$, and a single power law attempting to describe the same mass regime would overestimate both the high and low mass ends of the mass function in this regime, and underestimate the mass function in the intermediate regime, near the break mass of $0.5\,M_\odot$. That is, a single α power law over the same mass domain would have a slope greater than α_1 and less than α_2.

6.1 Initial Mass Function

The α parameters constrained by the models describe the global stellar mass functions of the clusters at the present day, and in order to examine the initial mass function of our clusters we must carefully consider the connection between the IMF and the PDMF. As discussed in Section 2.2, we have chosen not to model the dynamical loss of (preferentially low-mass) stars in the mass function evolution algorithm used, due to its complex dependence on the dynamical evolution and initial conditions of the cluster. Therefore, in our models, the IMF can most directly be inferred only in the high-mass ($\alpha_3, m > 1\,\mathrm{M}_\odot$) regime, while the lower-mass exponents (α_1, α_2) are more representative of the present-day mass function, which may have evolved away from the IMF significantly.

To quantify this assertion, we must examine the dynamical evolution of our clusters, as the dynamical loss of stars is not necessarily limited entirely to the lower-mass regime. In very dynamically evolved clusters, which have lost a substantial amount of their total initial mass to escaping stars, the characteristic mass of preferentially escaping stars will increase, potentially depleting even the population of higher-mass stars and white dwarfs, which had initial masses above $1\,\mathrm{M}_\odot$, and in such cases the inferred mass function exponent α_3 may also be shallower and less directly representative of the IMF. To account for this effect, we must determine which clusters have lost a large amount of their initial mass by the present day. We estimate this *remaining mass fraction* by the equation:

$$\frac{M_{\mathrm{today}}}{M_{\mathrm{initial}}} = 0.55 \times \left(1 - \frac{\mathrm{Age}}{\tau_{\mathrm{diss}}}\right) \tag{6.1}$$

where the factor 0.55 reflects the typically assumed mass loss from stellar evolution

of $\sim$ 55% of the initial cluster mass in the first Gyr of a cluster's evolution and the dissolution time $\tau_{\rm diss}$ represents the estimated total lifetime of the cluster. The estimated lifetimes of our clusters were computed according to the approach described in Section 3.2 of Baumgardt et al. (2019a), using the updated models of Baumgardt et al. (2022). This method is based on integrating the orbit of the clusters backwards in the Milky Way galactic potential (Irrgang et al., 2013), and estimating the resulting mass loss.

A related quantity is the "dynamical age", which we define as the ratio of the cluster's age over its half-mass relaxation time ($\tau_{\rm rel}$).

We have taken both the relaxation and dissolution times from the best-fitting models of Baumgardt et al. (2022), a companion study which determined the mass functions of 120 MW, LMC and SMC globular clusters by comparing the same HST mass function datasets as used in this work with a grid of direct N-body simulations. While we could technically extract the relaxation times self-consistently from our own set of models, we utilize the values obtained by Baumgardt et al. (2022) in order to most easily compare our results. Given the excellent match to the total mass and half-mass radii of their N-body models, as shown in Figure 5.4, the differences should be negligible.

These quantities, and their relationships with all mass function exponents, are shown for all clusters in Figure 6.2. The clusters to the left of these plots are thought to have lost a large amount of their initial mass and be dynamically very evolved. In these cases the lower-mass α_1 and α_2 slopes are shallower (with α_1 even becoming negative in the most dynamically evolved clusters), and the α_3 slope may also have been modified by dynamical evolution. As such, caution is advised when interpreting the slopes in these clusters as representative of the IMF. These quantities cannot be

used to define an exact division of where the global mass function parameters reflect the IMF, but it does provide useful context to our proceeding analysis of the IMF.

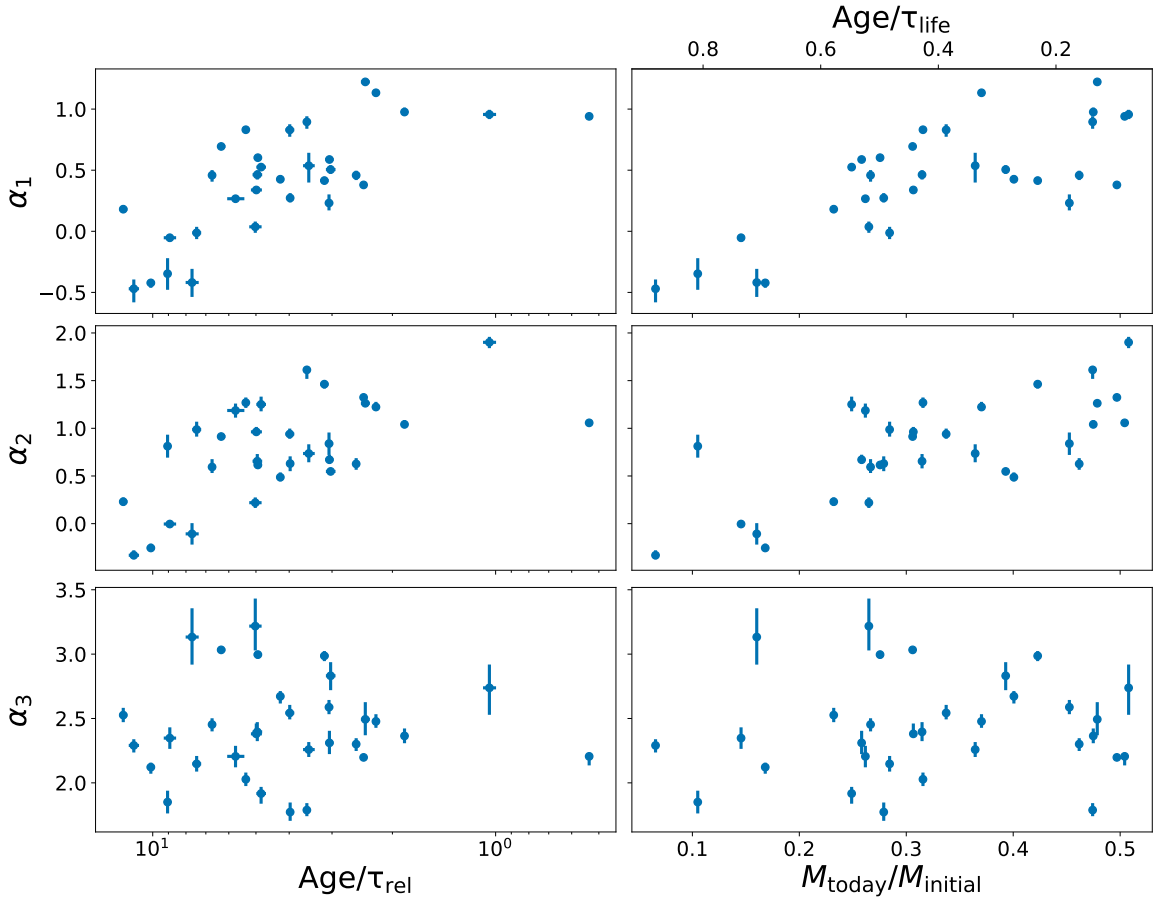

Figure 6.2: Relations between all three mass function exponent parameters and the remaining mass fraction and dynamical age of all clusters. Clusters with higher remaining mass fractions and relaxation times greater than their ages provide more reliable probes of the IMF.

We can clearly see that both lower-mass MF exponents (α_1, α_2) have distinct correlations with these two quantities, with the increasingly evolved clusters (short lifetimes / relaxation times compared to their ages) substantially more depleted in low-mass stars than their less evolved counterparts. No such correlation exists with α_3, which supports our assertion that the high-mass regime is less affected by the cluster's dynamical evolution, and thus, overall, most representative of the IMF. However, as stated before, caution should still be applied when interpreting the α_3 of the clusters

to the left side of this figure. We will examine this parameter in more detail in Section 6.1.2 below.

6.1.1 Low-Mass IMF

The correlations with the lower-mass exponents (α_1, α_2) also closely match the behaviour of the global mass functions inferred in Baumgardt et al. (2022), as can be seen in Figure 6.3. In fact, the mass function exponents of both of our models agree extremely well, as seen in the residual panels of Figure 6.3.

It is important, however, to note that our parametrization of the mass function is different from Baumgardt et al. (2022). Baumgardt et al. (2022) assume, for the most part, a single power-law MF, whereas, in the overlapping mass regime, we utilize a broken two-stage power law characterized by α_1 and α_2. As shown in Figure 6.1 above, a single power-law MF, while a useful approximation, will not provide an entirely accurate fit to the observed data in all clusters. In general, a single power-law will overestimate the amount of low-mass stars, a bias which can indeed be seen in the residuals of Figure 6.3. This bias is also explored in Section 4.4 of Baumgardt et al. (2022), for a handful of clusters with the deepest mass functions and longest relaxation times, and similar conclusions were reached.

If we assume that this correlation of the global mass functions slope with the remaining mass fractions is, as argued in Baumgardt et al. (2022), due to the internal evolution of the clusters and not a sign of initial variations, then the clusters to the far right of Figure 6.3 can be assumed to have PDMFs (in the mass regime of α_1 and α_2) that is representative of their IMFs. Examining the clusters with an estimated lifetime at least twice as long as the current age (i.e. a remaining mass fraction greater than ~ 0.275), we find median and 1σ values of $\alpha_1 = 0.46^{+0.45}_{-0.48}$ and $\alpha_2 = 0.79^{+0.54}_{-0.49}$.

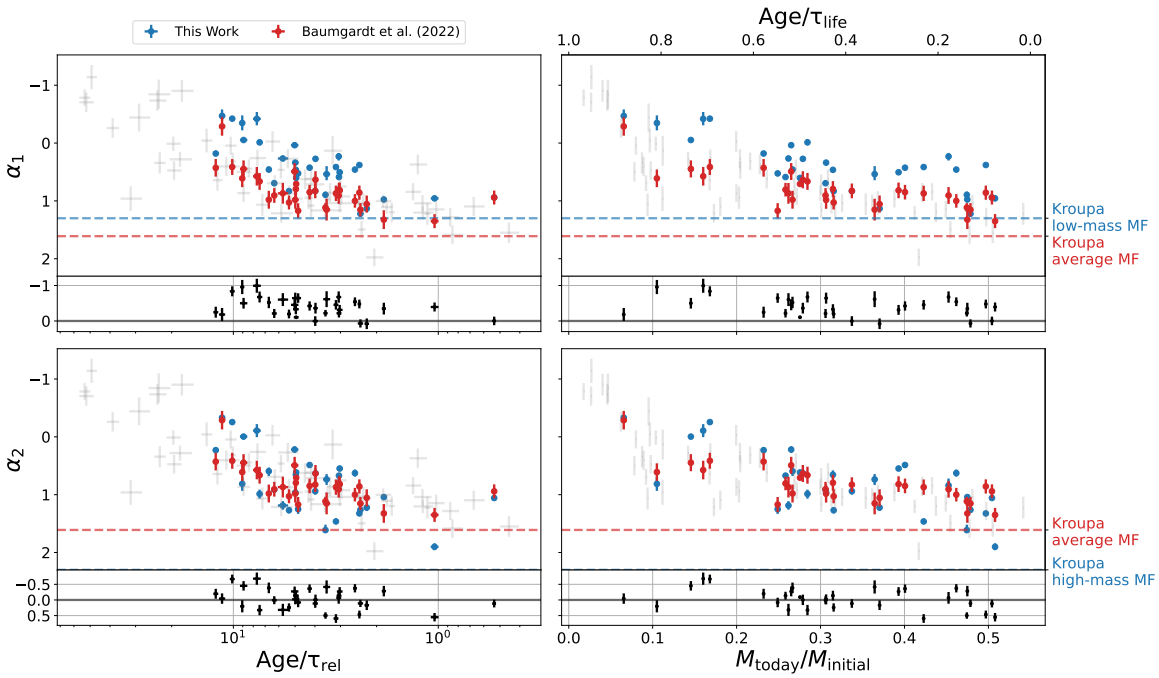

Figure 6.3: Relations between the PDMF exponents (α_1 and α_2) and the remaining mass fraction and dynamical age of all clusters, in comparison with the single power-law MF values computed by Baumgardt et al. (2022), shown in red. All clusters examined in Baumgardt et al. (2022) but not in this work are shown in grey in the background. Shown below each panel are the residuals of the two datasets, in black. The MF slope values of the canonical Kroupa IMF are shown as dashed lines, with blue representing the exact values of 1.3 and 2.3 for the low and high-mass regimes respectively, and red showing the averaged single-exponent power law slope of 1.61 used in Baumgardt et al. (2022).

The canonical Kroupa (2001) mass function has corresponding exponents of 1.3 and 2.3 in these same mass regimes. Our models therefore imply a low-mass mass function which is considerably flatter and more depleted in low mass stars compared to the typical Kroupa mass function, a result which is echoed by the single power-law MFs of Baumgardt et al. (2022). A similarly depleted, bottom-light initial mass function has also been previously suggested in studies of NGC 7078, NGC 7099 (Cadelano et al., 2020) and NGC 104 (Hénault-Brunet et al., 2020), all of which we reproduce well here.

Baumgardt et al. (2022) also demonstrated, through comparison of these MF results against N-body models evolved in an external potential, that only clusters with an initial BH retention fraction below 50% could reproduce the observed trend with

dynamical age, as larger populations of initial BHs would suppress the segregation between the least massive stars and prevent the observed depletion of low-mass stars. We will explore the black hole populations of our models more in Chapter 7. Further studies of the effects of a bottom-light IMF on cluster evolution, through N-body or Monte Carlo modelling, similar to the work done, for example, by Weatherford et al. (2021) on top-heavy IMFs, would greatly improve our understanding of the effects of these results on cluster evolution.

6.1.2 High-Mass IMF

We next examine the high-mass MF exponent, α_3, which, as shown in Figure 6.2, is uncorrelated with the dynamical age of the clusters, and thus more convincingly representative of the IMF.

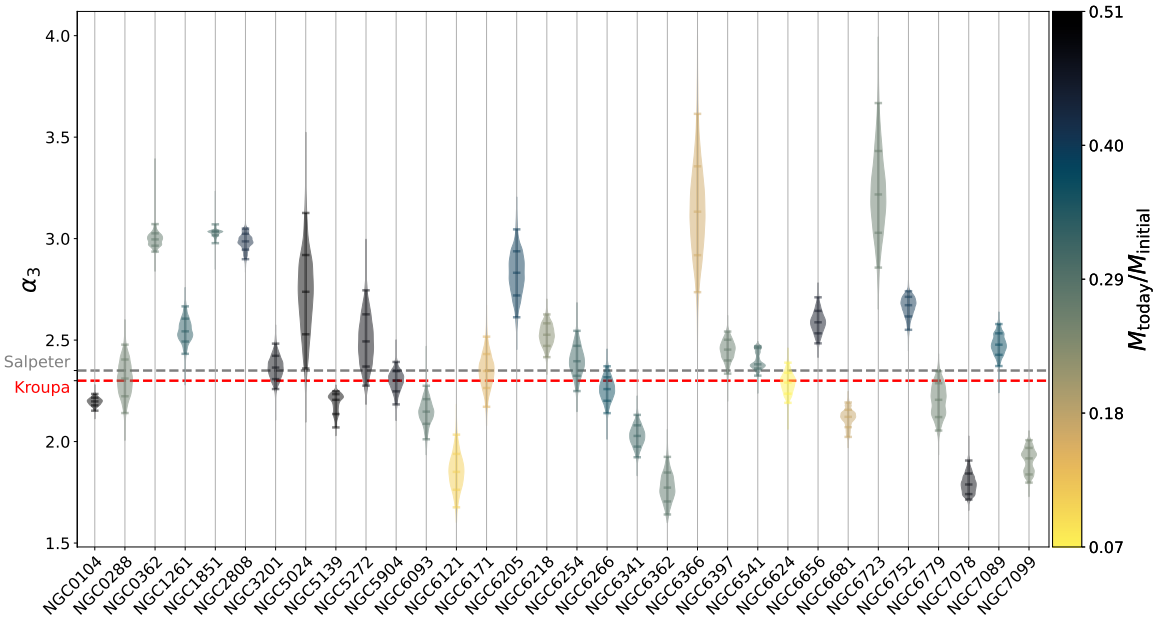

Figure 6.4: Violin plot of the α_3 parameter posterior distributions for all clusters. The median, 1σ and 2σ values are denoted by the horizontal ticks on each distribution. Colours represent the remaining mass fraction. The corresponding values of some canonical high-mass ($m > 1\,\mathrm{M}_\odot$) IMF formulations (Salpeter, 1955; Kroupa, 2001) are shown by dashed lines.

Figure 6.4 shows the posterior probability distributions of α_3 for all clusters. From this figure we can see that the distributions are, in the vast majority of cases, compatible within uncertainties with the typically assumed canonical high-mass ($m > 1\,\mathrm{M}_\odot$) IMF formulations (e.g. Salpeter, 1955; Kroupa, 2001), however with a large spread of α_3 values between $\sim 2{-}3$. The median and 1σ values over all clusters are $\alpha_3 = 2.37^{+0.48}_{-0.25}$. This matches remarkably well with the canonical IMFs, a striking result given the large freedom in the mass function of our models. It is even clearer that our fits *do not* favour any more extreme IMFs, neither exceedingly top-heavy nor top-light, especially when ignoring the most dynamically evolved clusters (shown in Figure 6.4 by the more yellow colours).

This result is counter to some recent suggestions in the literature (see Section 1.2.1) of top-heavy IMFs in GCs. It has been shown that clusters with top-heavy IMFs are expected to have lost a very large fraction of their mass early in their lifetimes due to stellar mass loss and supernova explosions, produce a large amount of black holes and could contribute significantly to the observed rate of binary BH mergers (Haghi et al., 2020; Weatherford et al., 2021). Given that our results seem to preclude any clusters as top-heavy as $\alpha_3 \sim 1.6$, there is thus no obvious need to consider top-heavy IMFs in estimates of BBH merger rates in globular clusters.

Due to the very small dissolution times of top-heavy GCs of typical masses ($\sim 10^5\,\mathrm{M}_\odot$), there remains the possibility that some GCs had formed with a more top-heavy IMF, and have simply dissolved to such an extent by the present day that they are undetectable. These clusters could still contribute significantly to the rate of BBH mergers and gravitational waves. Although, given the large range of GC parameter space covered by our models, it is unclear what would cause these top-heavy GCs to form alongside clusters with a more canonical or bottom-light IMF as we see here.

6.2 Relationship with Metallicity

We next examine possible correlations between the stellar IMF of GCs and metallicity. Variations of the initial mass function with metallicity have been suggested in the past based on theoretical studies of star and cluster formation, which indicate that increasing metallicity leads to more efficient cooling and helps limit stellar accretion, and thus should reduce the characteristic mass of formed stars and produce an increasingly bottom-heavy IMF in more metal-rich clusters (Larson, 1998; De Marchi et al., 2017; Chon et al., 2021). Marks et al. (2012) proposed a linear relationship between the high-mass IMF slope and metallicity, which begins with extremely top-heavy values of α_3 at lower metallicities, and reaches the canonical Kroupa value of 2.3 only at metallicities [Fe/H] > 0.5. Given the large amount of freedom available in our mass function slopes, and the excellent constraints we are able to place on the dark remnant populations in this mass regime, our model fits, which span nearly the full range of Milky Way GC metallicities, present an excellent opportunity to examine this potential relationship.

6.2.1 Relationship with High-Mass MF

Figure 6.5 shows the relationship between α_3 and cluster metallicity [Fe/H]. While a distinct correlation between these parameters is not immediately clear, a possible trend can be seen, after excluding the GCs with the smallest remaining mass fractions. The most metal-poor clusters have a value of α_3 closer to ~ 2.0, and the slope increases linearly (i.e. the mass function becomes steeper) with increasing metallicity past the canonical Salpeter value and towards ~ 3.0 in the more metal-rich clusters. This relation is, however, quite noisy, and prominent outliers exist. In particular, four clusters (NGC 104, NGC 6121, NGC 6362, NGC 6624) with higher metal-

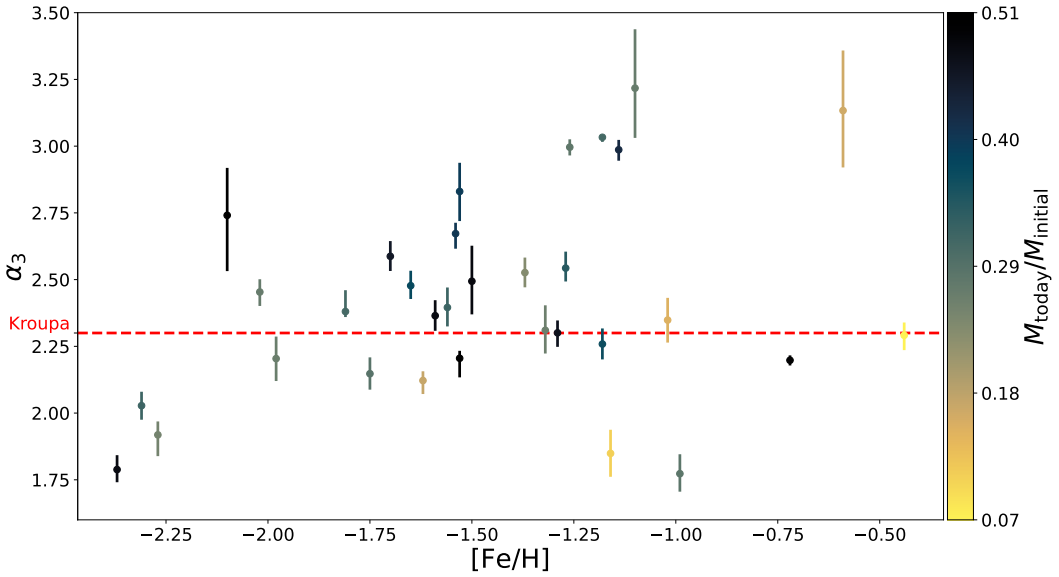

Figure 6.5: Relation between the high-mass IMF exponent α_3 and the cluster metallicity for all clusters. Colours represent the remaining mass fraction. The corresponding value of the Kroupa (2001) canonical high-mass ($m > 1\,\mathrm{M}_\odot$) IMF formulation is shown by the red dashed line.

licities ([Fe/H] $\gtrsim -1.2$) have α_3 exponents flatter than Salpeter, while the metal-poor NGC 5024 ([Fe/H] $= -2.1$) has a slope of ~ 2.7 (albeit with large uncertainties). It should again be emphasized that, as mentioned in Section 5.2, the uncertainties on these parameters are only the statistical uncertainties on the fits, under the assumption that our models are a good representation of the data, and as such may be underestimating the true errors.

To investigate this potential trend further, we attempt to directly fit a linear relation ($\alpha_3 = m \times [\mathrm{Fe/H}] + b$) to this plot, using a simple MCMC sampler with a Gaussian likelihood. To account for any biases and underestimated uncertainties in our inferred α_3 values, we also include a nuisance parameter, added in quadrature to the statistical errors. We also repeat this analysis multiple times, excluding all clusters below a certain remaining mass fraction threshold, to test the effect of including or excluding clusters which have lost a significant fraction of their initial mass and

therefore have a more depleted stellar mass function. Figure 6.6 shows the results of these fits. All linear fits show a slightly positive slope, indicating a general trend towards flatter high-mass IMFs at higher metallicities, as discussed. However, this relation should be regarded as very speculative, as the relative uncertainties on these fits are quite large, due to the outliers mentioned above. Within 2σ, these fits are also consistent with a slope of 0, indicating no obvious trend of IMF slope with metallicity. We can also see the adopted remaining mass fraction threshold slightly affects this slope. The slope increases very slightly with higher remaining mass fraction thresholds, until ~ 0.3, where the amount of discarded clusters becomes quite large and the results are less significant.

This analysis and conclusions are thus limited by the smaller number of clusters with a larger remaining mass fraction at both extremes of the metallicity range of Milky Way GCs, and further extension of this work to more metal-poor and metal-rich clusters is necessary to be able to say definitively whether a correlation exists between the metallicity and the stellar IMF of GCs. It is clear though, even with these caveats, that the very top-heavy IMF-metallicity relationship proposed by Marks et al. (2012) is not compatible with our results. As discussed in Section 6.1.2, none of our clusters favour a top-heavy IMF, and even our most metal-poor clusters have a value of α_3 much closer to the canonical ~ 2.3 than suggested by the fundamental plane of Marks et al. (2012).

6.2.2 Relationship with Low-Mass MF

Baumgardt et al. (2022) also examined the effects of the environment on the global mass function slope, finding a weak correlation with metallicity when considering their sample of least dynamically evolved GCs alongside a number of open, LMC and

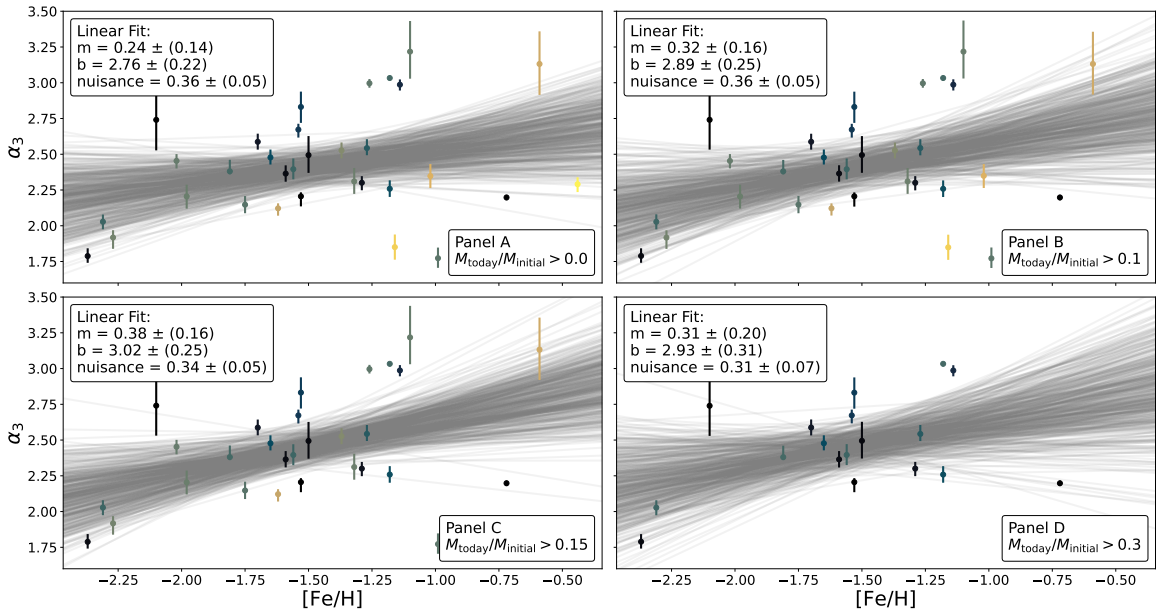

Figure 6.6: Figure 6.5 repeated with all clusters (panel A) and the the exclusion of all clusters with a remaining mass fraction less than 0.1 (panel B), 0.15 (panel C) and 0.3 (panel D). Colours represent the remaining mass fraction, on the same scale as Figure 6.5. Over-plotted in grey is the best-fit linear relation representing the given clusters, shown by 500 random draws of the converged MCMC chain. The median and 1σ uncertainties of the parameters of these fits are given in the upper-left corner of each panel.

SMC clusters and dwarf galaxies. However, this correlation was not present when only considering the globular clusters.

Figure 6.7 demonstrates the same fitting procedure as done in Figure 6.6, but repeated this time for the lower-mass exponents, in order to compare with the findings of Baumgardt et al. (2022). Negative slopes can be seen in the left panels, for both α_1 and α_2, when fitting on all clusters, suggesting an increasingly flatter, depleted low-mass MF at higher metallicities. However, this correlation largely disappears when restricting the analysis to only the least evolved clusters. This may suggest that any relationship with metallicity in the mass function below $1\,M_\odot$ can be explained, not by initial variations in the IMF, but instead by the dynamical evolution of the cluster, and could be driven by the underlying correlation between the metallicity and the galactocentric radii, and thus lifetimes, of the clusters (van den Bergh, 2011), as

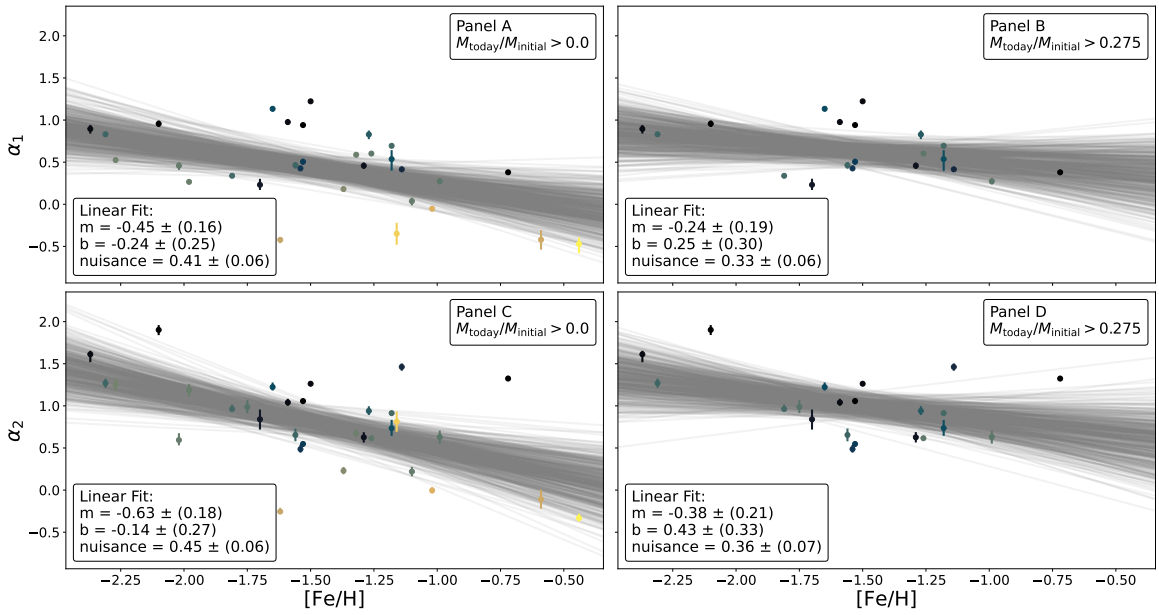

Figure 6.7: Relation between the low and intermediate-mass MF exponents (α_1, α_2) and the cluster metallicity for all clusters (panel A & C) and restricted to clusters with lifetimes twice as large as their ages (panel B & D). Colours represent the remaining mass fraction, on the same scale as Figure 6.5. Over-plotted in grey is the best-fit linear relation representing the given clusters, shown by 500 random samples of the converged MCMC chain. The median and 1σ uncertainties of the parameters of these fits are given in the bottom-left corner of each panel.

metal-rich GCs tend to occupy orbits nearer the galactic bulge. It should, of course, be noted again that the uncertainties associated with the linear fits of the unevolved clusters are quite large, and could be consistent both with a clear decreasing slope, or no correlation at all. Once again, further extension of this study to the most metal-rich and metal-poor regimes, for less evolved clusters, would help in firmly establishing these relationships.

Chapter 7

Black Hole Populations

In this chapter, we explore the populations of black holes (and other dark remnants) present in our best-fitting models. We will examine the distribution of the total mass and amount of black holes in our fits, comparing our results against a number of other studies, and explore any possible correlations present between the remnant populations and other cluster properties. We will also discuss in more detail the case of "core-collapsed" clusters and how we model them. Finally we will dive more deeply into results from the literature surrounding a few specific clusters of interest.

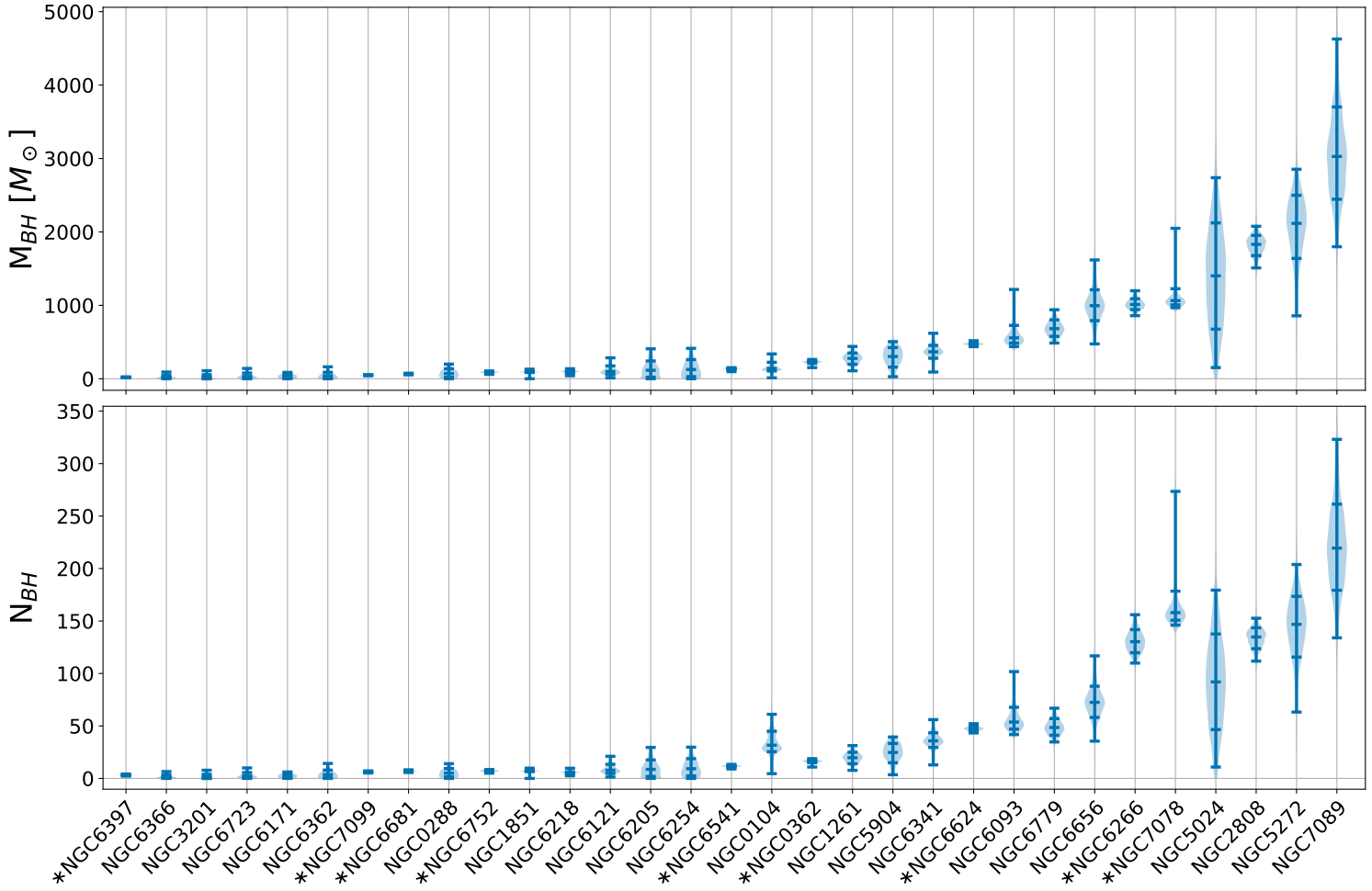

Figure 7.1: Violin plots of the posterior probability distribution of total mass (upper panel) and number (lower panel) of black holes in all clusters, except for NGC 5139, which has a median black hole mass of approximately $1.7 \times 10^5\,M_\odot$, and is excluded in order to highlight the distributions of the other clusters. The median, 1σ and 2σ values are denoted by the horizontal ticks on each distribution. All clusters classified as core-collapsed in Trager et al. (1995) are denoted by an asterisk.

Figure 7.1 shows the posterior probability distributions of the total mass and amount of black holes present in the best-fitting models of most clusters in our sample. NGC 5139 (ω Cen) is not included in Figure 7.1, due to the extraordinarily large mass in black holes ($M_{BH} = 1.70^{+0.05}_{-0.04} \times 10^5$ $M_\odot$) inferred, but it is discussed in more detail in Section 7.4 below.

A large number of the clusters are consistent, within 2σ, with harbouring little to no black holes, while the remainder possess, on average, at most a few thousand $M_\odot$ of stellar-mass black holes, with constituent individual BH masses between $\sim 5{-}15$ $M_\odot$. Other than ω Cen, it is clear that none of our models favour a very large population of black holes, with all clusters having a mass fraction in black holes of less than 0.5% at the present day. Our models are thus able to reproduce well the observables of all clusters without the need for any central intermediate-mass black hole, of any size. It should of course be noted however that it is currently not possible for us to self-consistently include an IMBH in our models to compare directly and explore any partial degeneracy between a central IMBH and a central concentration of stellar-mass BHs (e.g. Lützgendorf et al., 2013). Outside its sphere of influence, a central IMBH is expected to have dynamical signatures similar to a population of centrally concentrated BHs, for example by quenching mass segregation among the visible stars (Gill et al., 2008; Peuten et al., 2016), inflating cluster cores (Heggie et al., 2007; Peuten et al., 2017), or increasing the central velocity dispersion (e.g. Zocchi et al., 2019). In the future, it would also be interesting to expand this work, where possible, with the inclusion of millisecond pulsar spin-period derivatives, as done by Smith et al. (2022) for NGC 104, in order to provide even better constraints on the dark remnant populations and the possibility of IMBHs in these clusters.

7.1 Core-Collapsed Clusters

Due to the negative heat capacities of self-gravitating systems such as globular clusters, over time dynamical interactions are expected to inevitably lead to the "collapse" of the system's core. Globular clusters currently undergoing core-collapse are typically defined based on the shape of their central density profiles, with core-collapsed clusters showing a power-law density profile increasing all the way to their centres, while non core-collapsed clusters possess larger, isothermal cores with a flat central density profile (e.g. Djorgovski & King, 1986; Trager et al., 1995). Core-collapsed clusters are expected to contain very few, if any, black holes (Breen & Heggie, 2013a,b; Kremer et al., 2020b). In GCs with a population of stellar-mass BHs, core-collapse occurs within the BH sub-population but, due to the efficient heat transfer from BHs to stars, the visible core will actually remain large (relative to $r_{\rm h}$). The presence of BHs in a cluster may thus play a large role in explaining the observed population of core-collapsed Milky Way GCs, which, given the ages of most clusters, is smaller than would be expected when considering only stellar binaries as the sole delaying mechanism. It is not until almost all BHs (and the last BH binary) are ejected that a cluster core will collapse and exhibit the defining power-law central density profile (e.g. Chatterjee et al., 2013; Kremer et al., 2020b). Almost all GCs have likely reached a state of balanced evolution (Hénon, 1961; Gieles et al., 2011) but, due to BHs, only a minority of GCs *appear* to be post-collapse.

The nine clusters in our sample defined as core-collapsed in Trager et al. (1995) (NGC 362, NGC 6266, NGC 6397, NGC 6541, NGC 6624, NGC 6681, NGC 6752, NGC 7078, NGC 7099) are denoted in Figure 7.1 by an asterisk. Six of these clusters (NGC 362, NGC 6397, NGC 6541, NGC 6681, NGC 6752, NGC 7099) are consistent, within 2σ, with having less than 15 total black holes, a largely negligible population

in our mass models, however the remaining clusters favour a larger amount of total mass in black holes; around $\sim 500\,M_\odot$ for NGC 6624 and $\sim 1000\,M_\odot$ for NGC 6266 and NGC 7078.

This discrepancy between the theoretical expectations and the inferred BH populations for some core-collapsed clusters may arise simply due to the limitations of the LIMEPY models themselves. LIMEPY models, by definition, possess an isothermal core, characterized by a flat inner density profile, which is incompatible with the central cusp of core-collapsed clusters (see also Section 3.1.4 of Gieles & Zocchi 2015). As such, our models may struggle to accurately capture the inner density profiles of these clusters. Indeed this divergence can be seen in the profiles of the three core-collapsed clusters with substantial inferred BH populations in our best-fitting models, which tend to underestimate the amount of stars within a very small distance from the centre (typically $\sim 0.1\,\mathrm{pc}$ in these clusters), and overestimate the profile from there to $\sim 1{-}2\,\mathrm{pc}$ from the centre, as the models attempt to fit a flat inner density profile to the power-law form suggested by the data.

In order to investigate these systems further, as mentioned in Section 5.1, models of these clusters were also computed with the amount of retained black holes at the present day fixed to 0 (by fixing the BH_{ret} parameter to 0%). These models do not show a noticeable difference in the fits of the kinematics or mass functions, and the best-fitting parameters are not drastically different in most cases, in general showing a larger central potential and slightly increased anisotropy radius in models with no BHs. NGC 6624 shows the greatest change, increasing the mass segregation parameter δ from ~ 0.3 to ~ 0.5, as is expected (see Section 7.2 and Figure 7.4), and having a shallower truncation (larger g). The most noticeable change, as is expected, is in the number density profiles, shown in Figure 7.2. While there is a negligible change in NGC 6266, where the density profile was already fit quite well, the other

two clusters clearly demonstrate a constantly increasing inner profile, with no clear isothermal core, as would be expected in a core-collapsed cluster. However, it is difficult to quantify which fit is best, as the 0 BH models seem to overestimate the innermost profiles, where before they were underestimated. In the case of NGC 6624 and NGC 7078, the number density profiles of de Boer et al. (2019) (based on Trager et al. 1995) may simply not provide sufficient coverage in the core of the clusters. As shown by Gieles et al. (2018), HST number density profiles, which show much steeper density profiles in the core, might provide more accurate constraints in this regime and the 0 BH models may have actually been preferred if this data had been used. Overall, however, it is clear that caution must be applied when attempting to fit some core-collapsed clusters using LIMEPY models.

All profiles for both sets of models, for all core-collapsed clusters, can be found in Appendix A.

The original models (with BHs) are used in the rest of this chapter and in all discussion of black holes, however the results of these three clusters (NGC 6266, NGC 6624, NGC 7078) should be regarded with caution. As the large inferred BH populations are most likely not representative of the actual GCs, we elected to use the models introduced here, fixed to 0 BHs, in the relations in all previous chapters. However, there was no significant change in any of the correlations presented, when considering either set of models. NGC 6266 and NGC 6624 are explored in more detail and compared to other results from the literature below in Section 7.4.

7.2 Relationships Between BH Populations and Other Parameters

We next examine how the population of black holes and other remnants in our cluster models correlate with various related parameters.

Figure 7.3 shows the relationship between α_3 and both the black hole retention fraction, BH_{ret} and the total mass in black holes. This serves as a reminder to demonstrate the role of the BH_{ret} parameter, which is *not* directly proportional to the number of BHs. At high values of α_3, only a small number of black holes can be formed initially from the IMF, and a higher retention fraction is required to maintain any amount of black hole mass at the present day. Depending on the cluster mass, at steeper IMF slopes this parameter may functionally have minimal impact on the final amount (or lackthereof) of black holes, which would explain the broad uncertainty ranges on BH_{ret} seen in a large proportion of clusters in this regime. Similarly, the right panel of Figure 7.3 shows that no clear correlation is present between α_3 and the amount of black hole mass at the present day. However, it is clear the majority of black hole hosting clusters in our survey are clusters with intermediate values of α_3. This relates to the relationship with BH_{ret}; clusters at higher α_3 values produce few black holes initially. This of course does not imply a causal relationship between BH mass and neither α_3 nor BH_{ret}, but merely helps to explain the distribution of BH_{ret}.

An interesting relationship does appear between the amount of black hole mass and the δ parameter, a proxy of mass segregation, as shown in Figure 7.4. Clusters with little to no mass in black holes tend to converge near values of $\delta \sim 0.4{-}0.5$, which is typical of evolved and mass-segregated clusters, whereas the clusters with more substantial populations of black holes congregate closer to the lower bound of

~ 0.3. This is in agreement with the models of Peuten et al. (2017), who find, by comparing LIMEPY models against N-body models with and without black holes, that the majority of mass-segregated clusters should converge to a value of ~ 0.5, but also show that, in models with a significant population of black holes, only the black holes may be in energy equipartition, and the degree of mass segregation may be suppressed.

Figure 7.5 shows the relationship between both the total cluster mass in black holes and the fraction of the cluster mass in remnants (WD, NS and BH), against the dynamical age of the clusters. While there is no strong correlation between BH mass and the dynamical age of the cluster, it can be seen that clusters with a substantial population of black holes tend to be less dynamically evolved and to have lost a smaller fraction of their initial mass. This is as expected, as black holes segregate and are kicked from the clusters due to dynamical interactions over time (Kremer et al., 2019), and therefore more dynamically evolved clusters should have lost a larger fraction of their initial BH population from these dynamical ejections.

The evolution of the remnant fraction, which includes all types of remnants, shows a stronger relationship with the dynamical age of the clusters, as might be expected. As a cluster evolves and loses mass, as mentioned before, the mass lost is preferentially in the form of lower-mass stars, rather than the heavy remnants, and as such the fraction of mass in remnants should increase as the cluster's low-mass MF is depleted. Interestingly, some of the most dynamically evolved clusters have nearly 75% of their mass in dark remnants at the present day, which could have important implications for the mass-to-light ratios and inferred masses of unresolved GCs in distant galaxies.

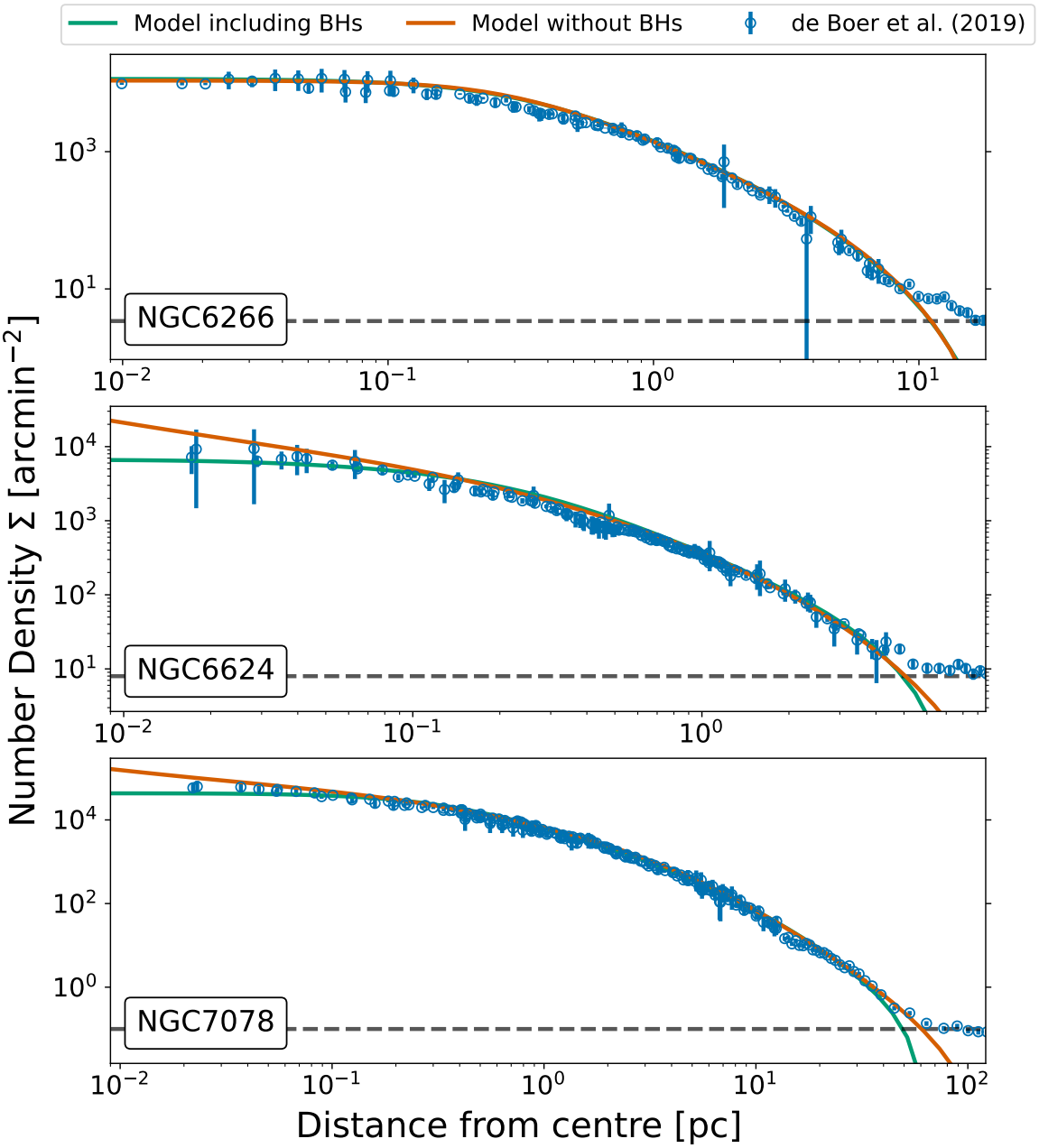

Figure 7.2: The number density profiles of the best-fitting models of NGC 6266, NGC 6624 and NGC 7078, with and without allowing for a population of BHs. The number density data used to constrain the models is shown by the open circles, and the subtracted background values are shown by the horizontal dashed lines.

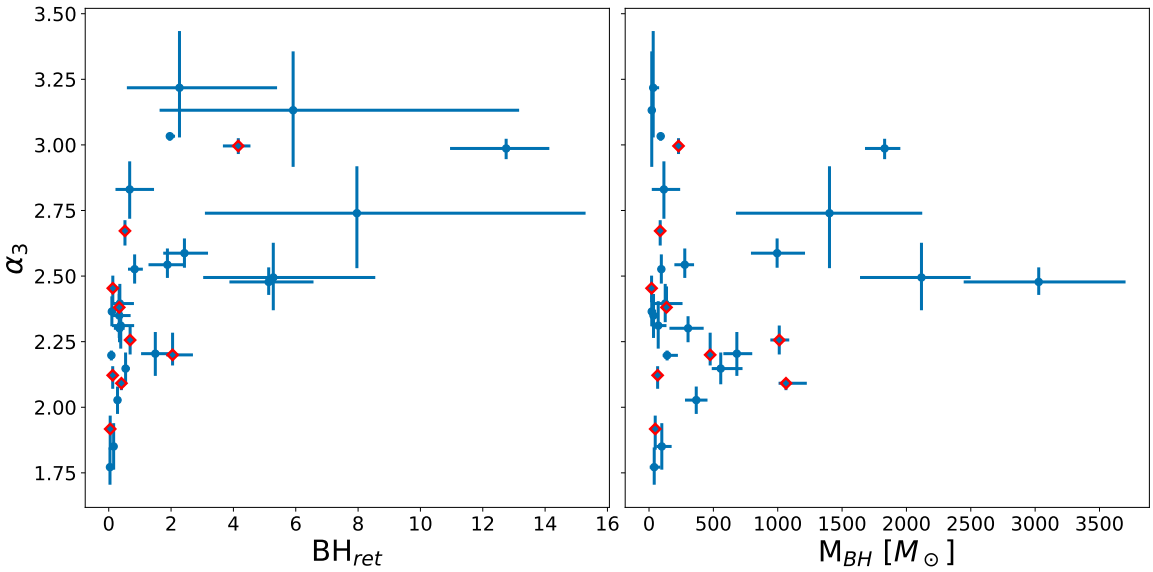

Figure 7.3: Relation between high-mass mass function exponent (α_3) and the black hole retention fraction parameter (BH_{ret}) and the total mass in black holes, for all clusters except for NGC 5139, which has a substantially higher BH_{ret} of $\sim 19\%$ and a more typical α_3 value of ~ 2.2. All core-collapsed clusters, whose inferred black hole populations may not be physical, are highlighted by a red diamond.

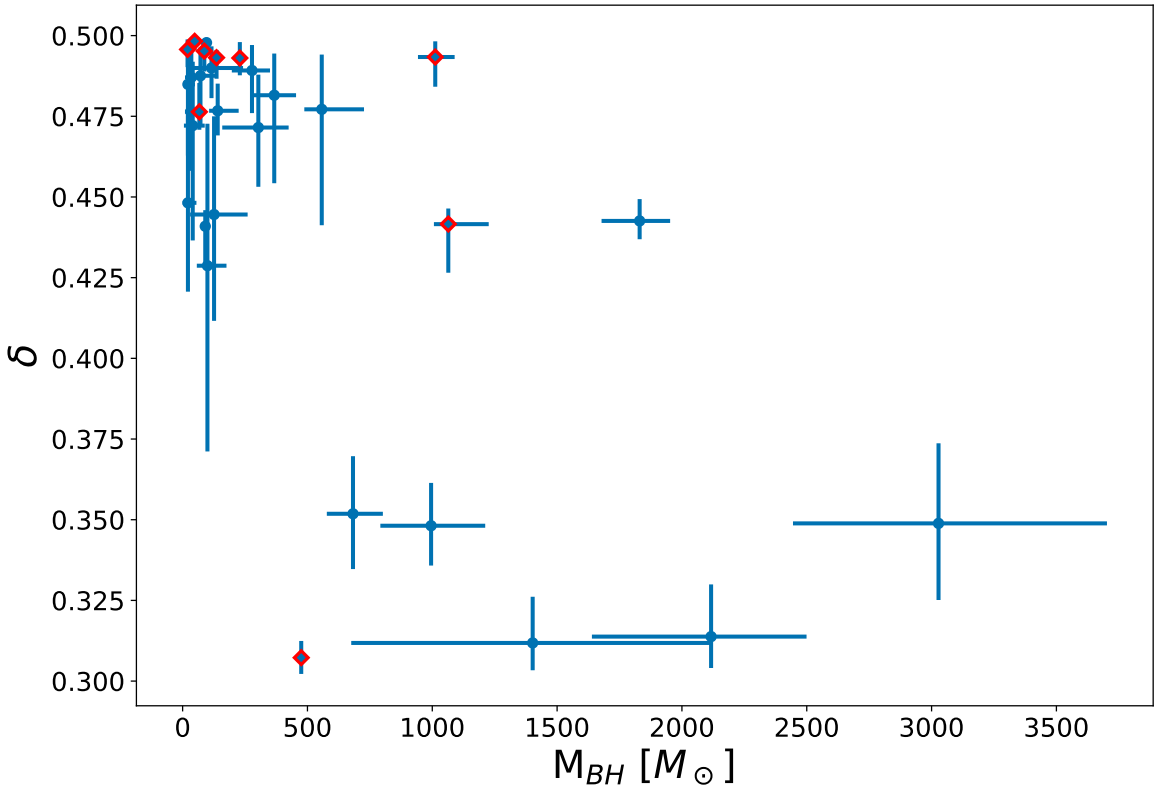

Figure 7.4: Relation between the mass-dependant velocity scale (δ) and the total mass in black holes for all clusters, except NGC 5139. All core-collapsed clusters, whose inferred black hole populations may not be physical, are highlighted by a red diamond.

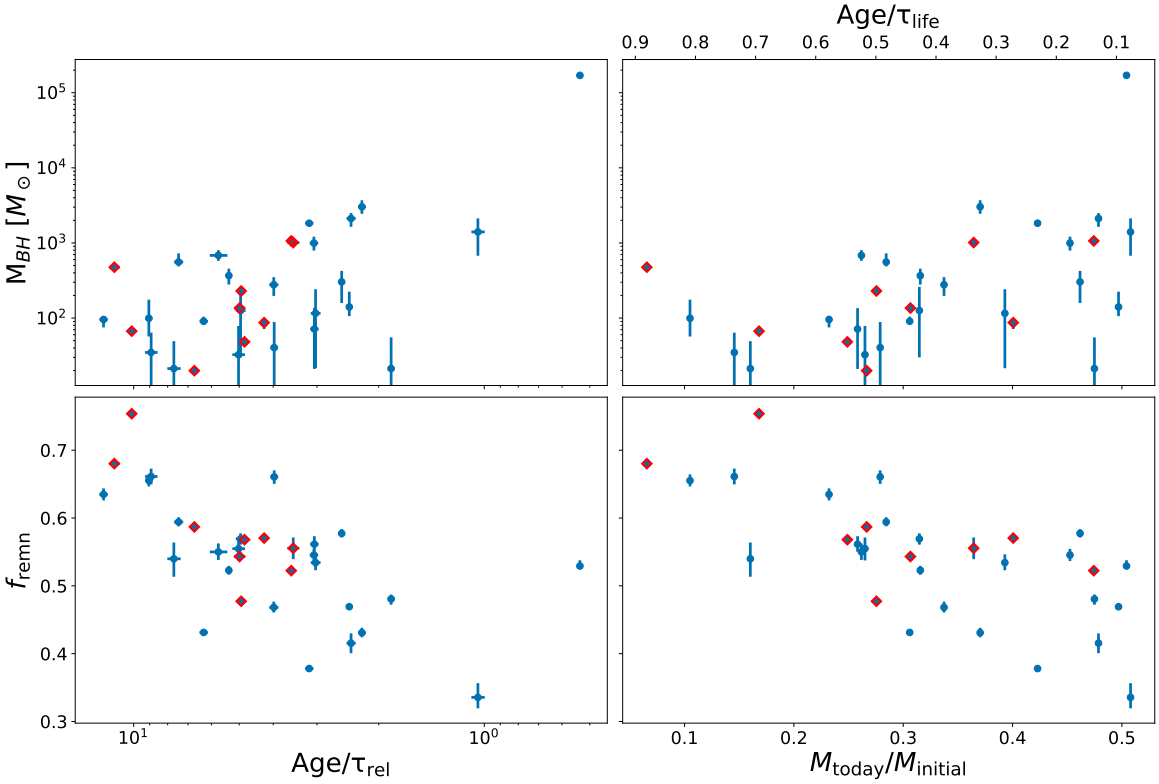

Figure 7.5: Relations between both the total mass in black holes (top row) and the fraction of cluster mass in dark remnants (bottom row) with the remaining mass fraction and dynamical age of all clusters. Black hole mass is presented on a log scale to show NGC 5139. All core-collapsed clusters, whose inferred black hole populations may not be physical, are highlighted by a red diamond.

7.3 Comparison with Literature Results

Figure 7.6 compares the distribution of mass in black holes in our models with that of Weatherford et al. (2020) and Askar et al. (2018). Weatherford et al. (2020) compared the amount of visible mass segregation in a number of Milky Way GCs to the anti-correlation found between the degree of mass segregation in a cluster and its BH population in the *Cluster Monte Carlo* (CMC) catalogue of models in Weatherford et al. (2018), in order to estimate the distribution of black holes mass, normalized to the total cluster mass. In similar fashion to their analysis, we scale their computed estimates of $M_{\rm BH}/M_{\rm cluster}$ (based on the median clustercentric mass segregation parameter Δ_{r50}) by the total cluster mass determined by our models, for comparison. Askar et al. (2018) predicted, in similar fashion, the amount of BHs in a number of Milky Way GCs based on the correlations found in Arca Sedda et al. (2018) between the density of inner BH-subsystems and the average surface brightness of the clusters in the *Monte Carlo Cluster Simulator* (MOCCA) survey database. A somewhat analogous analysis may be found in Rui et al. (2021a), who fit the surface brightness and velocity dispersion profiles of 26 Milky Way GCs to a grid of CMC models and explored seven in more detail. The number of black holes reported for the three overlapping clusters is also noted in Figure 7.6. Further analysis and comparison with other studies of interesting individual clusters is presented below in Section 7.4

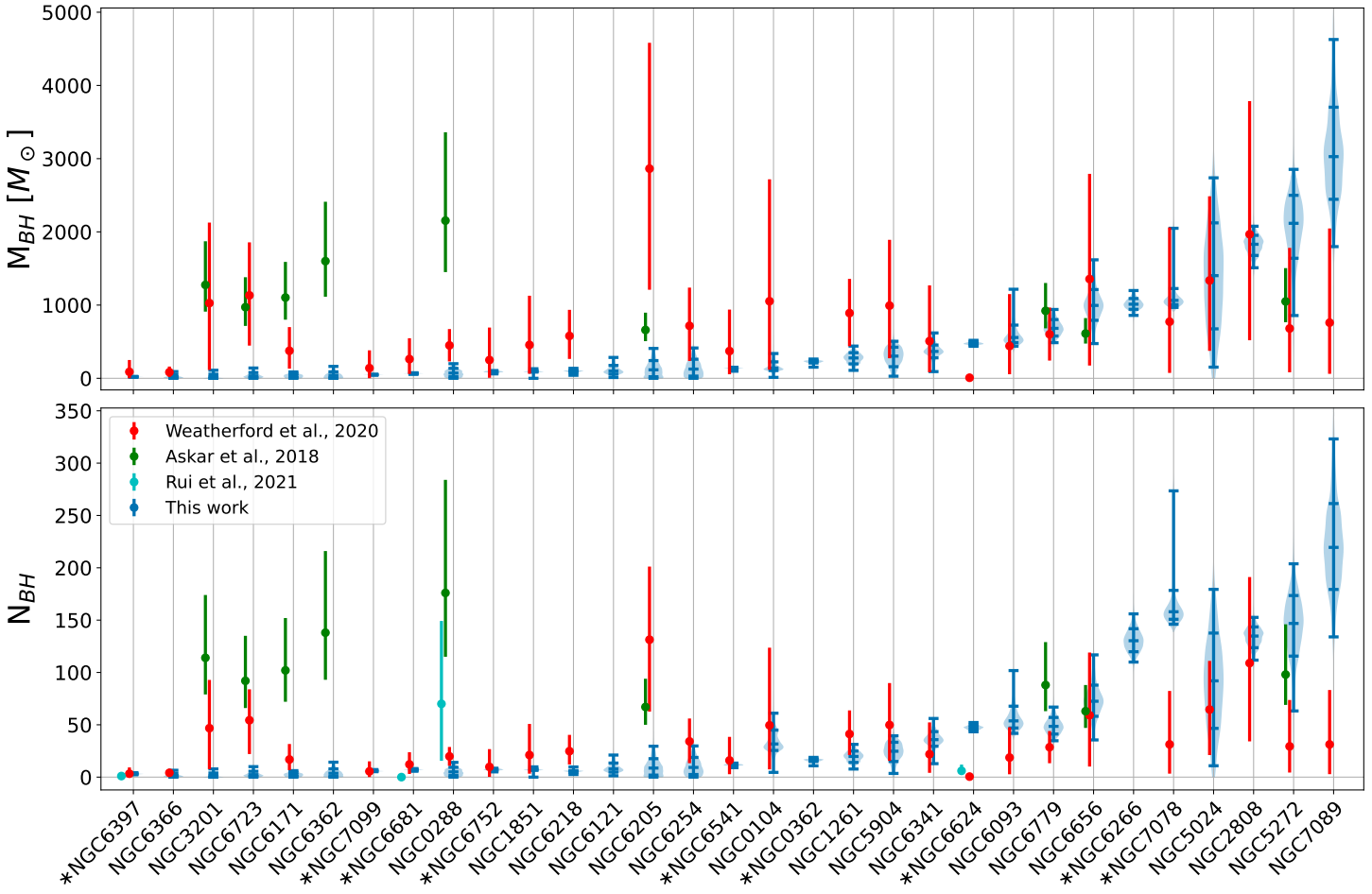

Figure 7.6: Figure 7.1 repeated with the inclusion of of the median and 1σ results for the mass (upper panel) and amount (lower panel) of black holes found by Weatherford et al. (2020); Rui et al. (2021a) and Askar et al. (2018), for the clusters overlapping with our sample. Weatherford et al. (2020) values are computed using our total cluster mass estimates and the median clustercentric mass segregation parameter Δ_{r50} (Table 1 of Weatherford et al. (2020)), while all other values are taken directly from the published values. All clusters classified as core-collapsed in Trager et al. (1995) are denoted by an asterisk.

The majority of our clusters agree well, within 2σ, with the total amount of mass in black holes estimated in these studies. We do find, however, a larger number of clusters consistent with little to no black holes, and estimate in these clusters, on average, fewer black holes than both Weatherford et al. (2020) and Askar et al. (2018). Despite the slight differences between specific clusters in our samples, we do agree with the overall conclusion that, in general, very few black holes are retained in most clusters, with only a handful of clusters retaining more than 100 BHs at the present day.

Our analysis of the black hole populations of individual clusters may be more robust than most of these literature results, which rely on general correlations between models with only a few varied initial parameters, and are fit on only a single observed property (mass segregation between two stellar populations for Weatherford et al. (2020) and the average surface luminosity for Askar et al. (2018)), whereas we self-consistently include the effect of BHs in our fits of numerous cluster observables, and account for many more varying parameters between clusters. In particular, as noted in Weatherford et al. (2020), the correlations of Askar et al. (2018) rely on a number of chained parametric fits, which may bias the final values. We are thus able to, in most clusters, place tighter constraints on the mass in BHs, although it should be noted again that our uncertainties account solely for the statistical uncertainties on the parameter fits and could thus be underestimated.

Another major difference between these results is the (initial) mass function formulation, which was identified by Weatherford et al. (2020) as a potential source of uncertainty in their analysis. The great freedom in the shape of our (initial) mass function, on a per-cluster basis, allows us to best explore the population of BHs and other heavy remnants, as well as their relative abundance compared to lower-mass stars. The generally bottom-light, depleted in low-mass stars, mass function which

was found in our fits (see Chapter 6) may affect the mass segregation correlation found in Weatherford et al. (2018) and thus the amount of mass in BHs found by Weatherford et al. (2020). However the exact effects of a bottom-light IMF on cluster evolution remain to be further explored.

7.4 Clusters of Interest

The results presented here comprise a large sample of Milky Way GCs with stringent constraints on their black hole populations based on accurate fits to a large number of observables, including their visible mass functions at different clustercentric distances. This allows us to compare our results with other dynamical studies of BHs in GCs, based on a number of different methods, in certain particularly interesting clusters.

7.4.1 NGC 5139

NGC 5139, or ω Cen, is the largest and most massive Milky Way GC, and stands apart from the population of Milky Way GCs due to its size, orbit and stellar populations (Harris, 1996). It has been suggested that ω Cen is not a classical globular cluster, but rather the possible remnant nuclear star cluster of an accreted and disrupted dwarf galaxy (e.g. Meza et al., 2005). It has also been hypothesized to harbour an elusive intermediate-mass black hole (Noyola et al., 2008; van der Marel & Anderson, 2010).

The characterization of ω Cen as a common outlier is supported by our results. While our models are able to fit the large amount of data very well, as shown in Figures 7.7 and 7.8, it does not appear in certain plots or relations above as some of its inferred best-fitting parameters are far apart from the rest of the clusters. As can be seen in Table 5.1, our fit of ω Cen has the lowest ϕ_0 of our sample, a cluster

mass 3 times larger than the next most massive GC, the highest (most extended) truncation parameter, and a black hole retention fraction far above all other clusters. It is also among the least evolved of the clusters, with a remaining mass fraction $\gtrsim 0.5$. Notably, the inferred global mass function exponents are *not* outliers, ω Cen fits remarkably well into all relations discussed in Chapter 6, and its high-mass α_3 exponent of $2.21^{+0.03}_{-0.07}$ matches the canonical Kroupa IMF value quite well.

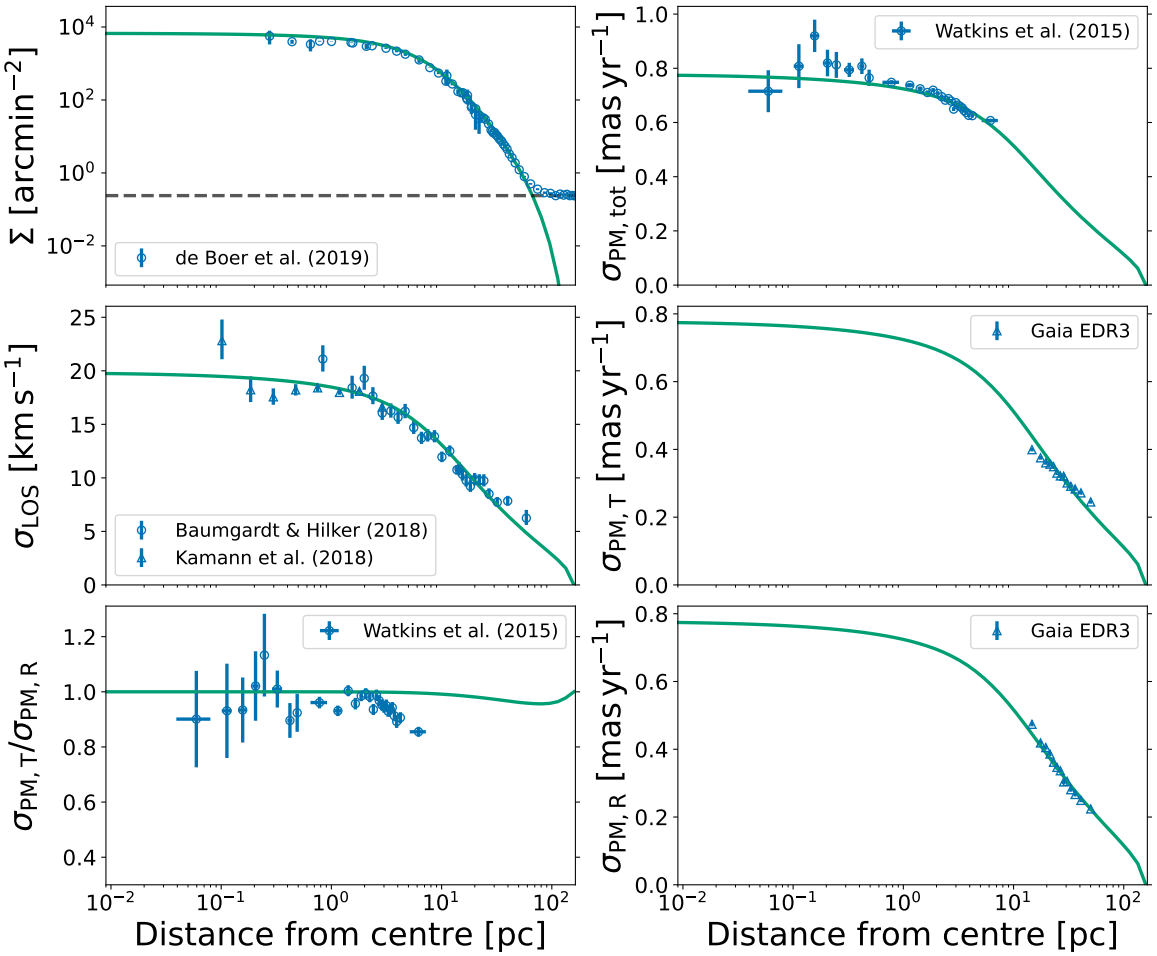

Figure 7.7: Figure 5.2 repeated for NGC 5139

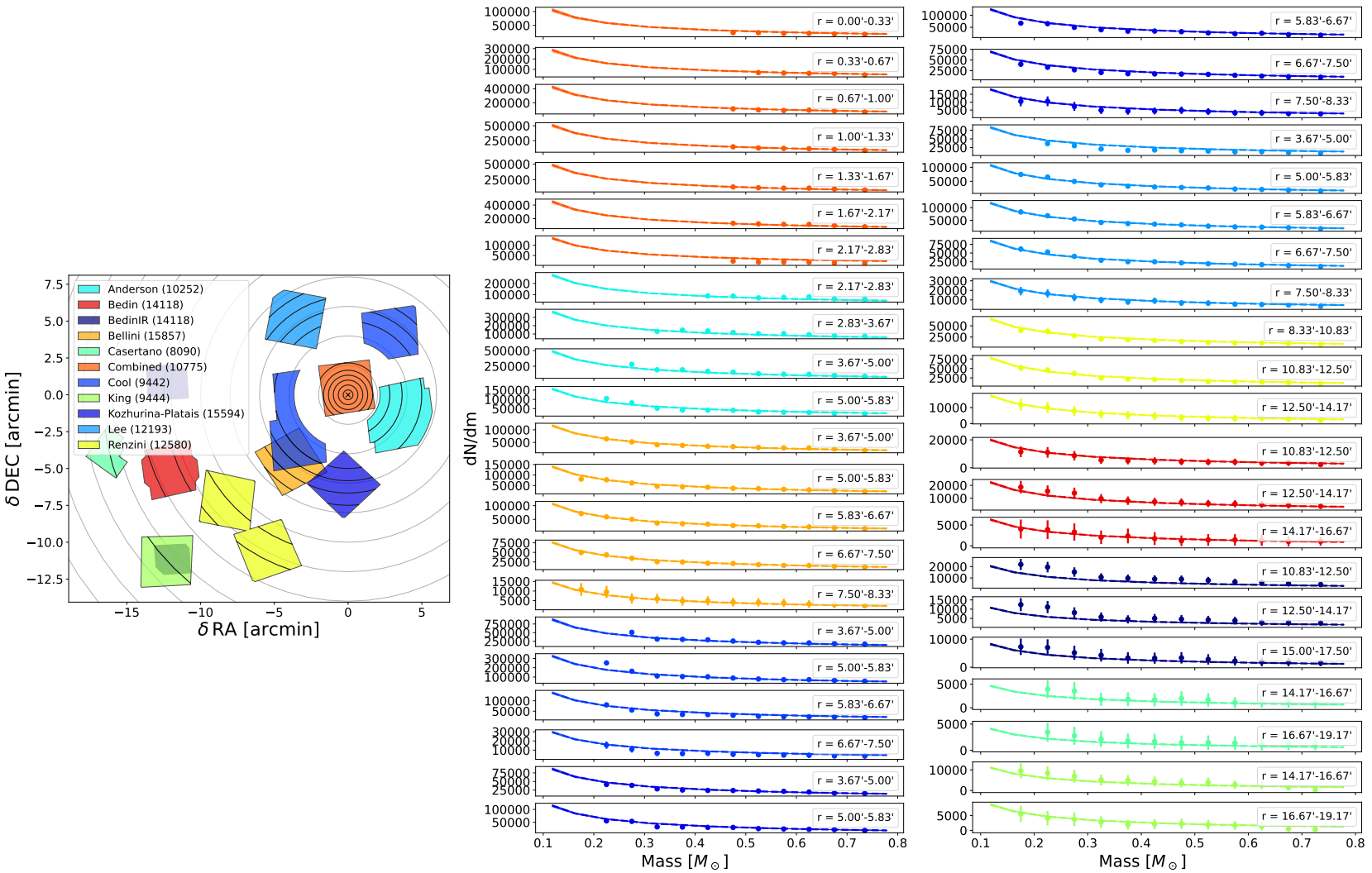

Figure 7.8: Figure 5.3 repeated for NGC 5139

The largest separation of ω Cen from the other clusters is in the black hole population. As shown in Figure 7.9, our fits favour $\sim 170\,000\,\mathrm{M}_\odot$ of mass in BHs, made up of $\sim 10\,000$ BHs, with an average individual BH mass of $\sim 17\,\mathrm{M}_\odot$. From the inferred cumulative mass profile of different cluster components, shown in Figure 7.10, we can see that this BH mass is largely concentrated in the very centre of the cluster. This amount of black holes is substantially higher than any other cluster.

The fraction of mass in black holes to total cluster mass of our best-fitting models ($F_{BH} = 0.054^{+0.002}_{-0.002}$) is exceptionally close to the results of Zocchi et al. (2019), who explored alternatives to the presence of an IMBH in ω Cen using two-component (one representing stellar-mass BHs and one capturing all other lower-mass remnants and visible stars) LIMEPY models. This is interesting given our inclusion of the full mass spectrum, and our fitting of the visible mass function, and reinforces the assertion of Zocchi et al. (2019) that a two-component model is a good approximation when modelling ω Cen, given its large number of black holes and young dynamical age.

Many claims have been made for the presence of an IMBH in the centre of ω Cen. As in the studies of Zocchi et al. (2019) and Baumgardt et al. (2019b), our models do not seem to require an IMBH of any size to reproduce any of the data used here, however we are also limited by the extent of the kinematical data available in the very centre of the cluster, where we would also be discrepant with the IMBH-containing models of Noyola et al. (2008); van der Marel & Anderson (2010)and Baumgardt (2017) (see Figure 5 of Zocchi et al. 2019). As such we cannot say for certain whether some of the dark mass we find may actually be in the form of a central IMBH, given the degeneracy between the effects produced by such an IMBH and a central concentration of smaller BHs.

However there is one caveat to our results; the Gaia proper motion anisotropy

profiles, presented by Vasiliev & Baumgardt (2021), shows that ω Cen transitions at about 20 arcmin from the centre from being radially anisotropic to being slightly tangentially anisotropic. As mentioned in Section 5.2.3, our LIMEPY models are unable to reproduce any amount of tangential anisotropy, and thus cannot match this feature, instead favouring a mostly isotropic fit as a compromise between the radial and tangential regimes, as seen in the lower left panel of Figure 7.7. There is a degeneracy present between the degree of radial anisotropy in a cluster and its mass in black holes (Zocchi et al., 2017), however the difference in the BH mass fraction between the isotropic and anisotropic models of Zocchi et al. (2019) is only on the order of ~ 0.007. Therefore, while further exploration of the effects of tangential anisotropy on the inferred remnant populations of ω Cen may be interesting, given our excellent fits of all other datasets, this should have a negligible impact on the results presented here.

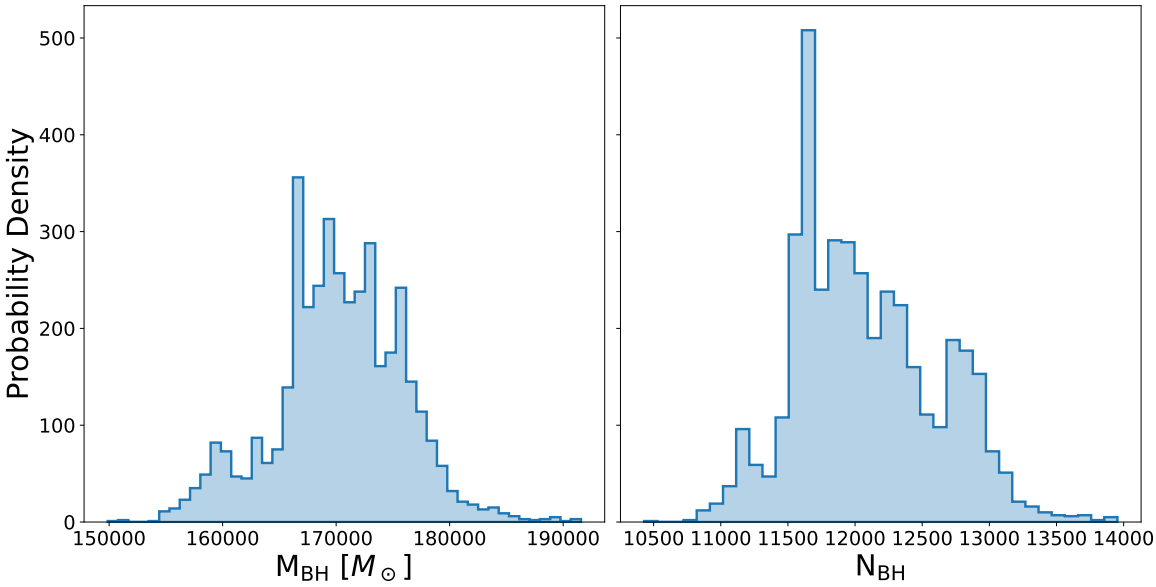

Figure 7.9: Posterior probability distributions of the total mass and number of black holes in ω Cen.

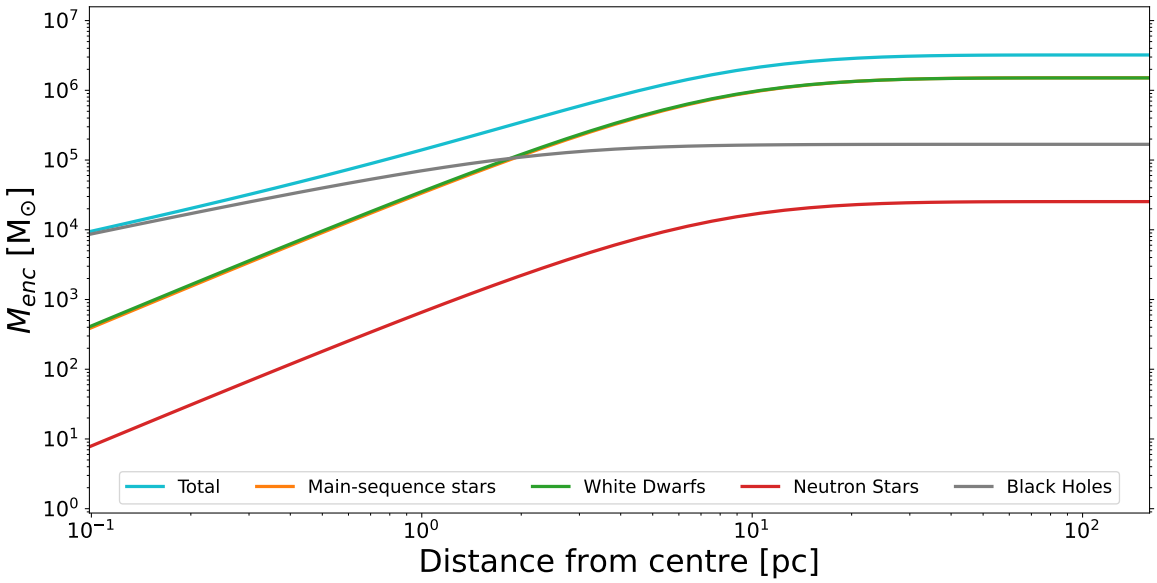

Figure 7.10: Cumulative mass profile of all components (main-sequence stars, white dwarfs, neutron stars and black holes) in ω Cen.

7.4.2 NGC 104

NGC 104, or 47 Tuc, is one of the nearest and most massive Milky Way GCs, and as such has been extensively studied in the past. Recent modelling efforts using both Monte-Carlo cluster models (Weatherford et al., 2020; Ye et al., 2022) and multimass LIMEPY models (in a very similar fashion to this work; Hénault-Brunet et al. 2020; Smith et al. 2022), have provided predictions on the amount of black holes in the cluster. As shown in Figure 7.11, our models tend to favour a lower amount of mass in BHs than other studies, however we are still consistent within 2σ with all except Ye et al. (2022).

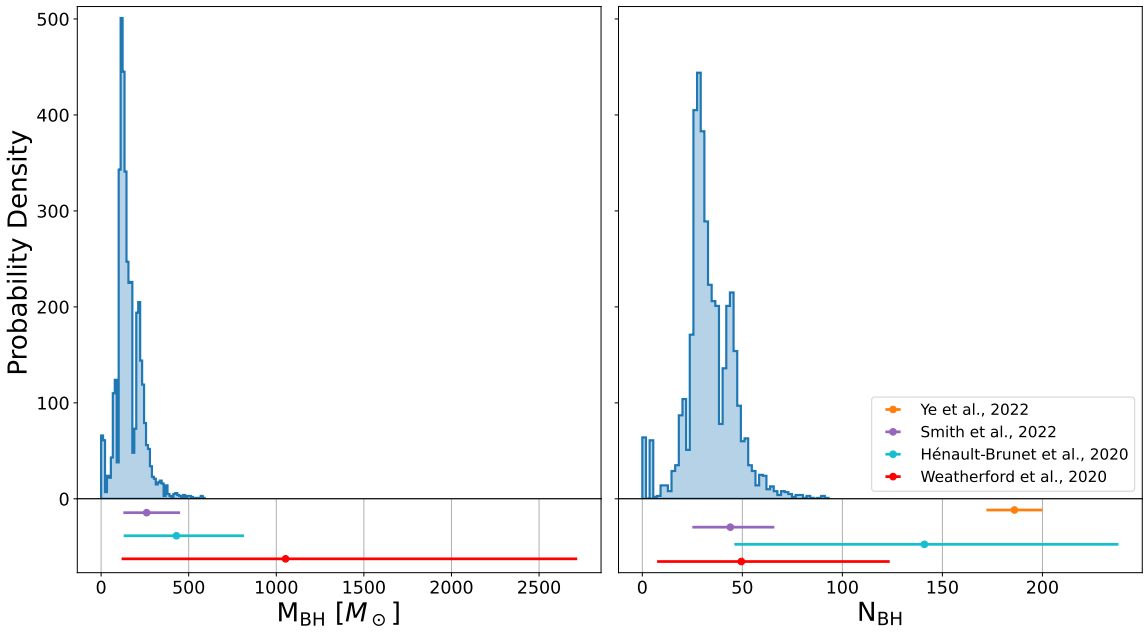

Figure 7.11: Posterior probability distributions of the total mass and number of black holes in 47 Tuc. The results (median and 1σ) of various recently inferred values from the literature are shown in the bottom panels.

It was postulated by Kızıltan et al. (2017) that 47 Tuc may host an IMBH of around 2300 $M_\odot$, based on the analysis of the accelerations of millisecond pulsars in the cluster and comparisons with N-body simulations. However follow-up studies using equilibrium models fit to various cluster observables (Hénault-Brunet et al., 2020;

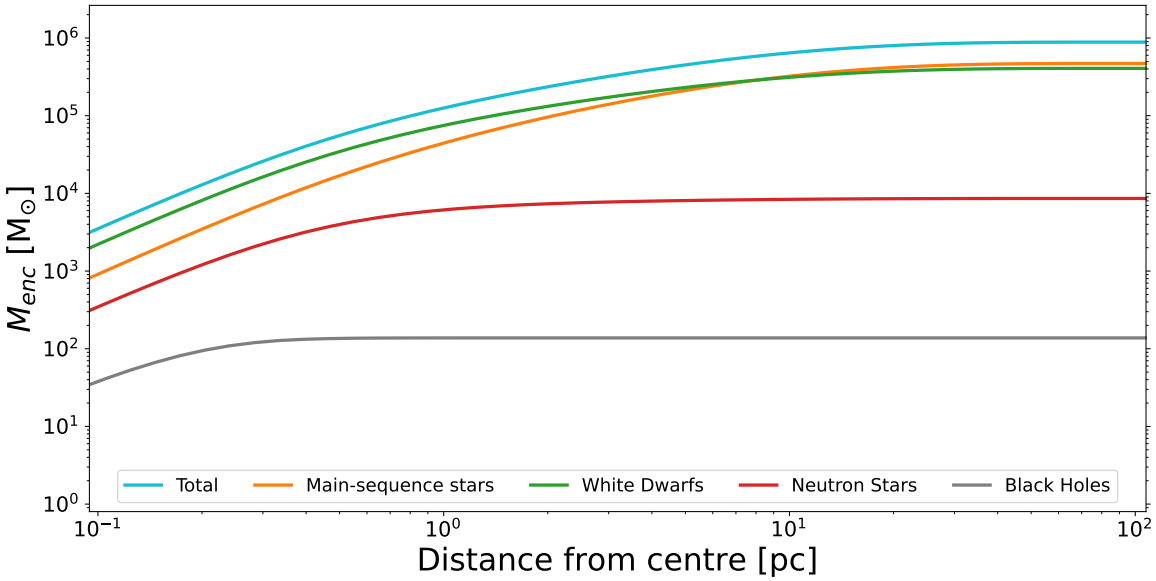

Figure 7.12: Cumulative mass profile of all components (main-sequence stars, white dwarfs, neutron stars and black holes) in 47 Tuc.

Mann et al., 2019, although see Mann et al., 2020) and including pulsar period derivatives (Smith et al., 2022) determined that there was no need for an IMBH to explain the observations, and that a central concentration of less-massive dark remnants may be preferred by the data. This conclusion is again reinforced by our results, which favour a small central concentration of stellar mass black holes, alongside a population of white dwarfs and neutron stars, as can be seen in Figure 7.12.

7.4.3 NGC 6624

The metal-rich, core-collapsed, bulge cluster NGC 6624 has been the source of IMBH claims in the past, posited as a potential explanation for the large spin-period derivatives of some of its millisecond pulsars (Peuten et al., 2014; Perera et al., 2017a,b). However, Gieles et al. (2018) demonstrated through fitting of multimass LIMEPY models (with no black holes) that an IMBH was not necessary to explain the pulsar timing solutions, and a central concentration of dark remnants (white dwarfs and neutron

stars) was more likely, a conclusion supported by the N-body modelling of Baumgardt et al. (2019b). Given its core-collapsed nature and high degree of mass segregation, Weatherford et al. (2020) and Rui et al. (2021a) also find evidence of very few BHs at all in the cluster.

Our best-fitting models of NGC 6624, as shown in Figures 7.13 to 7.15, favour a slightly larger population of stellar-mass BHs ($\sim$ 48 BHs with a total mass of $\sim 475\,M_\odot$), however the caveats discussed in Section 7.1 apply here, and our models containing this significant population of black holes may not be entirely physical. As mentioned, in the future, utilizing a deeper, HST based number density profile (e.g. Gieles et al., 2018) may act to substantially drop the amount of BHs preferred. Either way, however, it is clear that our models do not require a large population of BHs or an IMBH to reproduce the data of NGC 6624. Extending this analysis in the future to self-consistently include the pulsar accelerations in our fits, as done by Smith et al. (2022) for NGC 104, would be very useful in order to examine the constraints on the central density and remnants set by these objects.

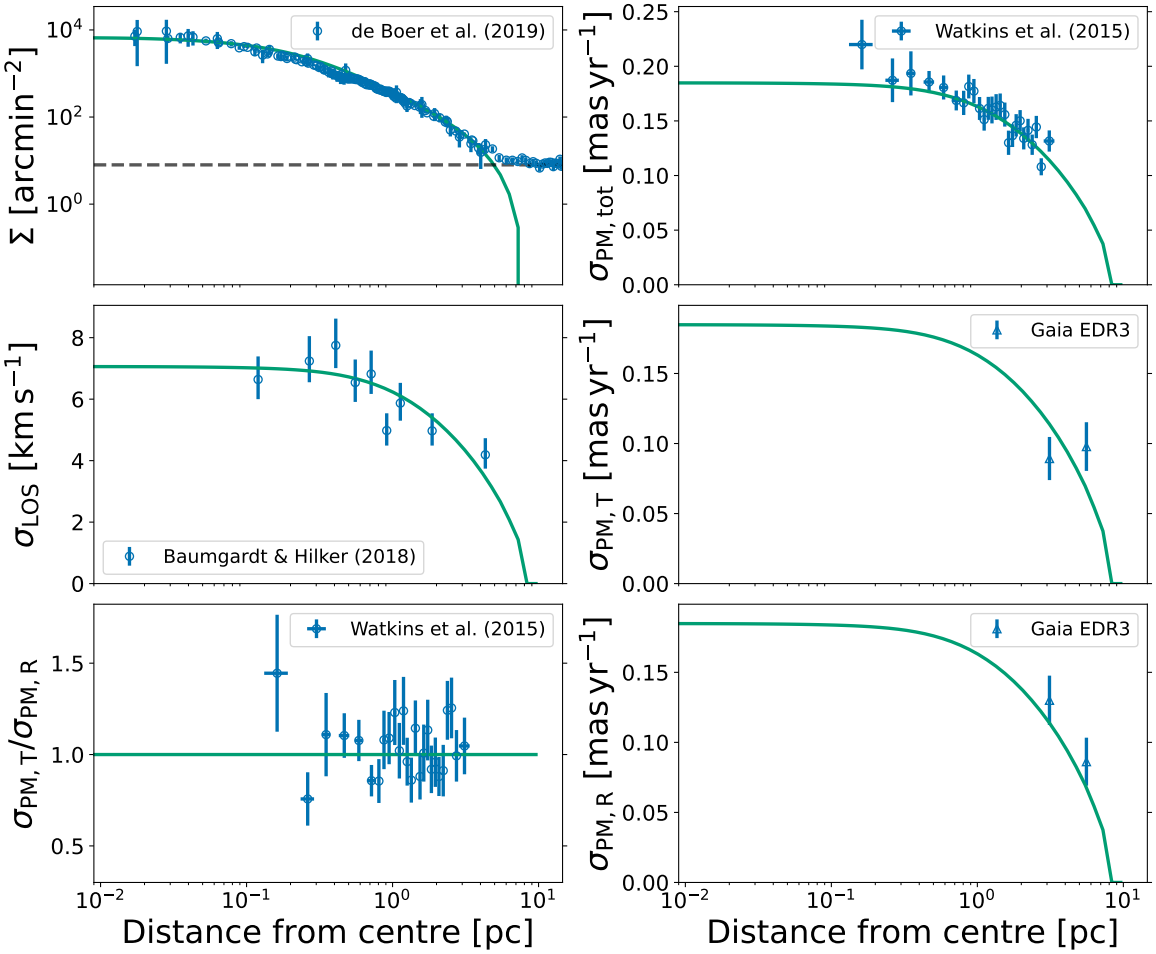

Figure 7.13: Figure 5.2 repeated for NGC 6624

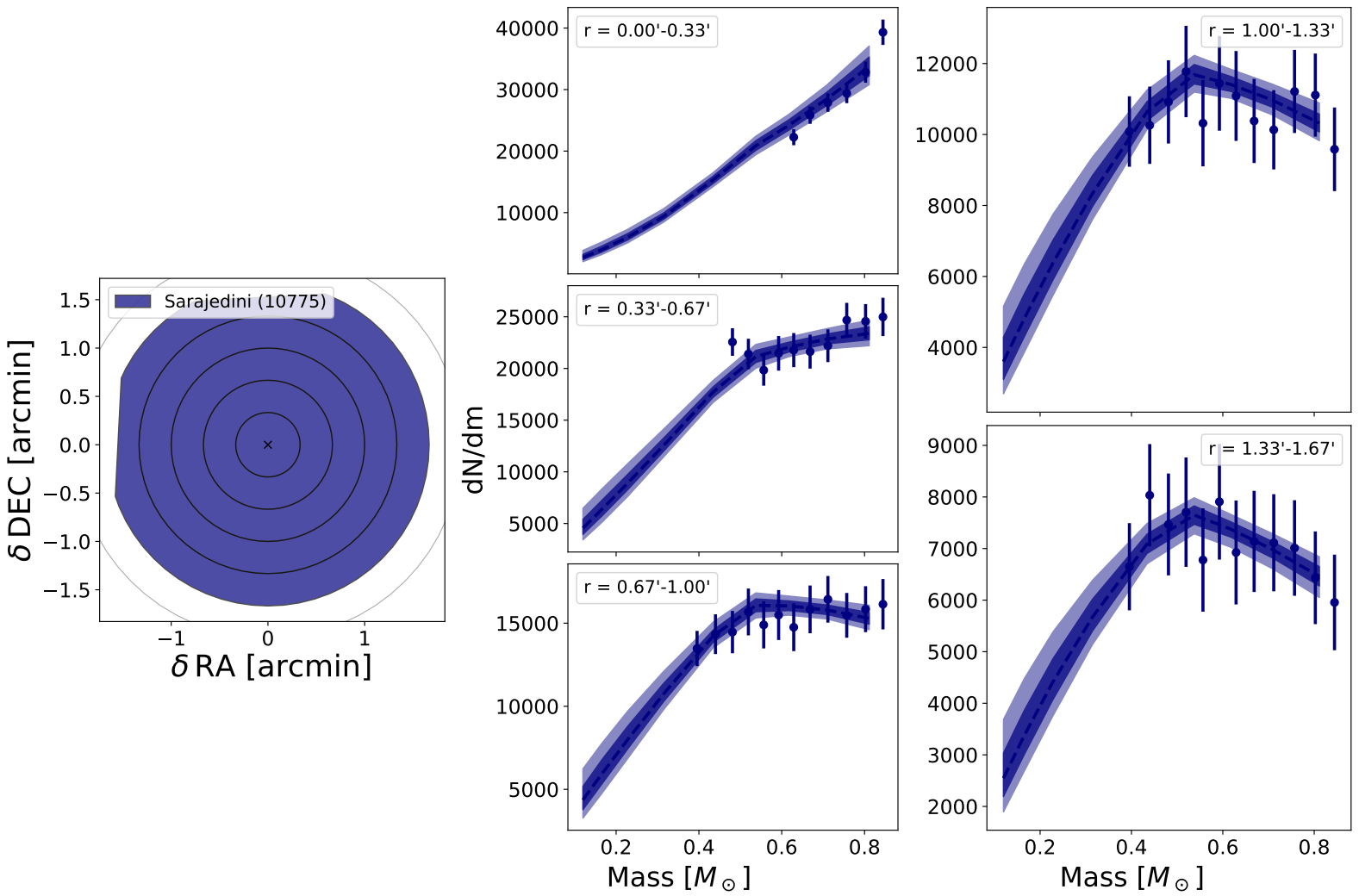

Figure 7.14: Figure 5.3 repeated for NGC 6624

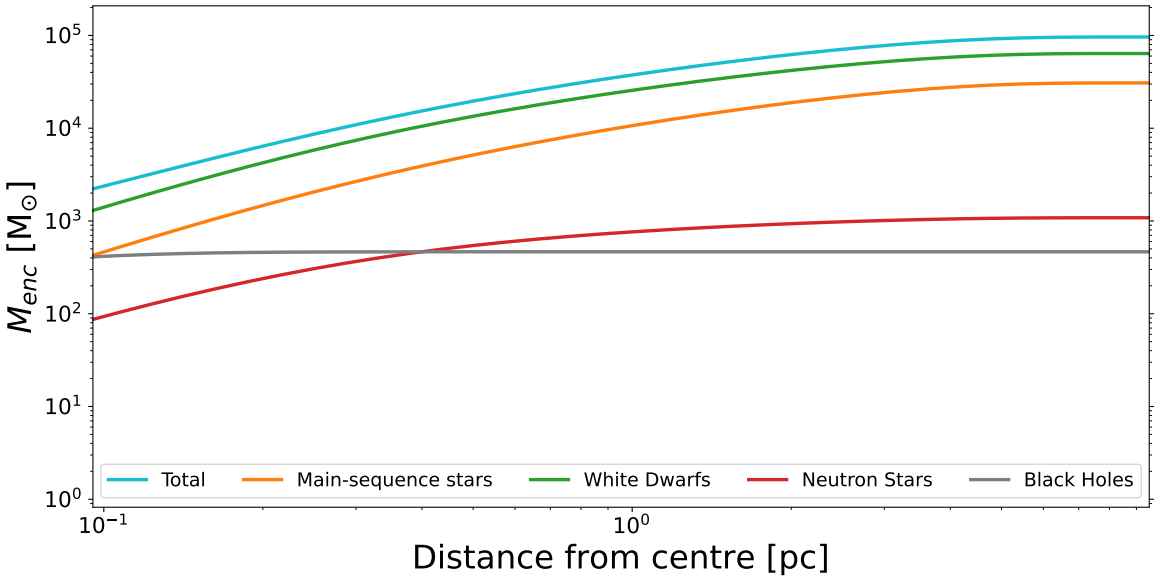

Figure 7.15: Cumulative mass profile of all components (main-sequence stars, white dwarfs, neutron stars and black holes) in the best-ftting models of NGC 6624.

7.4.4 NGC 6266

NGC 6266, or M 62, is a relatively metal-rich, core-collapsed Milky Way GC, which has been the source of a number of searches for IMBHs in the past. McNamara et al. (2012) explored the possibility of an IMBH through N-body modelling of the proper motion and surface brightness profiles of M 62, and found that they could not entirely exclude the presence of an IMBH, while Lützgendorf et al. (2013) expanded on this study, including new limits on the central velocity dispersions of the cluster, and predicted a central IMBH of $\sim 2000\,M_\odot$. This was, however, contested by the N-body models of Baumgardt (2017), which showed that the inclusion of an IMBH would fail to reproduce the inner density profile of the core-collapsed cluster. M 62 also hosts a number of binary millisecond pulsars close to the core, which Abbate et al. (2019) used to demonstrate that $\sim 4000\,M_\odot$ of dark remnants must lie within the inner 0.2 pc of the cluster. They could not, however, discern whether this mass

might be in the form of an IMBH or other lower-mass stellar remnants.

Our best-fitting models, shown in Figures 7.16 to 7.18, favour a distribution of $\sim 1000\,M_\odot$ stellar-mass black holes within 0.2 pc of the core. While this is well below the mass required by Abbate et al. (2019), it is of course much higher than what would be reasonable for a core-collapsed cluster (see again Section 7.1). However, in models of M 62 both with and without BHs, we find a much higher concentration of white dwarfs and neutron stars in the core of the cluster than necessary to match the predictions of Abbate et al. (2019). Again, extending this analysis to self-consistently include the pulsar accelerations in our fits would be very useful for examining and possibly alleviating this discrepancy with Abbate et al. (2019).

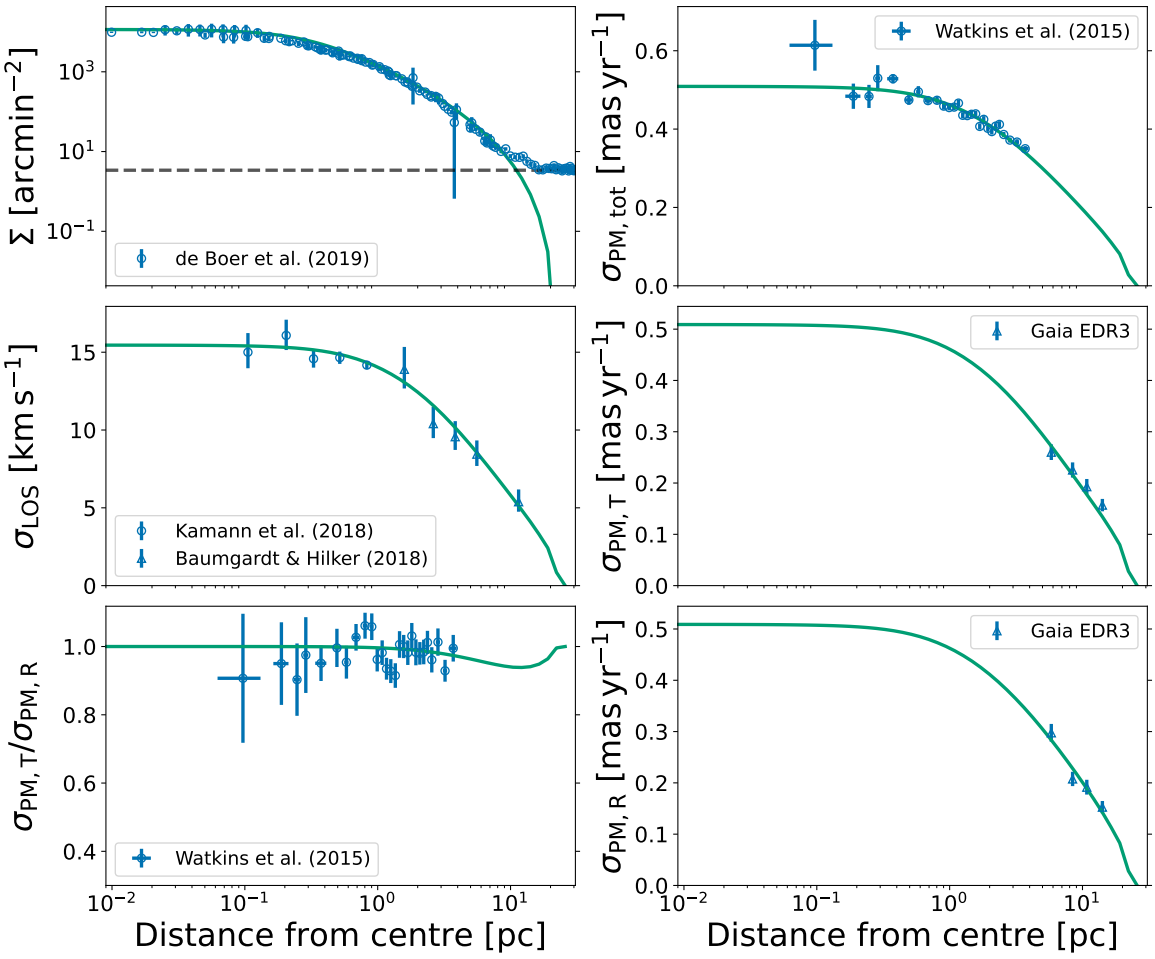

Figure 7.16: Figure 5.2 repeated for NGC 6266

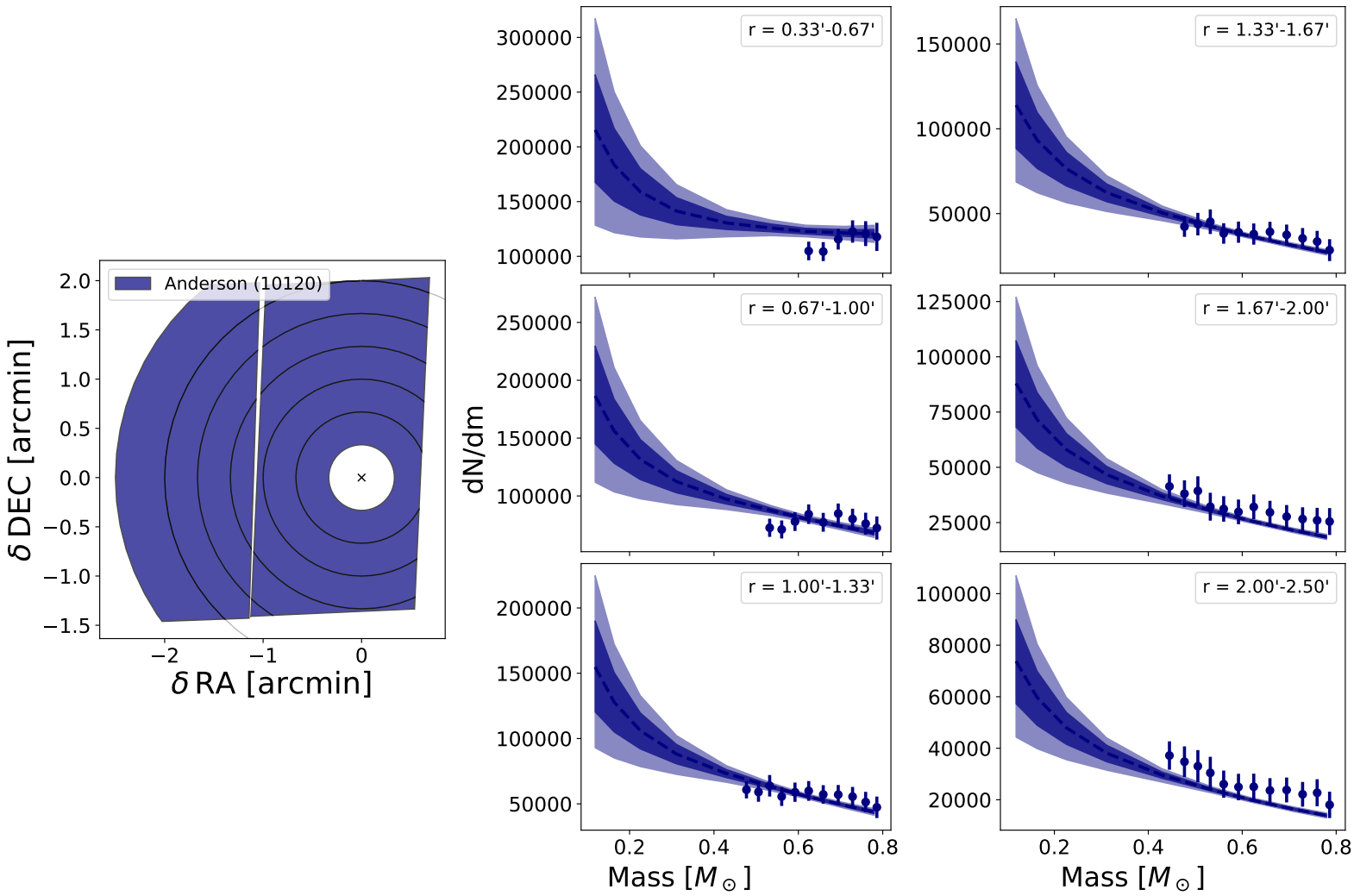

Figure 7.17: Figure 5.3 repeated for NGC 6266

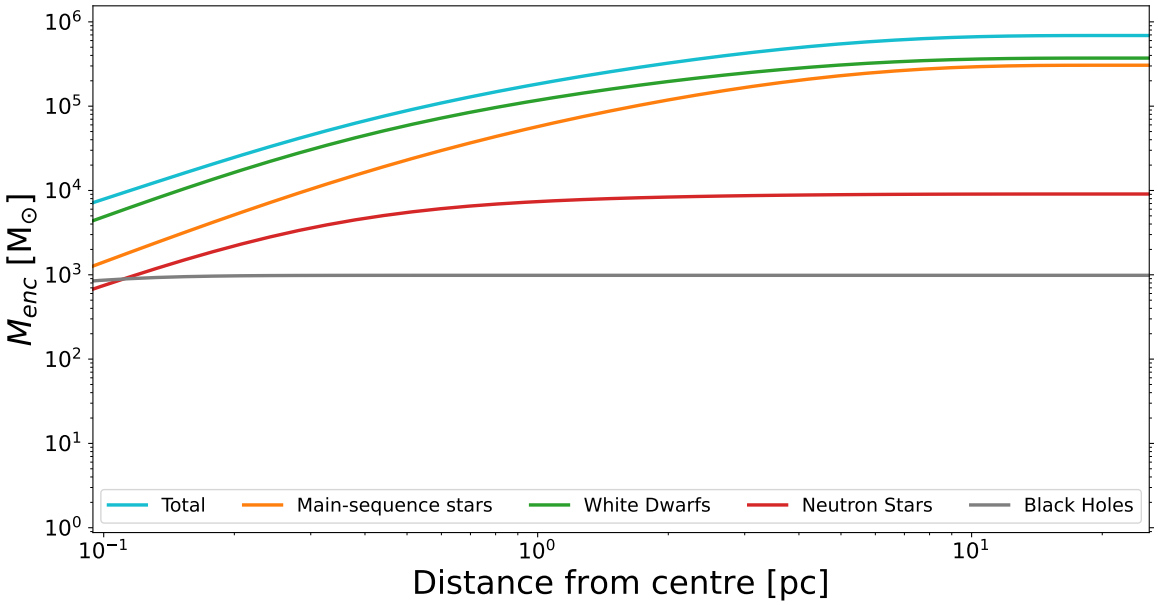

Figure 7.18: Cumulative mass profile of all components (main-sequence stars, white dwarfs, neutron stars and black holes) in the best-ftting models of NGC 6266.

7.4.5 NGC 6397

NGC 6397 is a metal-poor, core-collapsed Milky Way GC at a very short heliocentric distance (~ 2.4 pc; Harris, 1996), which has been well studied in the past. Kamann et al. (2016) first showed that models including an IMBH or very centrally concentrated cluster of stellar-mass BHs of $\sim 600\,M_\odot$ could best reproduce the central kinematics of this cluster. Vitral & Mamon (2021) showed, in turn, that Jeans models with more robust proper motion fitting disfavoured an IMBH, and instead proposed an inner sub-cluster of unresolved dark remnants measuring $\sim 1000-2000 M_\odot$, which they suggested is dominated by stellar-mass BHs. However, Rui et al. (2021b,a) demonstrated, through fits of CMC models, that no black holes were required to explain the kinematics of NGC 6397, in line with its definition as core-collapsed and reinforced by the mass segregation based estimates of Weatherford et al. (2020), and instead the central dark sub-cluster could be made up largely of white dwarfs (Kremer et al.,

2021). A subsequent re-examination of the Jeans modelling of NGC 6397 by Vitral et al. (2022), with updated proper motion datasets, lowered the claimed mass of the central cluster to $\sim 800\,M_\odot$, and concurred with a sub-cluster dominated by white dwarfs, instead of stellar-mass BHs.

Our best-fitting models of NGC 6397, shown in Figures 7.19 to 7.21, despite the caveats of modelling core-collapsed clusters discussed in Section 7.1, favour a negligible population of black holes, consistent with the results of Weatherford et al. (2020); Rui et al. (2021a). Our models also show a clear population of white dwarfs in the core of the cluster, with $\sim 866\,M_\odot$ in WDs within the central 6 arcsec, which would be consistent with the mass proposed by Vitral et al. (2022), but within a slightly larger radius than their proposed 3.4 arcsec. This discrepancy could arise due to the slight difference in the distances used to this very nearby cluster, with our median best-fitting distance parameter value of 2.435 kpc, slightly lower than the value of 2.48 kpc they used. Even accounting for these slight discrepancies, it is clear that our models concur with the general consensus that NGC 6397 hosts a massive central concentration of WDs, and little to no BHs, nor an IMBH.

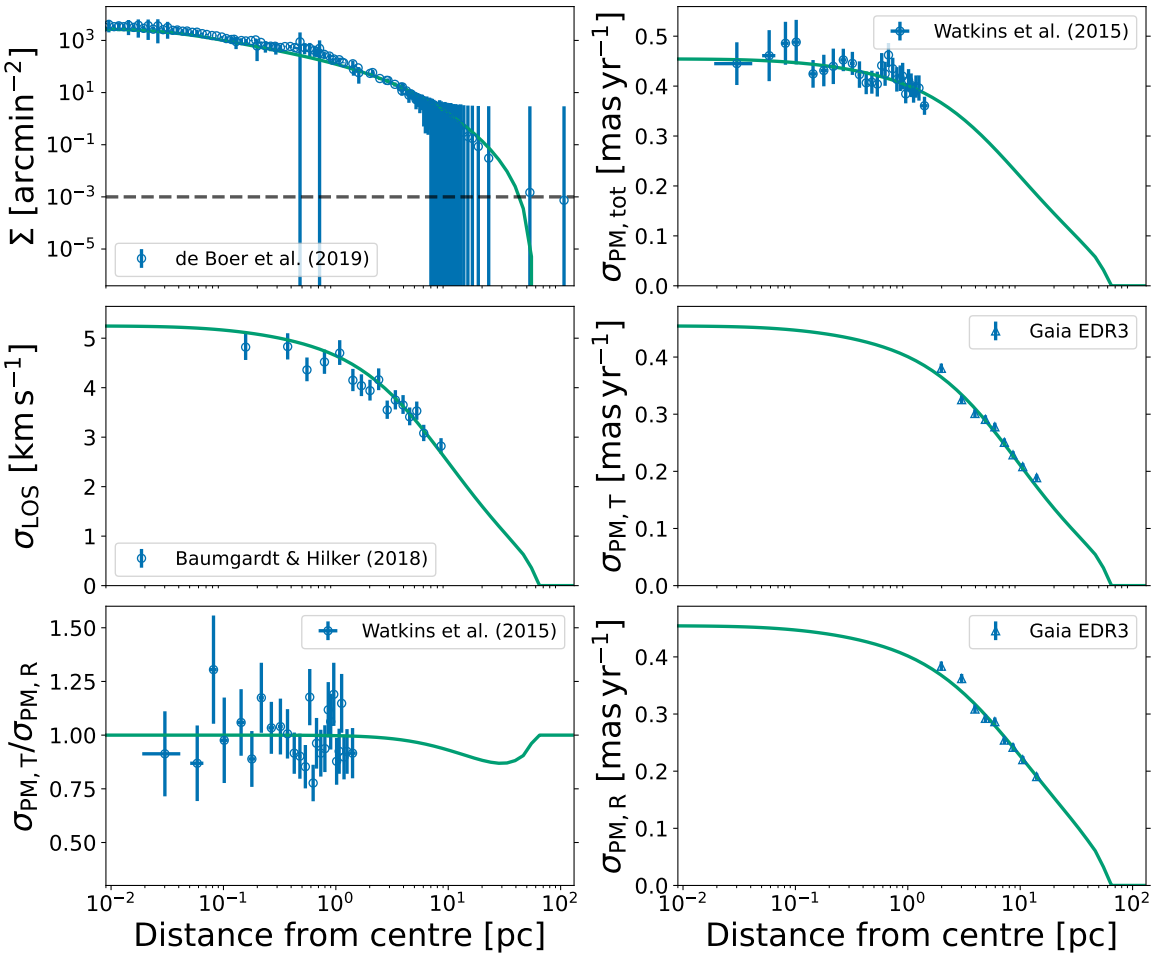

Figure 7.19: Figure 5.2 repeated for NGC 6397

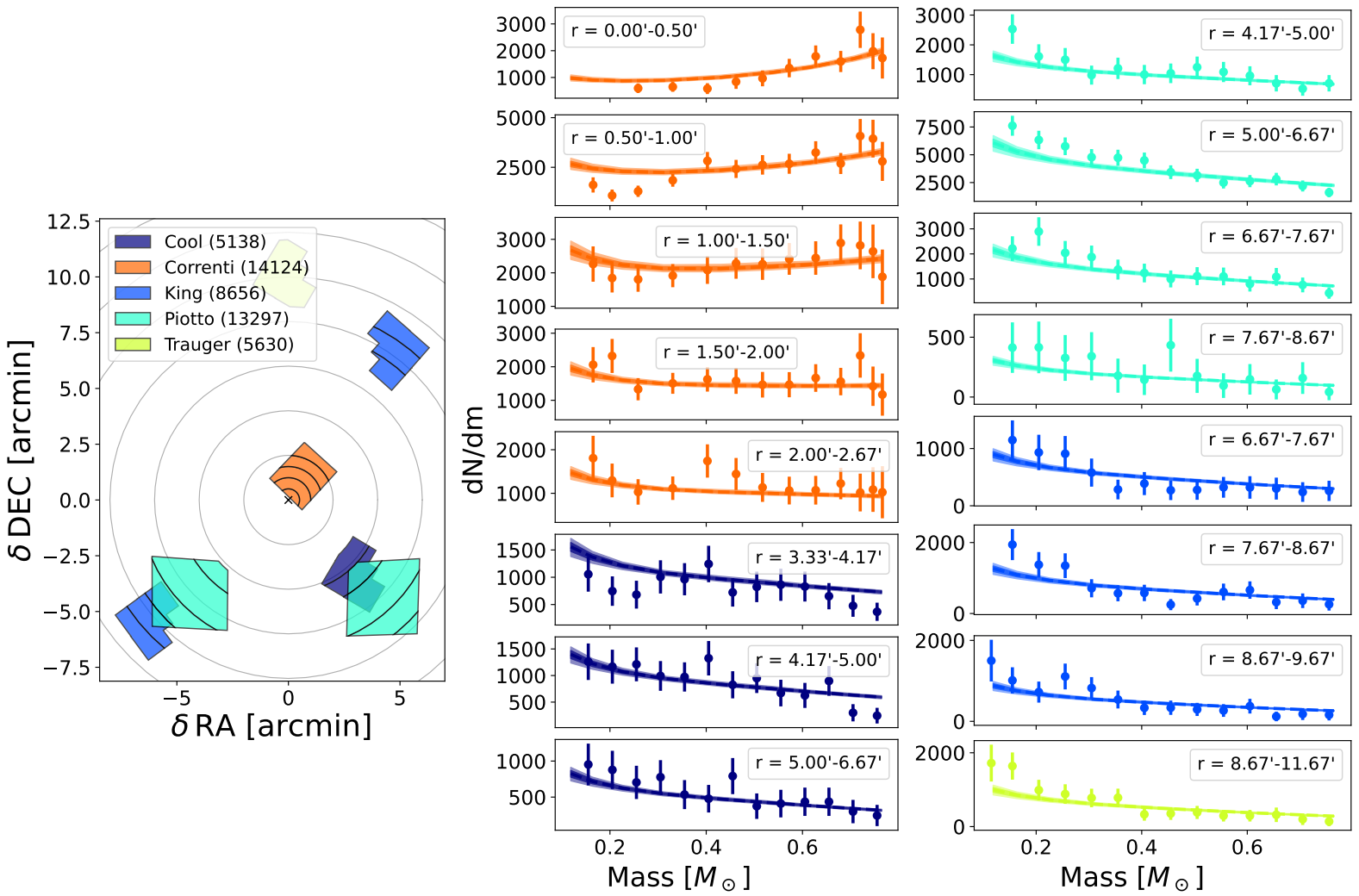

Figure 7.20: Figure 5.3 repeated for NGC 6397

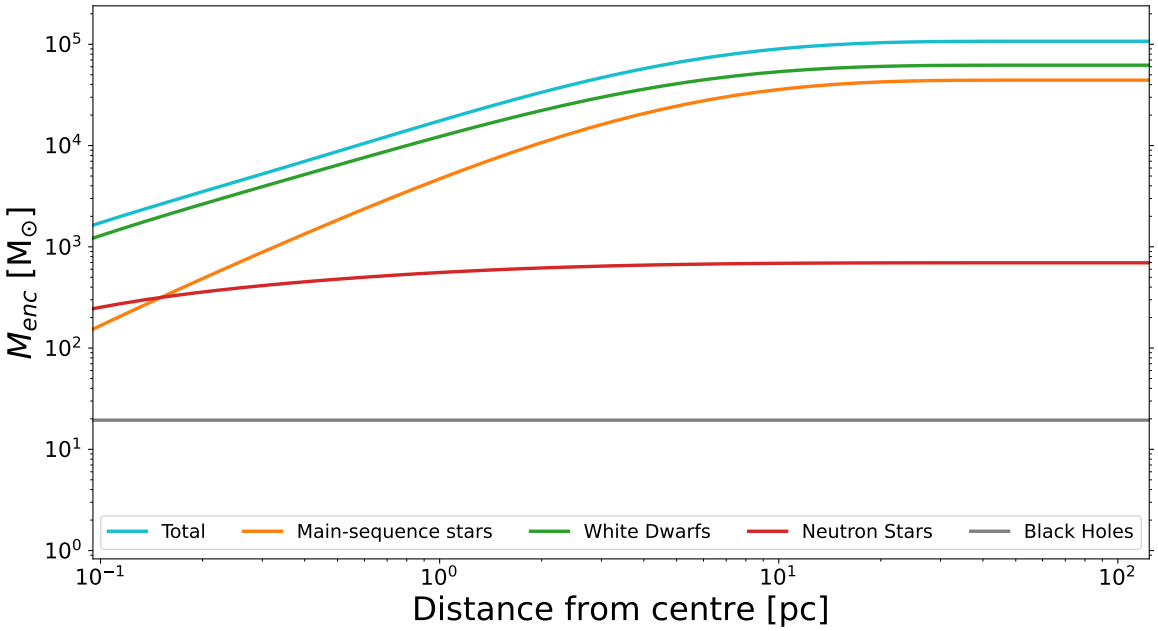

Figure 7.21: Cumulative mass profile of all components (main-sequence stars, white dwarfs, neutron stars and black holes) in NGC 6397.

7.4.6 NGC 3201

NGC 3201 is a nearby Milky Way GC which has a notably low and flat core density profile (i.e. far from core-collapsed), and is the host of three confirmed stellar-mass black hole candidates in detached binaries (Giesers et al., 2018, 2019).

CMC models of NGC 3201 (Kremer et al., 2018, 2019) demonstrated that models with ~ 120 stellar mass black holes were best able to recreate the velocity dispersion and surface brightness profiles, in general agreement with the results of Askar et al. (2018) and the inner dark sub-cluster found by Vitral et al. (2022). Weatherford et al. (2020) in turn favoured a slightly lower, but still consistent, ~ 44 BHs. In contrast, our best-fitting models of NGC 3201, shown in Figures 7.22 to 7.24, favour a remarkably small amount of BHs, with the distribution peaking at 0 BH (95% probability of containing less than 7 BHs). This is somewhat surprising, given the literature results

and the shape of the cluster density profile, but is technically in agreement, within 2σ with the results of Weatherford et al. (2020), and follows the trend in our results of predicting fewer BHs than other studies in the literature. It should be noted that the fit of our models to the number density profile is not perfectly satisfying, as it overestimates the outer parts of the cluster, and underestimates the core profile. This is likely due to the irregular shape of the inner surface brightness profile published by Trager et al. (1995), and could have an impact on the amount of BHs recovered in our models.

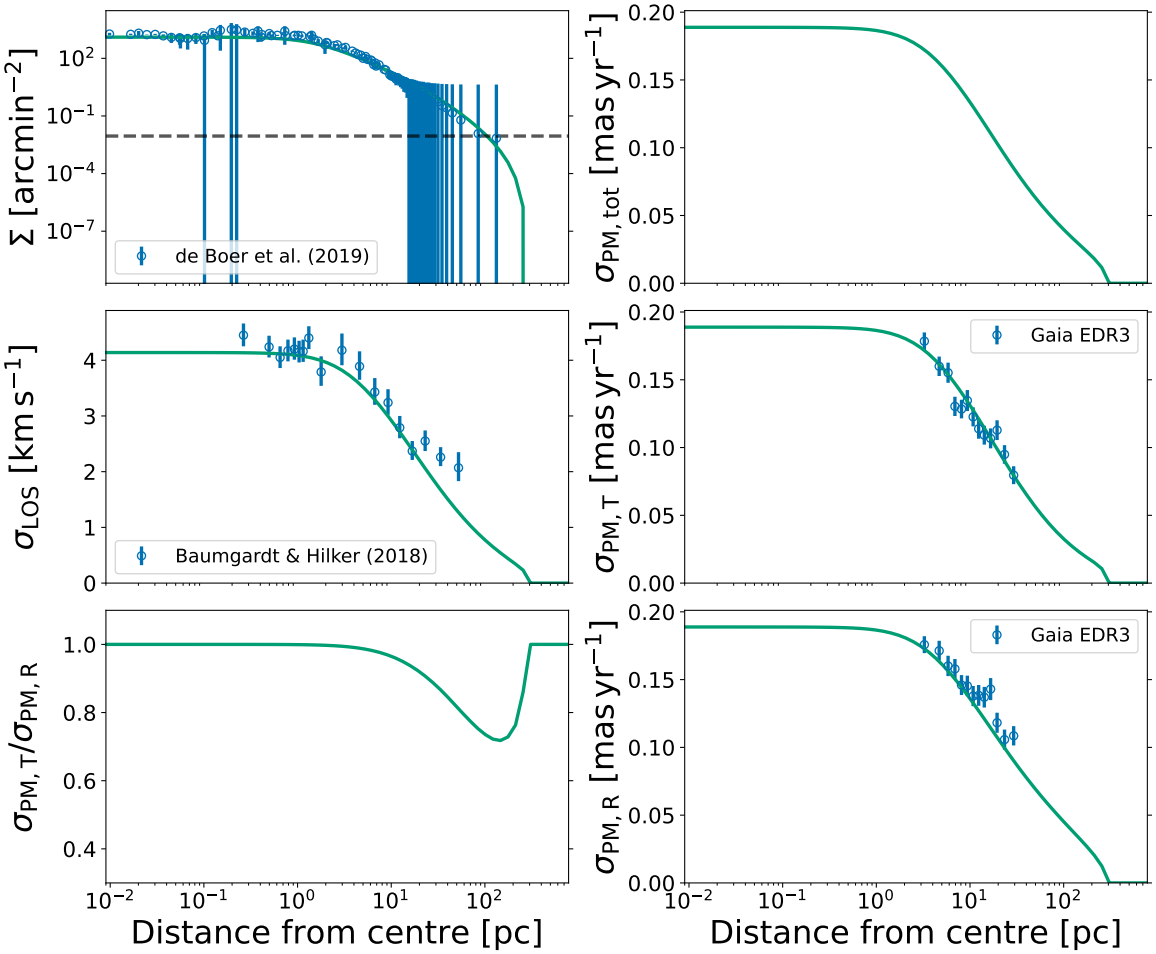

Figure 7.22: Figure 5.2 repeated for NGC 3201

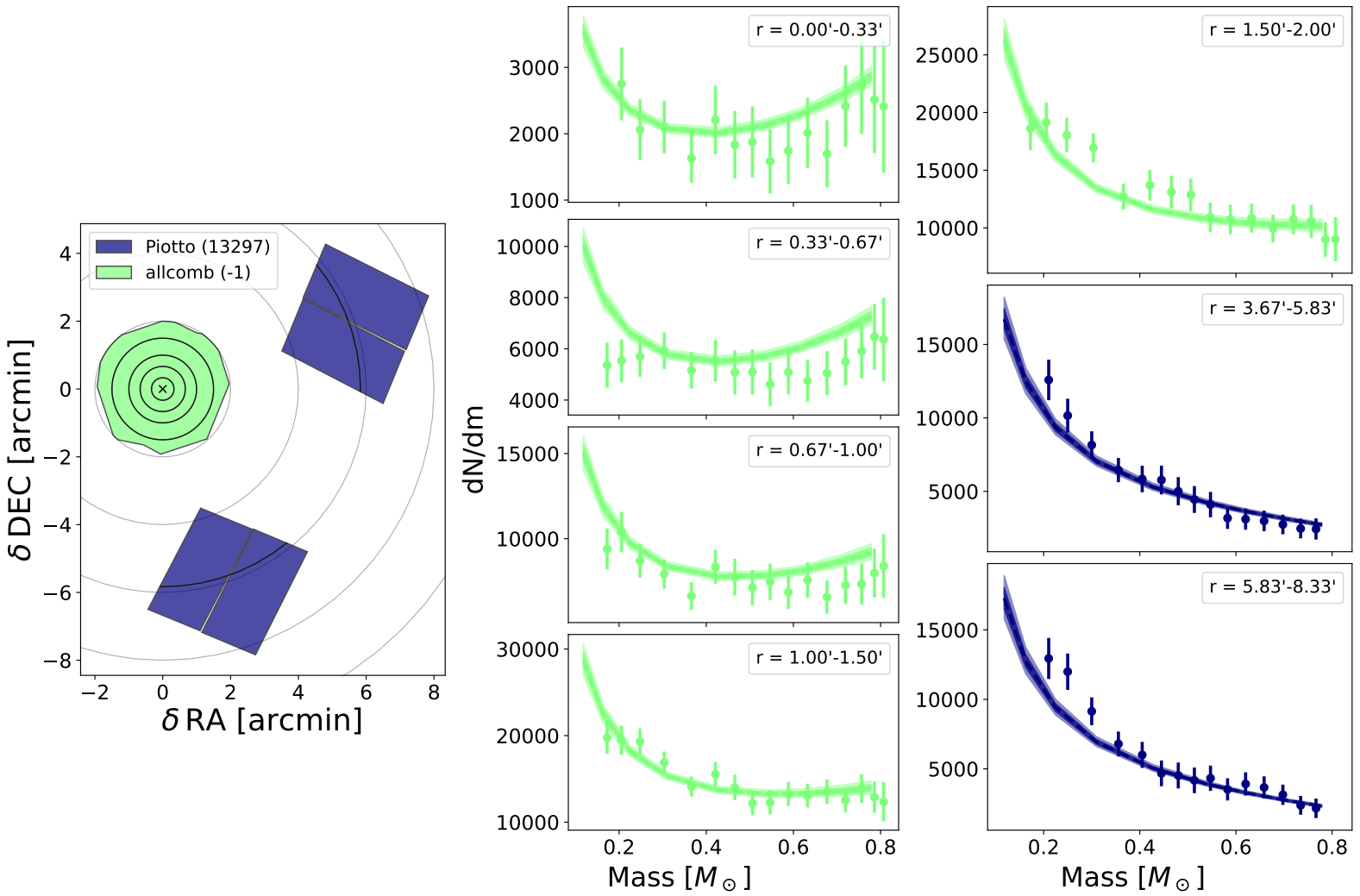

Figure 7.23: Figure 5.3 repeated for NGC 3201

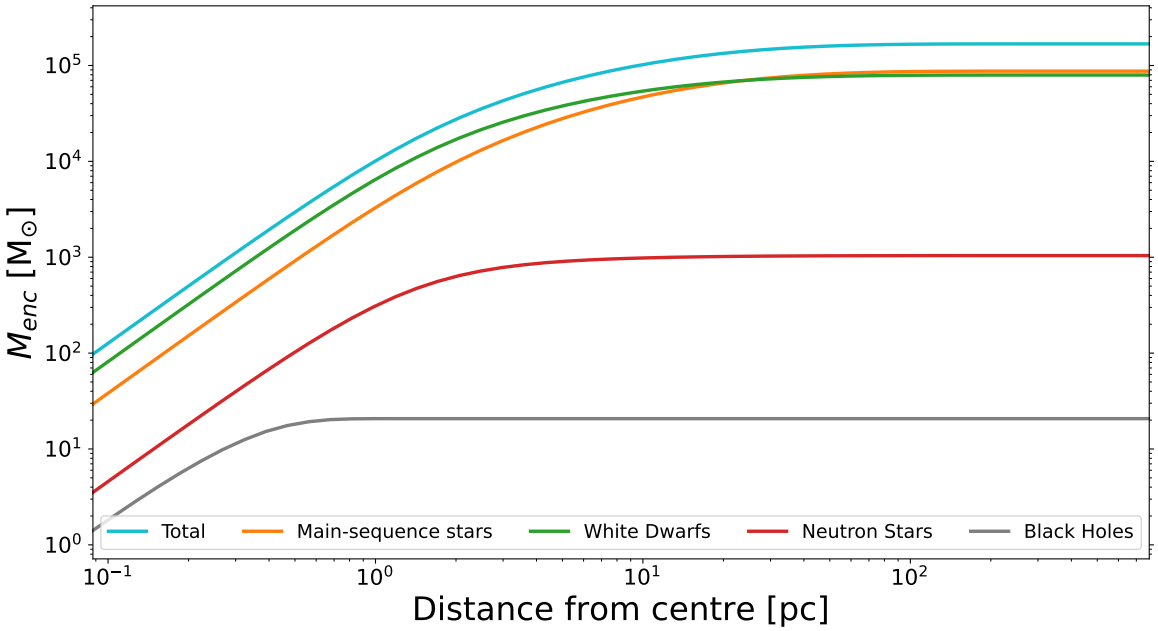

Figure 7.24: Cumulative mass profile of all components (main-sequence stars, white dwarfs, neutron stars and black holes) in NGC 3201.

Chapter 8

Conclusions

In this thesis we have inferred, through dynamic nested sampling, the best-fitting model parameter distributions of multimass LIMEPY models for a large sample of Milky Way globular clusters, subject to a number of observed proper motion, line-of-sight velocity, number density and stellar mass function datasets. This process has resulted in well-fit models for 32 Milky Way GCs, with full, well constrained, posterior distributions for the structural, mass functions, and helicocentric distance parameters of each cluster. These results show excellent matches with the properties of the N-body models computed by Baumgardt & Hilker (2018), and demonstrated many of the same correlations between structural parameters as seen by de Boer et al. (2019).

These models allow us to explore in detail the stellar (initial) mass functions and remnant populations of a large sample of Milky Way GCs, and yield a number of important conclusions:

1. Deviations of the low and intermediate-mass stellar mass function slopes from the $\alpha_1 = \alpha_2$ line demonstrate that a two-component power law is necessary in

order to describe the (initial) mass function in this mass regime.

2. We show that, while the low and intermediate-mass MF slopes are strongly dependent on the dynamical age of the clusters, the high-mass α_3 slope is not, indicating that the MF in this regime has generally been less affected by dynamical losses, and is most representative of the IMF.

3. Examination of the low and intermediate mass MF slopes, in the least evolved clusters, suggests an IMF in these regimes which is considerably flatter and more depleted in low mass stars ($\alpha_1 = 0.46^{+0.45}_{-0.48}$, $\alpha_2 = 0.79^{+0.54}_{-0.49}$), in comparison to canonical IMFs (Kroupa, 2001). This finding is in agreement with the results of Baumgardt et al. (2022). In contrast, the high-mass IMF slope ($\alpha_3 = 2.37^{+0.48}_{-0.25}$) is found to be in excellent agreement with the canonical values (Salpeter, 1955; Kroupa, 2001). This result precludes the need for any more extreme high-mass IMF formulation for globular clusters, such as a top-heavy IMF.

4. A potential linear relationship is noted between the high-mass stellar IMF and cluster metallicity, with a general trend towards flatter high-mass IMFs at higher metallicities. However, this analysis is somewhat limited by the small amount of very metal-rich or metal-poor GCs, with smaller dynamical ages, in our sample. A similar (but inverted) relationship also appears in the low and intermediate-mass MFs, however this largely disappears when focusing only on the least dynamically evolved clusters, and likely is simply a manifestation of the correlation between metallicity and cluster orbits.

5. The models also allow us to infer best-fitting, posterior probability distributions for the total mass and number of black holes in all our clusters. These results indicate that a large number of the GCs are consistent with hosting little to

no BHs, with the largest BH populations reaching masses in BHs up to a few thousand $M_\odot$ (save for ω Cen). We find good agreement within uncertainties between our results and those of other BH studies (where the number of BHs is inferred from comparison with dynamical Monte Carlo models) in the literature (e.g. Askar et al., 2018; Weatherford et al., 2020). Our inferred masses in BHs are, generally, slightly smaller than these studies. This difference could be caused by biases introduced due to the differences between the adopted IMFs, however further work is required to better understand the possible sources of the discrepancies.

6. We find a general relationship between the mass in BHs and the δ parameter, a proxy of mass segregation, with clusters with little mass in BHs congregating around ~ 0.5, while mass segregation is increasingly suppressed in clusters with more substantial BH populations, in agreement with the findings of Peuten et al. (2017). A relationship is also found between the dynamical age of the clusters and the total mass in BHs. Clusters with a substantial population of black holes tend to be less dynamically evolved, as would be expected based on our understanding of the dynamical interactions and kicks of BHs over time. An even clearer correlation is seen with the overall remnant mass fraction, which increases as clusters evolve and lose low-mass stars. Our results show that the most evolved GCs in our sample may be made up of nearly 75% dark remnants, by mass, at the present day.

7. Closer inspection of a number of interesting clusters with previous claims of hosting an IMBH reveal no need for a large population of BHs or an IMBH to explain the large amount of data used in our model fitting.

In summary, we have determined best-fitting model parameter distributions for a

large sample of Milky Way GCs, which have indicated a potentially more bottom-light low-mass IMF than typically assumed, and have precluded the need for any top-heavy high-mass IMFs. A potential relationship between said high-mass IMF and cluster metallicity was also noted, however further investigation is required to confirm this correlation. Our models have also allowed us to infer constraints on the remnant populations of our clusters, where we find generally small numbers of BHs, and no need for any IMBH in order to explain the observables used.

8.1 Future Work

The results and conclusions presented in this thesis could, in the future, be enhanced with the inclusion of additional ingredients and datasets, and the exploration of a number of the implications of our results.

Firstly, extension of the methods presented here to a larger sample of Milky Way GCs would greatly increase the confidence on the stellar mass function results. In particular, the inclusion of more dynamically young GCs in the very metal-rich or metal-poor regimes would help to further study the potential relationship seen between the high-mass (initial) mass function and metallicity. This expansion to more clusters is unfortunately limited mostly by the amount of data available. An increased amount of and depth in the stellar mass function datasets used here, perhaps with novel, dedicated HST observations or programs on future space-based observatories like the Nancy Grace Roman Space Telescope or the Cosmological Advanced Survey Telescope for Optical and ultraviolet Research (CASTOR), would improve the constraints that can be placed on the distribution of the stellar populations, while further improved proper motion and line-of-sight velocity dispersions, especially near the cluster cores, would help provide better constraints on the cluster mass and its

distribution. For example, an adaptive optics-assisted survey of the inner regions of GCs in the Milky Way bulge is being planned with the upcoming Gemini Infrared Multi-Object Spectrograph (GIRMOS) which would significantly improve the amount and quality of available kinematic data for many metal-rich clusters in this region of the Galaxy.

Our models could also be improved further with the inclusion of realistic populations of binary stars, which may be slightly degenerate with the mass in BHs, and have important implications in clusters with large suspected binary fractions (Smith, 2022). Further, the constraints on the black hole populations could be improved by the inclusion of pulsar timing solutions, in selected clusters where significant observed pulsar populations exist (Smith et al., 2022).

The implications of some of the results presented in this thesis could be explored more. For example, dynamical N-body or Monte-Carlo models of GCs with a bottom-light IMF, depleted in low-mass stars, as we infer here, would help illuminate the evolution of such clusters, and any consequences on cluster properties and phenomena, such as BH populations and BBH merger rates.

Finally, the methodology applied here to fit the static LIMEPY models to the present-day properties of globular clusters could be coupled to evolutionary dynamical models, such as the fast-cluster-evolution models presented by Antonini & Gieles (2020), allowing for a more detailed study of the evolution of the BH populations of Milky Way GCs, and in turn providing constraints on, for example, the BBH merger rate from dynamical formation in dense star clusters in the Universe.

Bibliography

Aarseth S. J., 1999, PASP, 111, 1333 20

Aarseth S. J., 2003, Gravitational N-body simulations: tools and algorithms. Cambridge Monographs on Mathematical Physics, Cambridge University Press 20, 32

Abbate F., Possenti A., Colpi M., Spera M., 2019, ApJ, 884, L9 113, 114

Abbott B. P., et al., 2016, Phys. Rev. Lett., 116, 061102 11

Alessandrini E., Lanzoni B., Ferraro F. R., Miocchi P., Vesperini E., 2016, ApJ, 833, 252 4

Antonini F., Gieles M., 2020, MNRAS, 492, 2936 129

Antonini F., Gieles M., Gualandris A., 2019, MNRAS, 486, 5008

Arca Sedda M., Askar A., Giersz M., 2018, MNRAS, 479, 4652 99

Askar A., Arca Sedda M., Giersz M., 2018, MNRAS, 478, 1844 ix, 99, 100, 101, 121, 127

Balbinot E., Gieles M., 2018, MNRAS, 474, 2479 23, 31

Banerjee S., Belczynski K., Fryer C. L., Berczik P., Hurley J. R., Spurzem R., Wang L., 2020, A&A, 639, A41 34

Bastian N., Lardo C., 2018, ARA&A, 56, 83 2

Bastian N., Covey K. R., Meyer M. R., 2010, ARA&A, 48, 339 6

Baumgardt H., 2017, MNRAS, 464, 2174 22, 39, 44, 105, 113

Baumgardt H., Hilker M., 2018, MNRAS, 478, 1520 2, 37, 44, 125

Baumgardt H., Vasiliev E., 2021, MNRAS, 505, 5957 54

Baumgardt H., Hilker M., Sollima A., Bellini A., 2019a, MNRAS, 482, 5138 44, 67, 76

Baumgardt H., et al., 2019b, MNRAS, 488, 5340 105, 110

Baumgardt H., Sollima A., Hilker M., 2020, PASA, 37, e046 8

Baumgardt H., Sollima A., Hénault-Brunet V., Dickson N., 2022, in prep. viii, 46, 67, 76, 78, 79, 84, 85, 126

Bellini A., et al., 2014, ApJ, 797, 115 42, 43

Bertin G., 2014, Dynamics of Galaxies, 2nd edn. Cambridge University Press

Binney J., Merrifield M., 1998, Galactic Astronomy. Princeton University Press 2, 3

Binney J., Tremaine S., 2008, Galactic Dynamics, 2nd edn. Princeton University Press 4

Breen P. G., Heggie D. C., 2013a, MNRAS, 432, 2779 34, 90

Breen P. G., Heggie D. C., 2013b, MNRAS, 436, 584 34, 90

Cadelano M., Dalessandro E., Webb J. J., Vesperini E., Lattanzio D., Beccari G., Gomez M., Monaco L., 2020, MNRAS, 499, 2390 79

Cappellari M., 2008, MNRAS, 390, 71 18

Chabrier G., 2003, PASP, 115, 763 6, 7

Chandrasekhar S., 1960, Principles of stellar dynamics. Dover 13

Chandrasekhar S., 1967, An introduction to the study of stellar structure. Dover Books on Astronomy, Dover 13

Chatterjee S., Umbreit S., Fregeau J. M., Rasio F. A., 2013, MNRAS, 429, 2881 90

Choi J., Dotter A., Conroy C., Cantiello M., Paxton B., Johnson B. D., 2016, ApJ, 823, 102 32

Chon S., Omukai K., Schneider R., 2021, MNRAS, 508, 4175 82

Chopin N., Ridgway J., 2017, Statistical Science, 32, 64 54

Cournoyer-Cloutier C., et al., 2021, MNRAS, 501, 4464 3

Da Costa G. S., Freeman K. C., 1976, ApJ, 206, 128 17

Dalgleish H., et al., 2020, MNRAS, 492, 3859 44

De Marchi G., Paresce F., Pulone L., 2007, ApJ, 656, L65 8

De Marchi G., Panagia N., Beccari G., 2017, ApJ, 846, 110 82

Djorgovski S., King I. R., 1986, ApJ, 305, L61 90

Dolphin A. E., 2000, PASP, 112, 1383 46

Dolphin A., 2016, DOLPHOT: Stellar photometry, Astrophysics Source Code Library, record ascl:1608.013 46

Dotter A., 2016, ApJS, 222, 8 32

Dotter A., Chaboyer B., Jevremović D., Baron E., Ferguson J. W., Sarajedini A., Anderson J., 2007, AJ, 134, 376 31

Dotter A., Chaboyer B., Jevremović D., Kostov V., Baron E., Ferguson J. W., 2008, ApJS, 178, 89 31

Ebrahimi H., Sollima A., Haghi H., Baumgardt H., Hilker M., 2020, MNRAS, 494, 4226 8

Elmegreen B. G., Scalo J., 2006, ApJ, 636, 149 4

Foreman-Mackey D., Hogg D. W., Lang D., Goodman J., 2013, PASP, 125, 306 54

Fregeau J. M., Joshi K. J., Portegies Zwart S. F., Rasio F. A., 2002, ApJ, 570, 171 4

Gaia Collaboration et al., 2018, A&A, 616, A12 39, 40

Gaia Collaboration et al., 2021, A&A, 649, A1 39

Gieles M., Zocchi A., 2015, mnras, 454, 576 13, 16, 26, 28, 70, 91

Gieles M., Heggie D. C., Zhao H., 2011, MNRAS, 413, 2509 90

Gieles M., Balbinot E., Yaaqib R. I. S. M., Hénault-Brunet V., Zocchi A., Peuten M., Jonker P. G., 2018, MNRAS, 473, 4832 92, 109, 110

Giersz M., Heggie D. C., 2009, MNRAS, 395, 1173 60

Giersz M., Heggie D. C., Hurley J. R., Hypki A., 2013, MNRAS, 431, 2184 22

Giesers B., et al., 2018, MNRAS, 475, L15 10, 121

Giesers B., et al., 2019, A&A, 632, A3 10, 121

Gill M., Trenti M., Miller M. C., van der Marel R., Hamilton D., Stiavelli M., 2008, ApJ, 686, 303 4, 11, 89

Gomez-Leyton Y. J., Velazquez L., 2014, Journal of Statistical Mechanics: Theory and Experiment, 2014, 04006 15, 16

Gomez-Leyton Y. J., Velazquez L., 2019, MNRAS, 488, 362

Haghi H., Khalaj P., Zonoozi A. H., Kroupa P., 2017, The Astrophysical Journal, 839, 60 8

Haghi H., Safaei G., Zonoozi A. H., Kroupa P., 2020, apj, 904, 43 9, 53, 81

Harris W. E., 1996, AJ, 112, 1487 1, 37, 102, 117

Heggie D., Hut P., 2003, The Gravitational Million-Body Problem: A Multidisciplinary Approach to Star Cluster Dynamics. Cambridge Univiversity Press 3, 12, 19

Heggie D. C., Hut P., Mineshige S., Makino J., Baumgardt H., 2007, PASJ, 59, L11 11, 89

Hénault-Brunet V., Gieles M., Sollima A., Watkins L. L., Zocchi A., Claydon I., Pancino E., Baumgardt H., 2019, mnras, 483, 1400 12, 18, 19, 22, 23

Hénault-Brunet V., Gieles M., Strader J., Peuten M., Balbinot E., Douglas K. E. K., 2020, MNRAS, 491, 113 22, 23, 33, 50, 79, 108

Hénon M., 1961, Annales d'Astrophysique, 24, 369 90

Hénon M., 1971a, Ap&SS, 13, 284 20

Hénon M. H., 1971b, Ap&SS, 14, 151 21

Higson E., Handley W., Hobson M., Lasenby A., 2019, Statistics and Computing, 29, 891 56

Hobbs G., Lorimer D. R., Lyne A. G., Kramer M., 2005, MNRAS, 360, 974 33

Hurley J. R., Pols O. R., Tout C. A., 2000, MNRAS, 315, 543 32

Hypki A., Giersz M., 2013, MNRAS, 429, 1221 21, 23

Irrgang A., Wilcox B., Tucker E., Schiefelbein L., 2013, A&A, 549, A137 76

Ivanova N., Belczynski K., Fregeau J. M., Rasio F. A., 2005, MNRAS, 358, 572 3

Kamann S., et al., 2016, A&A, 588, A149 117

Kamann S., et al., 2018, MNRAS, 473, 5591 45

King I. R., 1966, AJ, 71, 64 14

Kish L., 1965, Survey Sampling. A Wiley Interscience Publication, Wiley 57

Kızıltan B., Baumgardt H., Loeb A., 2017, Nature, 542, 203 11, 108

Krause M. G. H., et al., 2020, Space Sci. Rev., 216, 64 2

Kremer K., Ye C. S., Chatterjee S., Rodriguez C. L., Rasio F. A., 2018, ApJ, 855, L15 121

Kremer K., Chatterjee S., Ye C. S., Rodriguez C. L., Rasio F. A., 2019, ApJ, 871, 38 94, 121

Kremer K., et al., 2020a, ApJS, 247, 48 21, 23

Kremer K., Ye C. S., Chatterjee S., Rodriguez C. L., Rasio F. A., 2020b, in Bragaglia A., Davies M., Sills A., Vesperini E., eds, Vol. 351, Star Clusters: From the Milky Way to the Early Universe. pp 357–366, doi:10.1017/S1743921319007269 11, 90

Kremer K., Rui N. Z., Weatherford N. C., Chatterjee S., Fragione G., Rasio F. A., Rodriguez C. L., Ye C. S., 2021, ApJ, 917, 28 117

Kroupa P., 2001, MNRAS, 322, 231 6, 7, 30, 79, 80, 81, 83, 126

Larson R. B., 1998, MNRAS, 301, 569 6, 82

Libralato M., Bellini A., Piotto G., Nardiello D., van der Marel R. P., Anderson J., Bedin L. R., Vesperini E., 2019, ApJ, 873, 109 43

Lützgendorf N., et al., 2013, A&A, 552, A49 11, 89, 113

Mackey A. D., Wilkinson M. I., Davies M. B., Gilmore G. F., 2008, MNRAS, 386, 65 4

Mann C. R., et al., 2019, ApJ, 875, 1 109

Mann C. R., et al., 2020, ApJ, 893, 86 109

Marks M., Kroupa P., Dabringhausen J., Pawlowski M. S., 2012, Monthly Notices of the Royal Astronomical Society, 422, 2246 7, 82, 84

McNamara B. J., Harrison T. E., Baumgardt H., Khalaj P., 2012, ApJ, 745, 175 11, 113

Meza A., Navarro J. F., Abadi M. G., Steinmetz M., 2005, MNRAS, 359, 93 102

Michie R. W., 1963, MNRAS, 125, 127 15

Miller-Jones J. C. A., et al., 2015, MNRAS, 453, 3918 10

Miocchi P., et al., 2013, ApJ, 774, 151 45

Morscher M., Pattabiraman B., Rodriguez C., Rasio F. A., Umbreit S., 2015, ApJ, 800, 9 11, 34

Noyola E., Gebhardt K., Bergmann M., 2008, ApJ, 676, 1008 11, 102, 105

Oh K. S., Lin D. N. C., 1992, ApJ, 386, 519 28

Perera B. B. P., et al., 2017a, MNRAS, 468, 2114 11, 109

Perera B. B. P., et al., 2017b, MNRAS, 471, 1258 109

Peuten M., Brockamp M., Küpper A. H. W., Kroupa P., 2014, ApJ, 795, 116 109

Peuten M., Zocchi A., Gieles M., Gualandris A., Hénault-Brunet V., 2016, MNRAS, 462, 2333 11, 89

Peuten M., Zocchi A., Gieles M., Hénault-Brunet V., 2017, MNRAS, 470, 2736 29, 53, 70, 89, 94, 127

Pfahl E., Rappaport S., Podsiadlowski P., 2002, ApJ, 573, 283 33

Raso S., et al., 2020, ApJ, 895, 15 43

Rodriguez C. L., Morscher M., Wang L., Chatterjee S., Rasio F. A., Spurzem R., 2016, MNRAS, 463, 2109 11

Rui N. Z., Weatherford N. C., Kremer K., Chatterjee S., Fragione G., Rasio F. A., Rodriguez C. L., Ye C. S., 2021a, Research Notes of the American Astronomical Society, 5, 47 ix, 99, 100, 110, 117, 118

Rui N. Z., Kremer K., Weatherford N. C., Chatterjee S., Rasio F. A., Rodriguez C. L., Ye C. S., 2021b, ApJ, 912, 102 22, 117

Salpeter E. E., 1955, ApJ, 121, 161 5, 7, 80, 81, 126

Sarajedini A., et al., 2007, AJ, 133, 1658 46

Shanahan R. L., Gieles M., 2015, MNRAS, 448, L94 8, 18

Simioni M., et al., 2018, MNRAS, 476, 271 46

Skilling J., 2004, in Fischer R., Preuss R., Toussaint U. V., eds, American Institute of Physics Conference Series Vol. 735, Bayesian Inference and Maximum Entropy Methods in Science and Engineering: 24th International Workshop on Bayesian Inference and Maximum Entropy Methods in Science and Engineering. pp 395–405, doi:10.1063/1.1835238 55

Skilling J., 2006, Bayesian Analysis, 1, 833 55

Smith P. J., 2022, Bachelor's thesis, Saint Mary's University 129

Smith P., Hénault-Brunet V., Dickson N., Gieles M., 2022, in prep. 89, 108, 109, 110, 129

Sollima A., Baumgardt H., 2017, MNRAS, 471, 3668

Sollima A., Baumgardt H., Zocchi A., Balbinot E., Gieles M., Hénault-Brunet V., Varri A. L., 2015, MNRAS, 451, 2185 18

Sollima A., et al., 2016, MNRAS, 462, 1937 18, 19

Speagle J. S., 2020, MNRAS, 493, 3132 57

Spitzer Lyman J., 1969, ApJ, 158, L139 3

Spitzer L. S., 1987, Dynamical Evolution of Globular Clusters. Princeton University Press 3, 13, 15

Strader J., Caldwell N., Seth A. C., 2011, AJ, 142, 8 7, 8

Strader J., Chomiuk L., Maccarone T. J., Miller-Jones J. C. A., Seth A. C., 2012, Nature, 490, 71 10

Tiongco M. A., Vesperini E., Varri A. L., 2016, MNRAS, 455, 3693 28

Trager S. C., King I. R., Djorgovski S., 1995, AJ, 109, 218 45, 46, 88, 90, 92, 100, 122

VandenBerg D. A., Brogaard K., Leaman R., Casagrande L., 2013, ApJ, 775, 134 2

Vasiliev E., 2019, MNRAS, 489, 623 39, 42

Vasiliev E., Baumgardt H., 2021, MNRAS, 505, 5978 39, 40, 41, 67, 106

Vitral E., Mamon G. A., 2021, A&A, 646, A63 117

Vitral E., Kremer K., Libralato M., Mamon G. A., Bellini A., 2022, MNRAS, 514, 806 118, 121

Wang L., Spurzem R., Aarseth S., Nitadori K., Berczik P., Kouwenhoven M. B. N., Naab T., 2015, MNRAS, 450, 4070 20

Watkins L. L., van de Ven G., den Brok M., van den Bosch R. C. E., 2013, MNRAS, 436, 2598 18

Watkins L. L., van der Marel R. P., Bellini A., Anderson J., 2015, ApJ, 803, 29 42, 43, 70, 72

Weatherford N. C., Chatterjee S., Rodriguez C. L., Rasio F. A., 2018, ApJ, 864, 13 99, 102

Weatherford N. C., Chatterjee S., Kremer K., Rasio F. A., 2020, ApJ, 898, 162 ix, 21, 99, 100, 101, 102, 108, 110, 117, 118, 121, 122, 127

Weatherford N. C., Fragione G., Kremer K., Chatterjee S., Ye C. S., Rodriguez C. L., Rasio F. A., 2021, apjl, 907, L25 9, 53, 80, 81

Wilson C. P., 1975, AJ, 80, 175 14

Woolley R. V. D. R., 1954, MNRAS, 114, 191 13

Ye C. S., Kremer K., Rodriguez C. L., Rui N. Z., Weatherford N. C., Chatterjee S., Rasio F. A., Fragione G., 2022, ApJ, 931, 84 108

Zocchi A., Gieles M., Hénault-Brunet V., Varri A. L., 2016, MNRAS, 462, 696 21, 28

Zocchi A., Gieles M., Hénault-Brunet V., 2017, MNRAS, 468, 4429 11, 70, 106

Zocchi A., Gieles M., Hénault-Brunet V., 2019, MNRAS, 482, 4713 11, 89, 105, 106

de Boer T. J. L., Gieles M., Balbinot E., Hénault-Brunet V., Sollima A., Watkins L. L., Claydon I., 2019, MNRAS, 485, 4906 45, 46, 69, 92, 125

van den Bergh S., 2011, PASP, 123, 1044 8, 85

van der Marel R. P., Anderson J., 2010, ApJ, 710, 1063 11, 102, 105

APPENDICES

Appendix A

Model Fits

A.1 All Best-Fitting Models

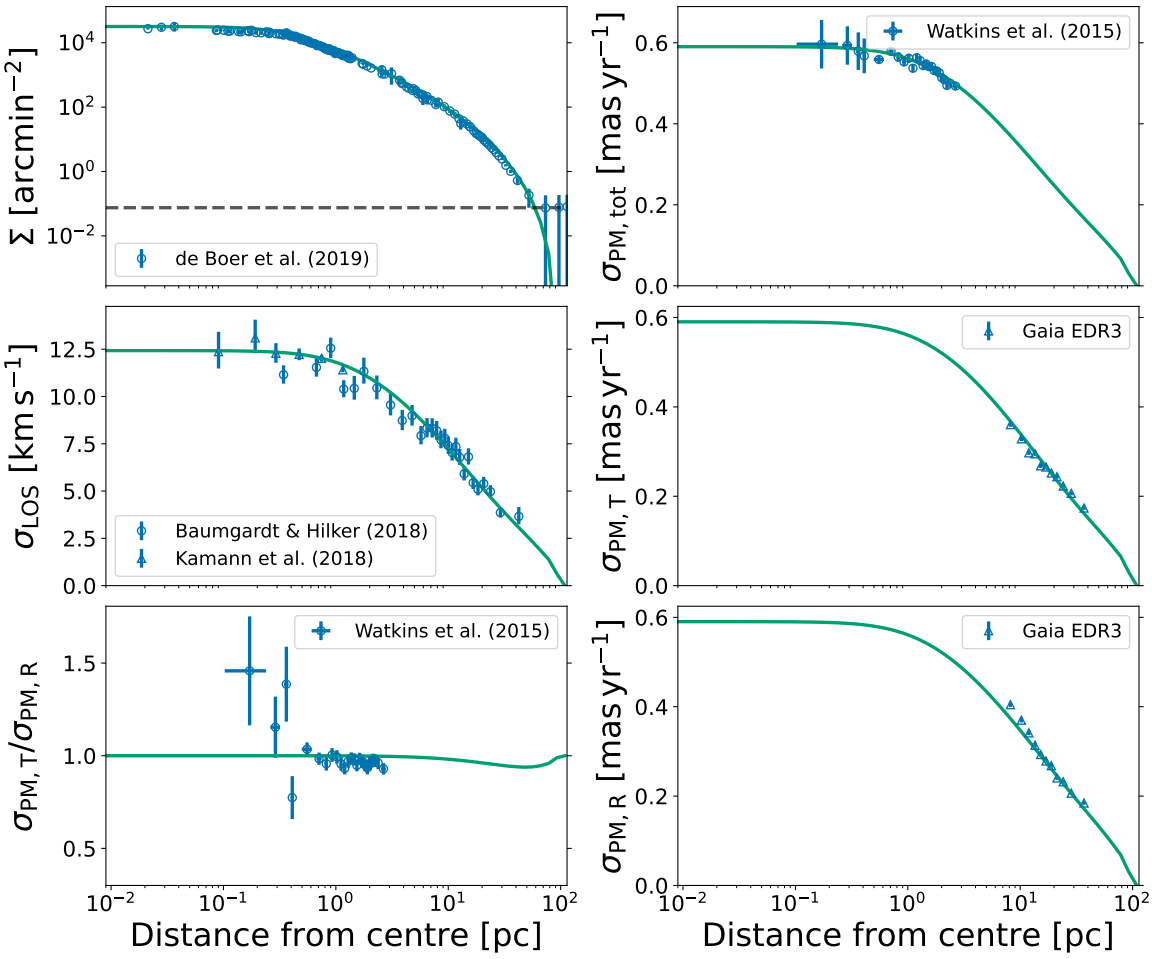

Figure A.1: Figure 5.2 repeated for NGC 104

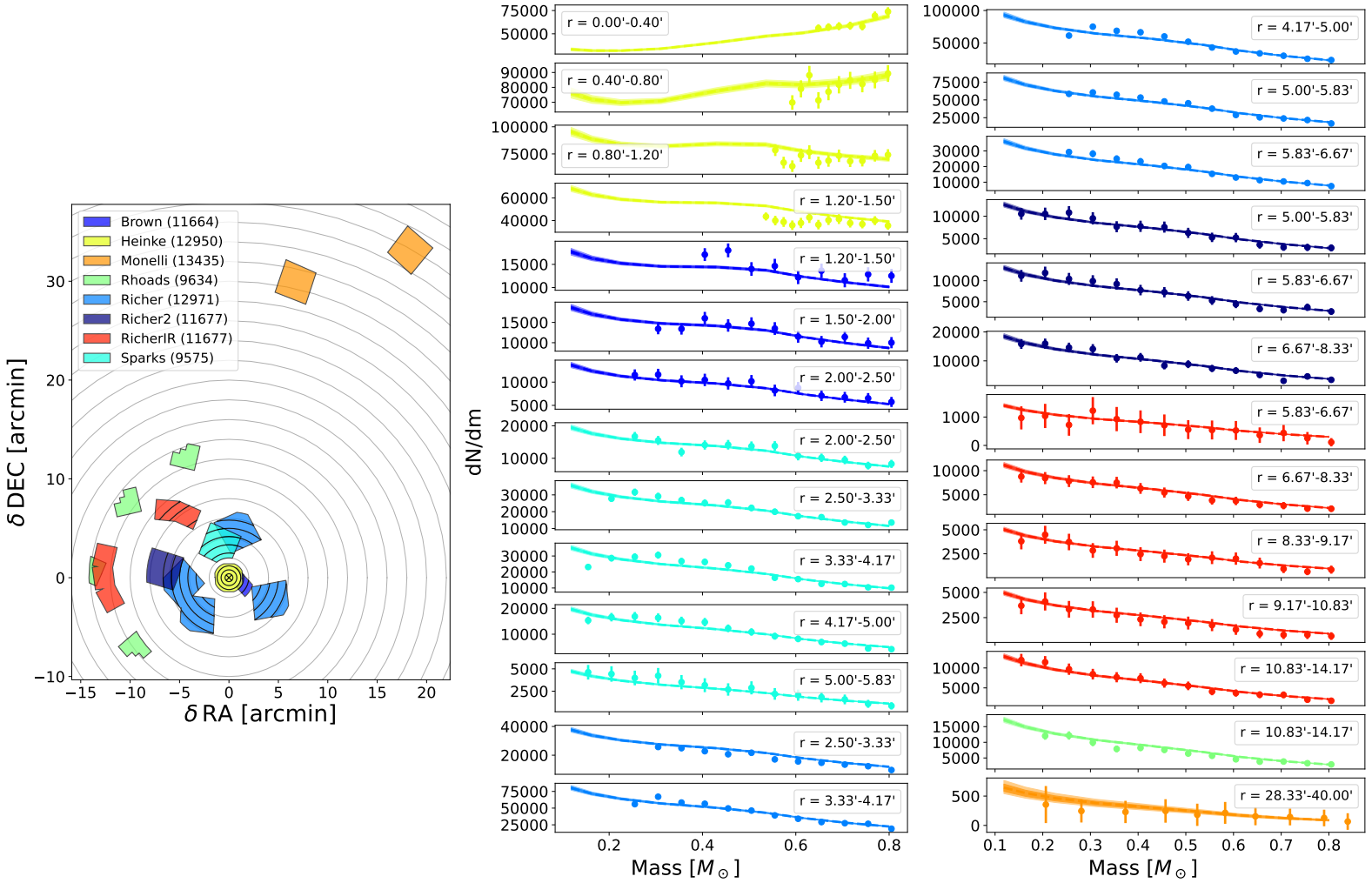

Figure A.2: Figure 5.3 repeated for NGC 104

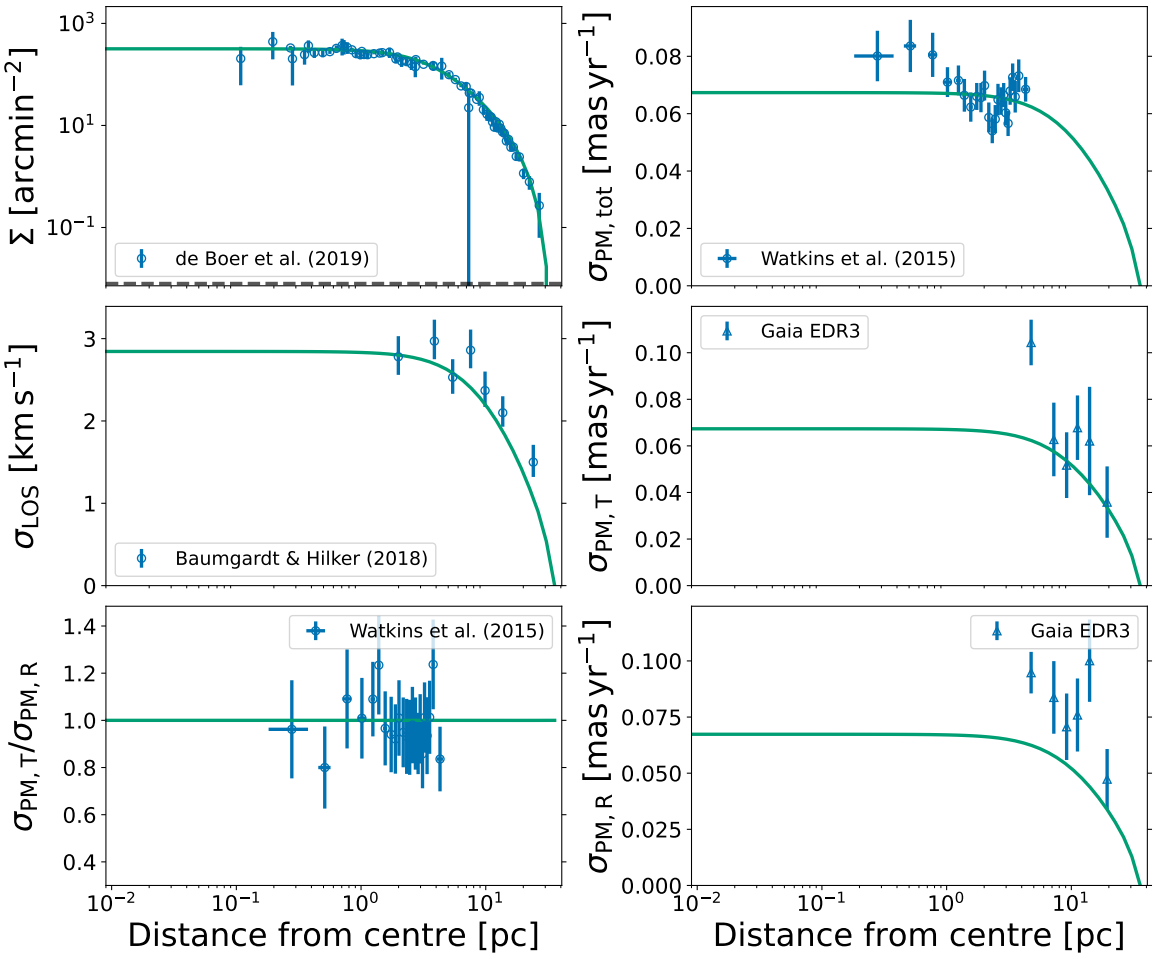

Figure A.3: Figure 5.2 repeated for NGC 288

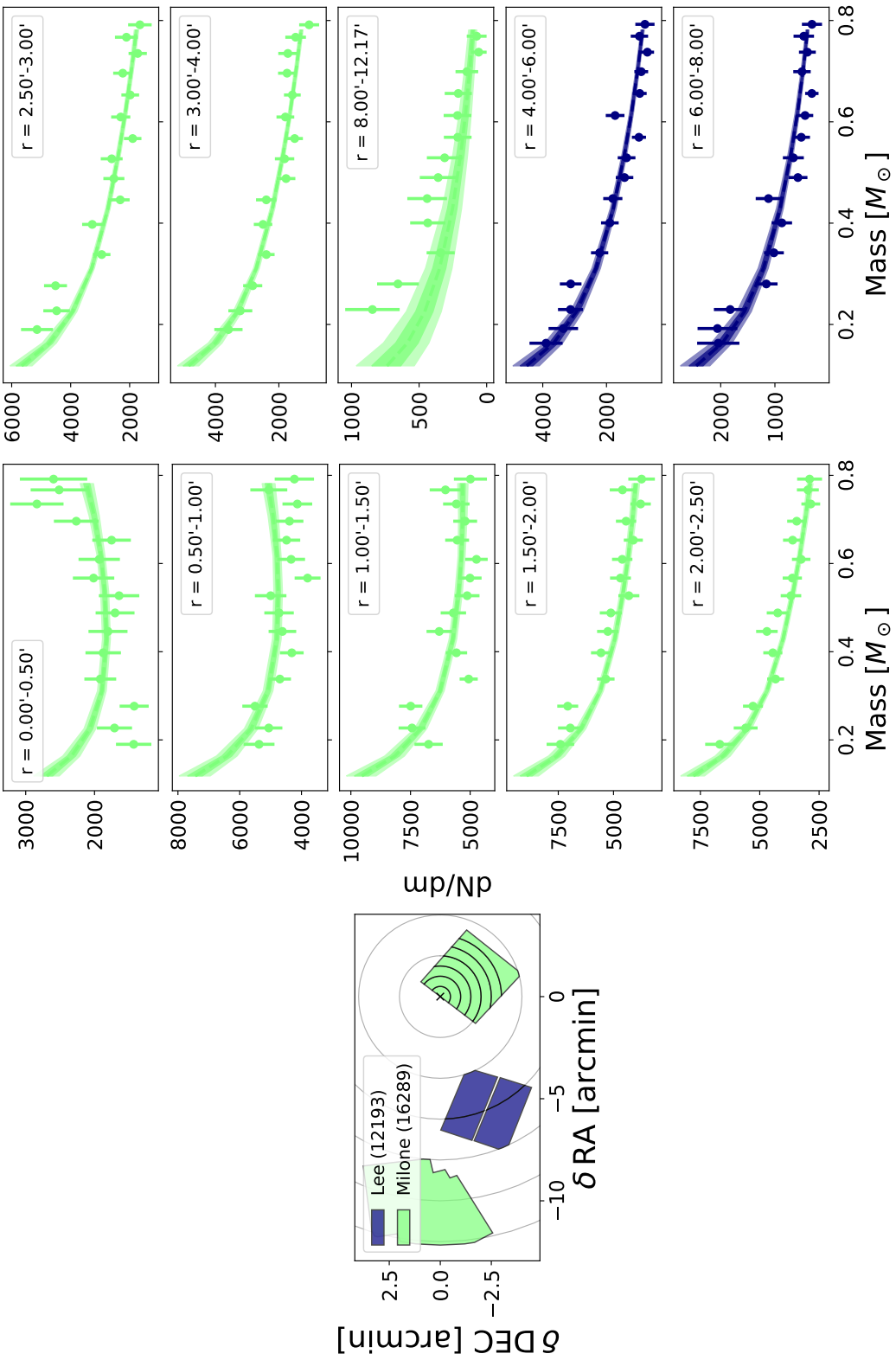

Figure A.4: Figure 5.3 repeated for NGC 288

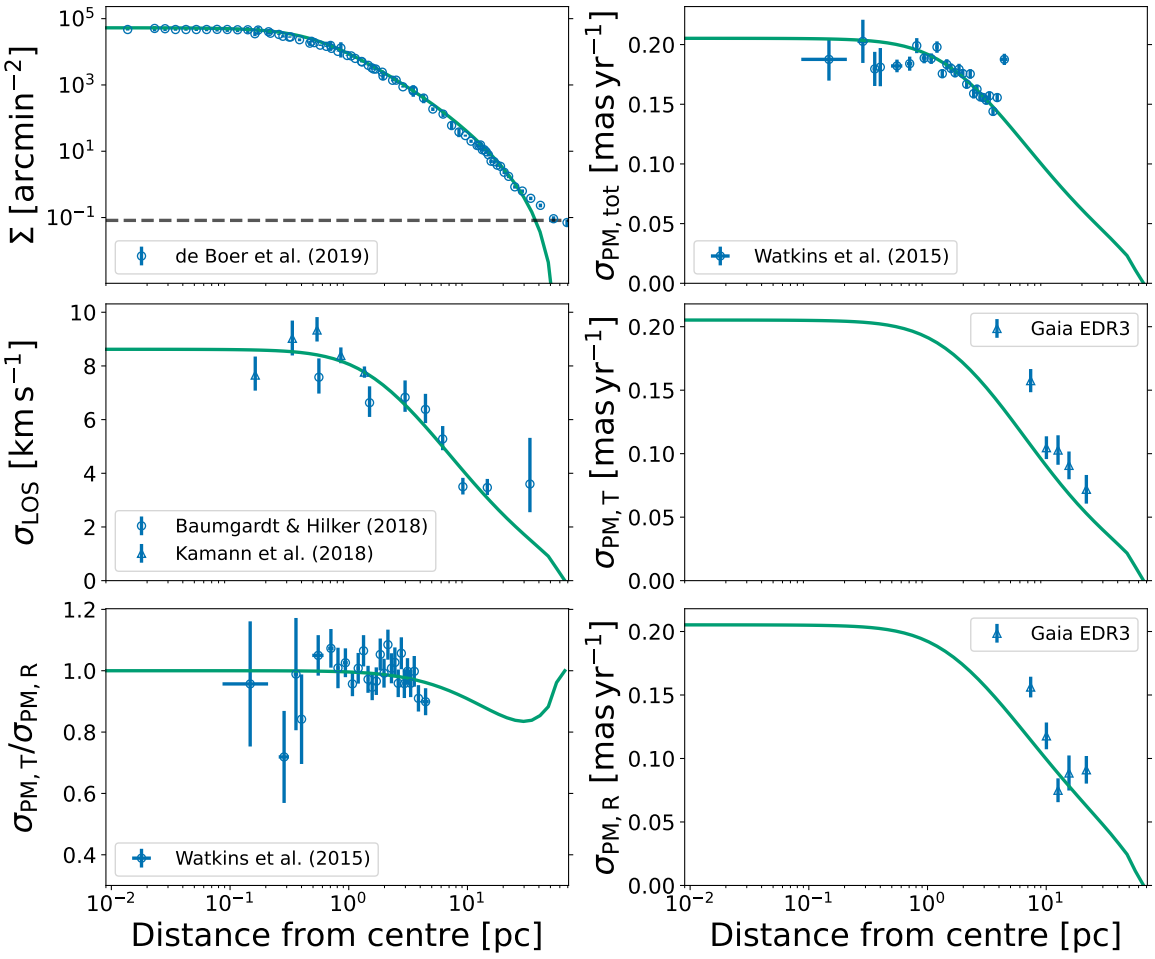

Figure A.5: Figure 5.2 repeated for NGC 362

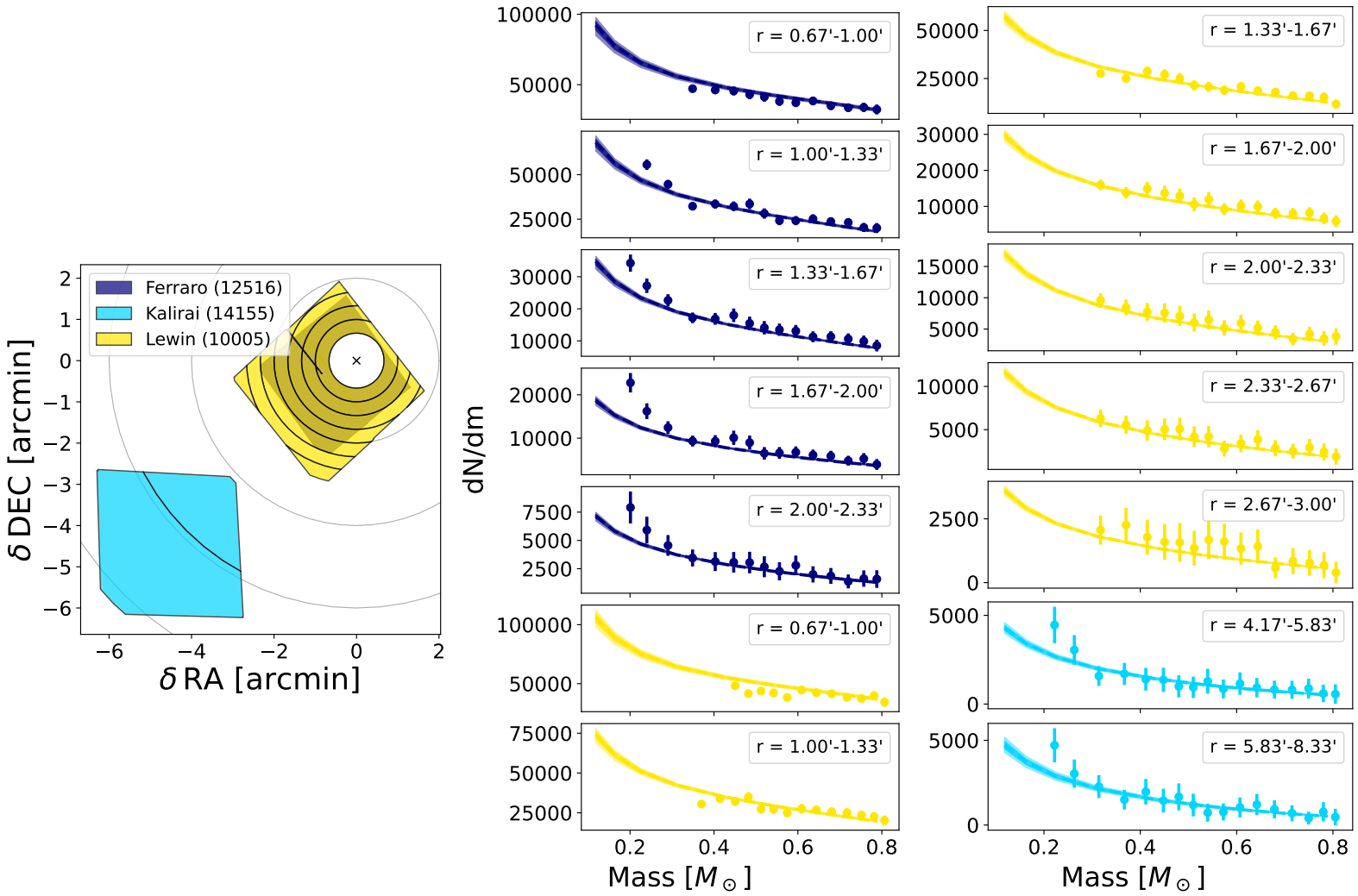

Figure A.6: Figure 5.3 repeated for NGC 362

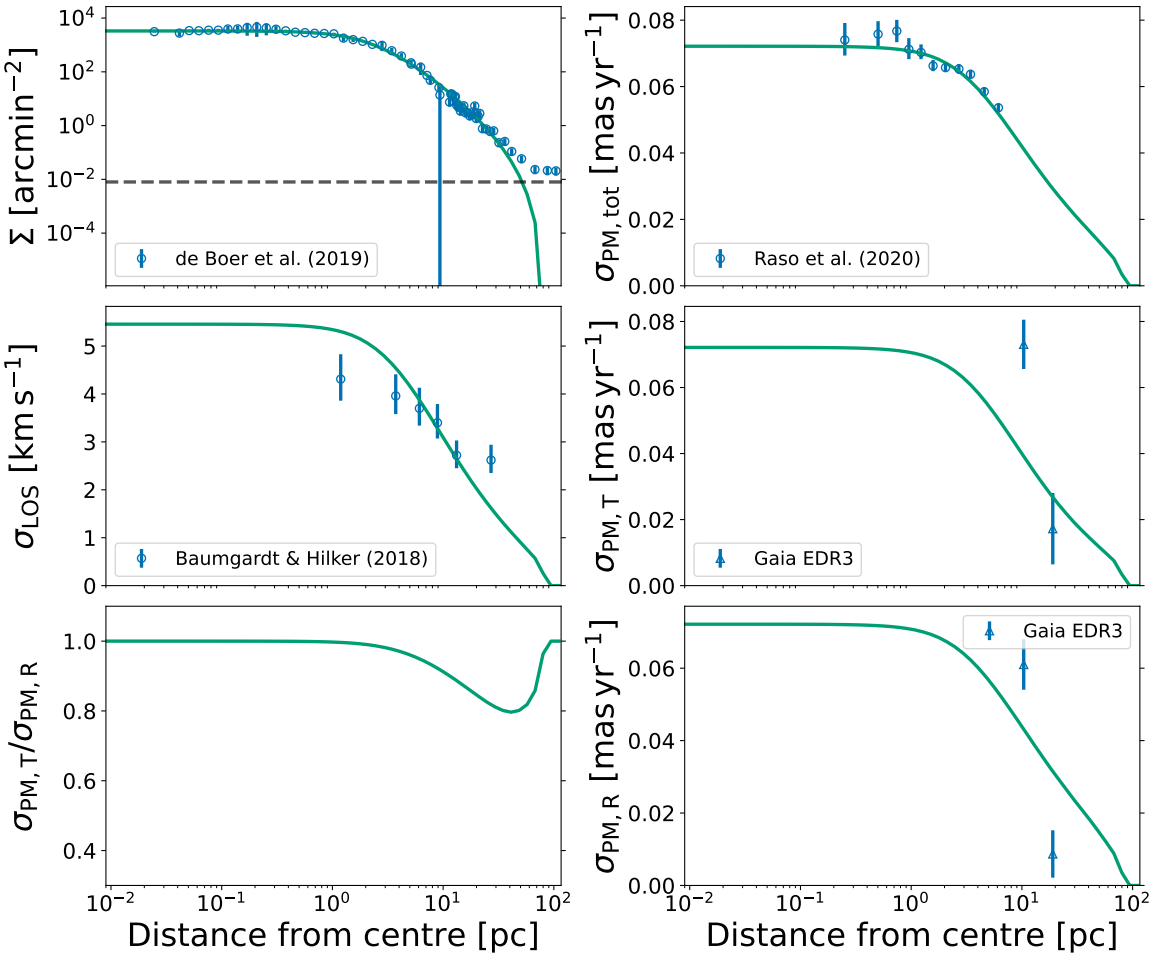

Figure A.7: Figure 5.2 repeated for NGC 1261

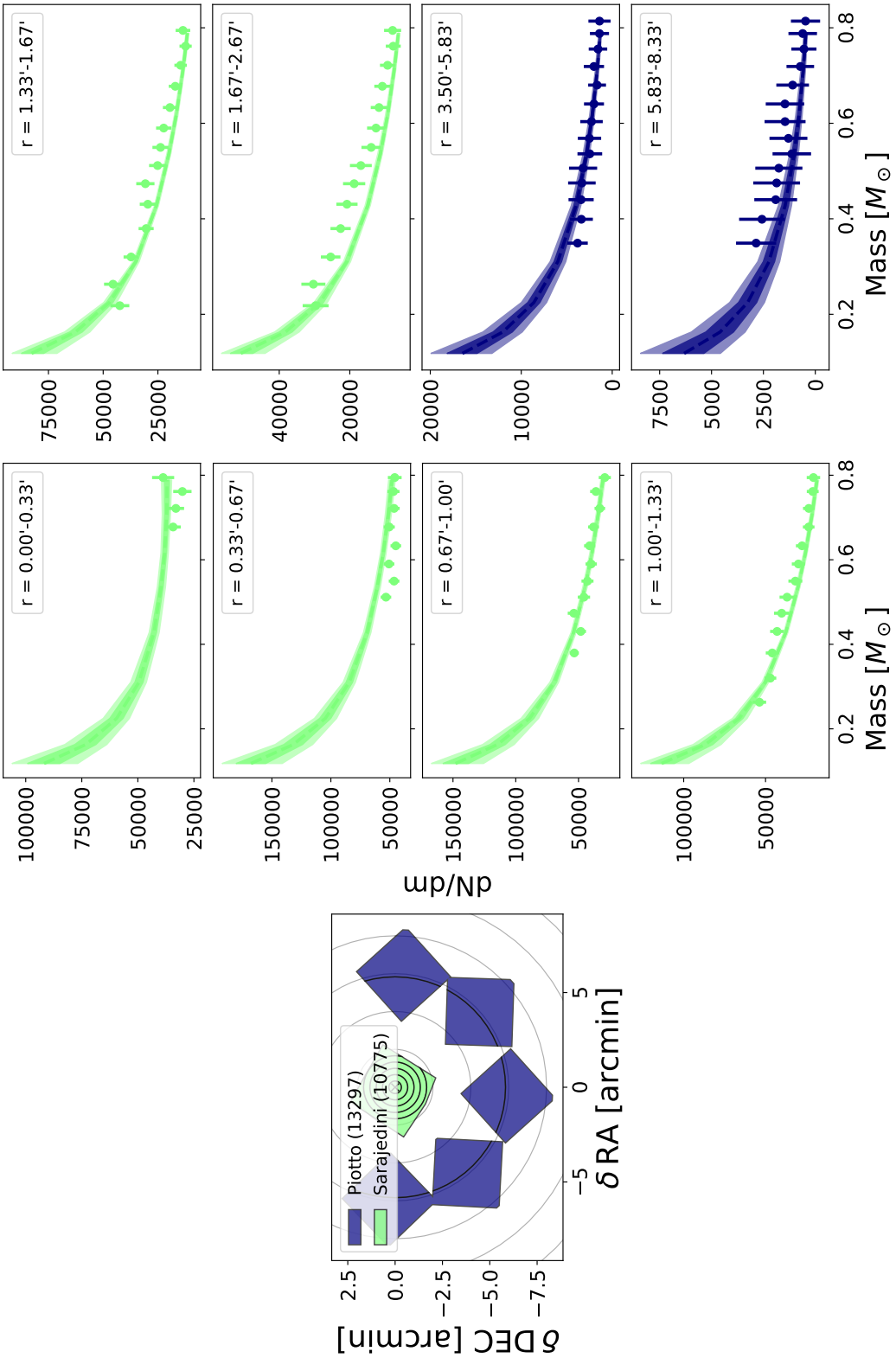

Figure A.8: Figure 5.3 repeated for NGC 1261

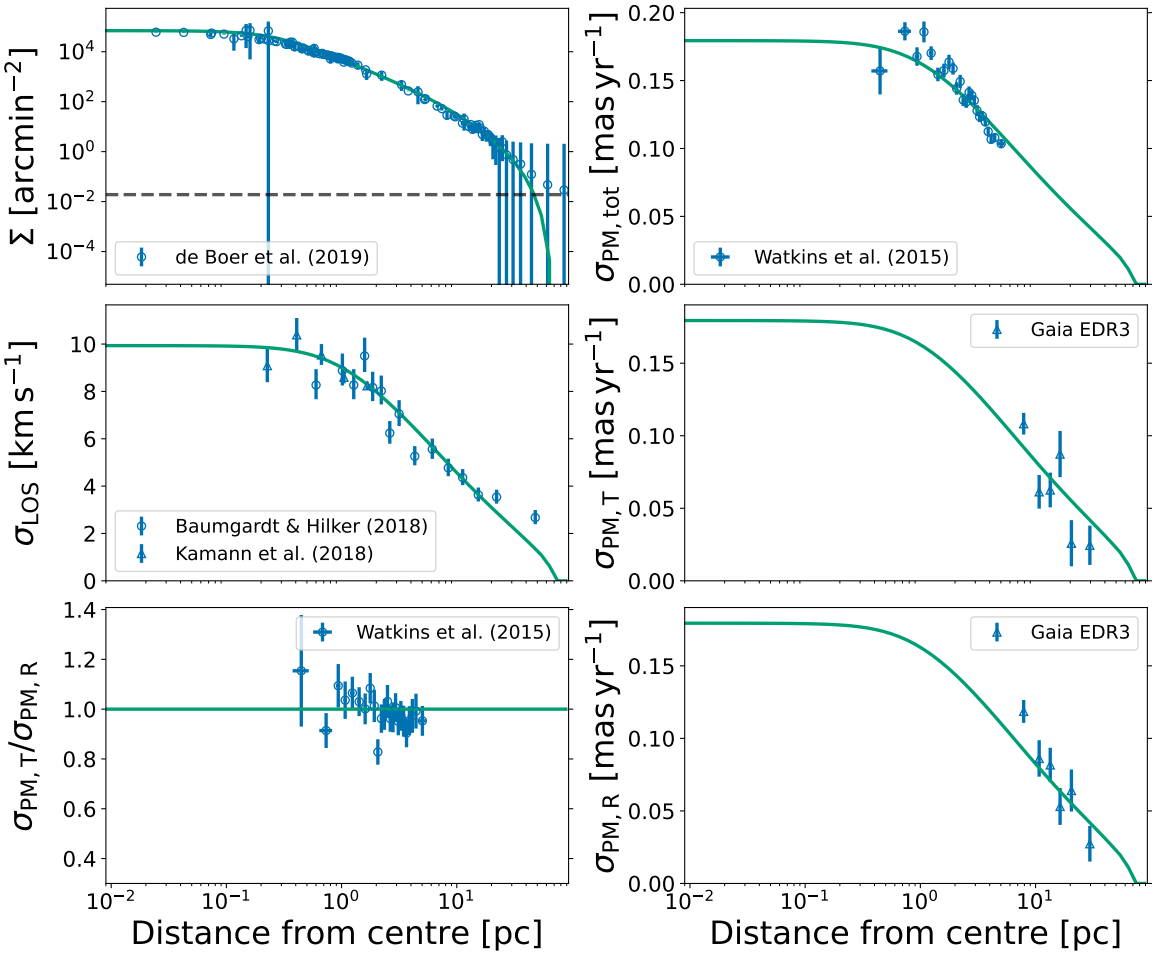

Figure A.9: Figure 5.2 repeated for NGC 1851

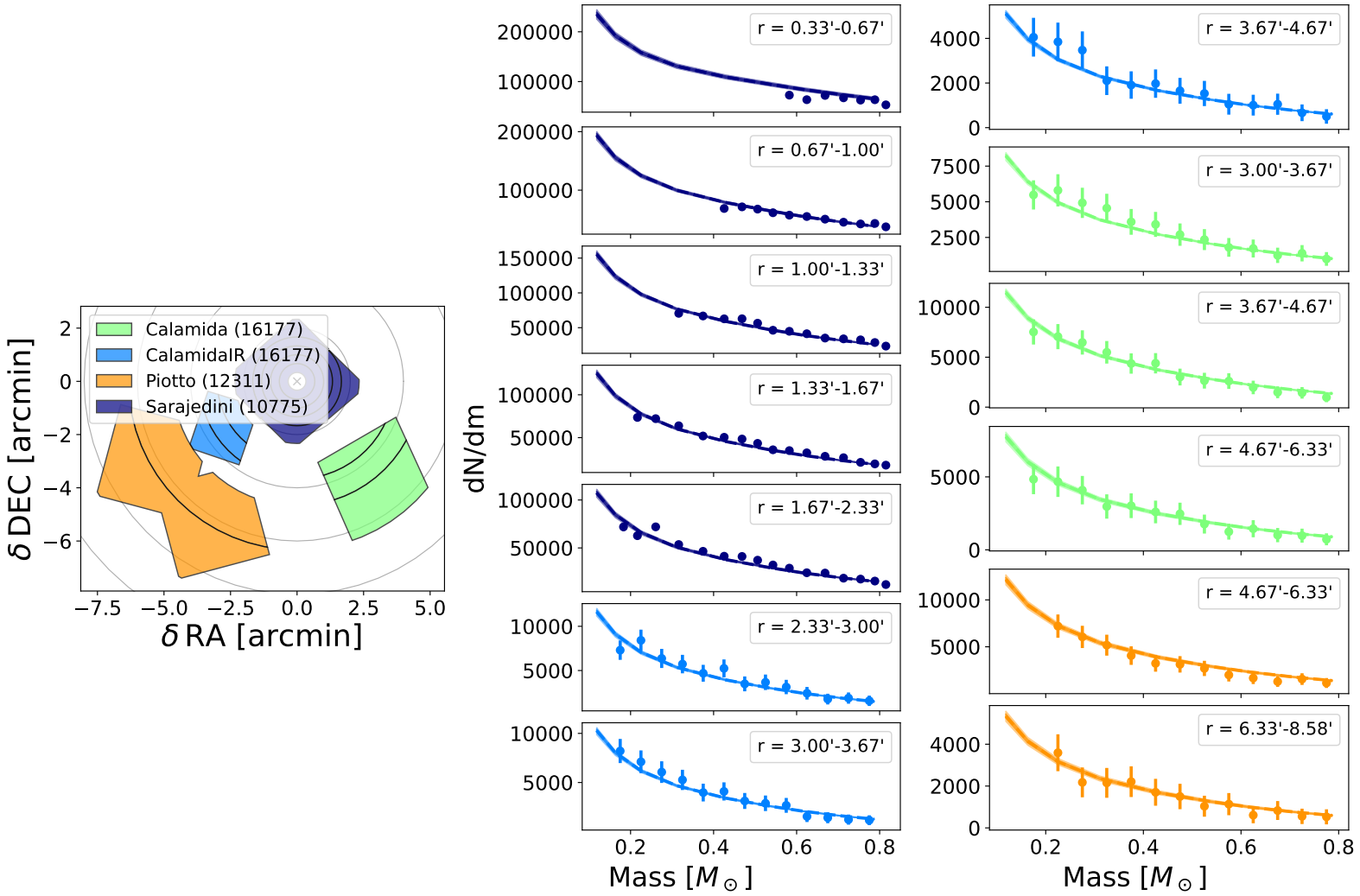

Figure A.10: Figure 5.3 repeated for NGC 1851

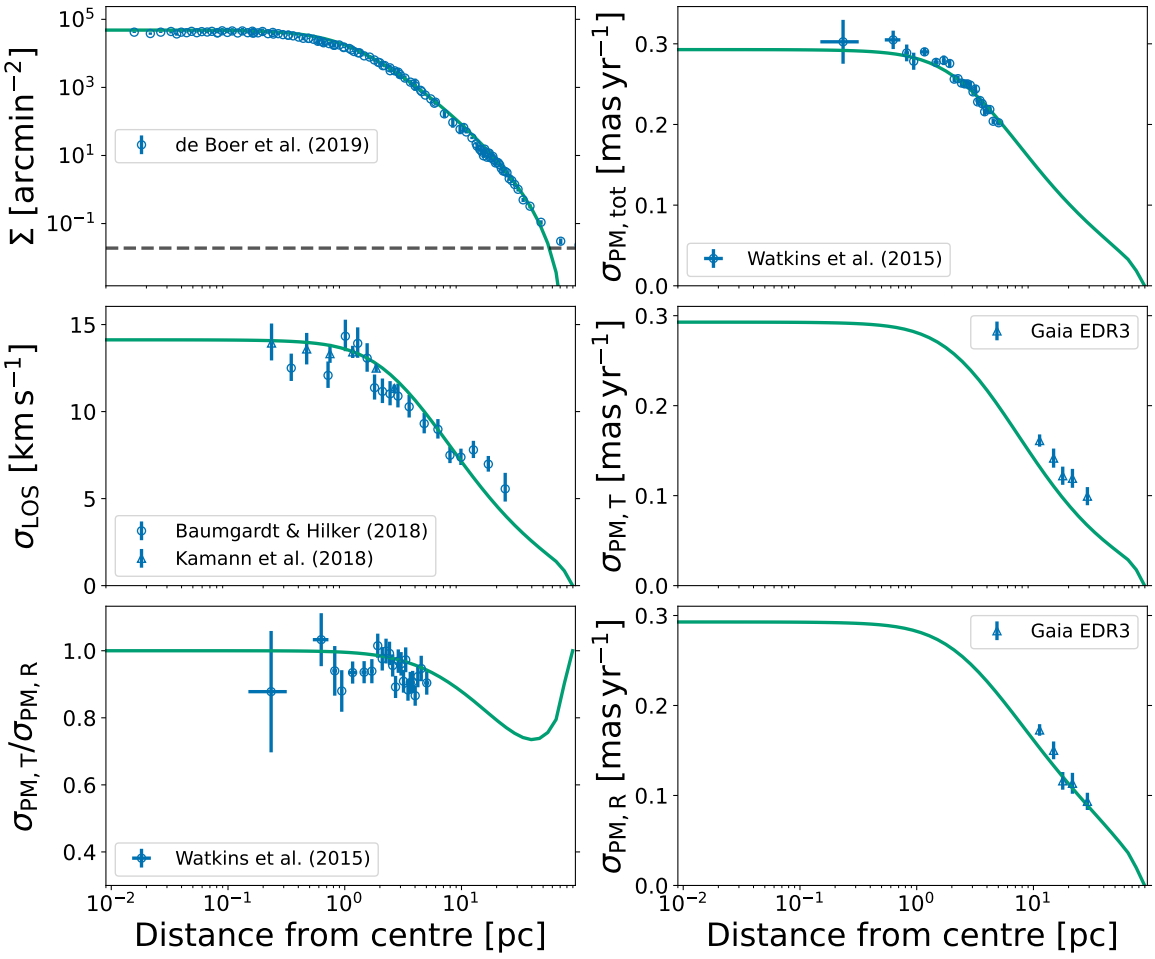

Figure A.11: Figure 5.2 repeated for NGC 2808

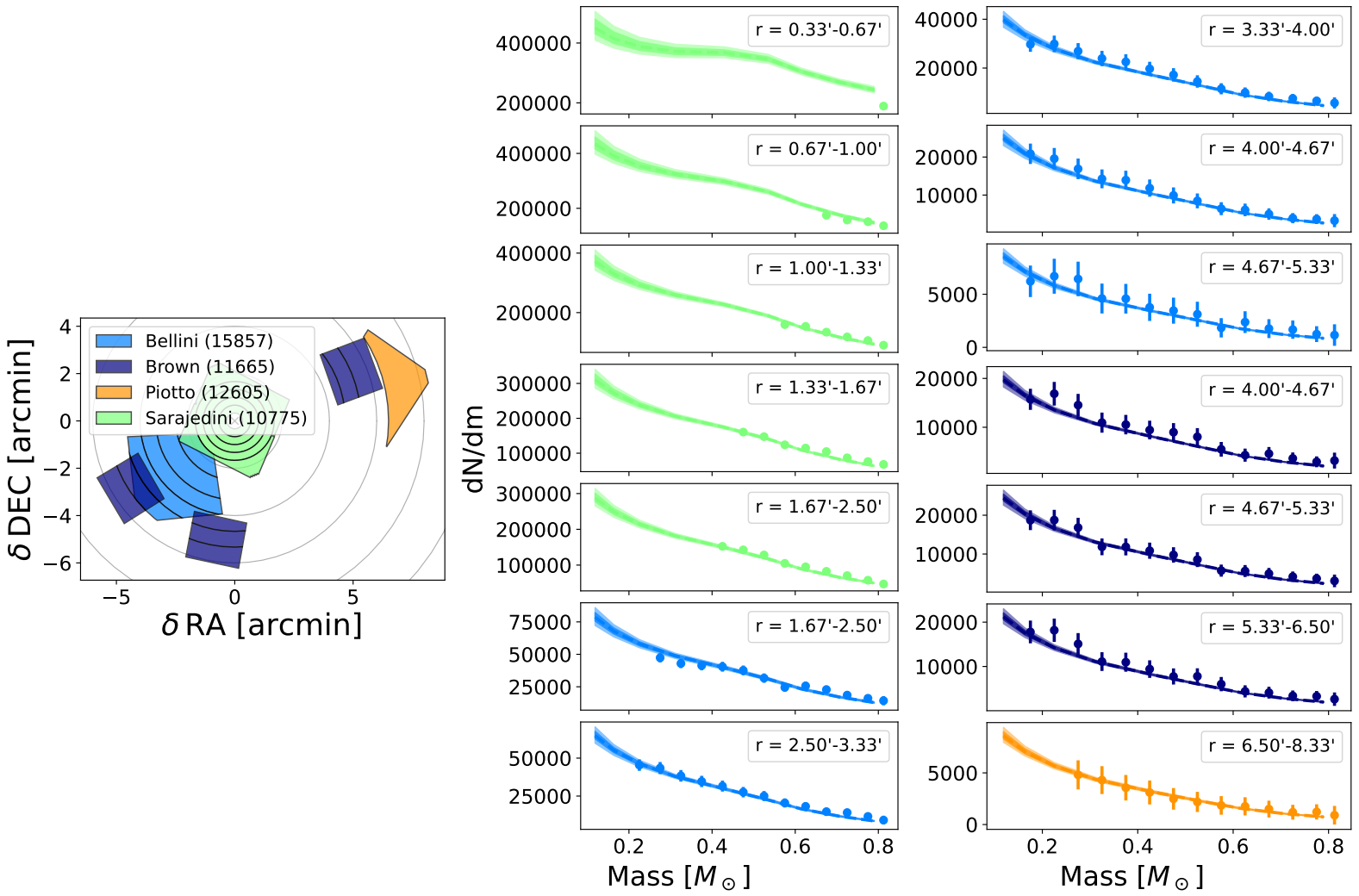

Figure A.12: Figure 5.3 repeated for NGC 2808

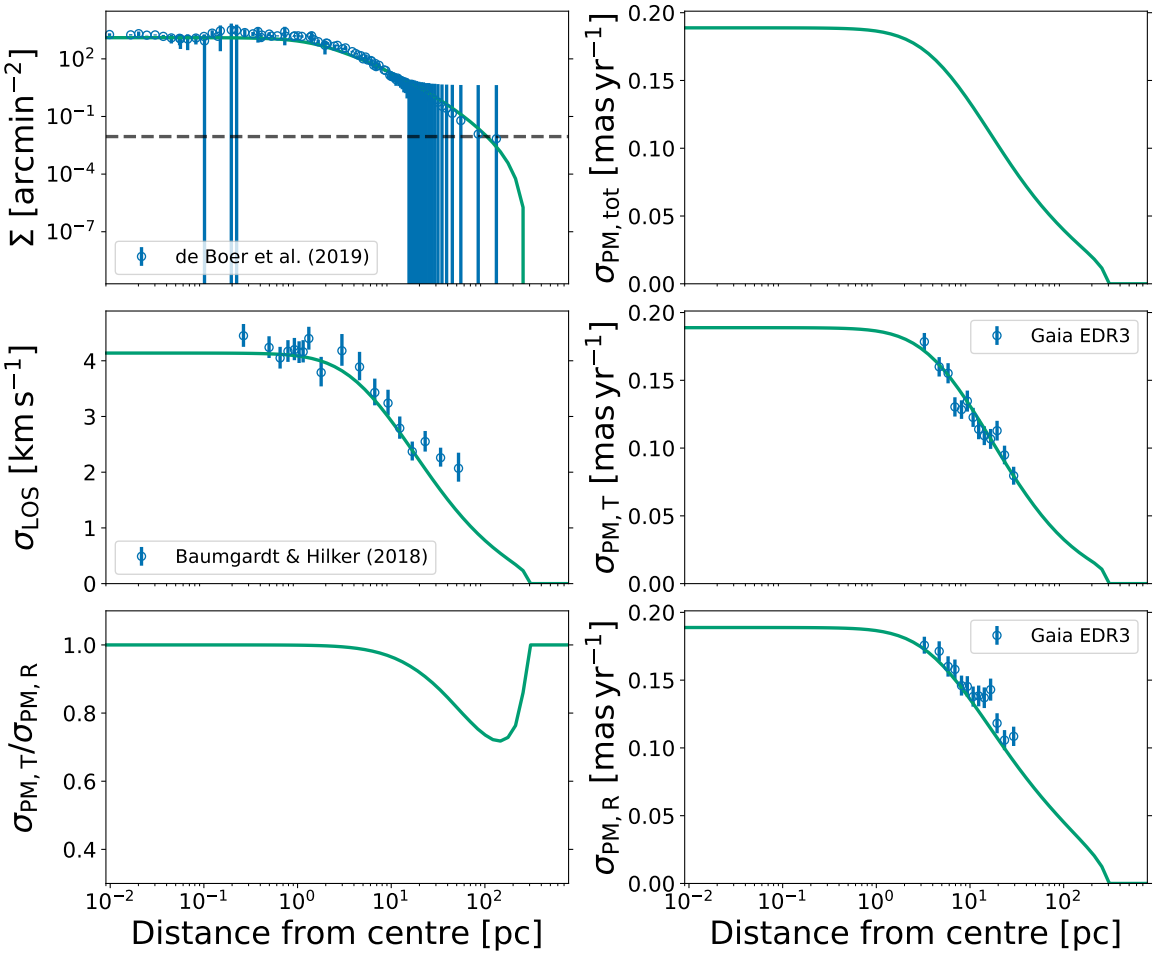

Figure A.13: Figure 5.2 repeated for NGC 3201

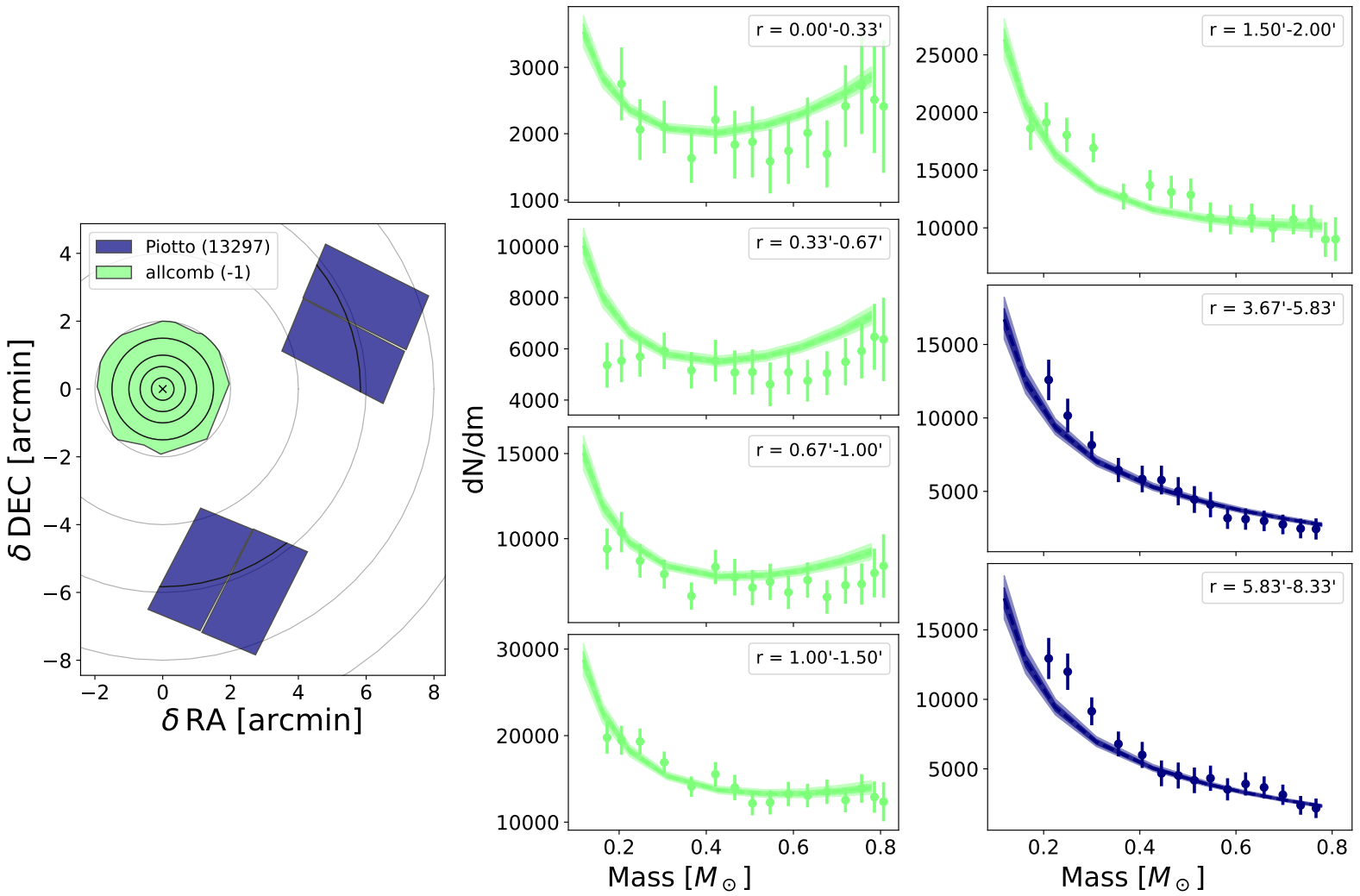

Figure A.14: Figure 5.3 repeated for NGC 3201

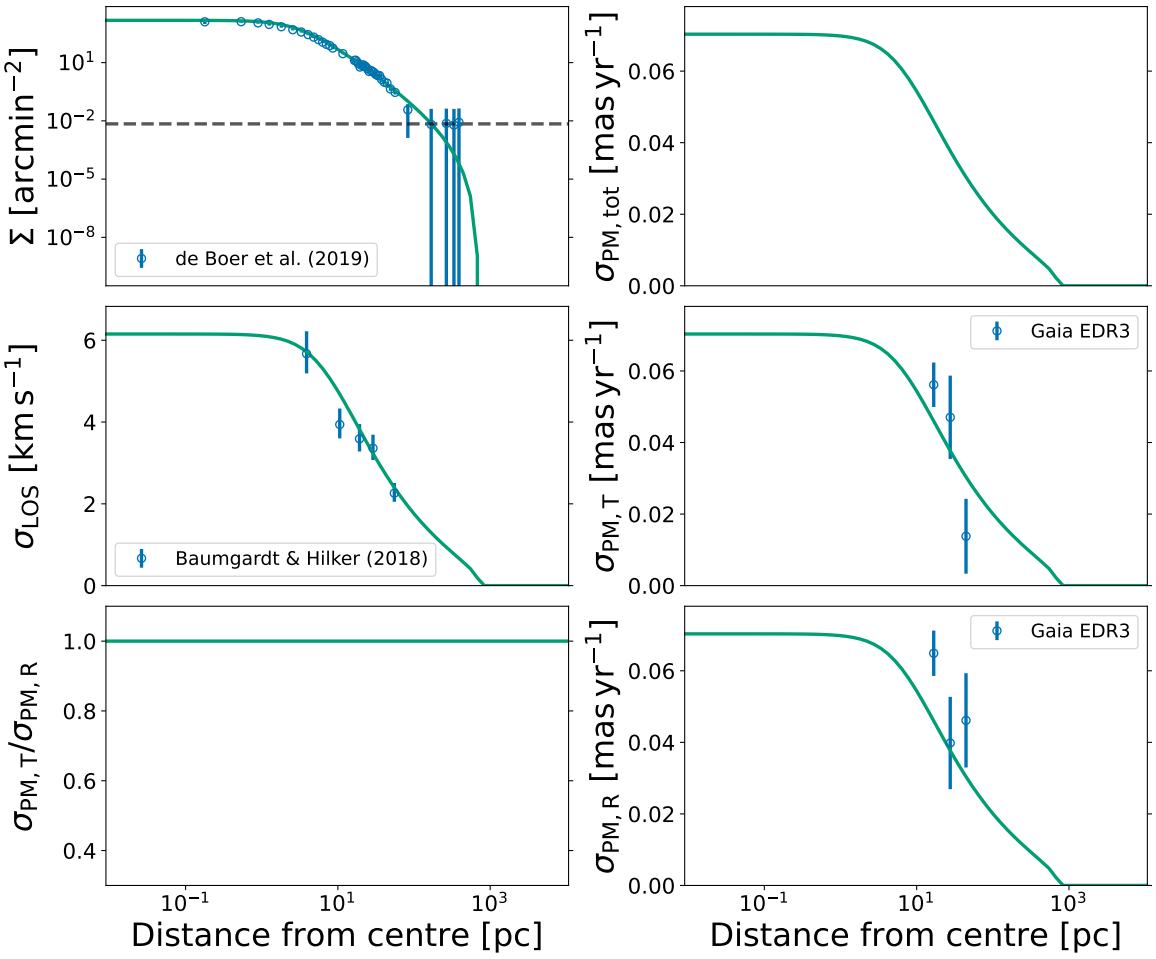

Figure A.15: Figure 5.2 repeated for NGC 5024

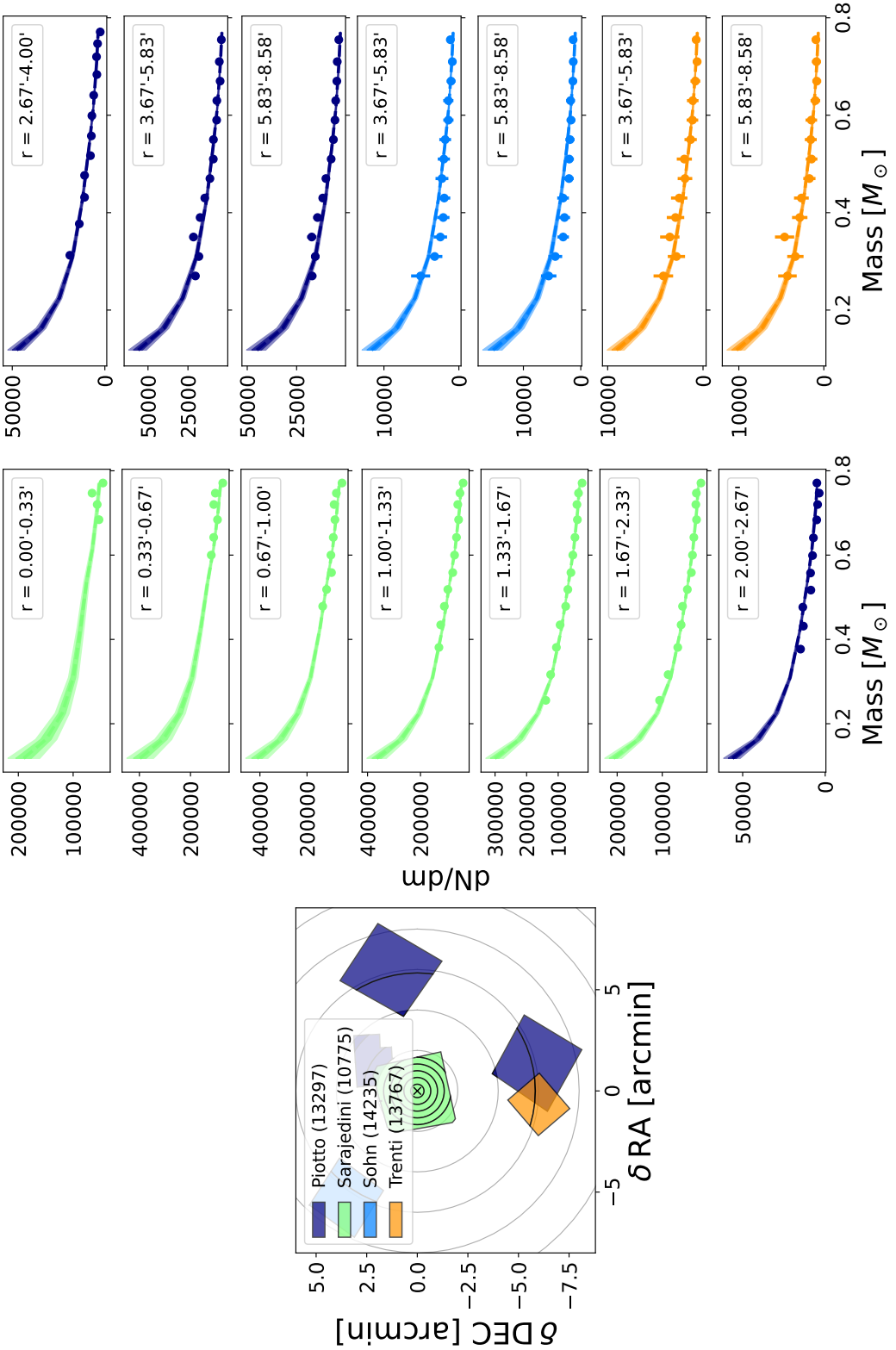

Figure A.16: Figure 5.3 repeated for NGC 5024

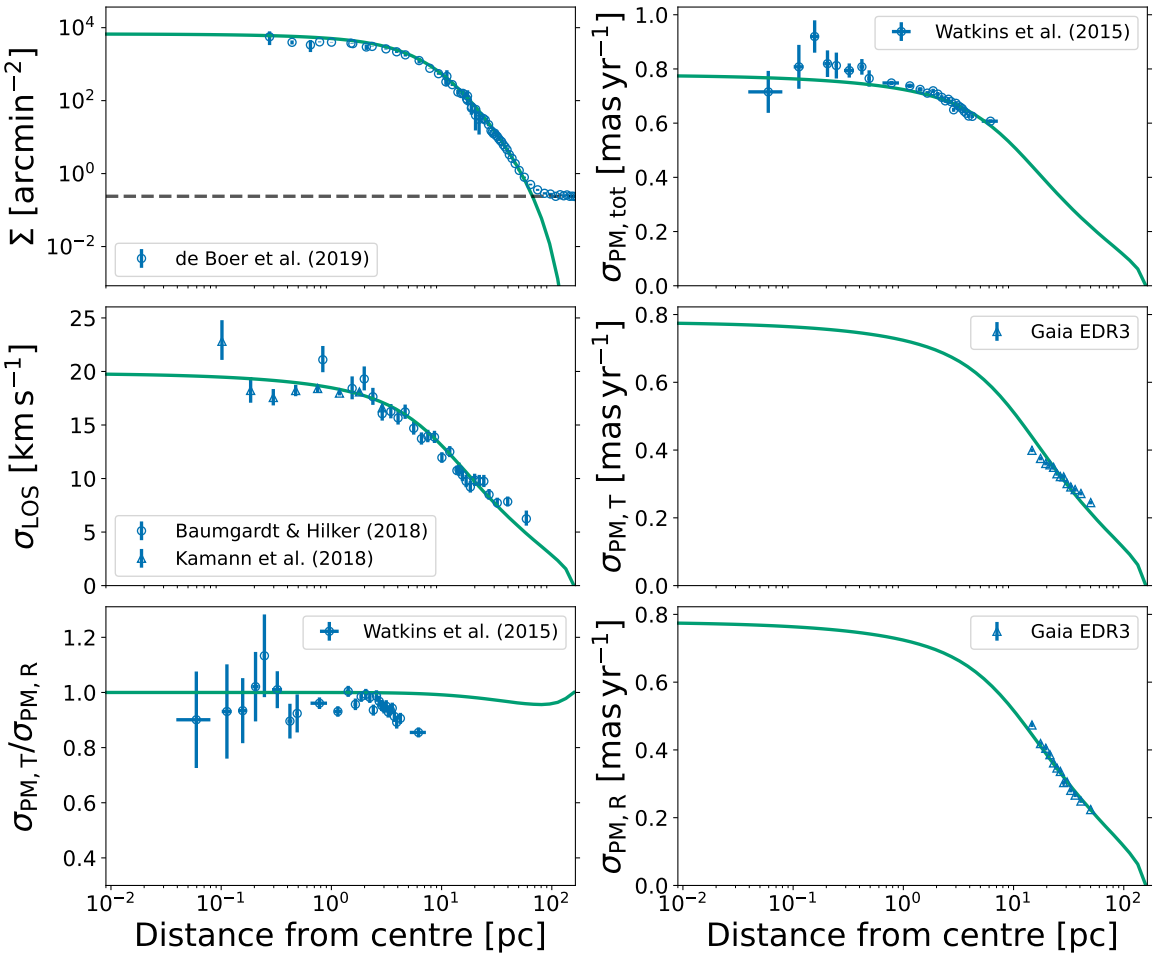

Figure A.17: Figure 5.2 repeated for NGC 5139

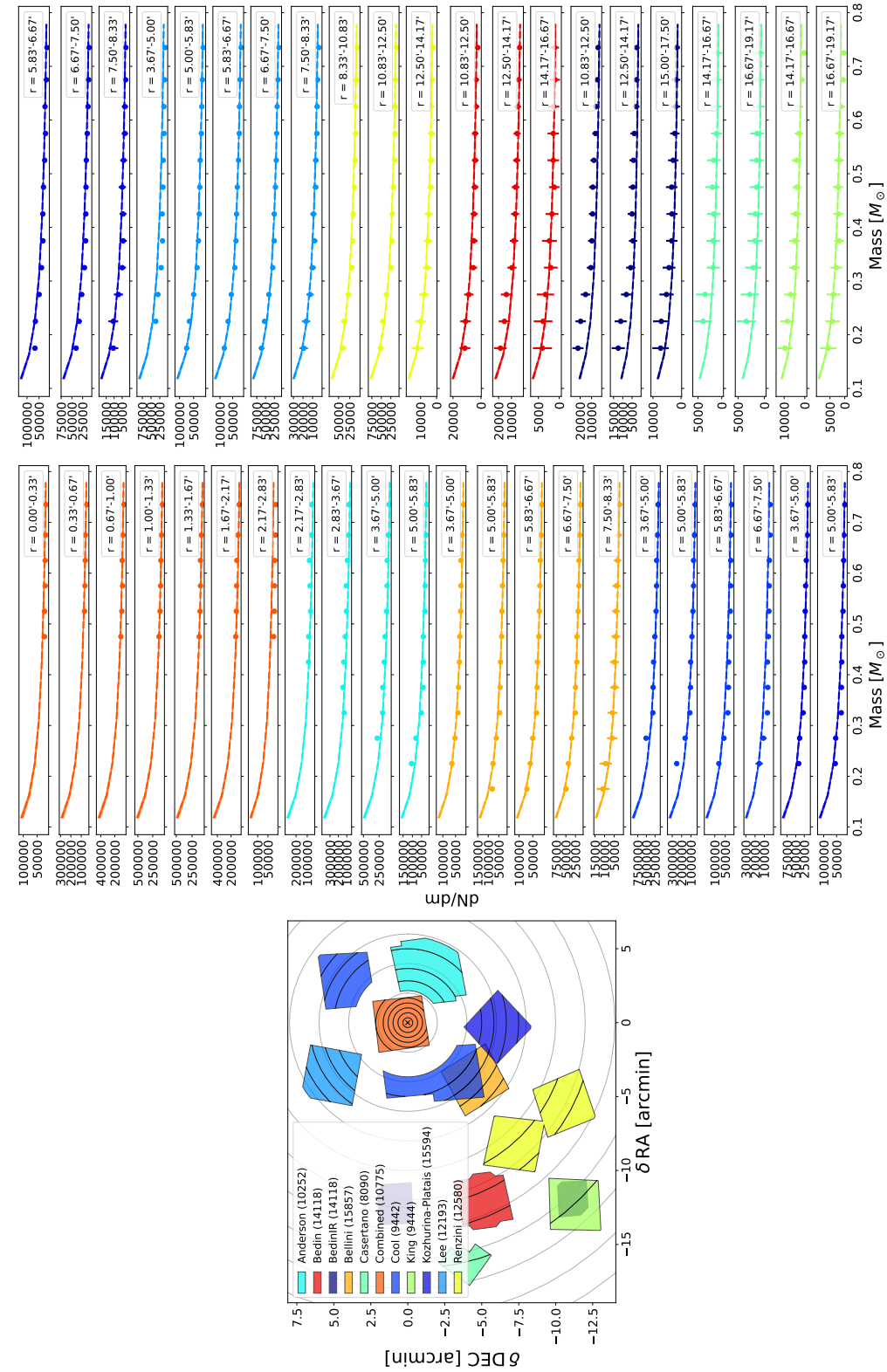

Figure A.18: Figure 5.3 repeated for NGC 5139

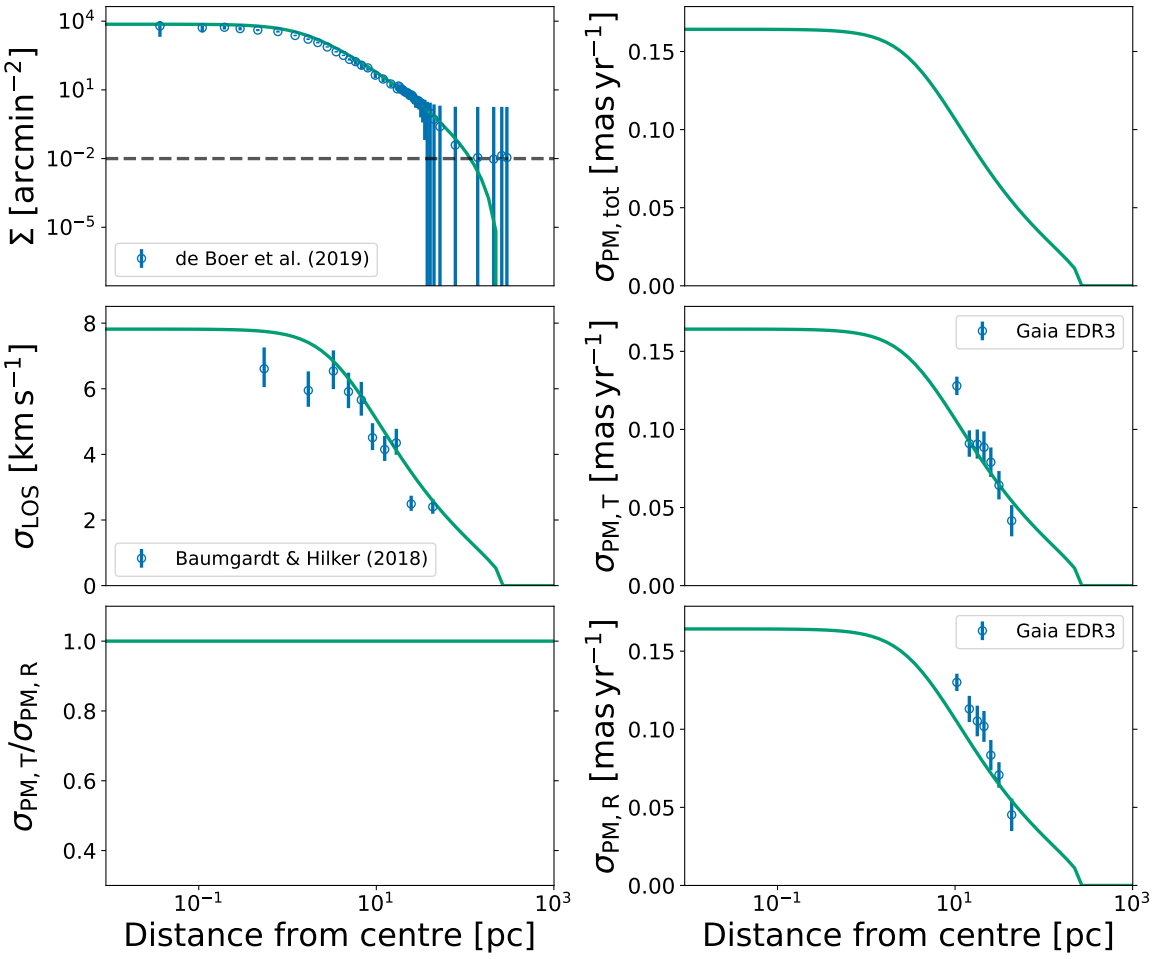

Figure A.19: Figure 5.2 repeated for NGC 5272

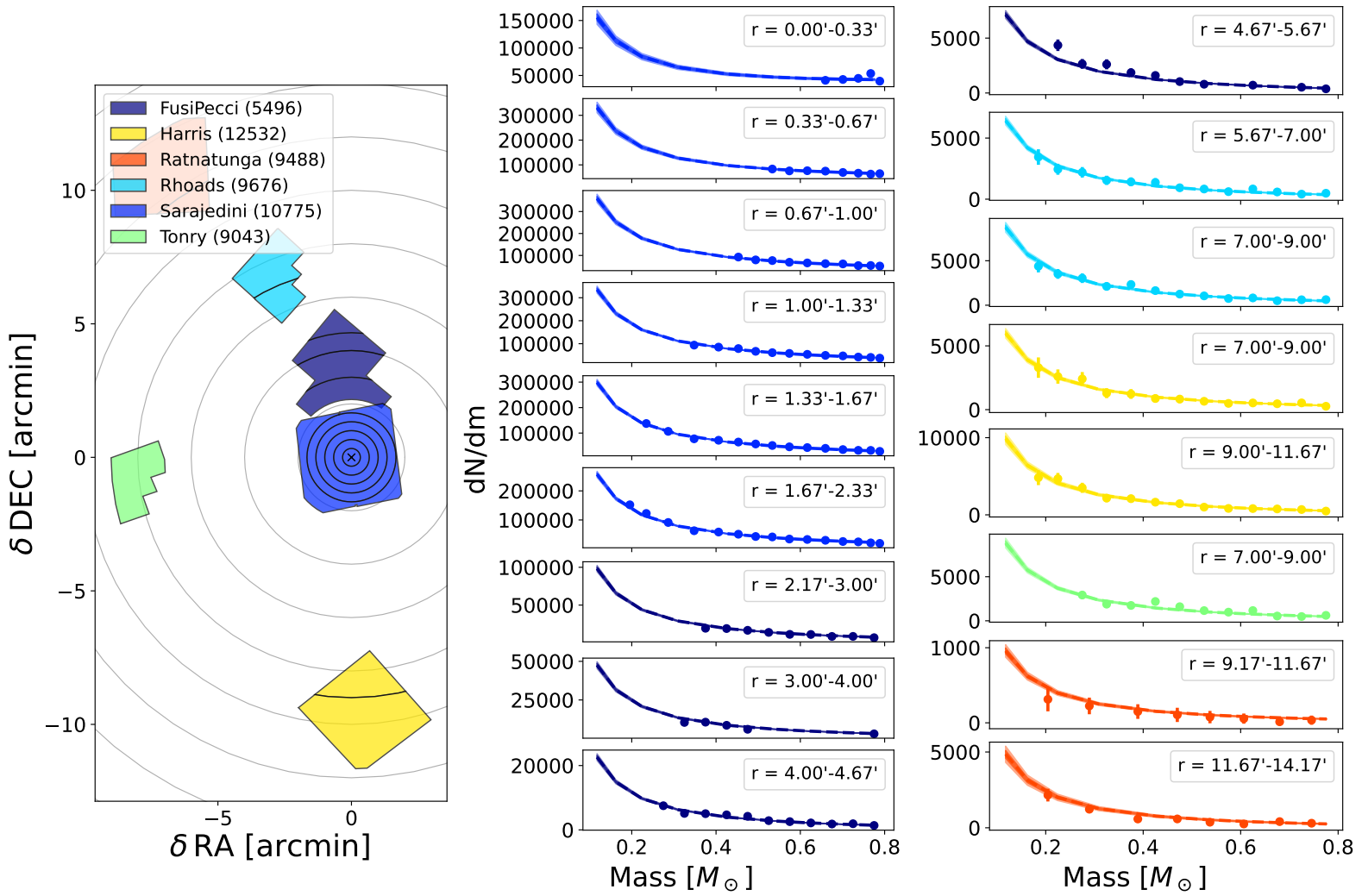

Figure A.20: Figure 5.3 repeated for NGC 5272

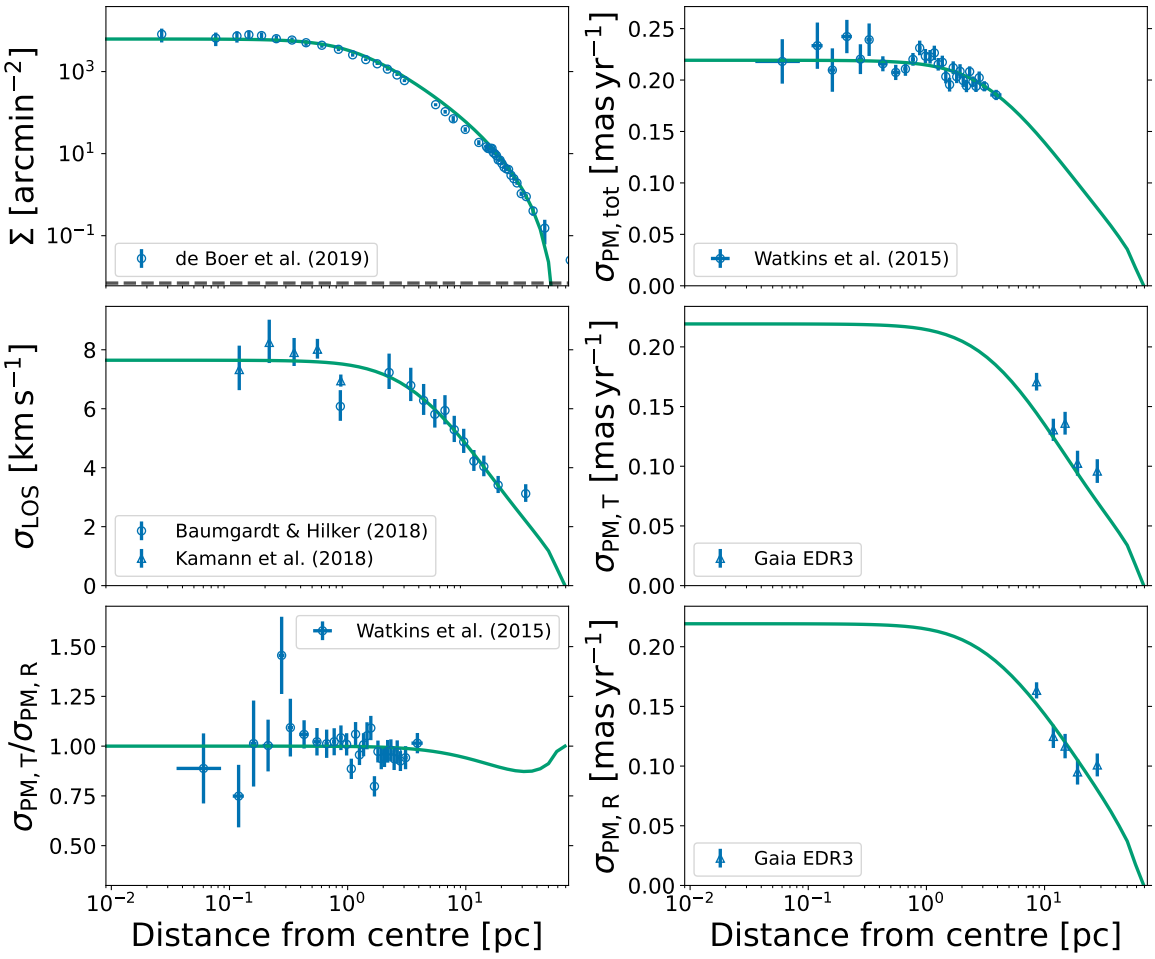

Figure A.21: Figure 5.2 repeated for NGC 5904

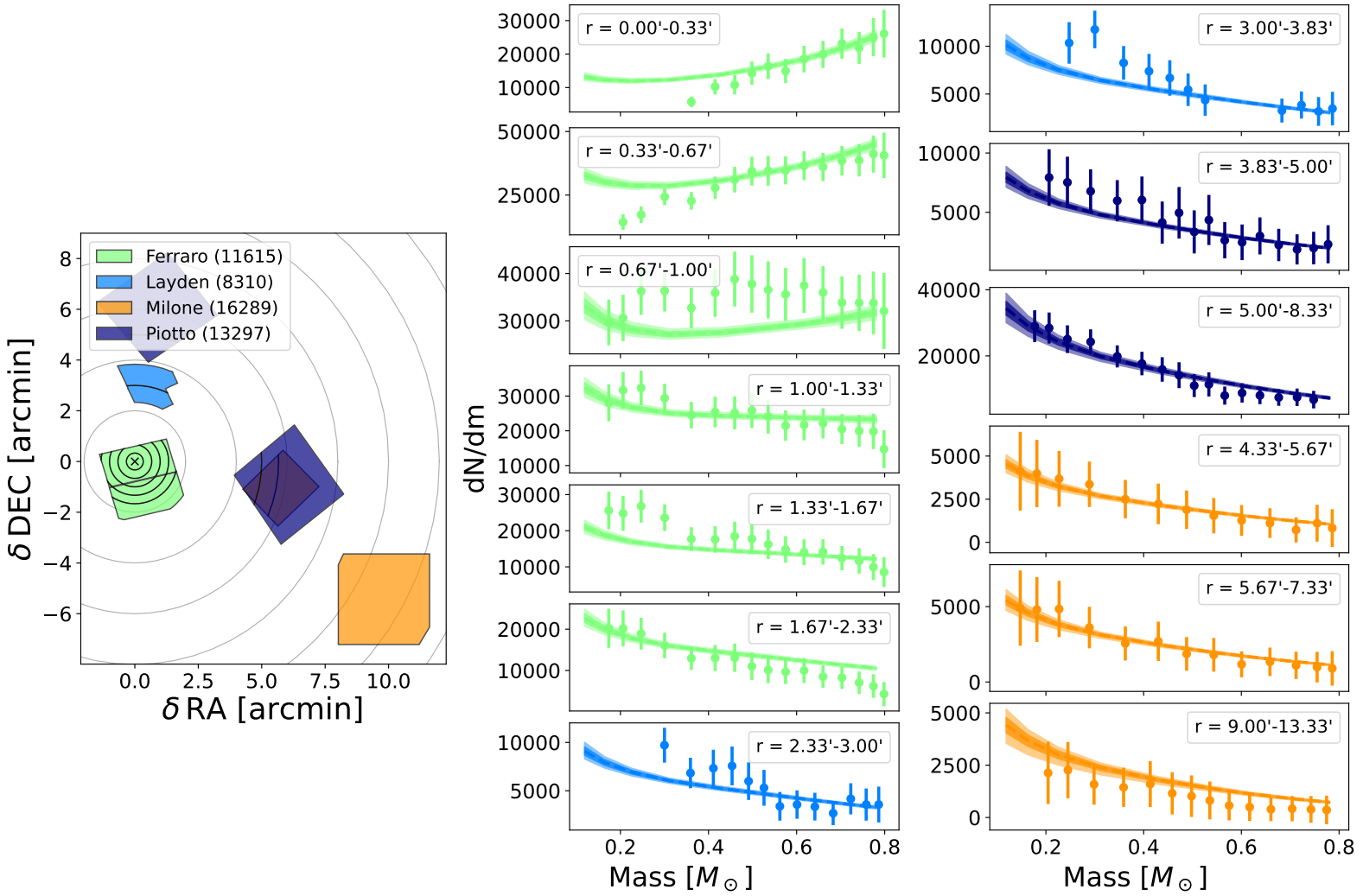

Figure A.22: Figure 5.3 repeated for NGC 5904

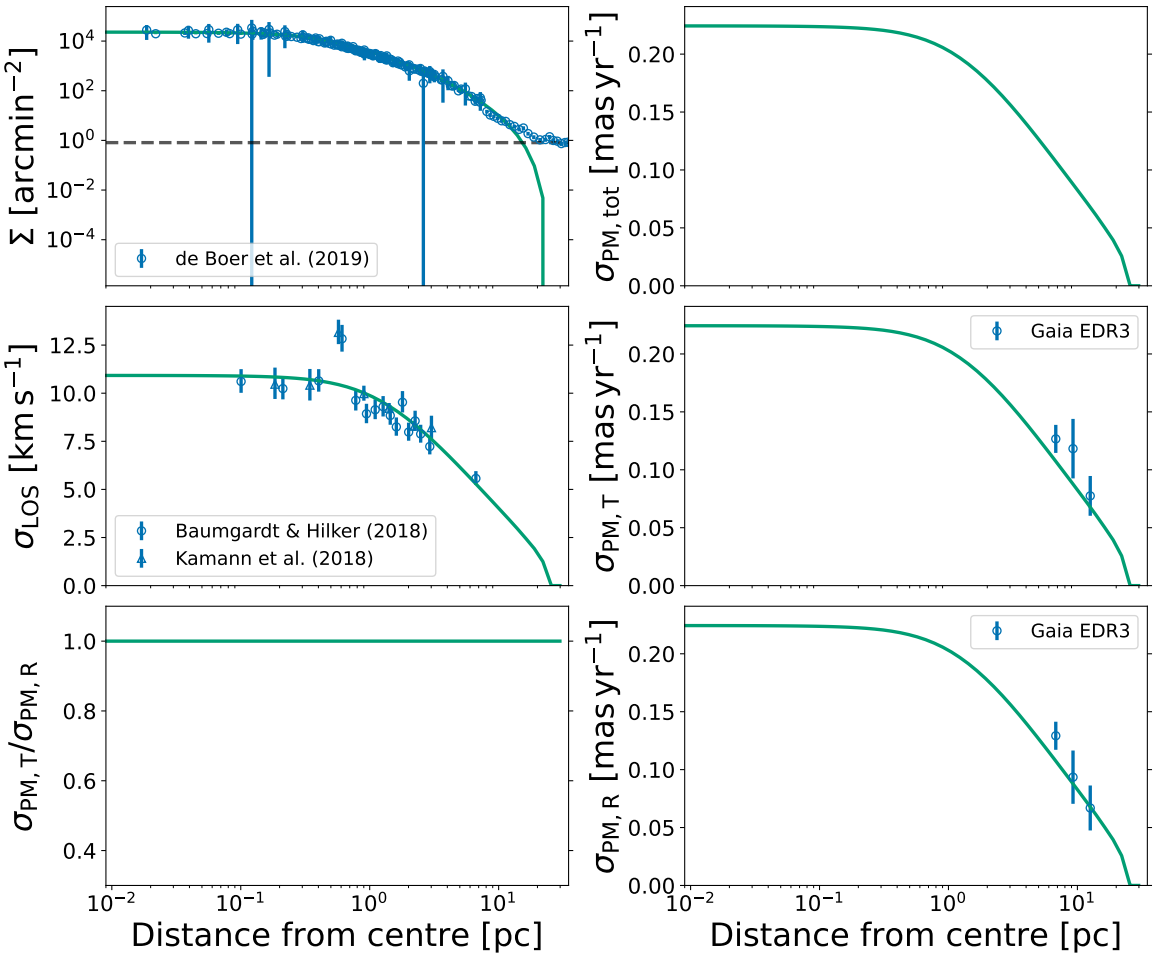

Figure A.23: Figure 5.2 repeated for NGC 6093

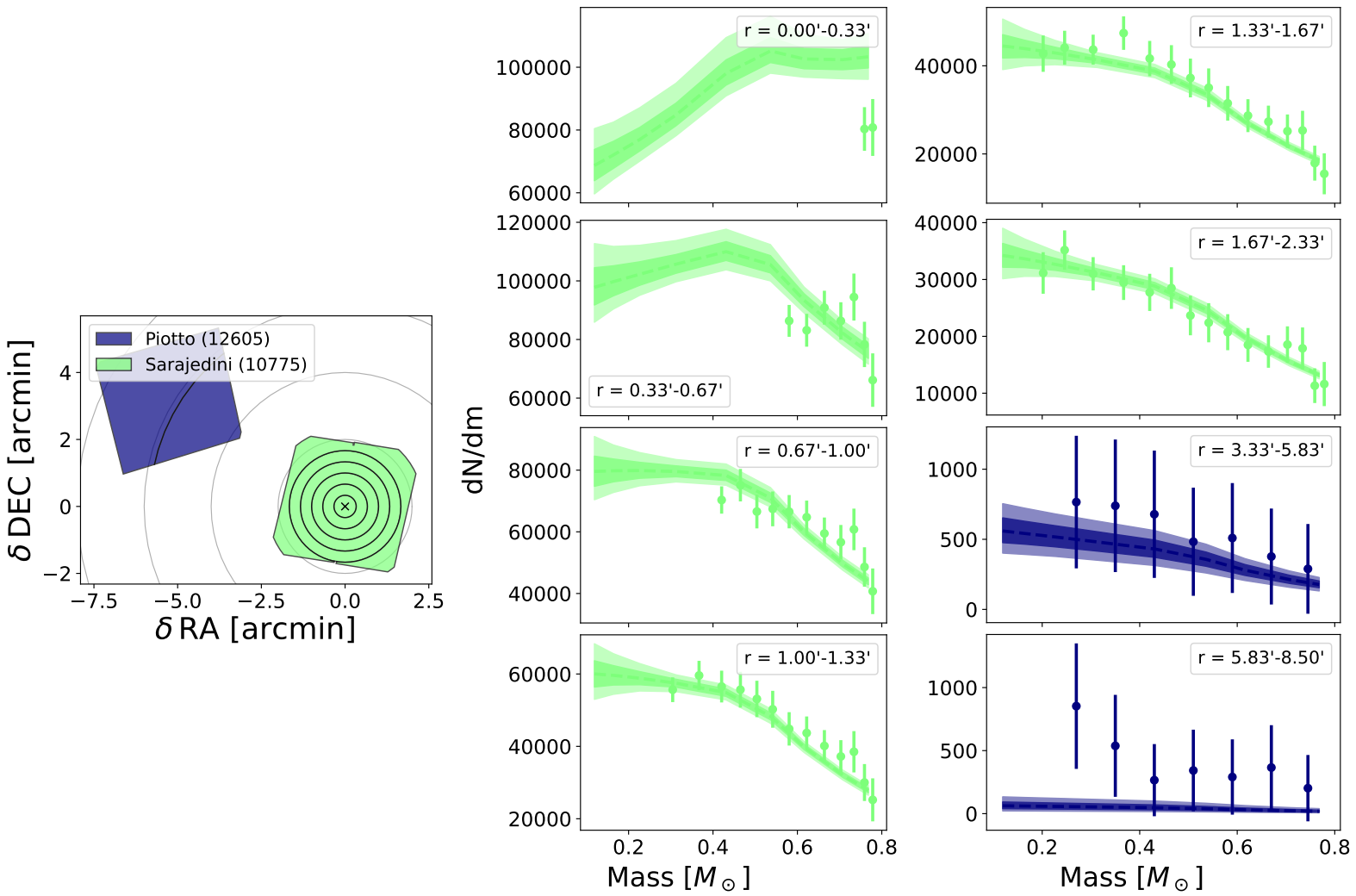

Figure A.24: Figure 5.3 repeated for NGC 6093

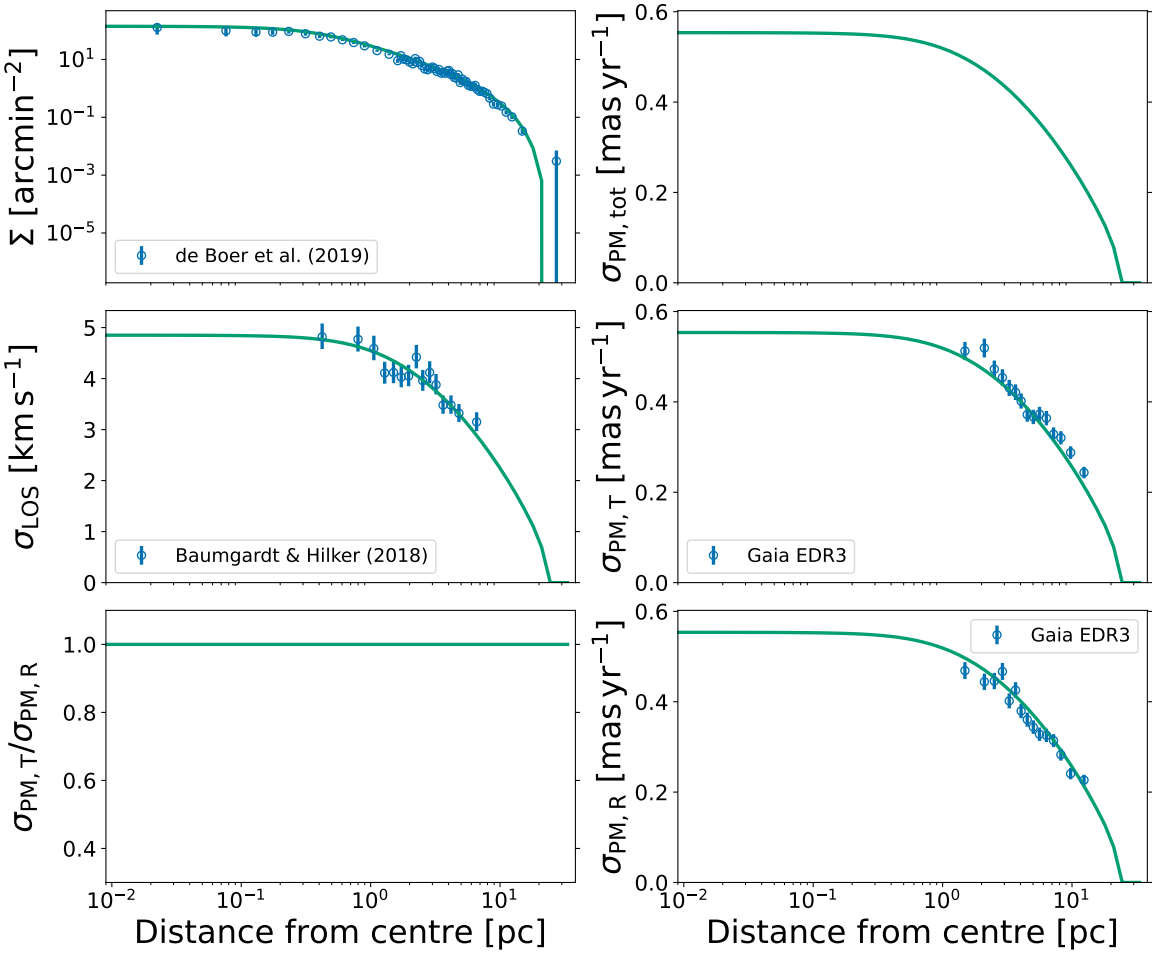

Figure A.25: Figure 5.2 repeated for NGC 6121

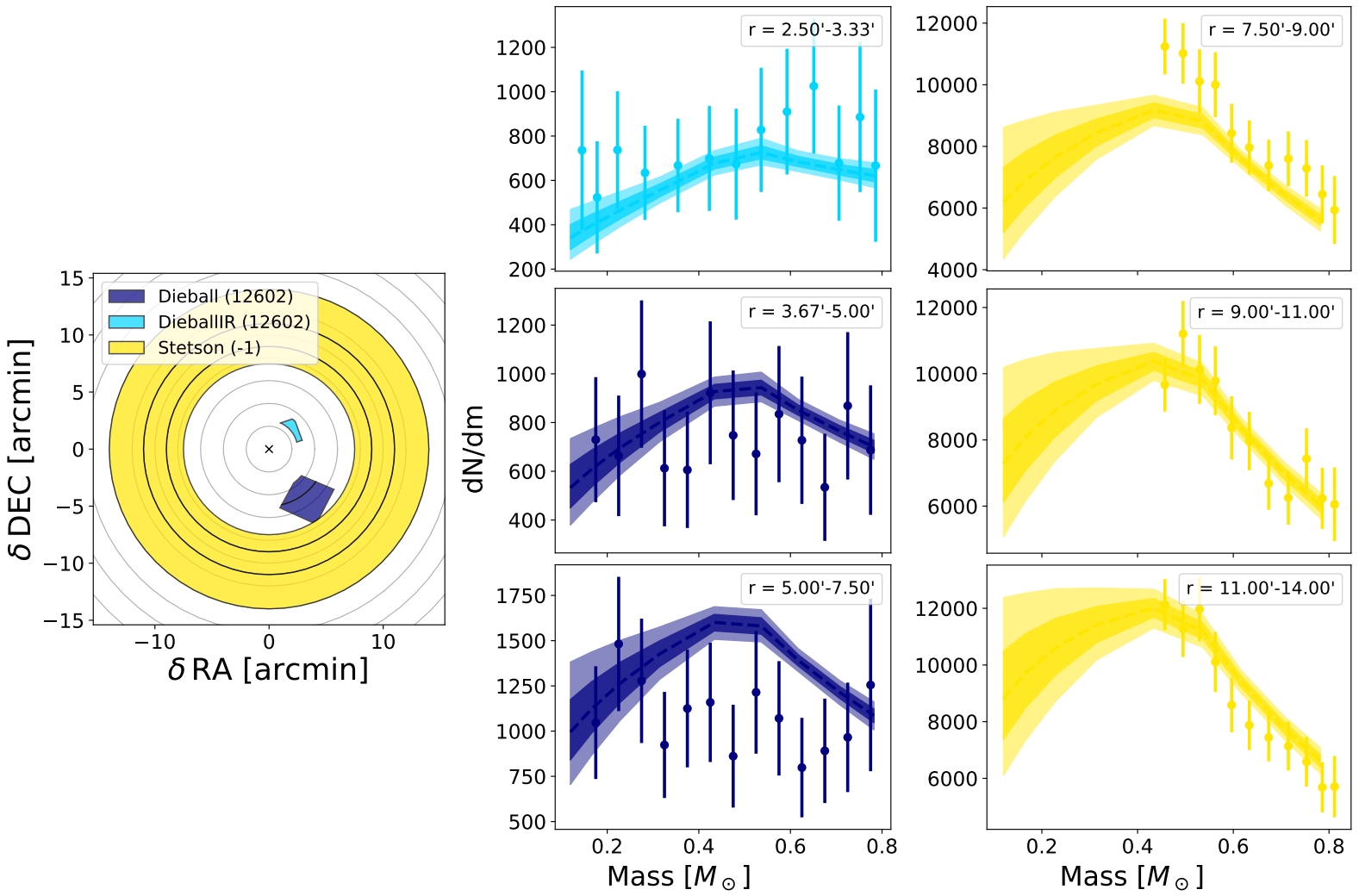

Figure A.26: Figure 5.3 repeated for NGC 6121

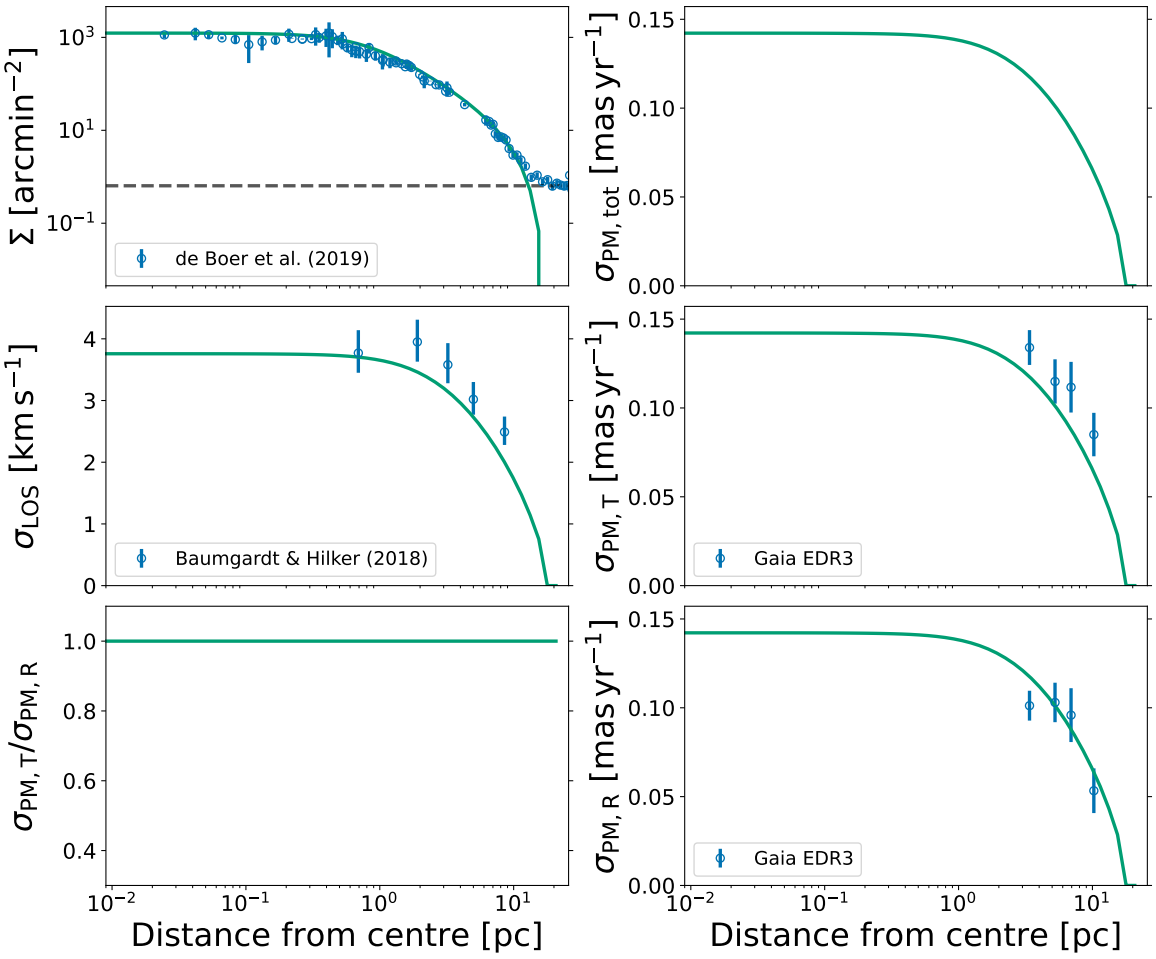

Figure A.27: Figure 5.2 repeated for NGC 6171

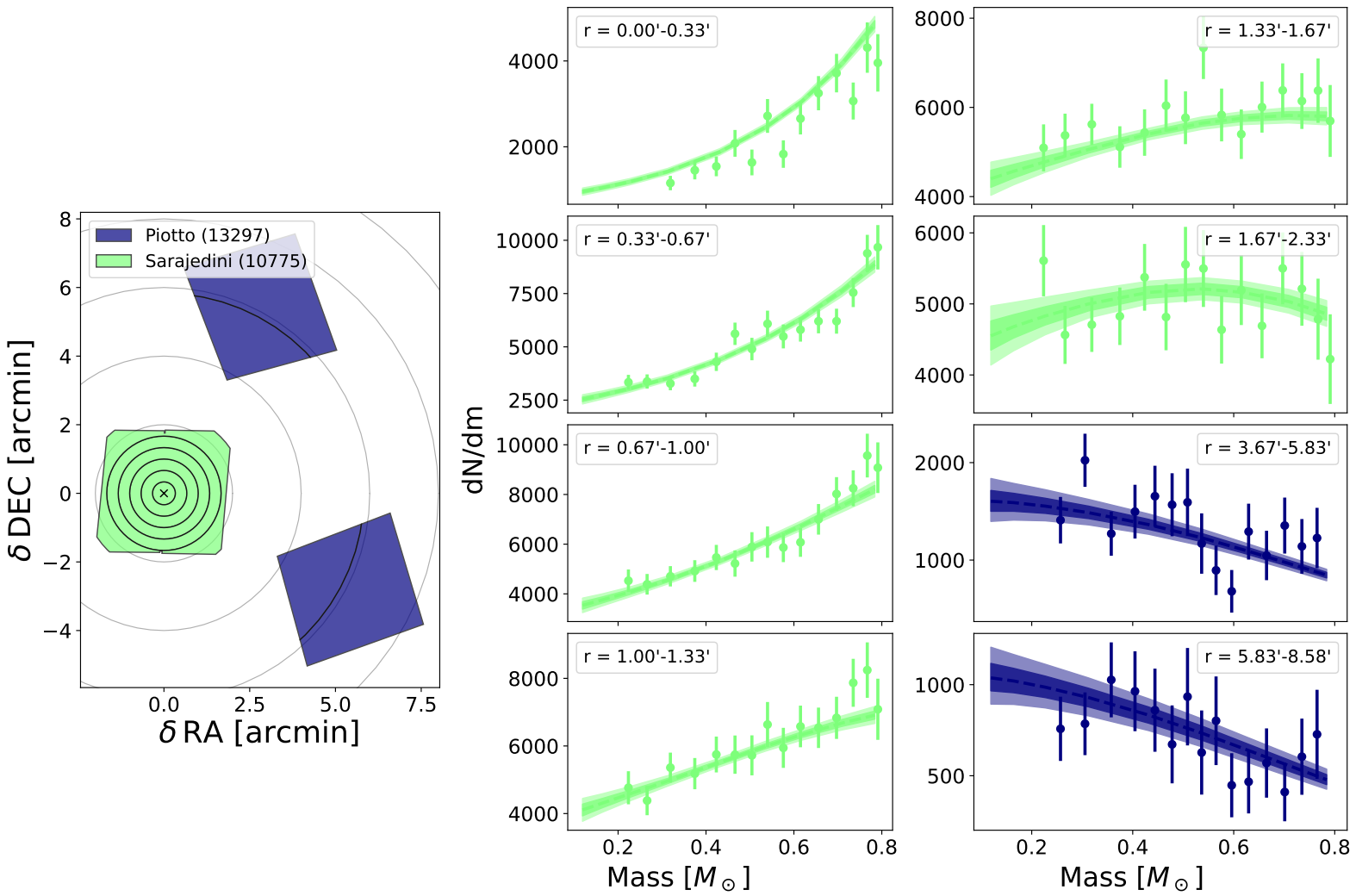

Figure A.28: Figure 5.3 repeated for NGC 6171

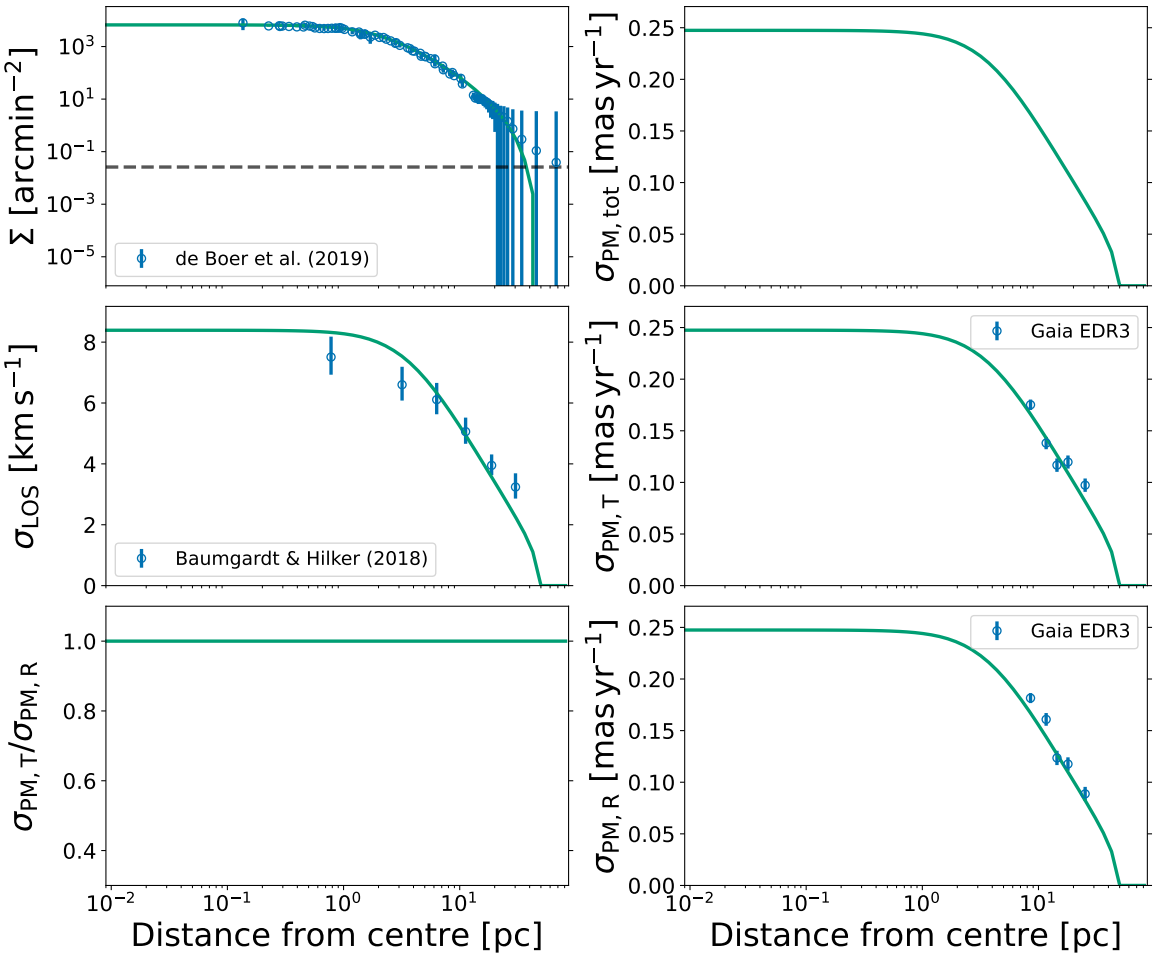

Figure A.29: Figure 5.2 repeated for NGC 6205

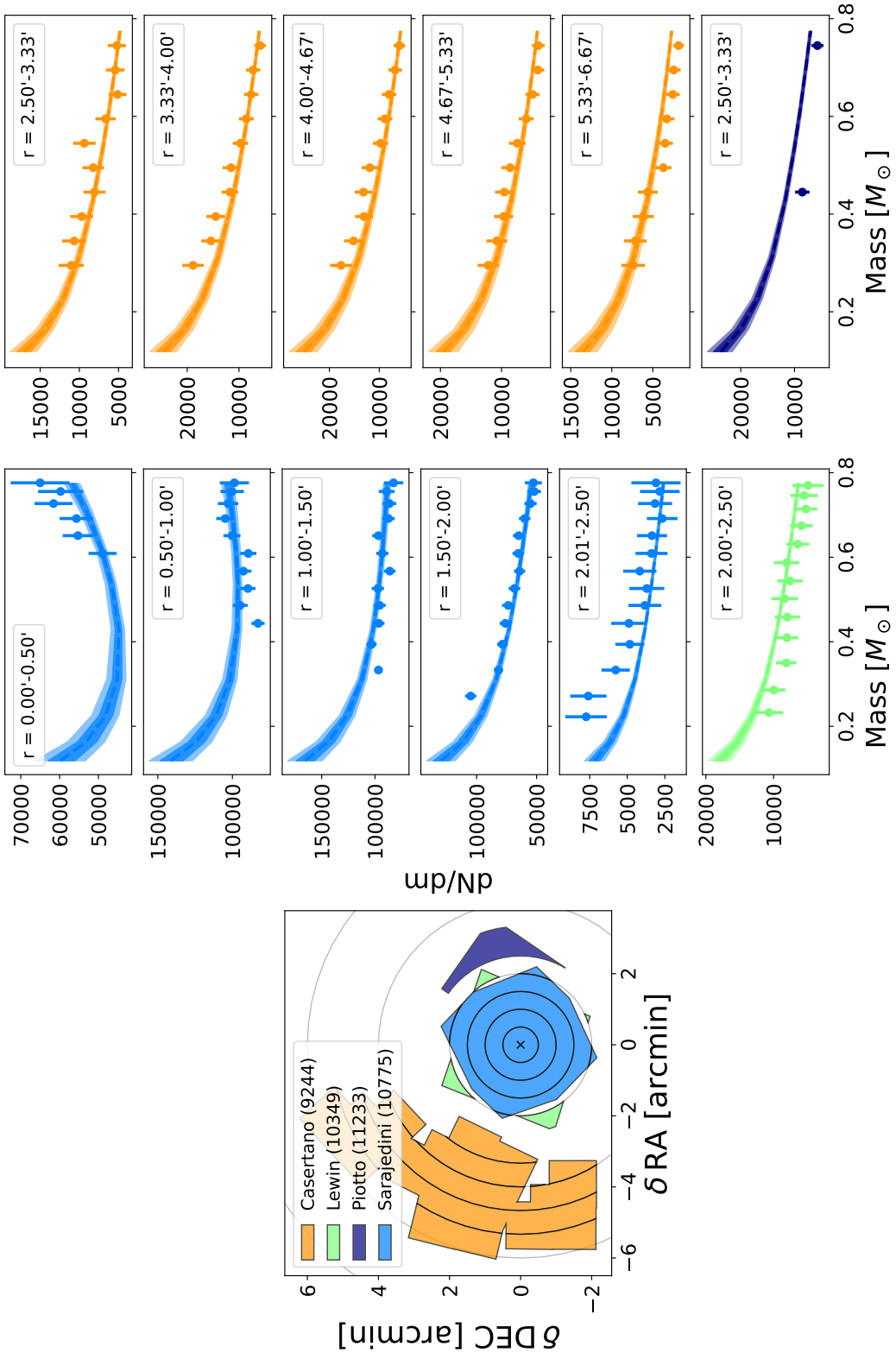

Figure A.30: Figure 5.3 repeated for NGC 6205

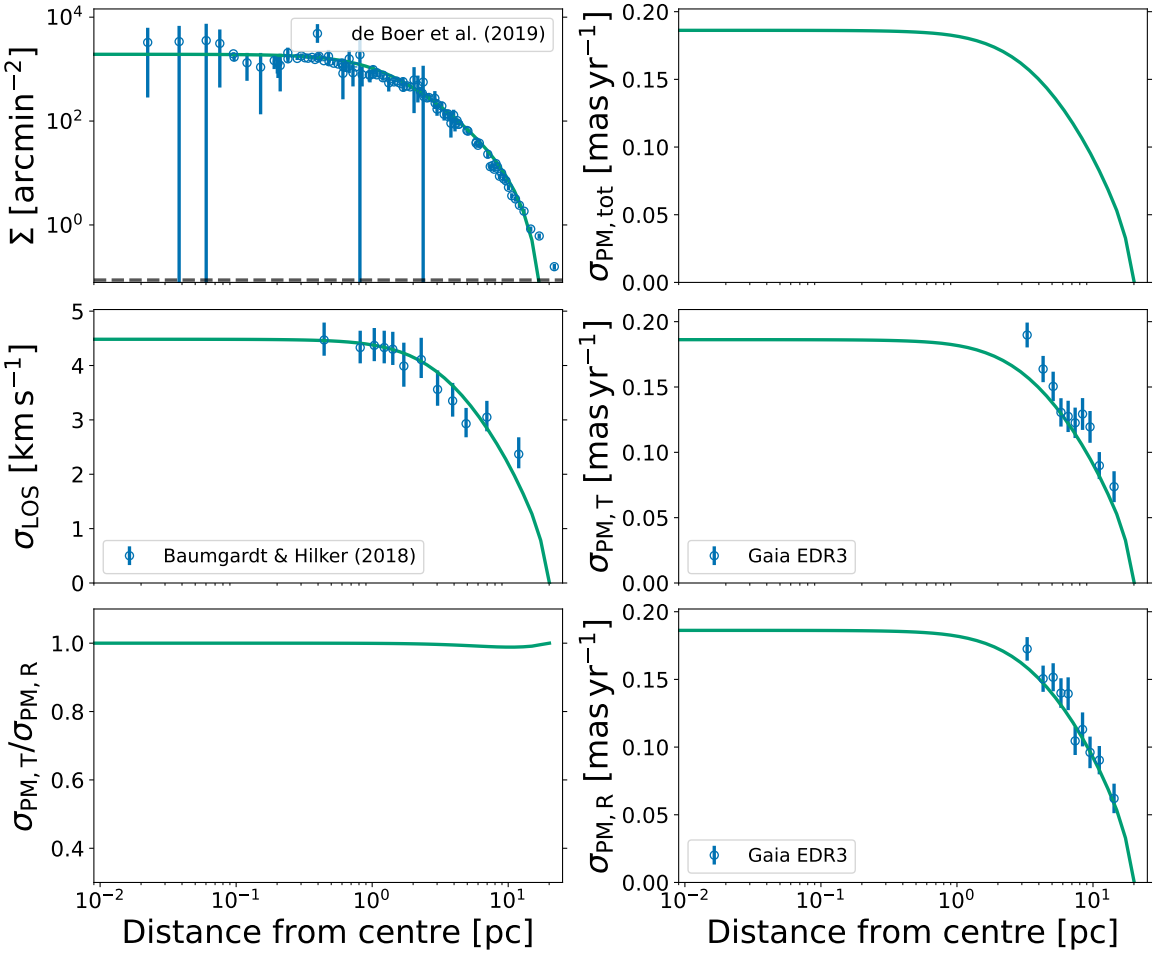

Figure A.31: Figure 5.2 repeated for NGC 6218

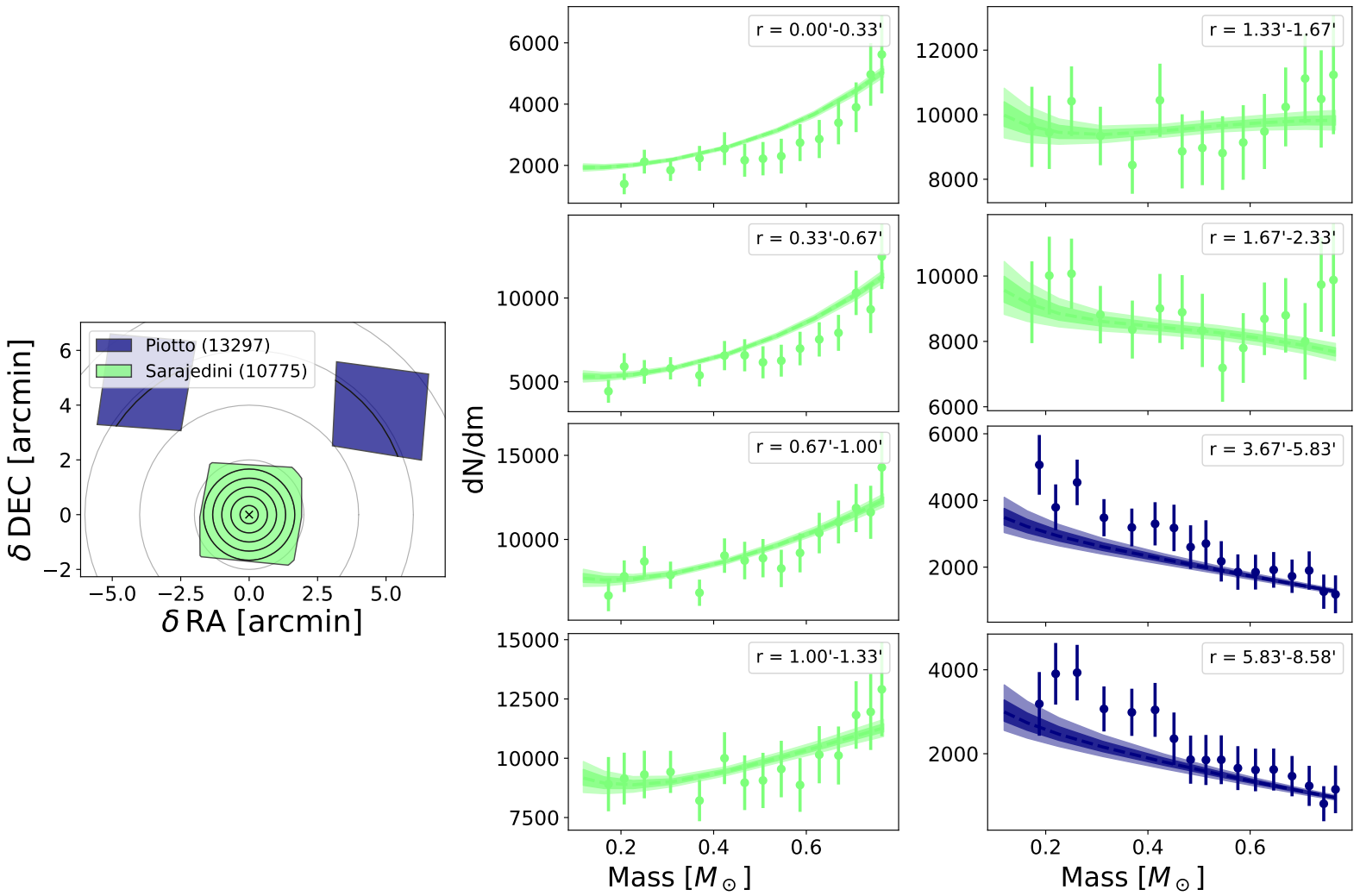

Figure A.32: Figure 5.3 repeated for NGC 6218

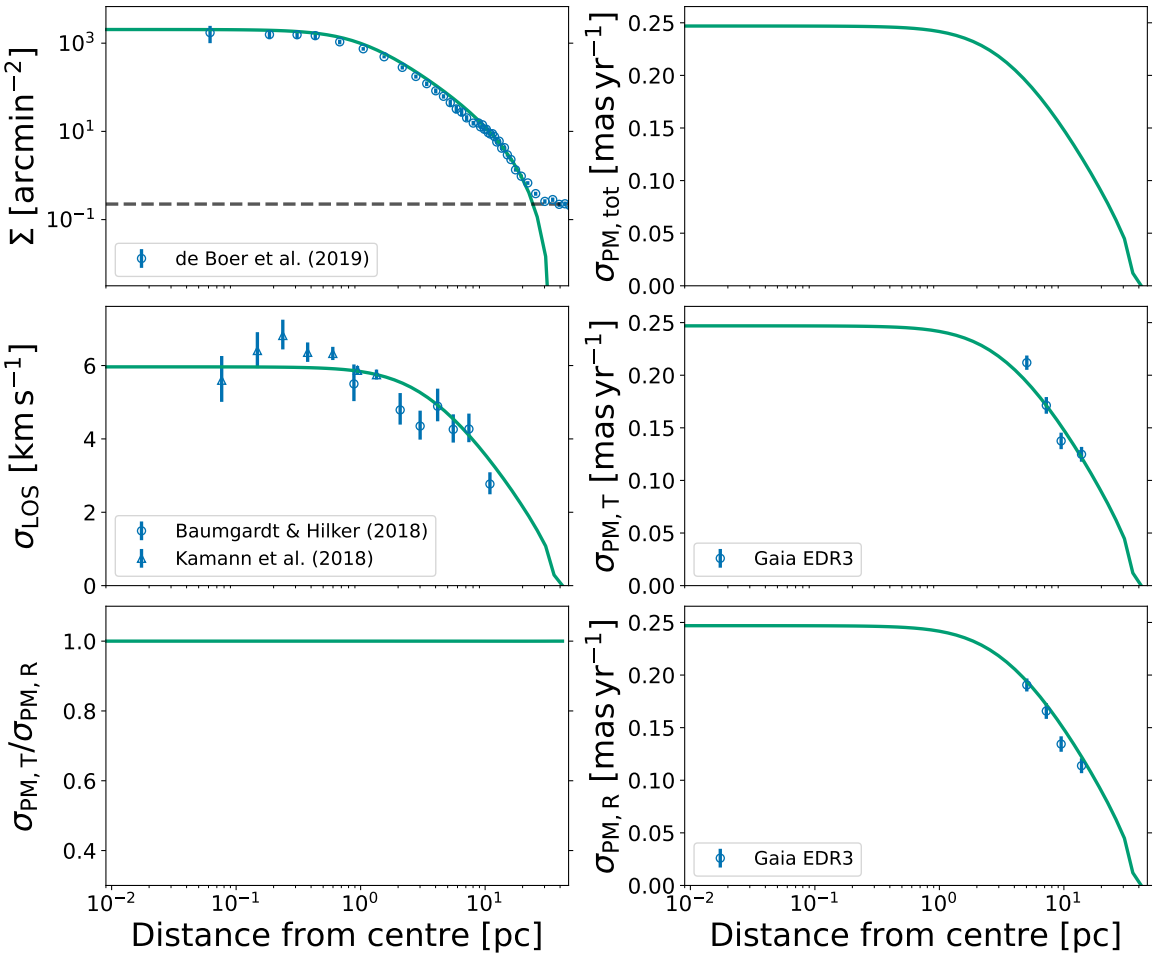

Figure A.33: Figure 5.2 repeated for NGC 6254

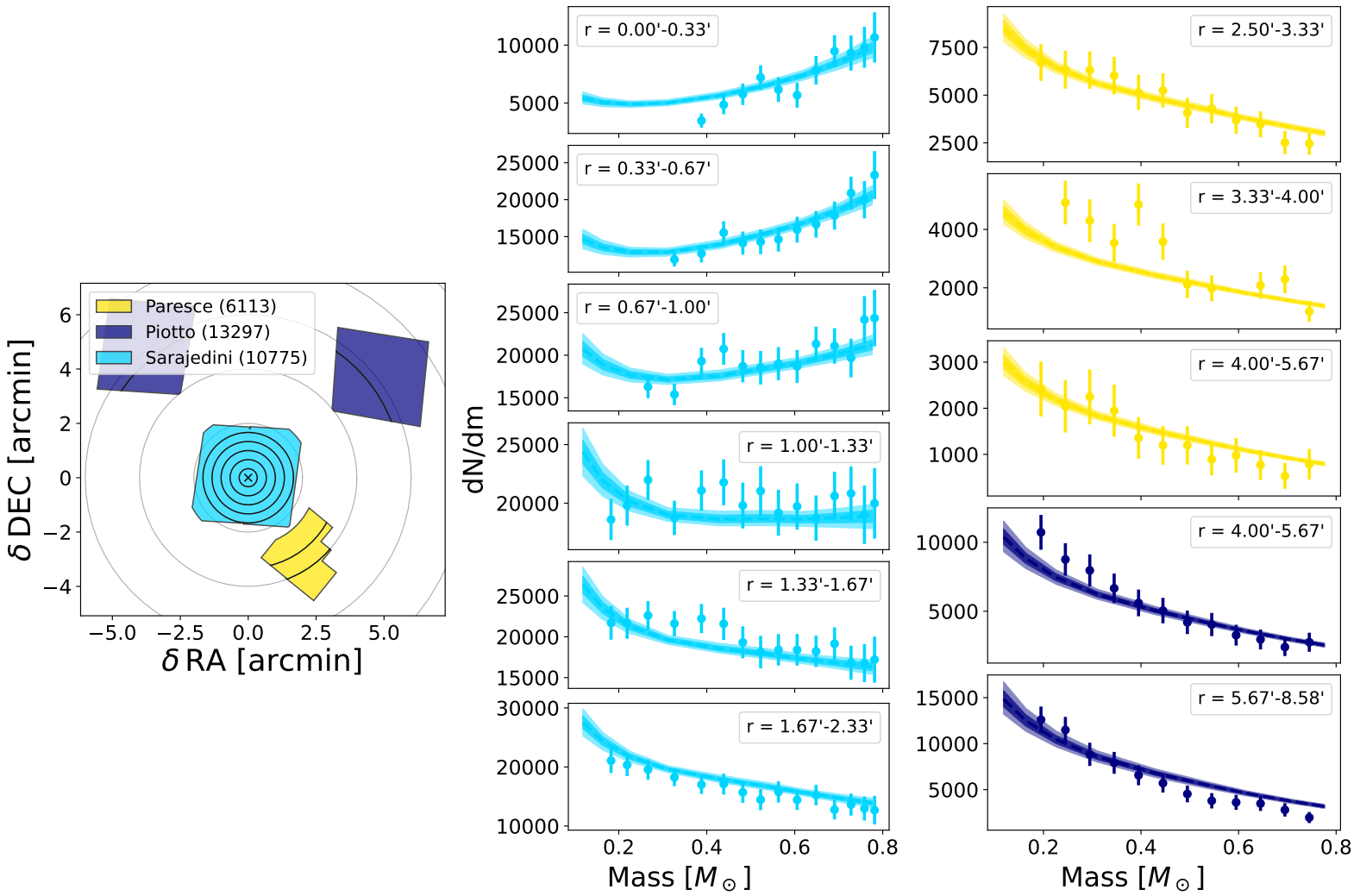

Figure A.34: Figure 5.3 repeated for NGC 6254

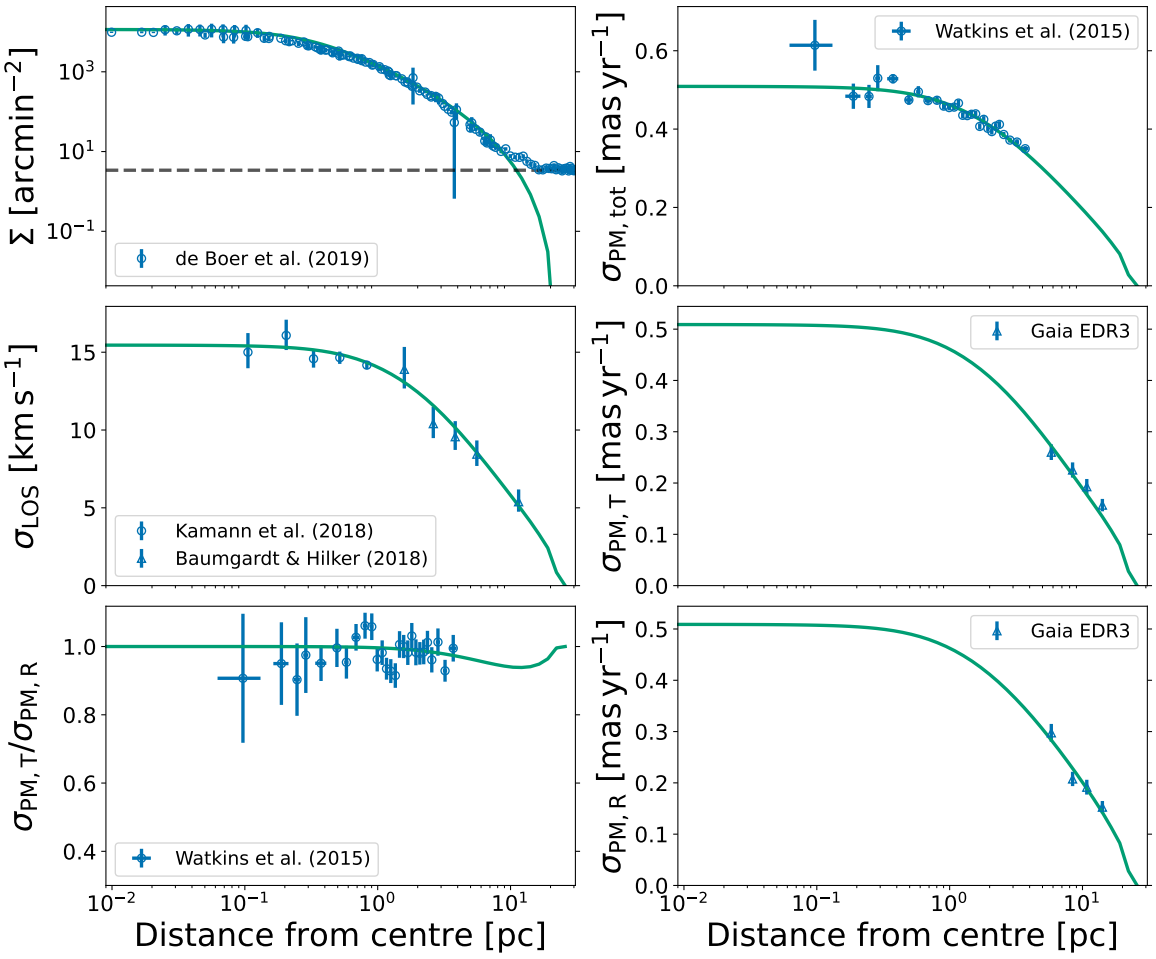

Figure A.35: Figure 5.2 repeated for NGC 6266

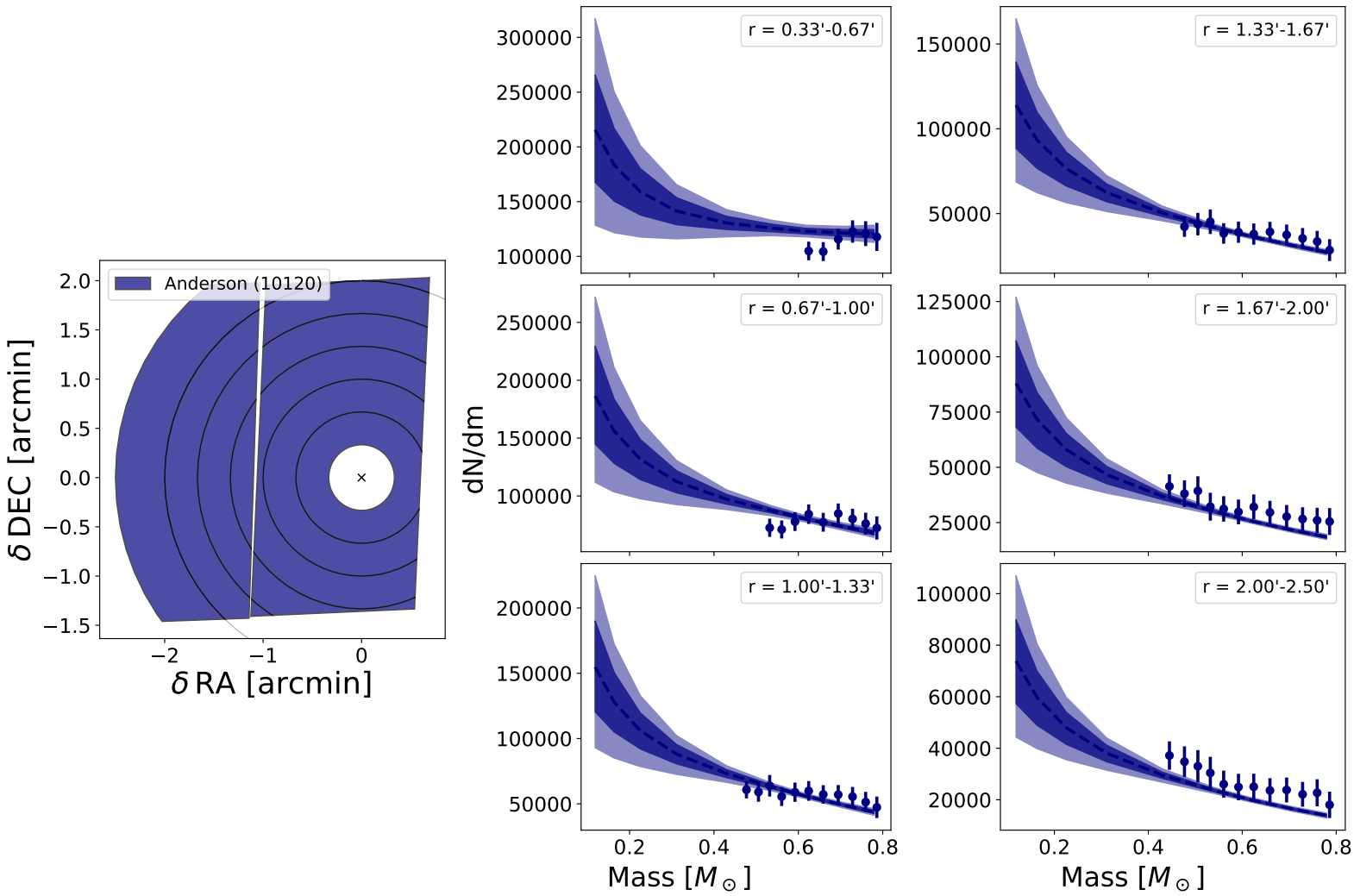

Figure A.36: Figure 5.3 repeated for NGC 6266

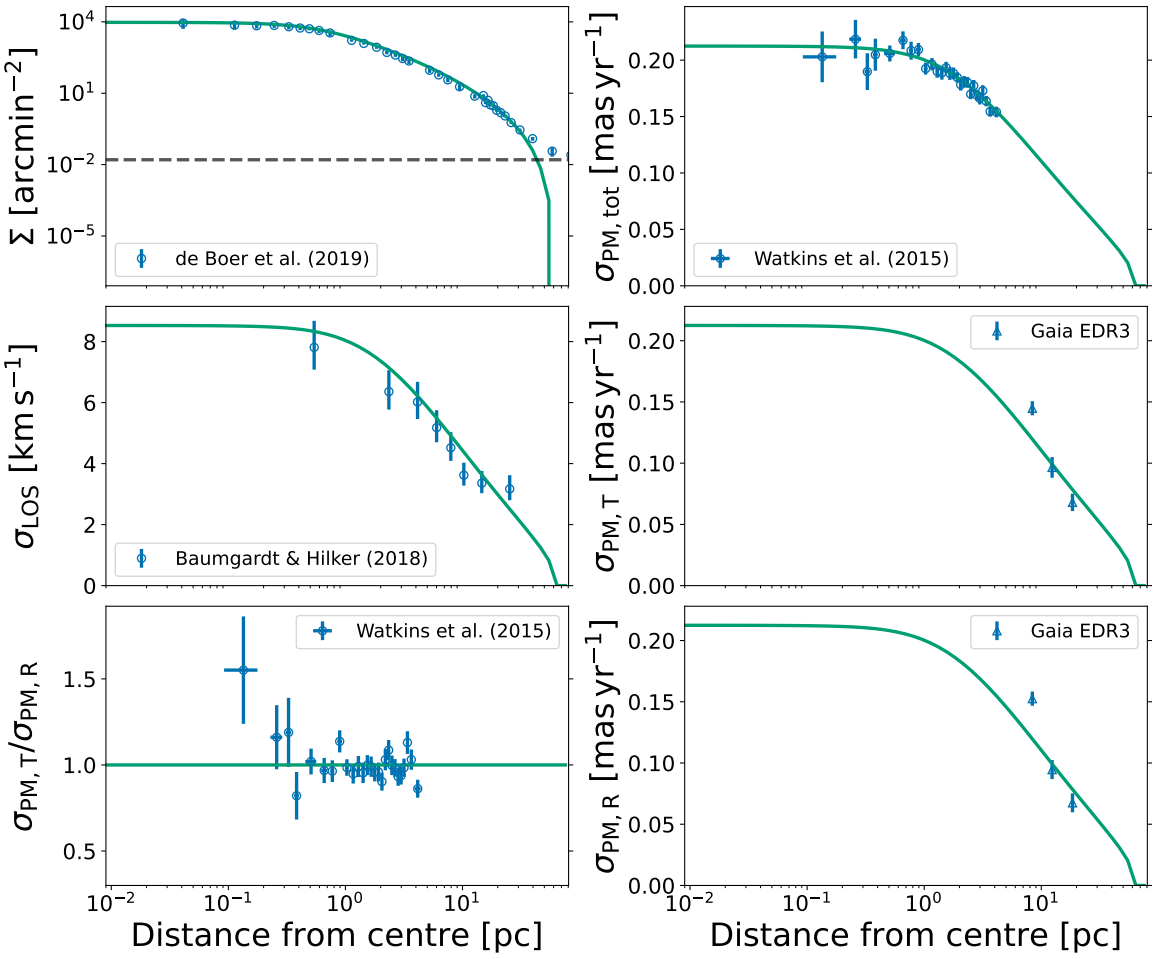

Figure A.37: Figure 5.2 repeated for NGC 6341

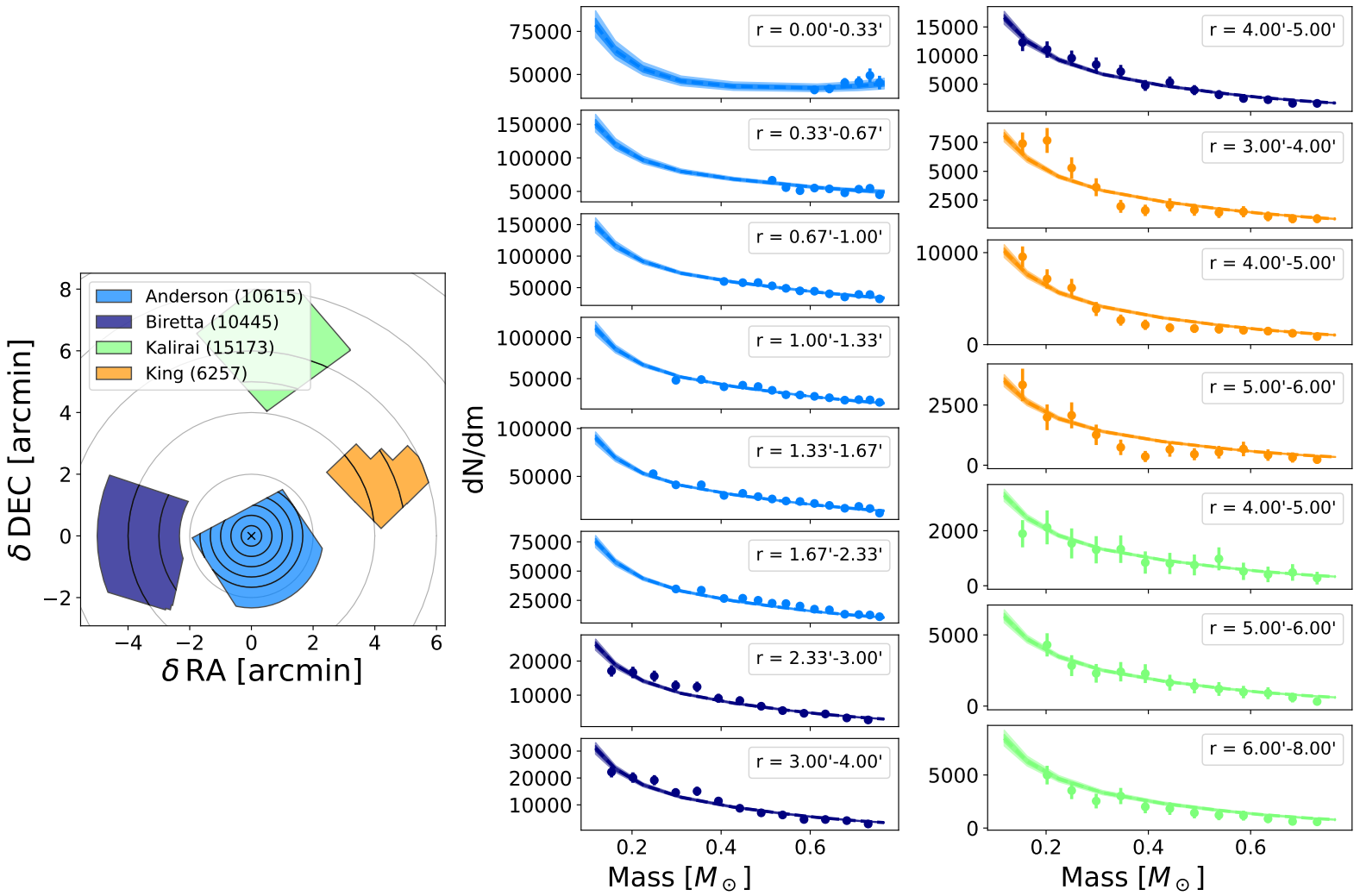

Figure A.38: Figure 5.3 repeated for NGC 6341

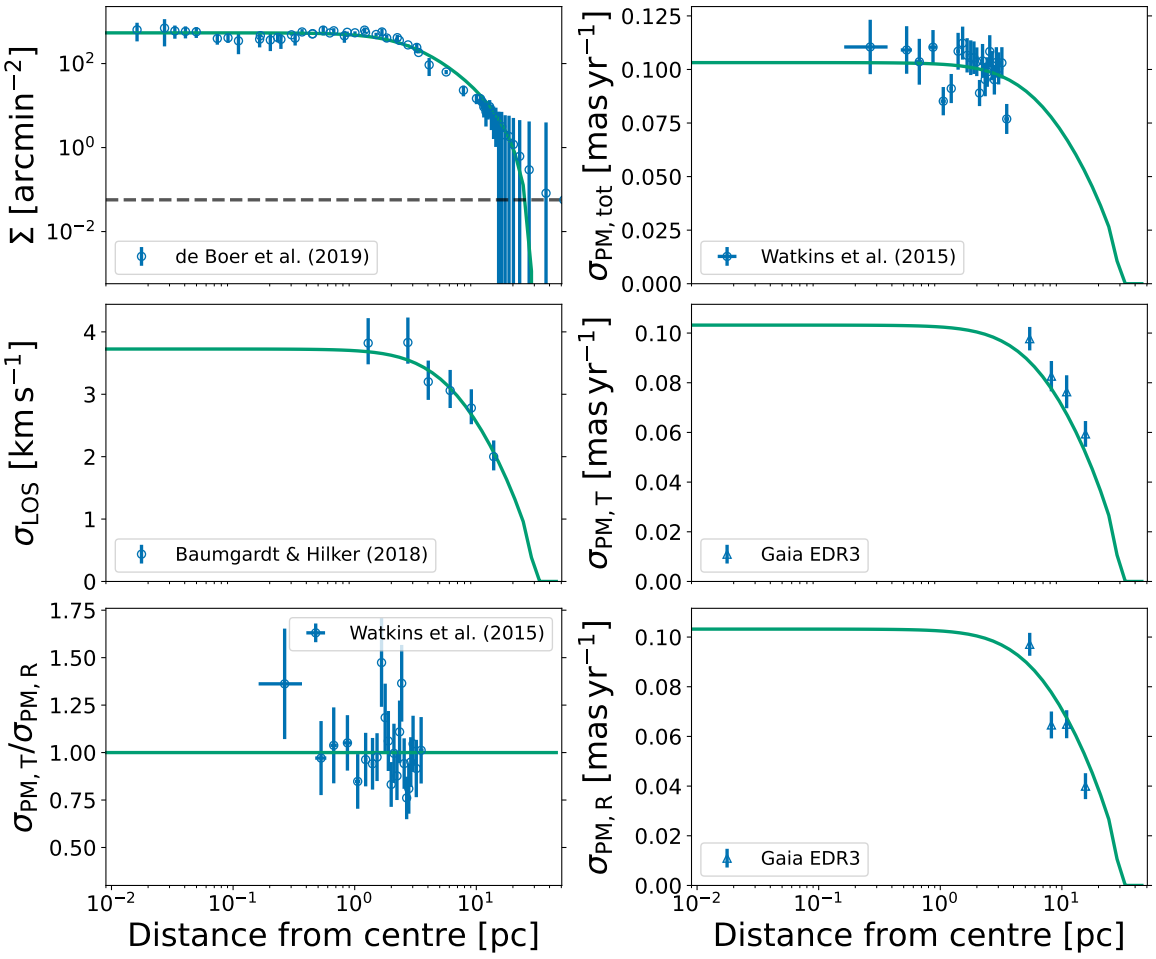

Figure A.39: Figure 5.2 repeated for NGC 6362

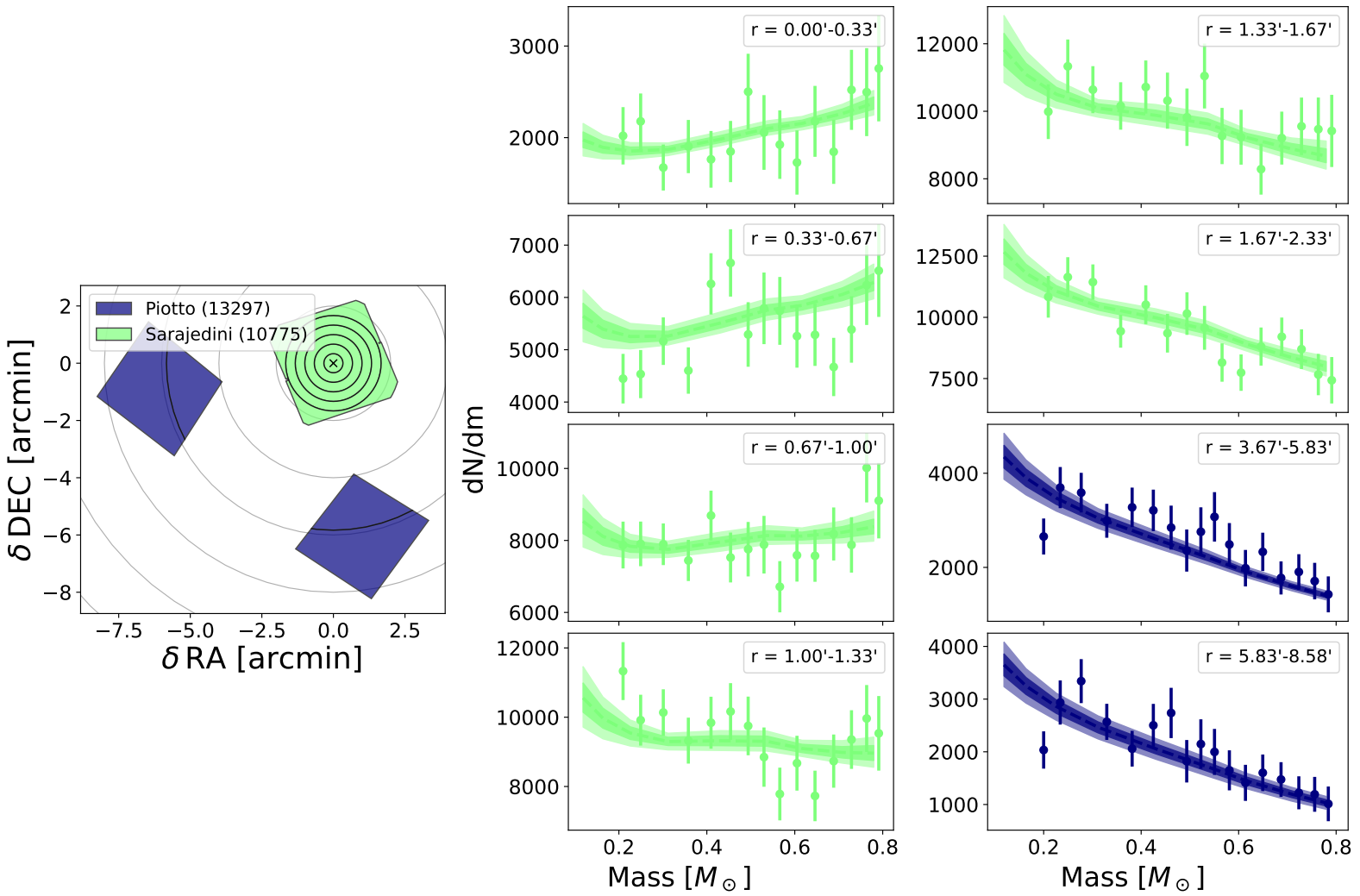

Figure A.40: Figure 5.3 repeated for NGC 6362

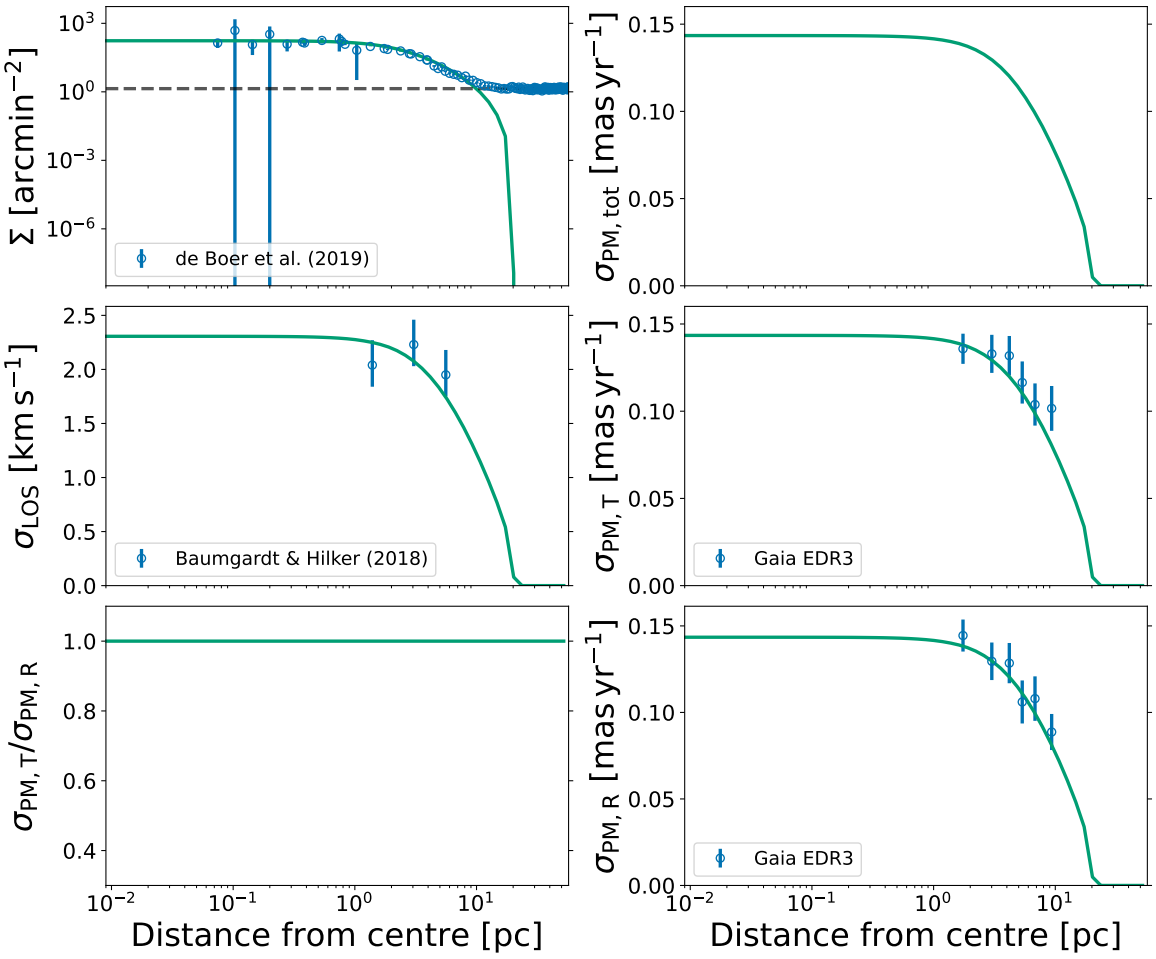

Figure A.41: Figure 5.2 repeated for NGC 6366

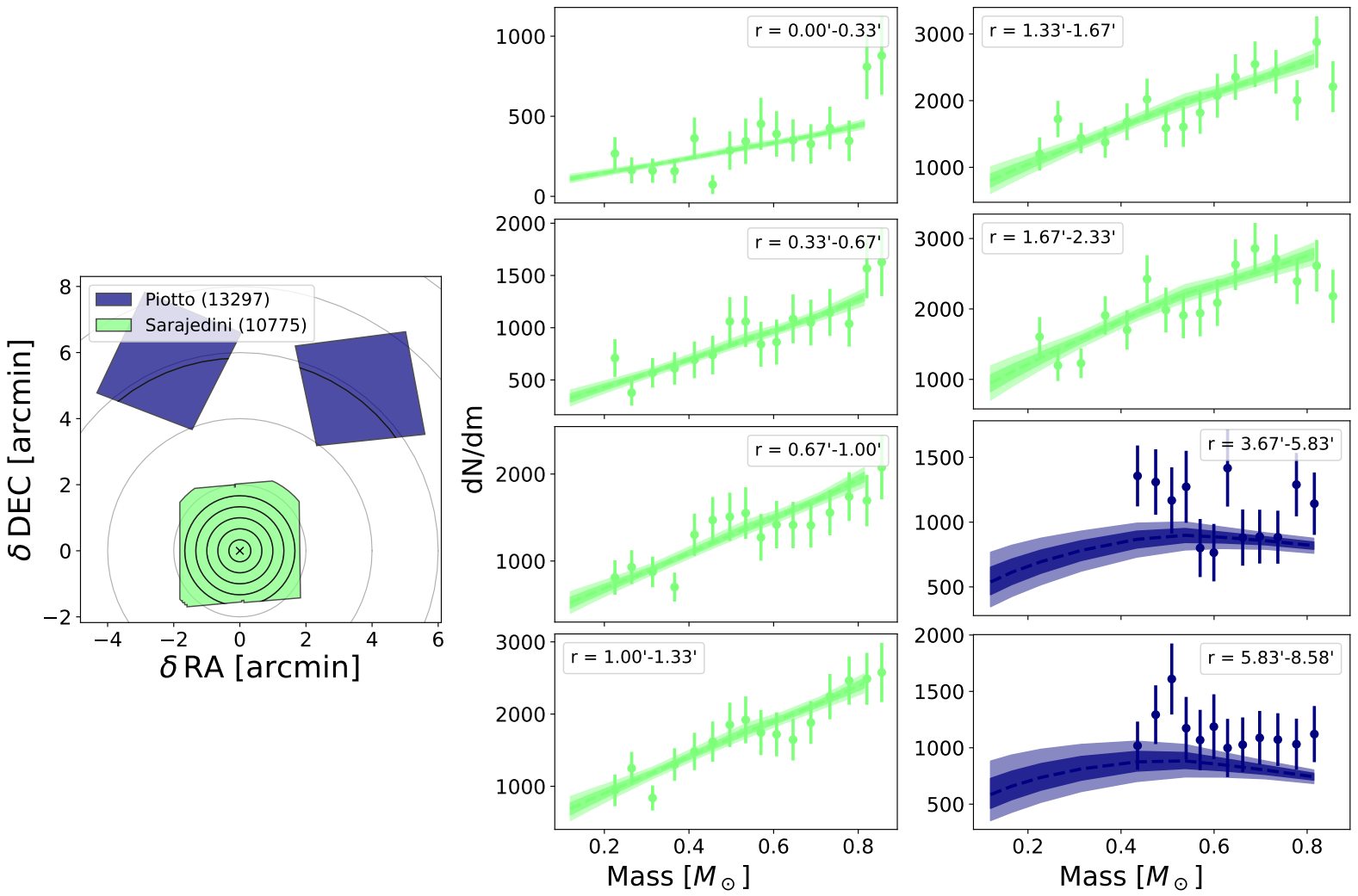

Figure A.42: Figure 5.3 repeated for NGC 6366

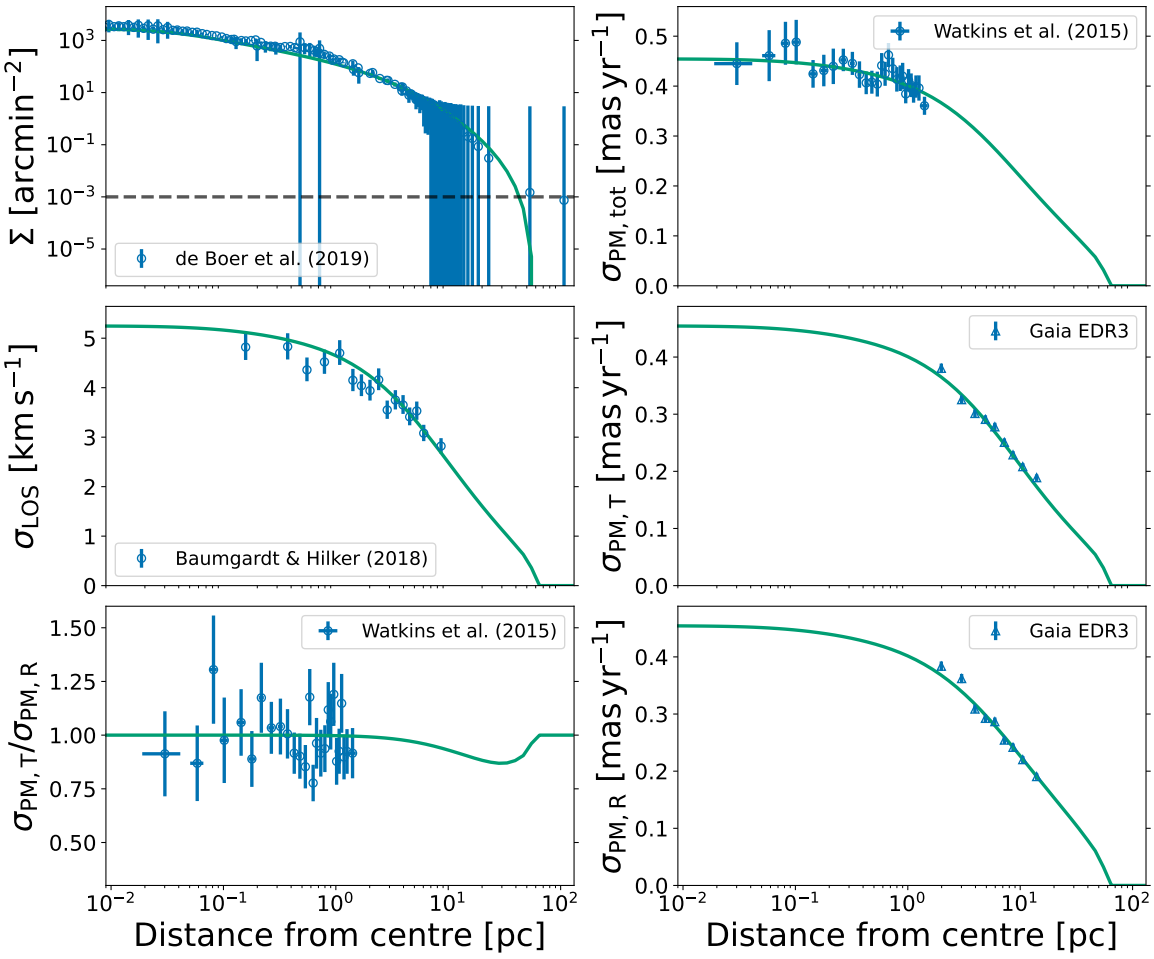

Figure A.43: Figure 5.2 repeated for NGC 6397

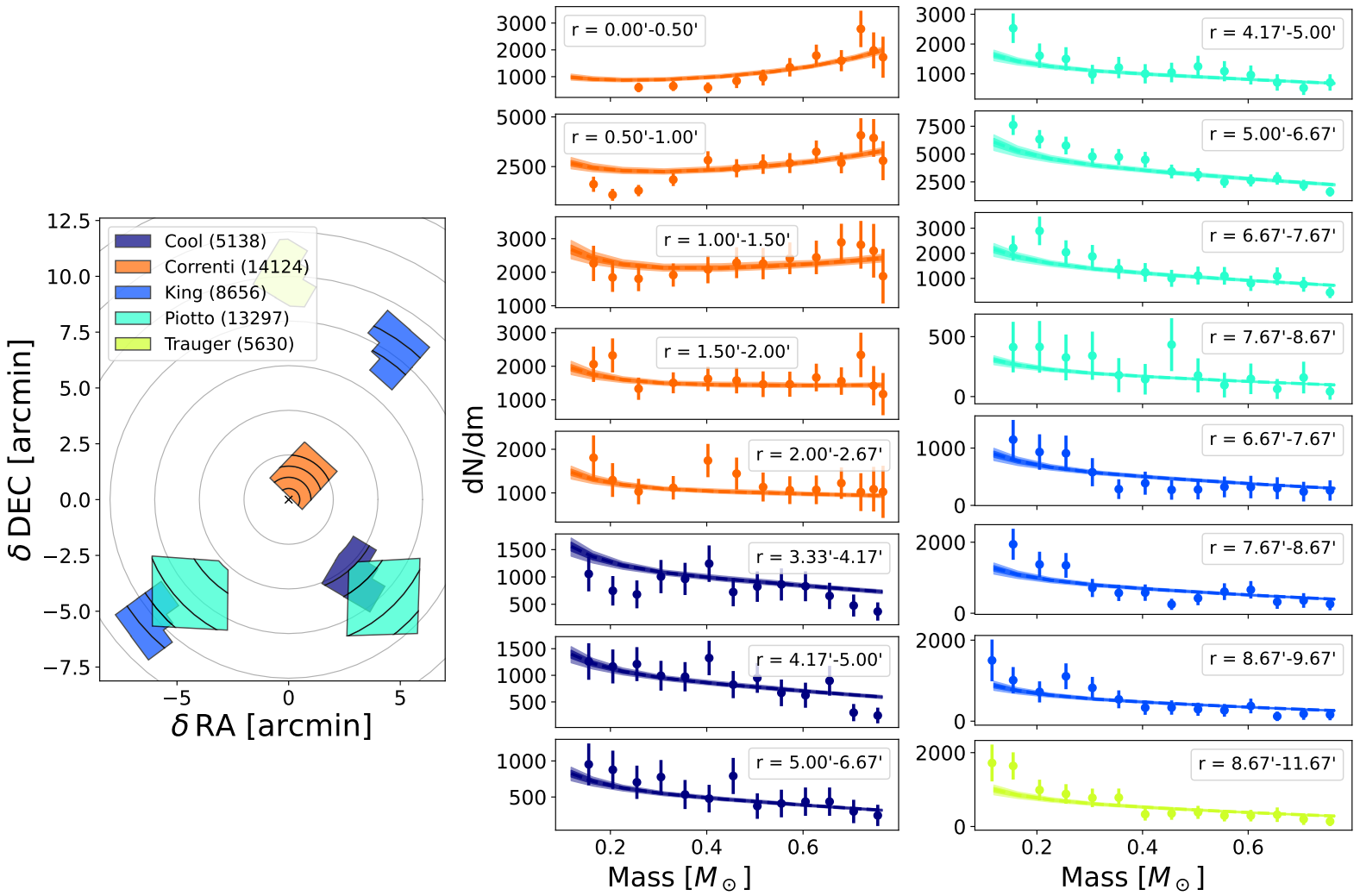

Figure A.44: Figure 5.3 repeated for NGC 6397

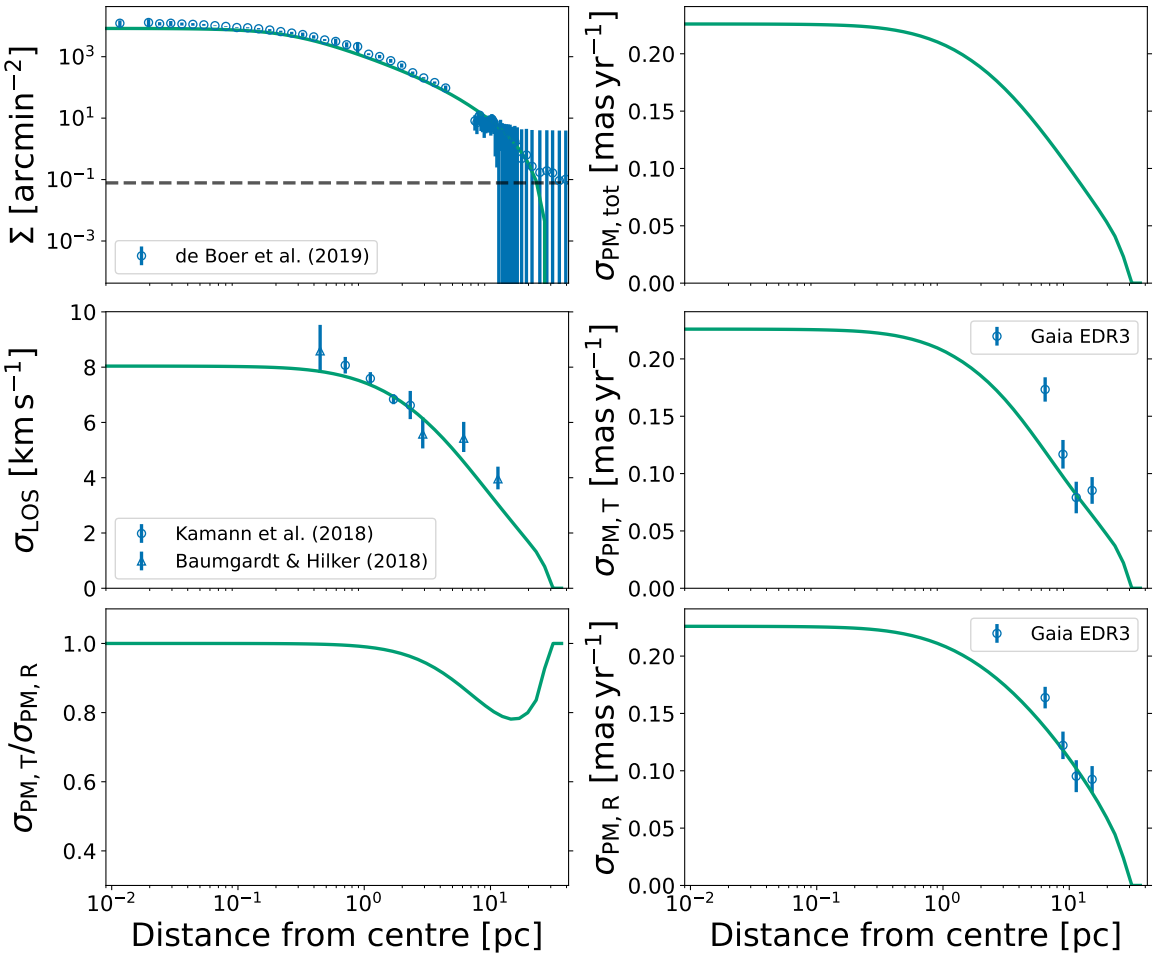

Figure A.45: Figure 5.2 repeated for NGC 6541

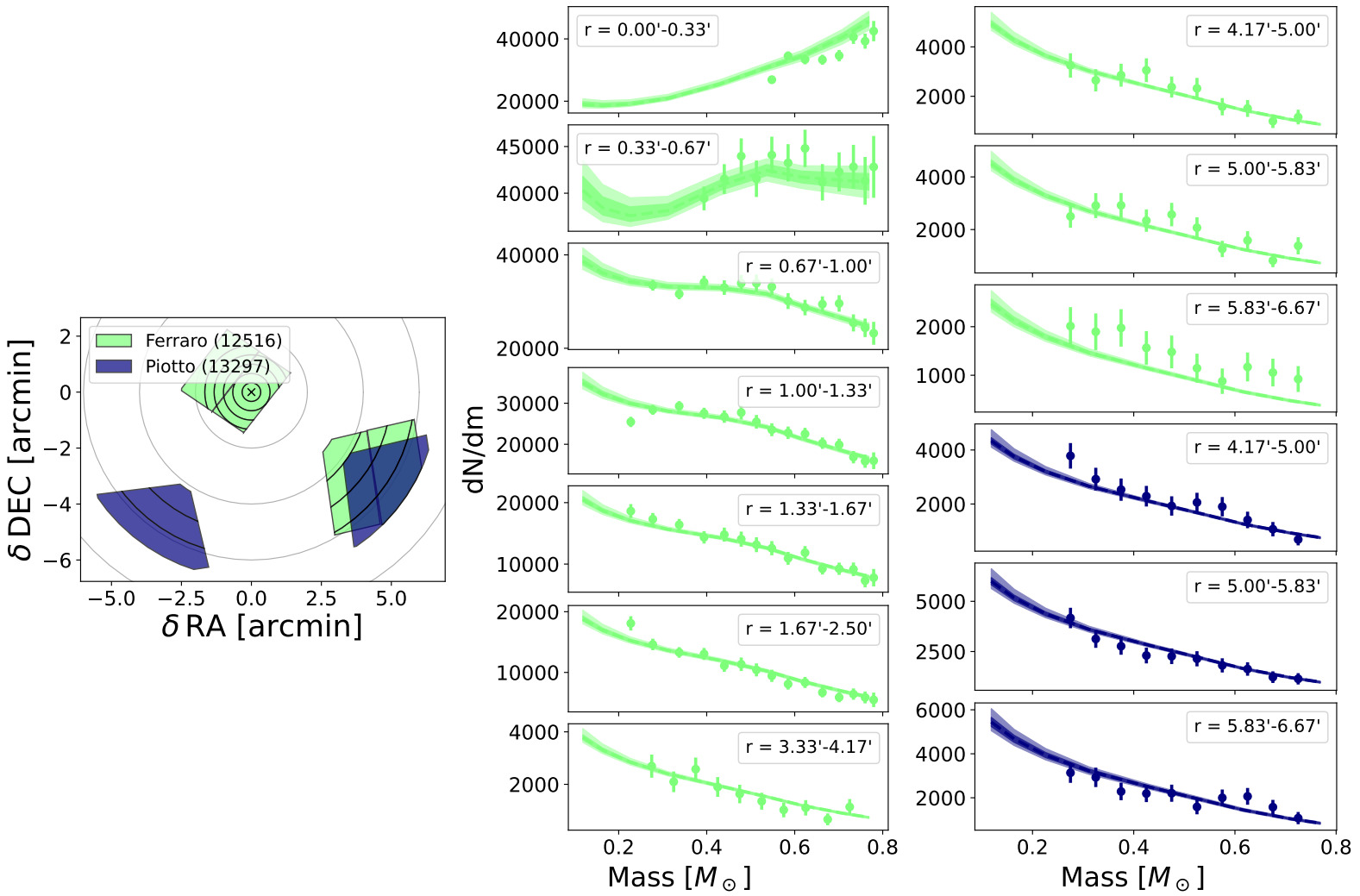

Figure A.46: Figure 5.3 repeated for NGC 6541

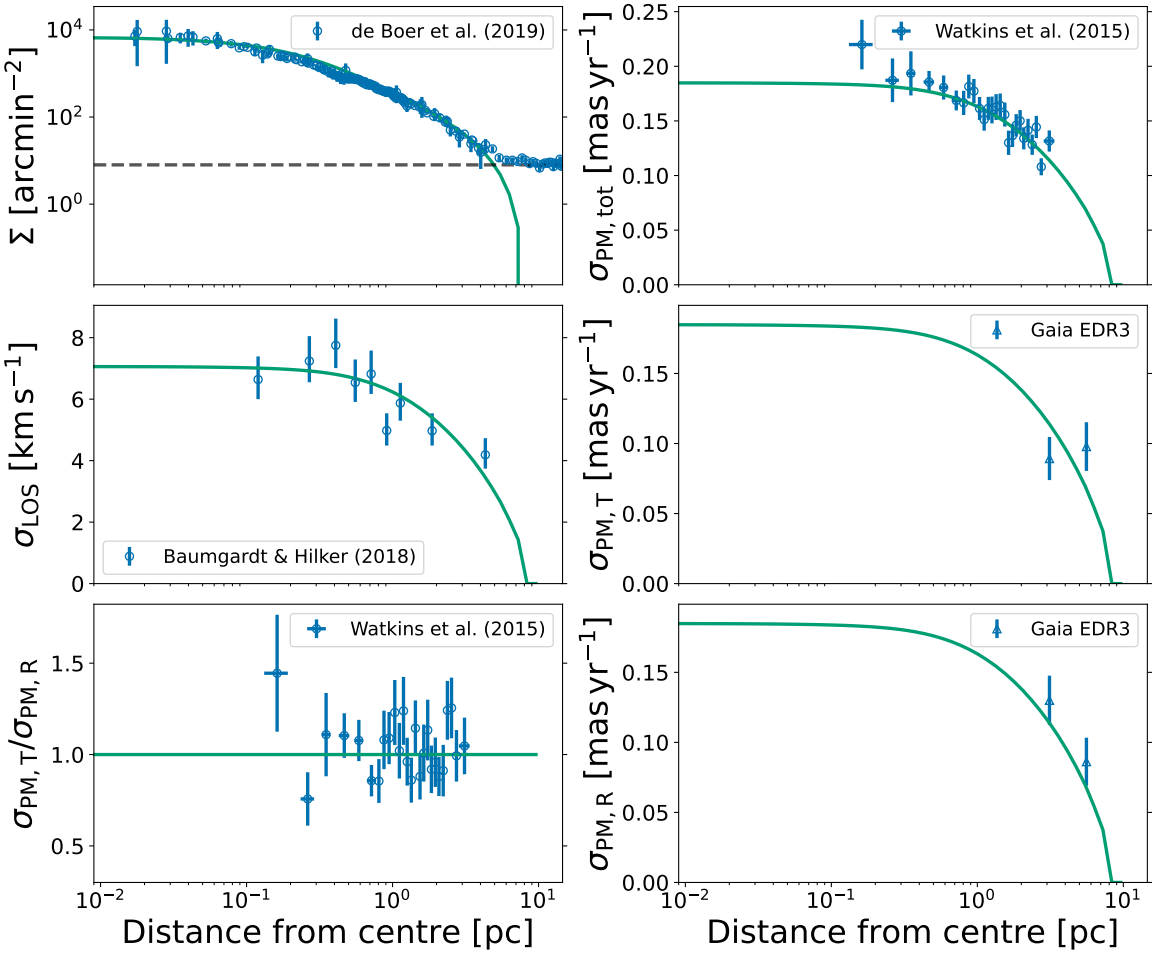

Figure A.47: Figure 5.2 repeated for NGC 6624

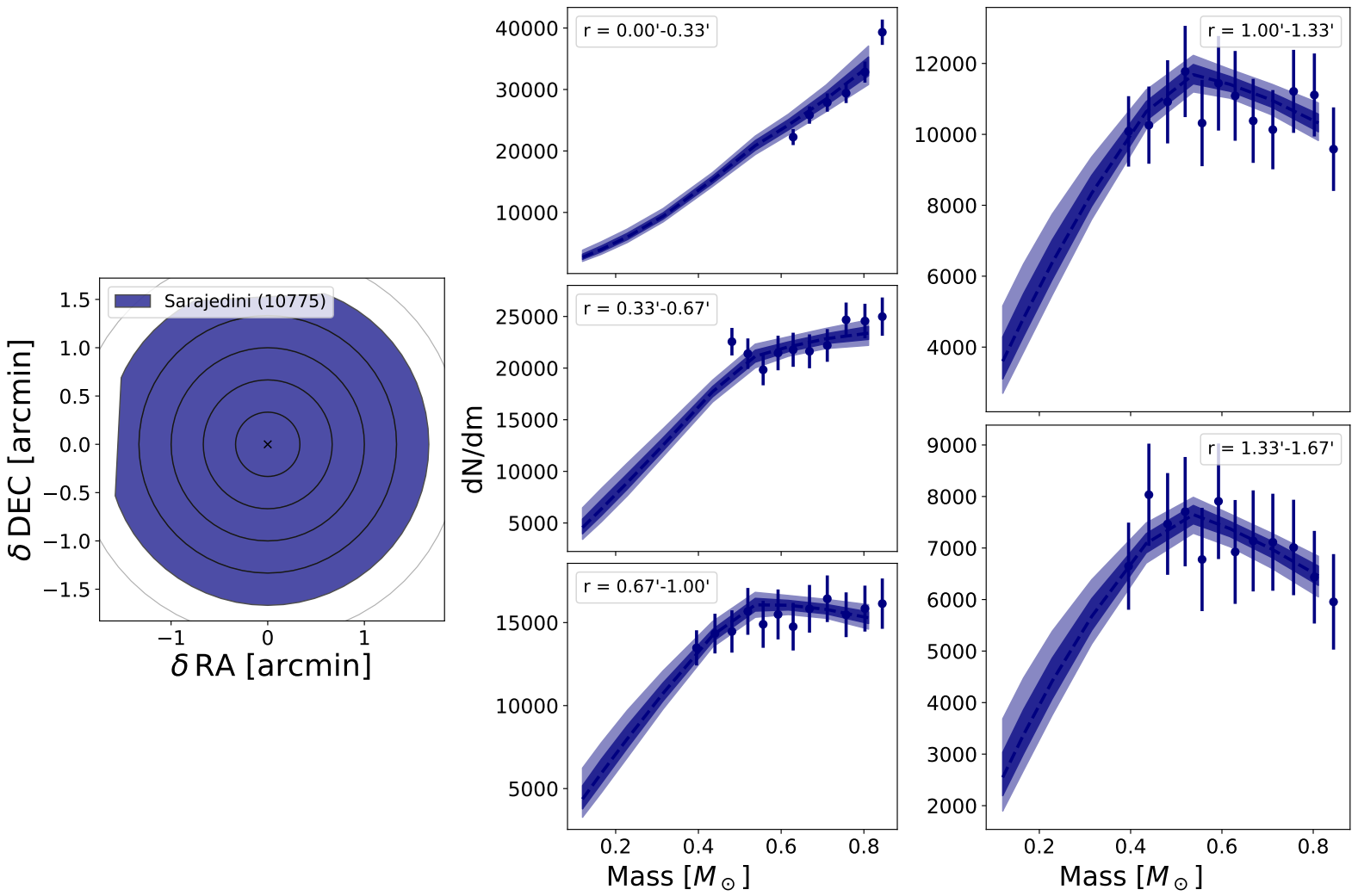

Figure A.48: Figure 5.3 repeated for NGC 6624

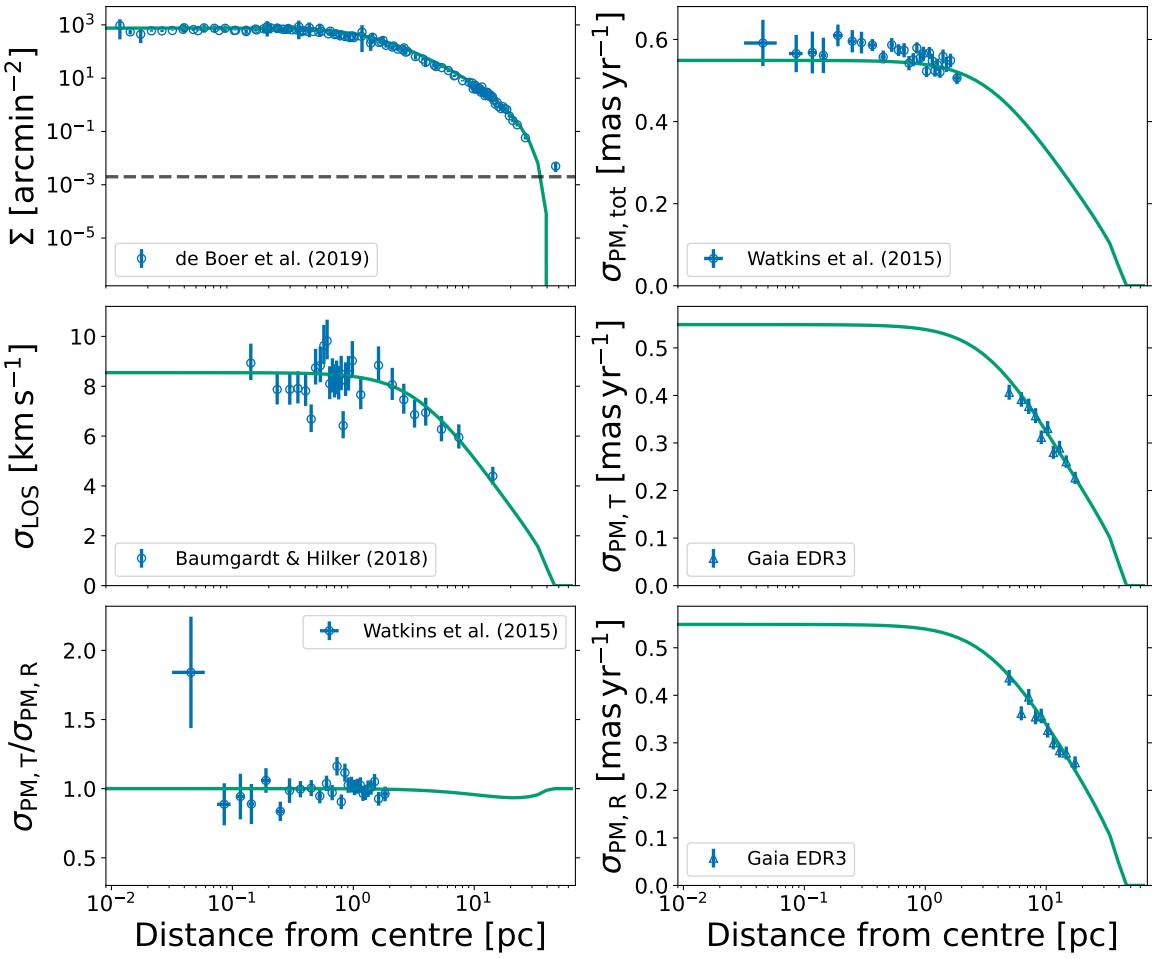

Figure A.49: Figure 5.2 repeated for NGC 6656

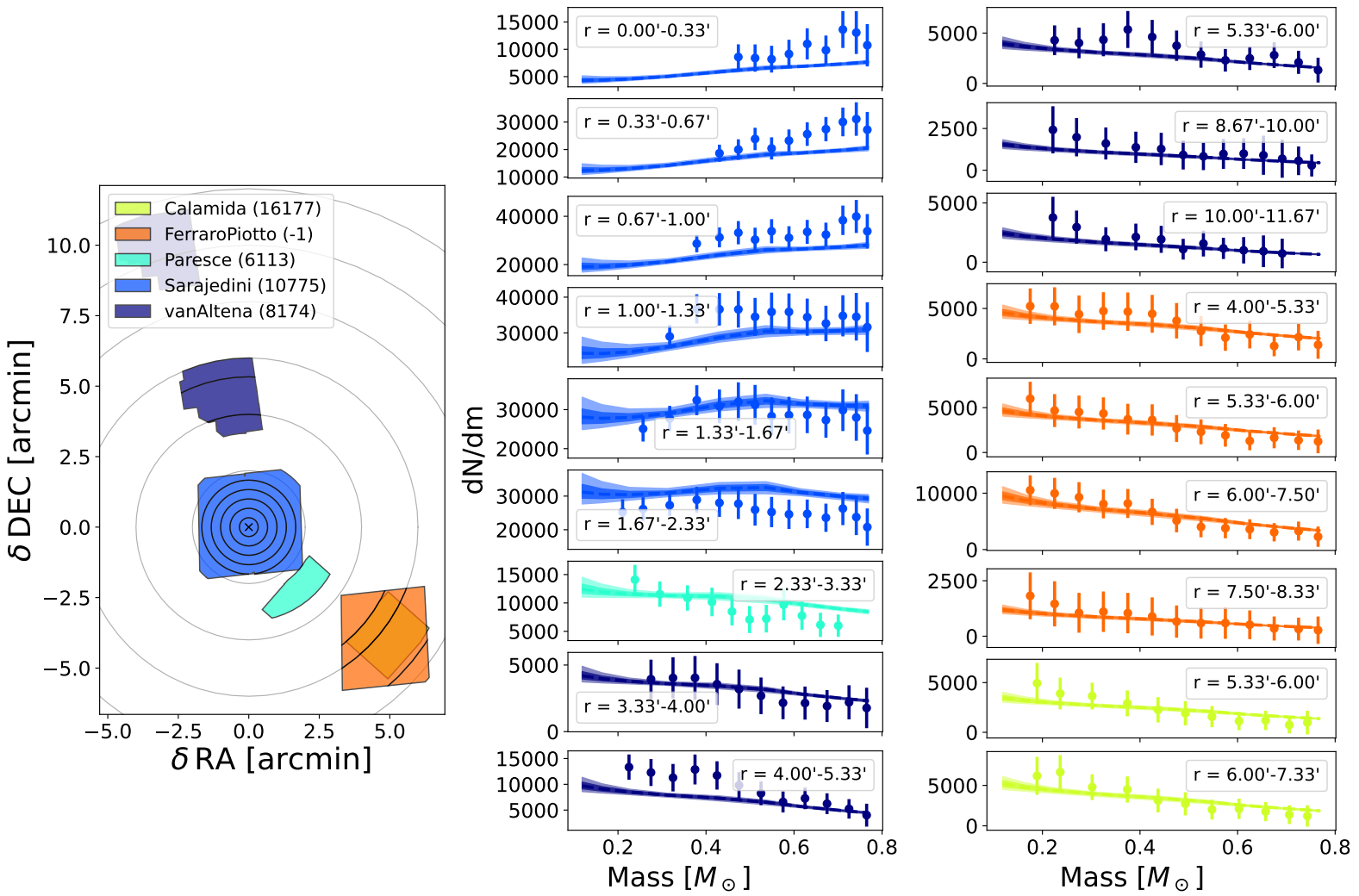

Figure A.50: Figure 5.3 repeated for NGC 6656

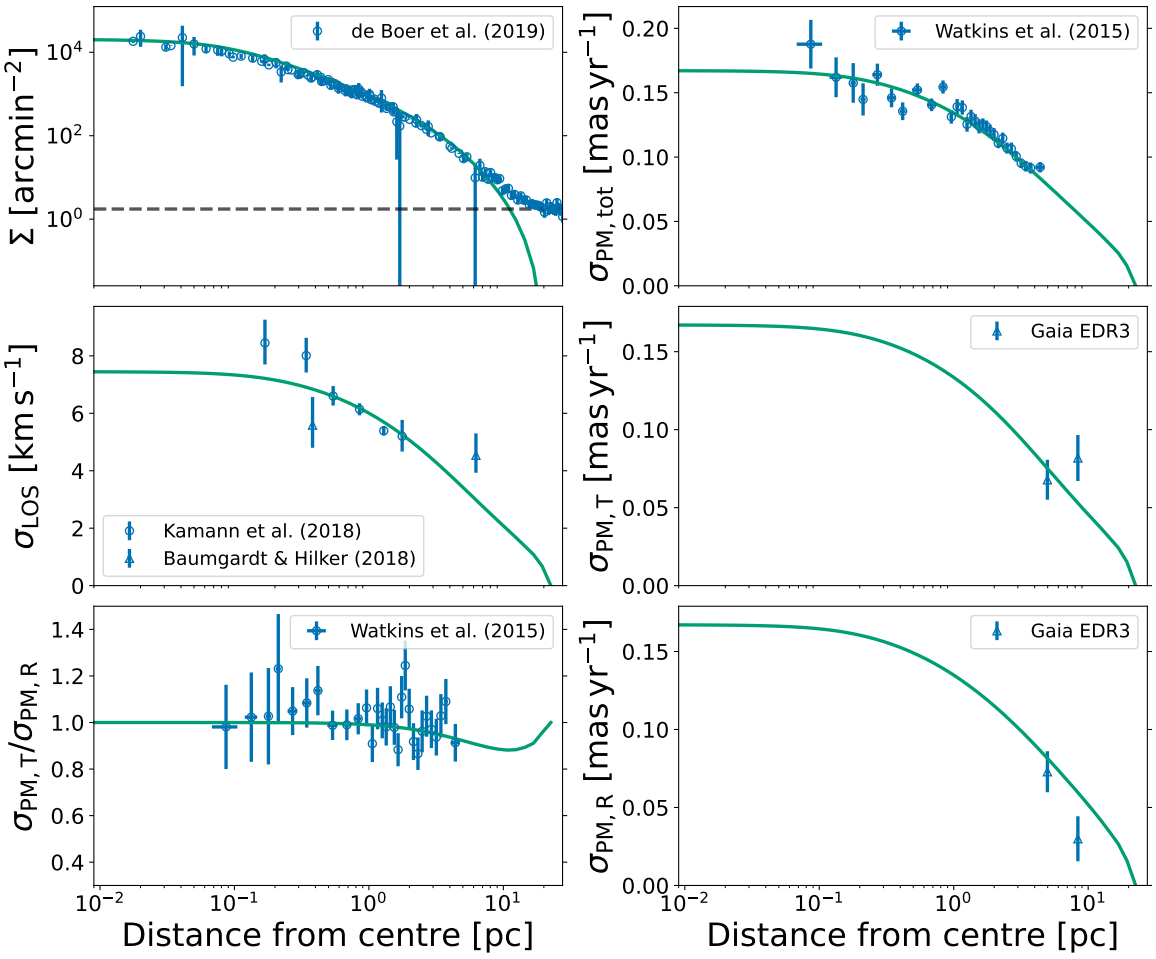

Figure A.51: Figure 5.2 repeated for NGC 6681

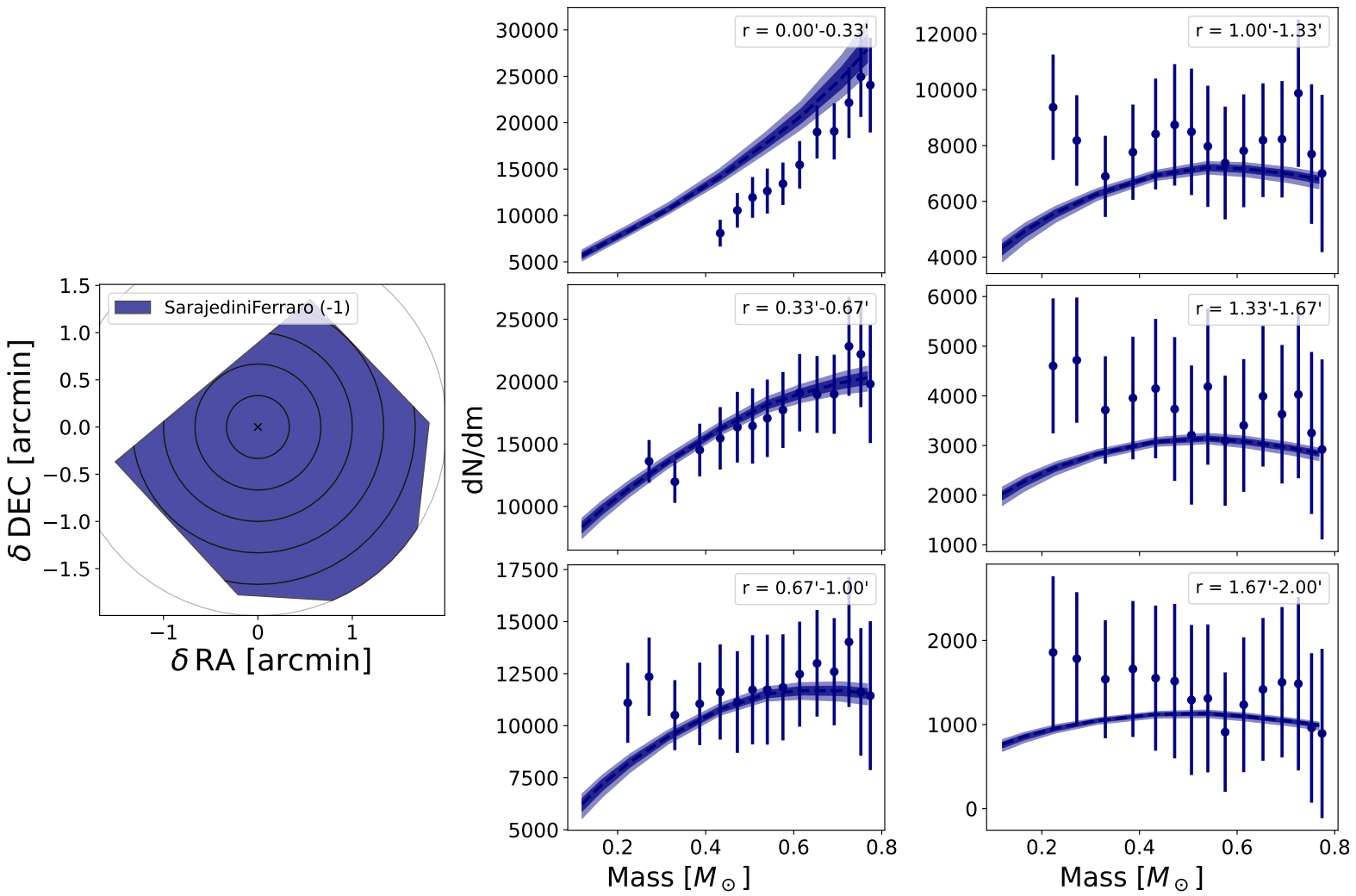

Figure A.52: Figure 5.3 repeated for NGC 6681

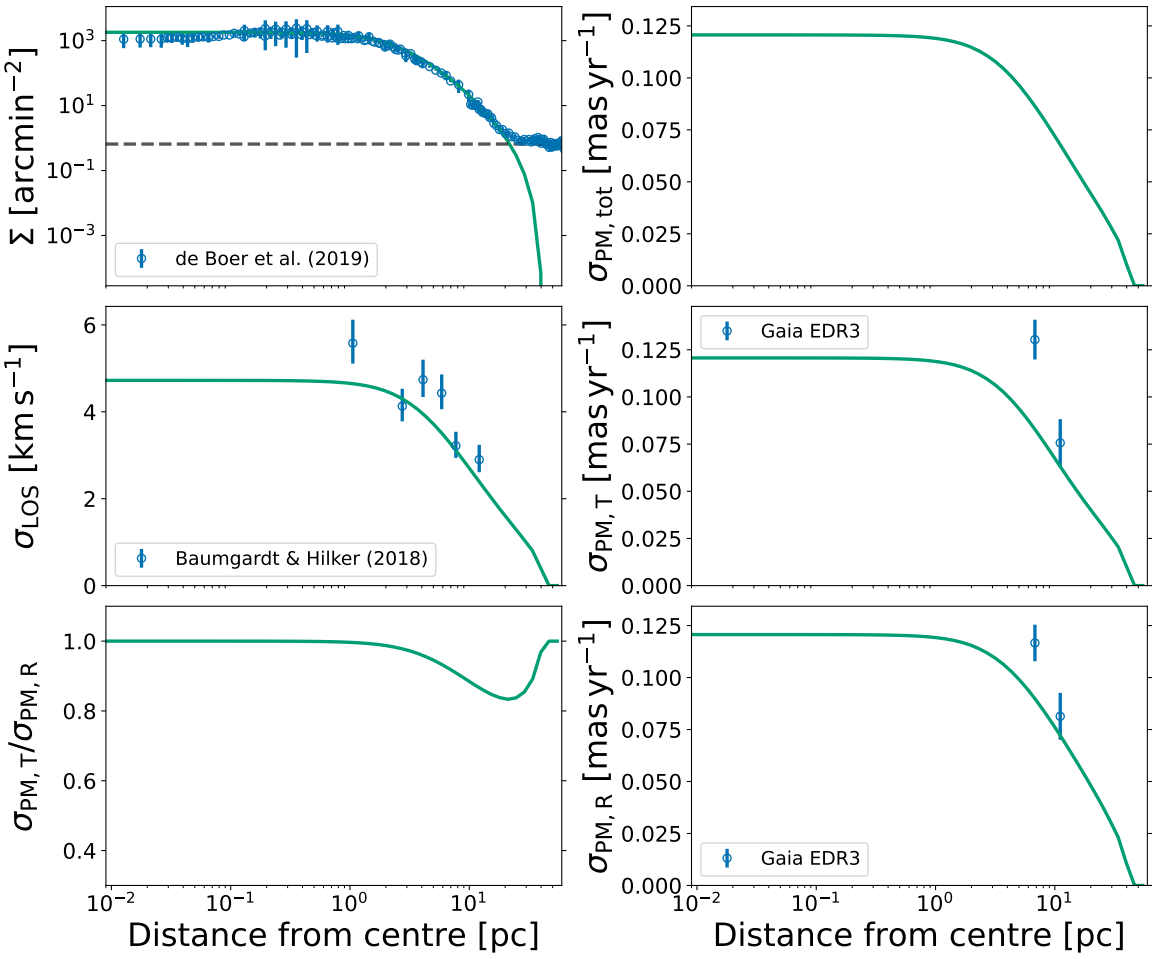

Figure A.53: Figure 5.2 repeated for NGC 6723

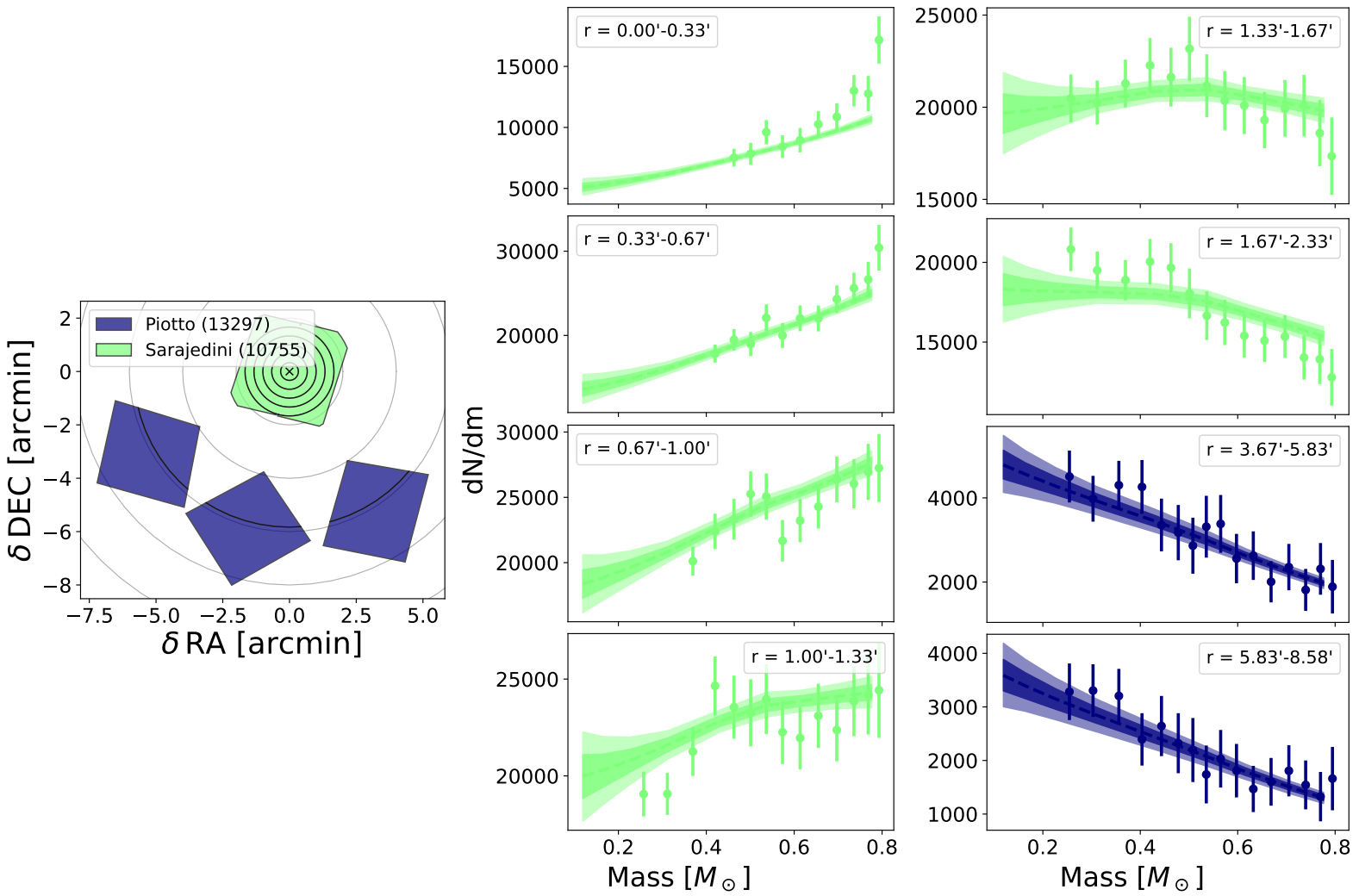

Figure A.54: Figure 5.3 repeated for NGC 6723

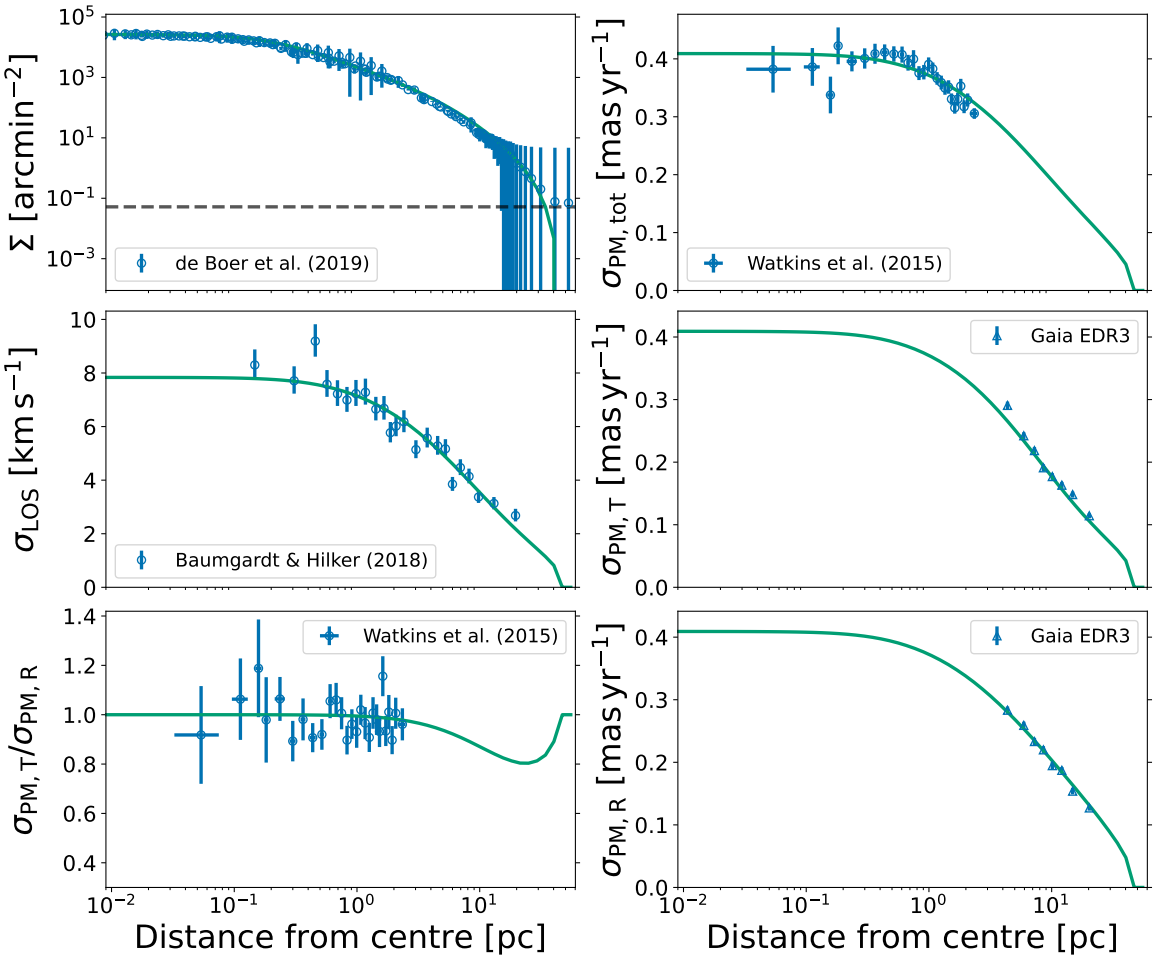

Figure A.55: Figure 5.2 repeated for NGC 6752

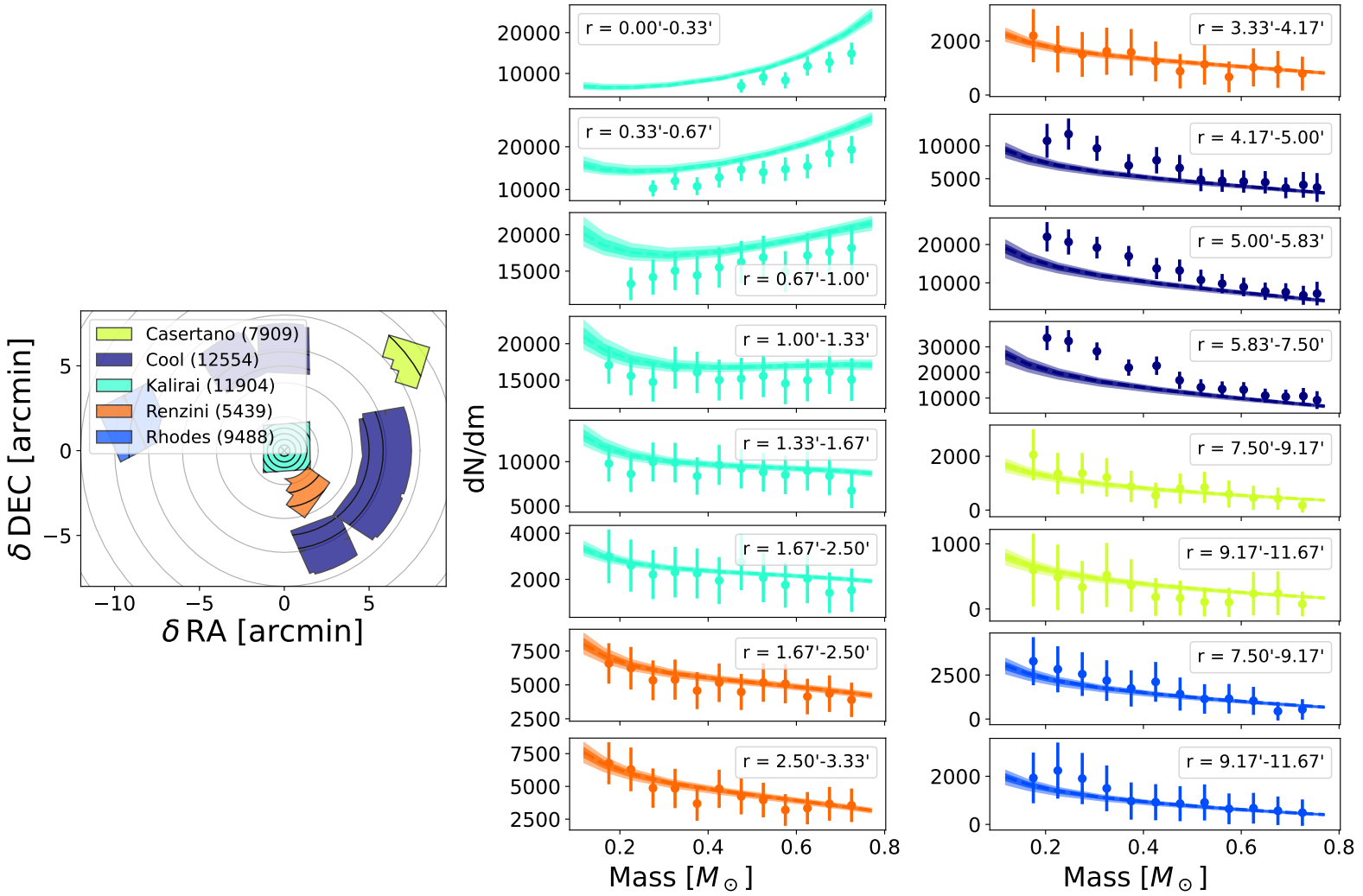

Figure A.56: Figure 5.3 repeated for NGC 6752

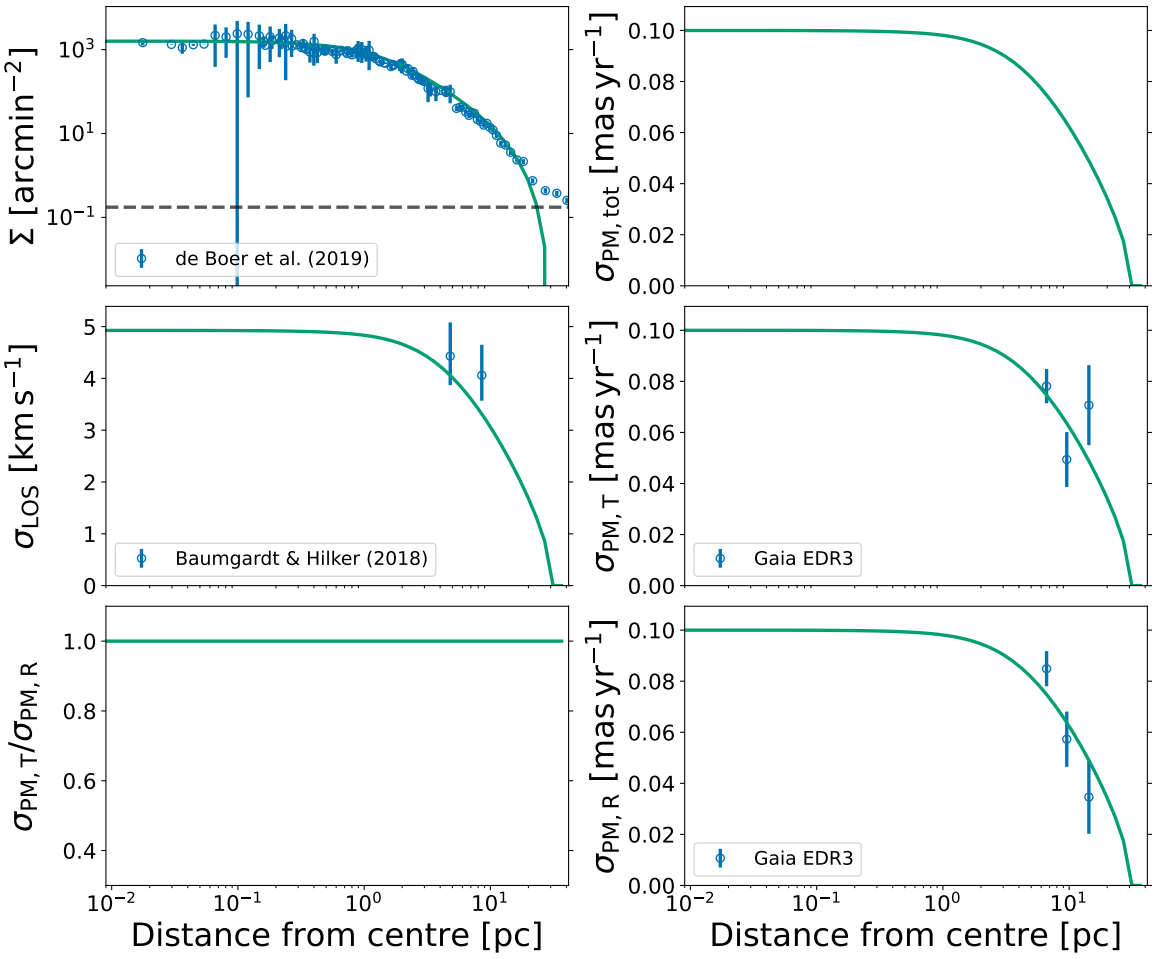

Figure A.57: Figure 5.2 repeated for NGC 6779

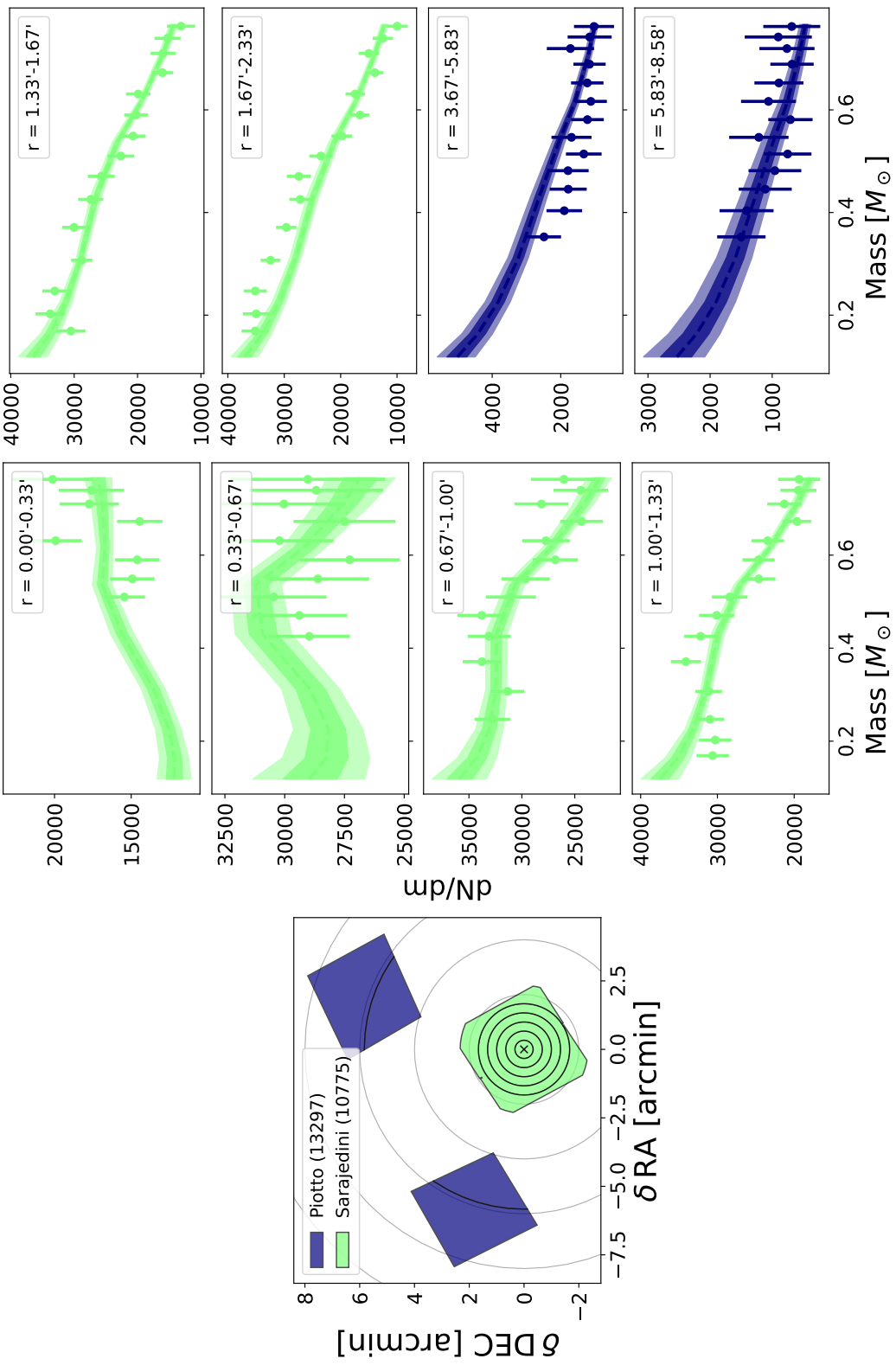

Figure A.58: Figure 5.3 repeated for NGC 6779

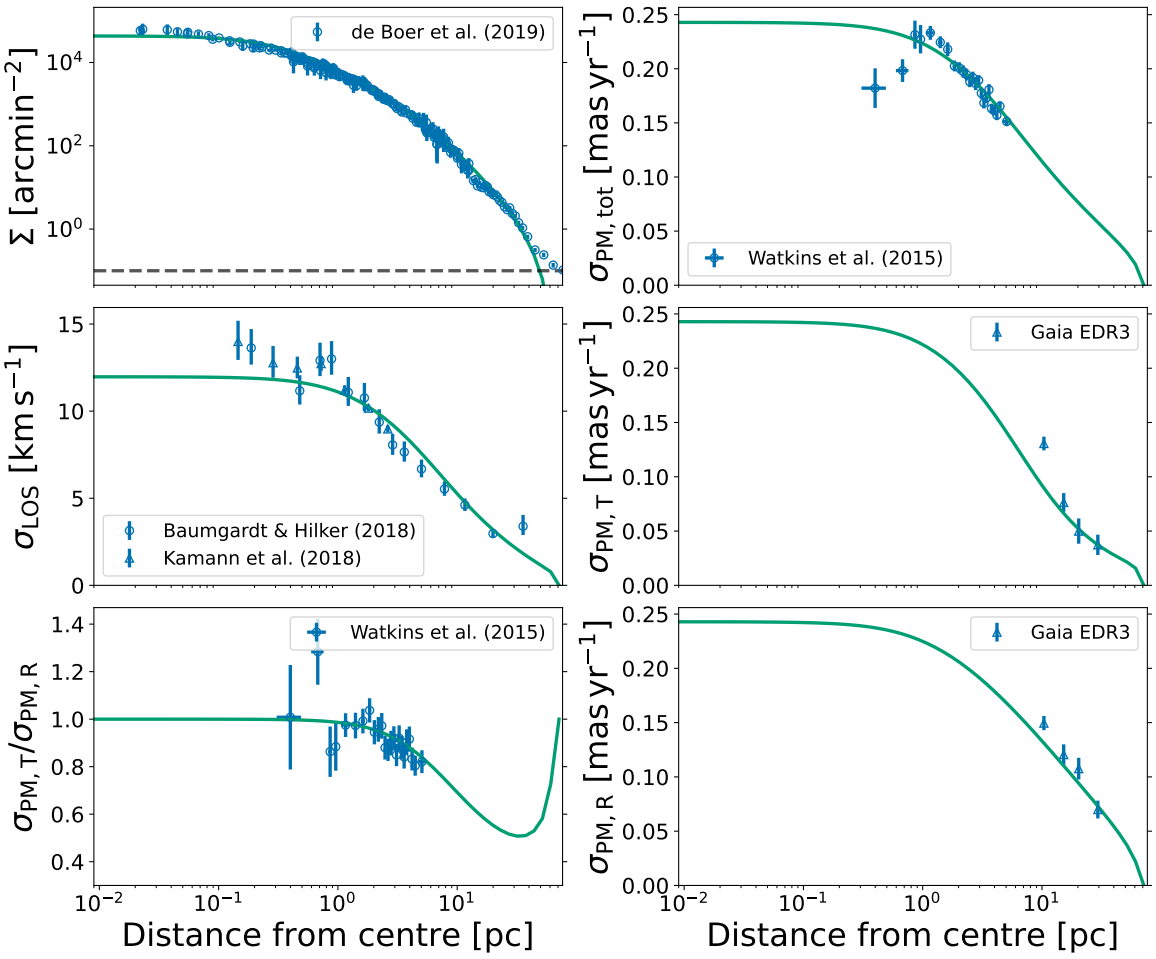

Figure A.59: Figure 5.2 repeated for NGC 7078

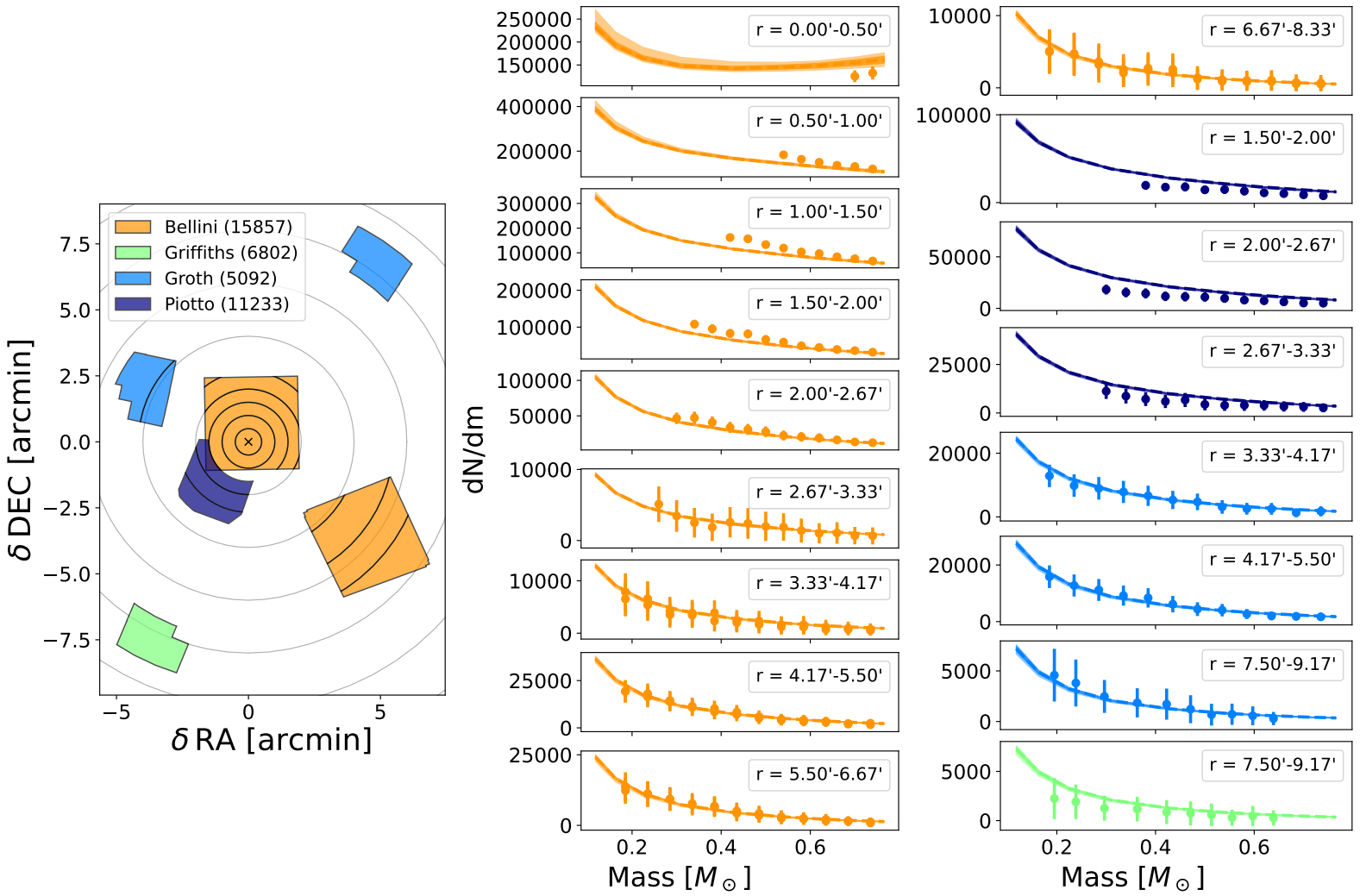

Figure A.60: Figure 5.3 repeated for NGC 7078

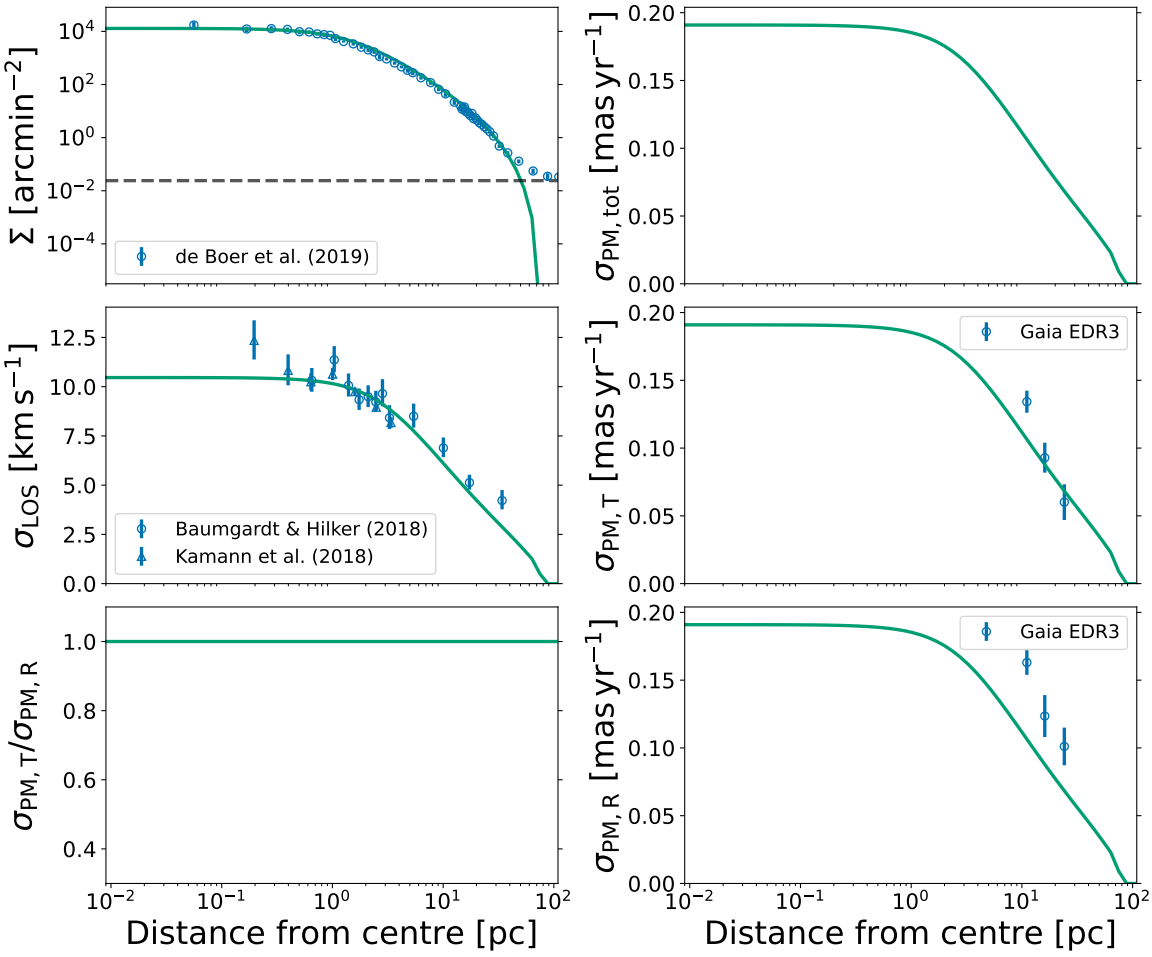

Figure A.61: Figure 5.2 repeated for NGC 7089

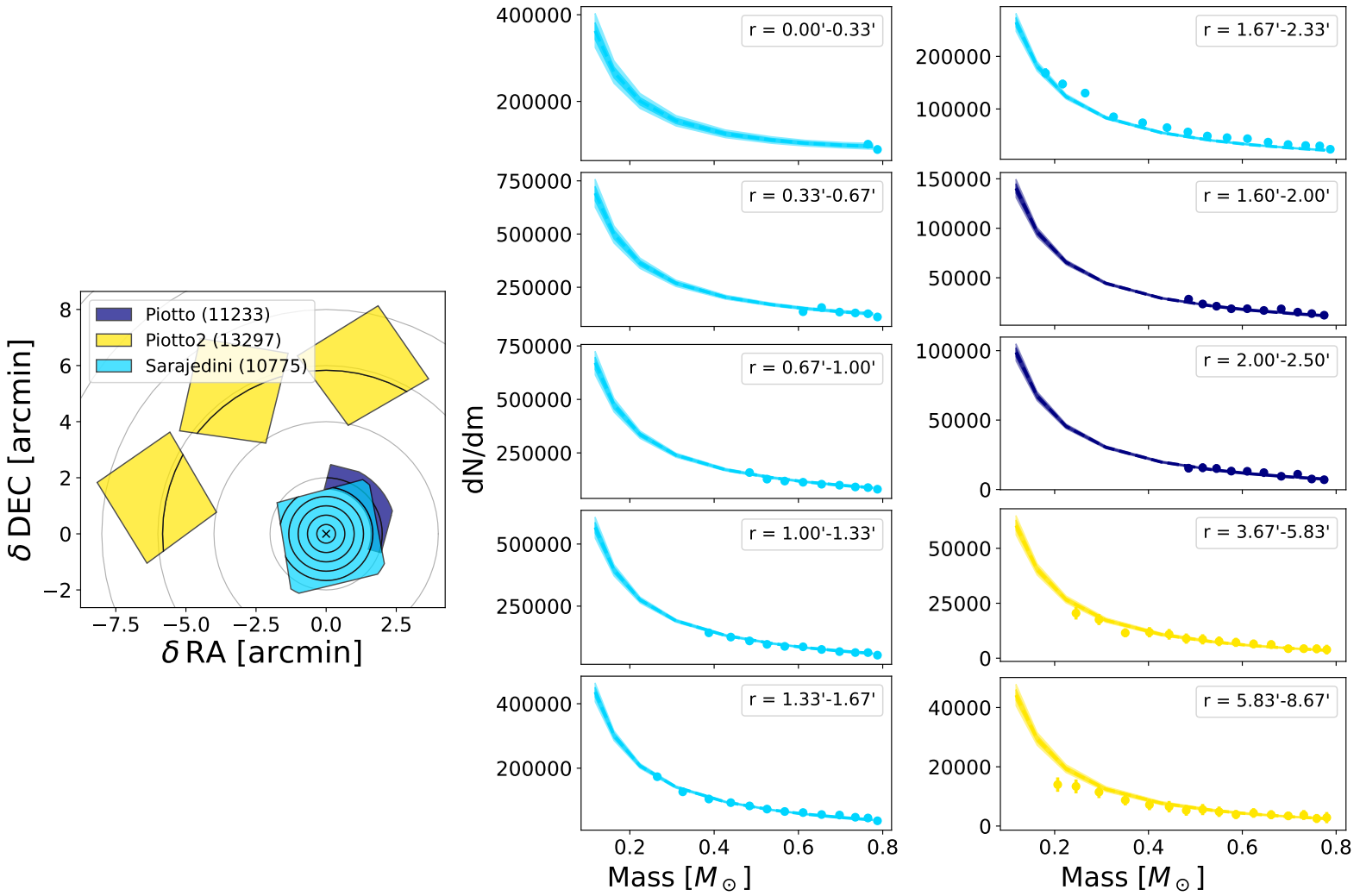

Figure A.62: Figure 5.3 repeated for NGC 7089

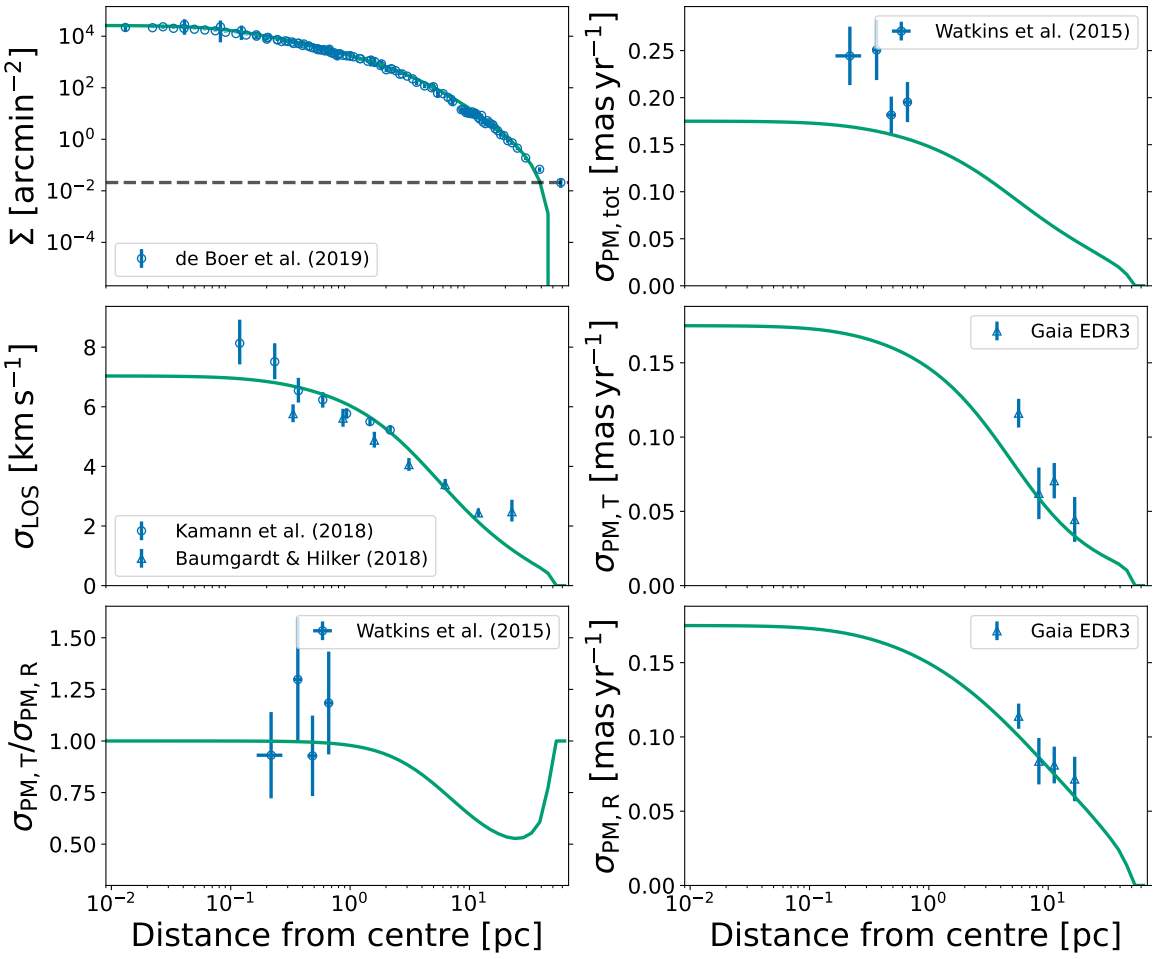

Figure A.63: Figure 5.2 repeated for NGC 7099

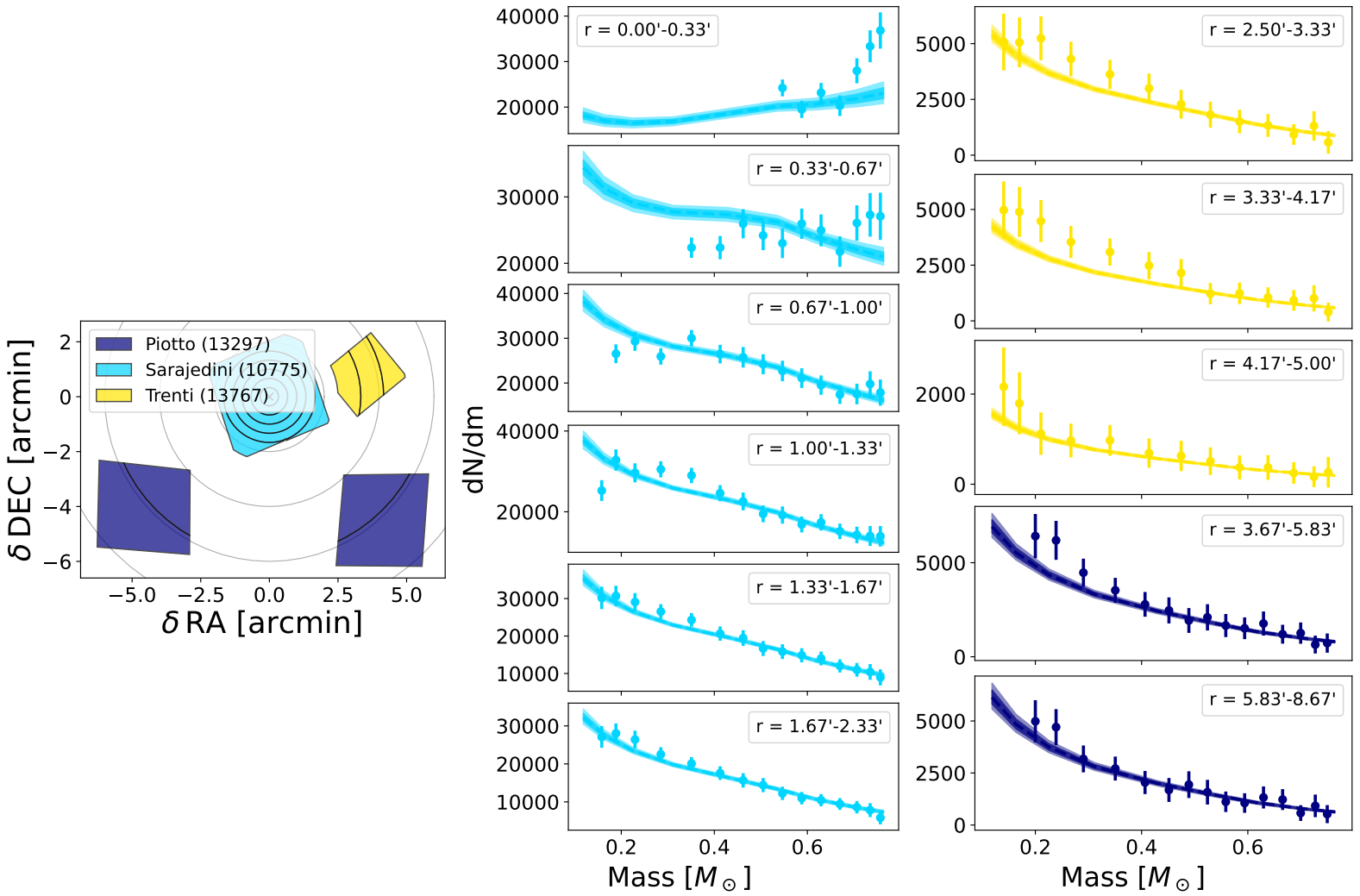

Figure A.64: Figure 5.3 repeated for NGC 7099

A.2 Core-Collapsed Models with no Black Holes

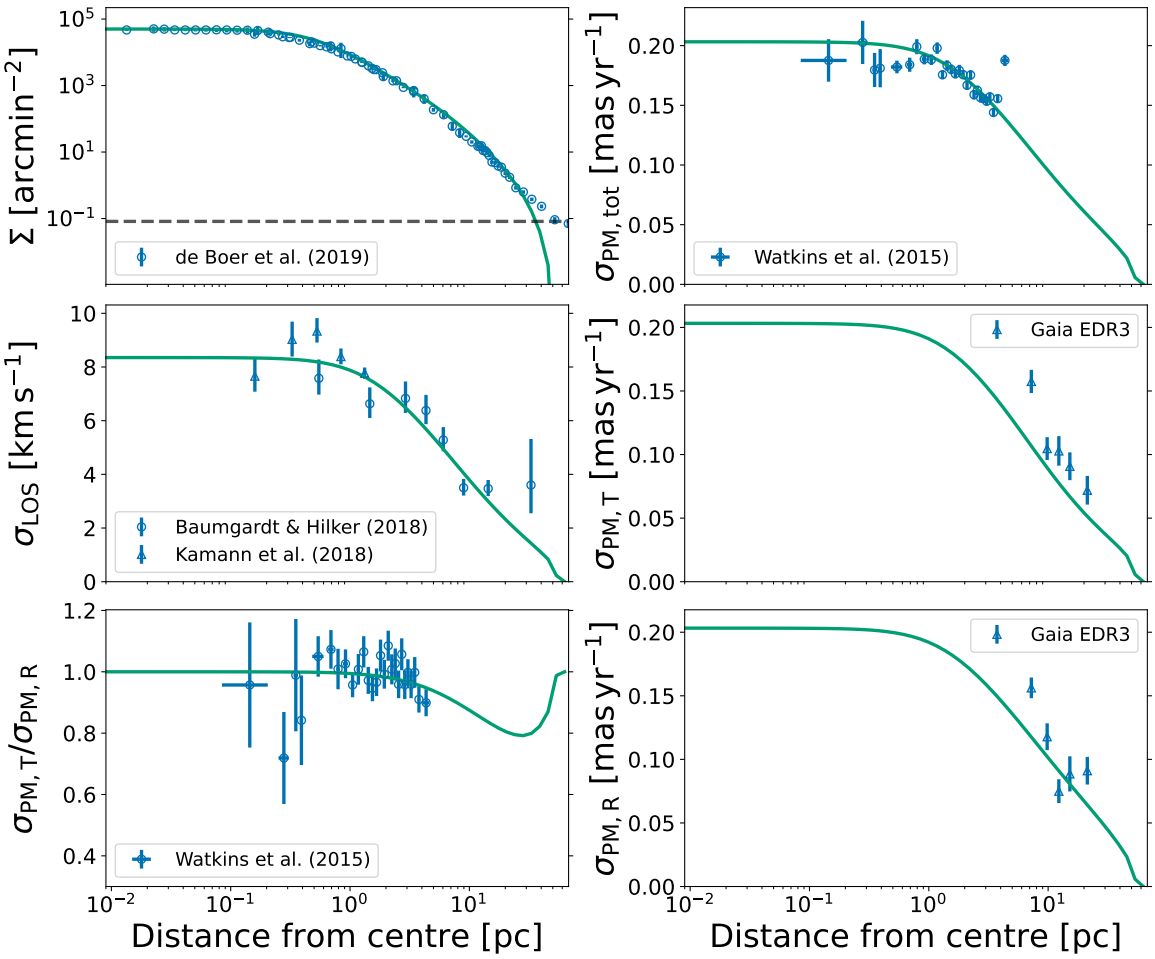

Figure A.65: Figure 5.2 repeated for NGC 362, with the amount of black holes retained at the present day fixed to zero

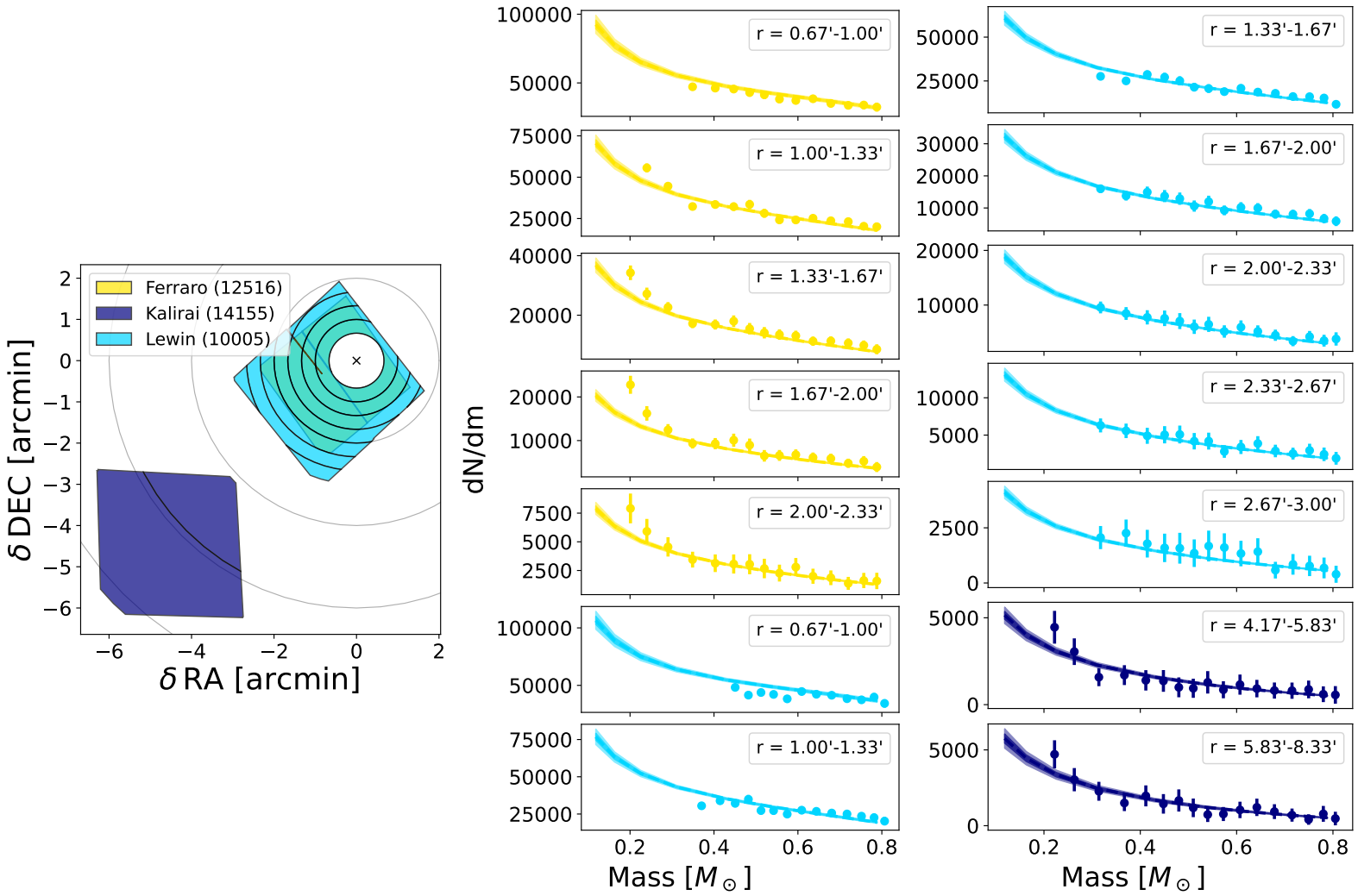

Figure A.66: Figure 5.3 repeated for NGC 362, with the amount of black holes retained at the present day fixed to zero

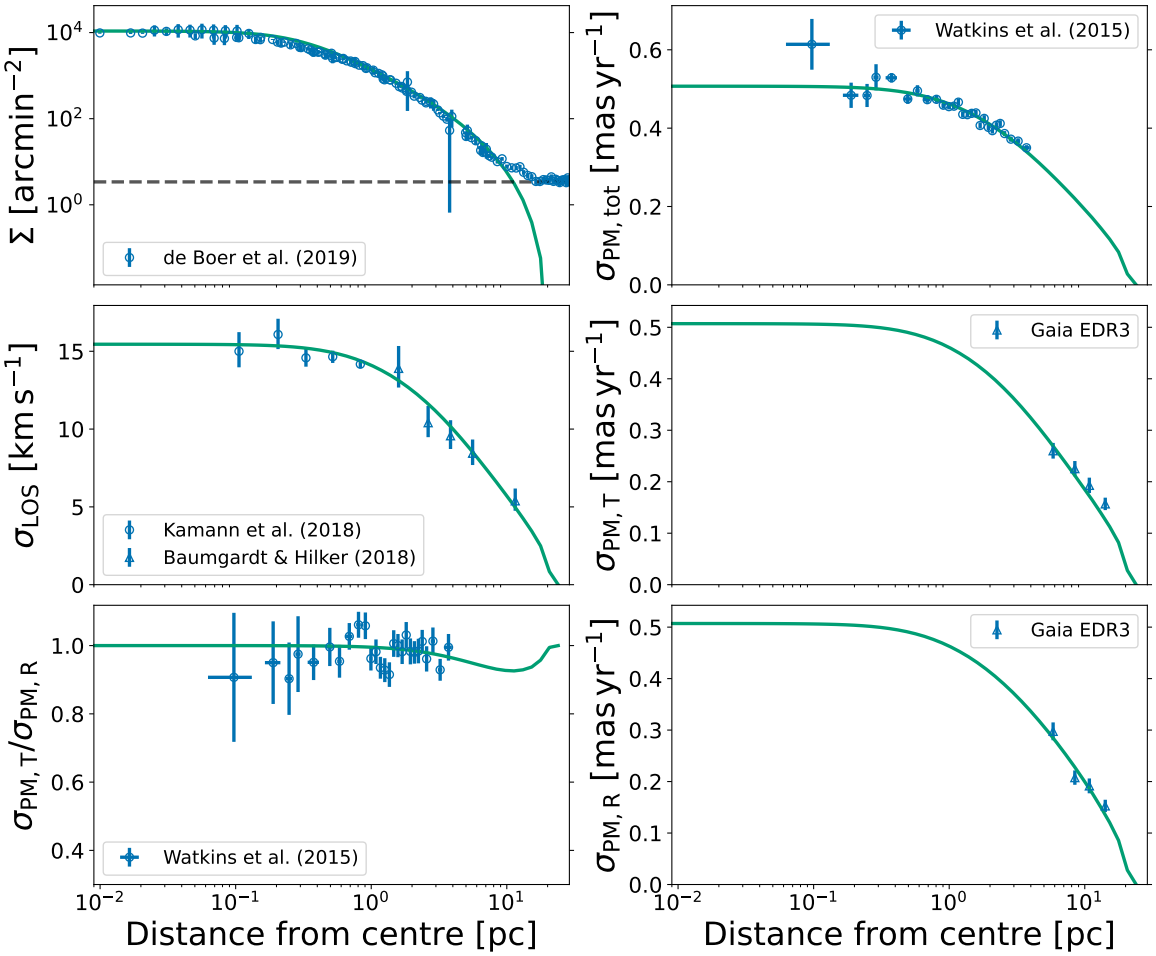

Figure A.67: Figure 5.2 repeated for NGC 6266, with the amount of black holes retained at the present day fixed to zero

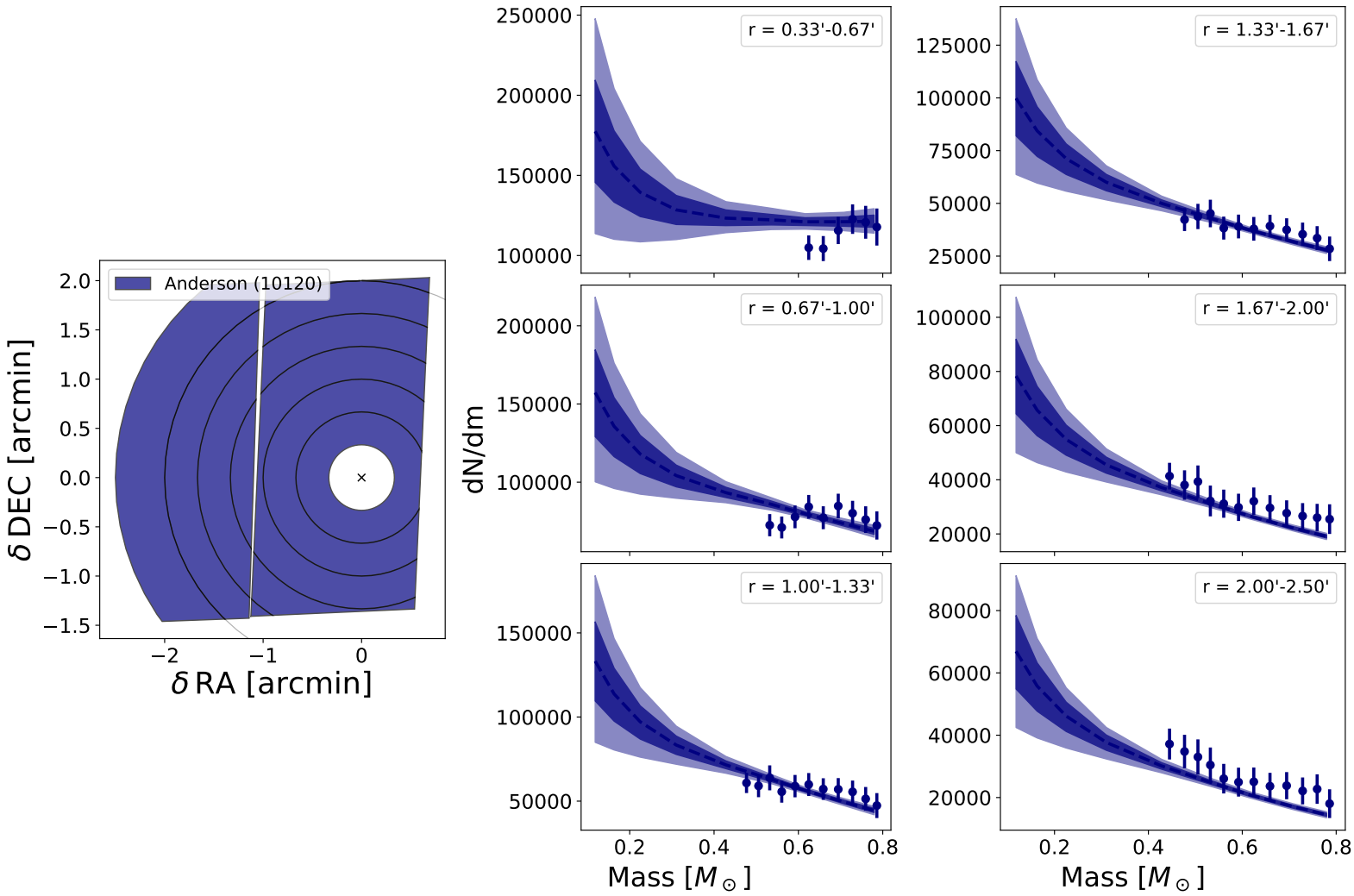

Figure A.68: Figure 5.3 repeated for NGC 6266, with the amount of black holes retained at the present day fixed to zero

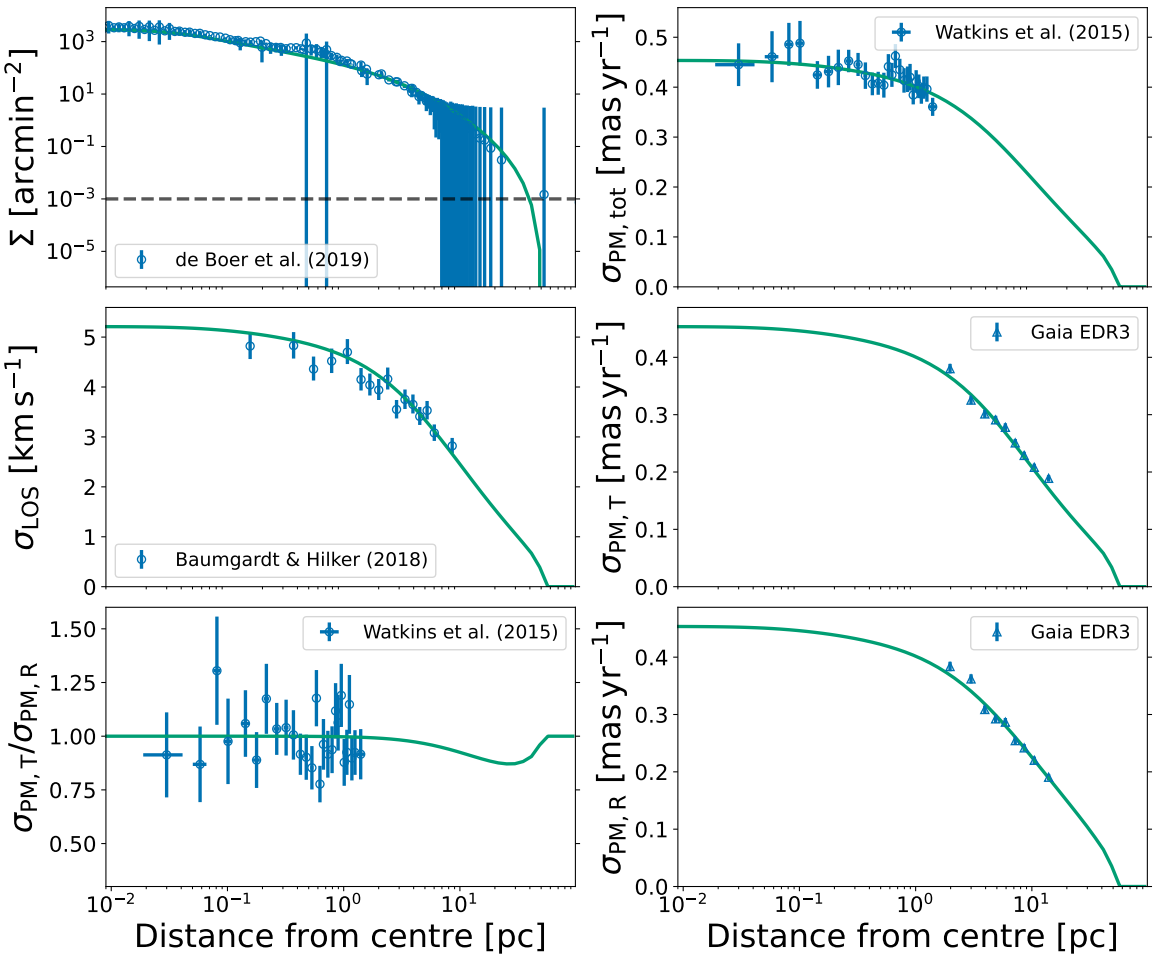

Figure A.69: Figure 5.2 repeated for NGC 6397, with the amount of black holes retained at the present day fixed to zero

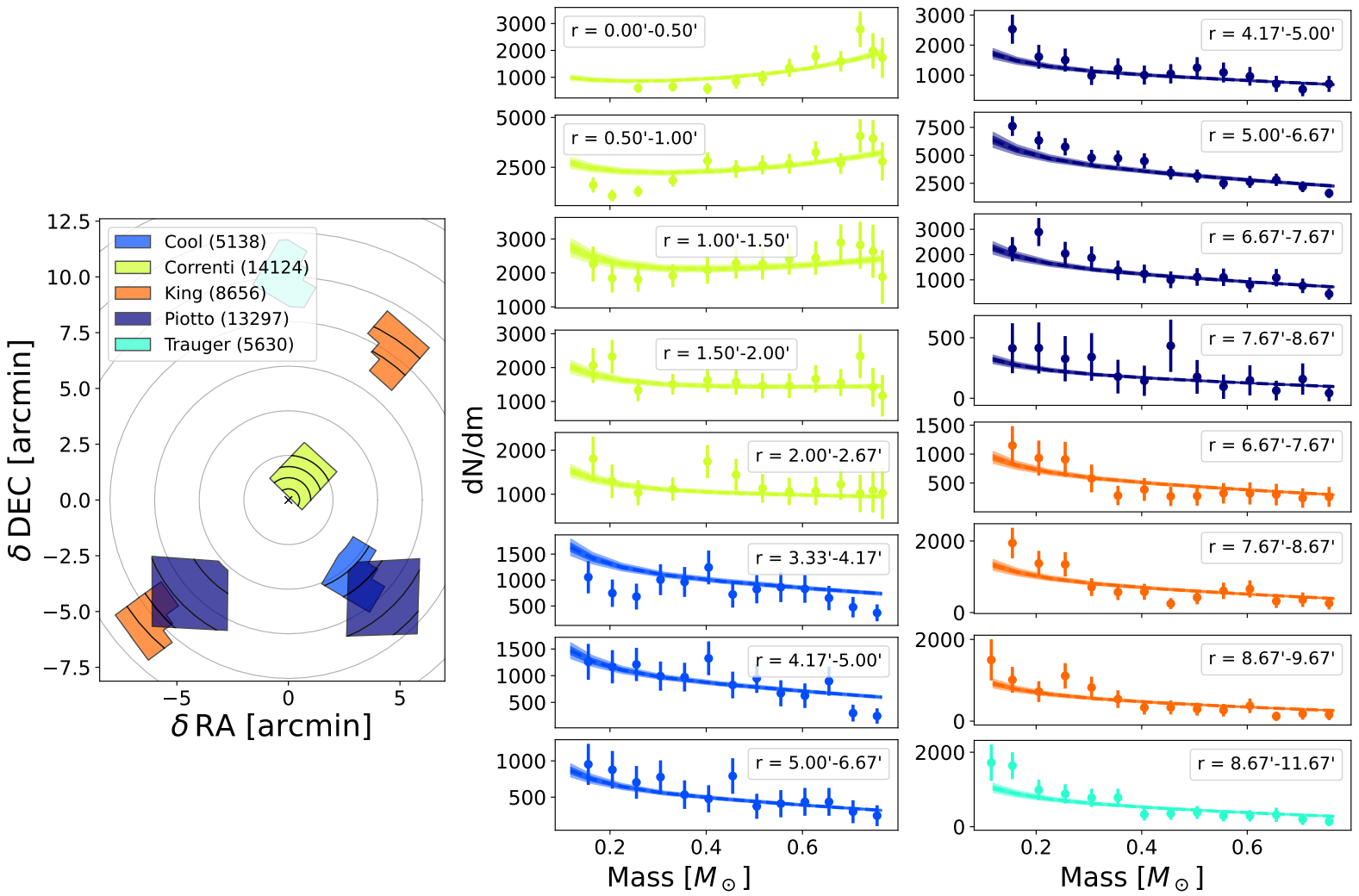

Figure A.70: Figure 5.3 repeated for NGC 6397, with the amount of black holes retained at the present day fixed to zero

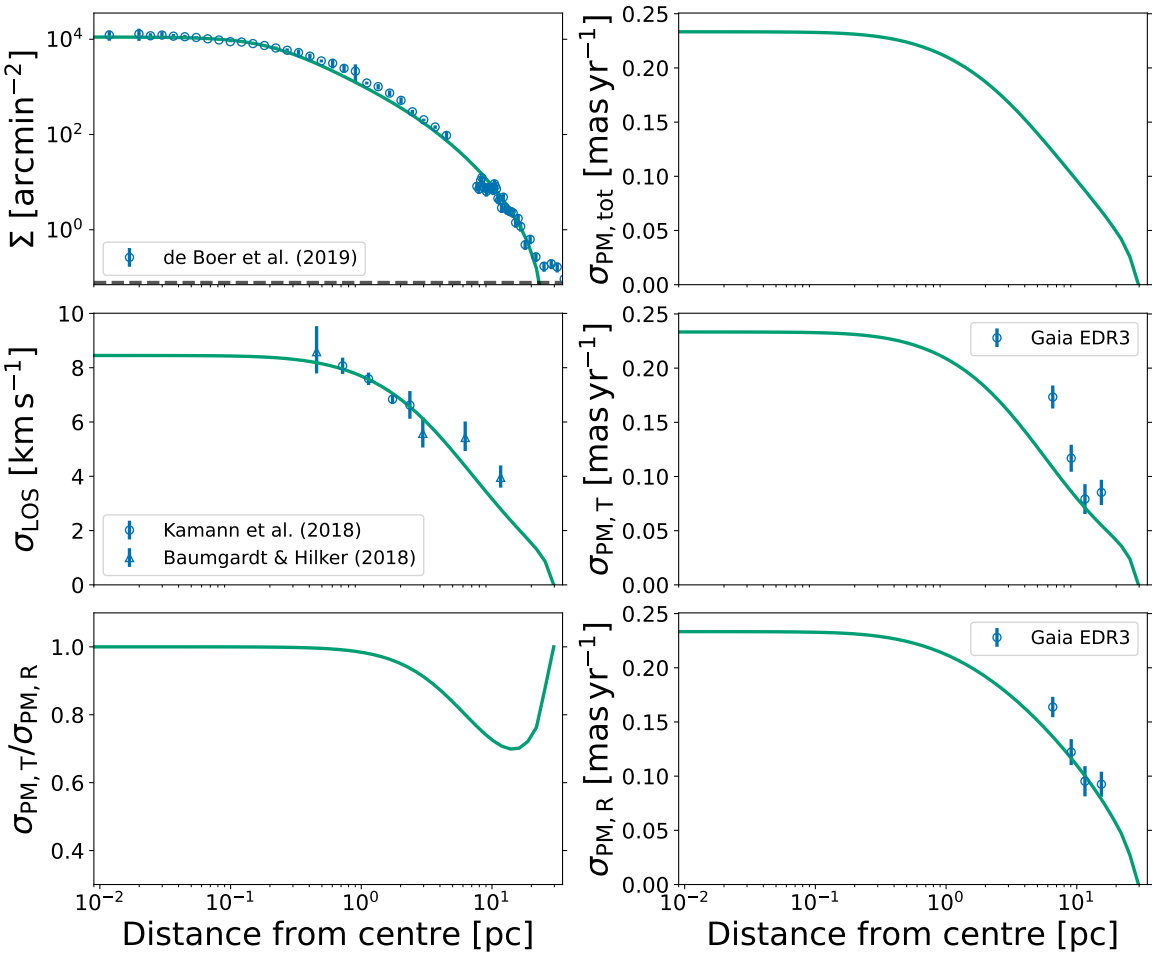

Figure A.71: Figure 5.2 repeated for NGC 6541, with the amount of black holes retained at the present day fixed to zero

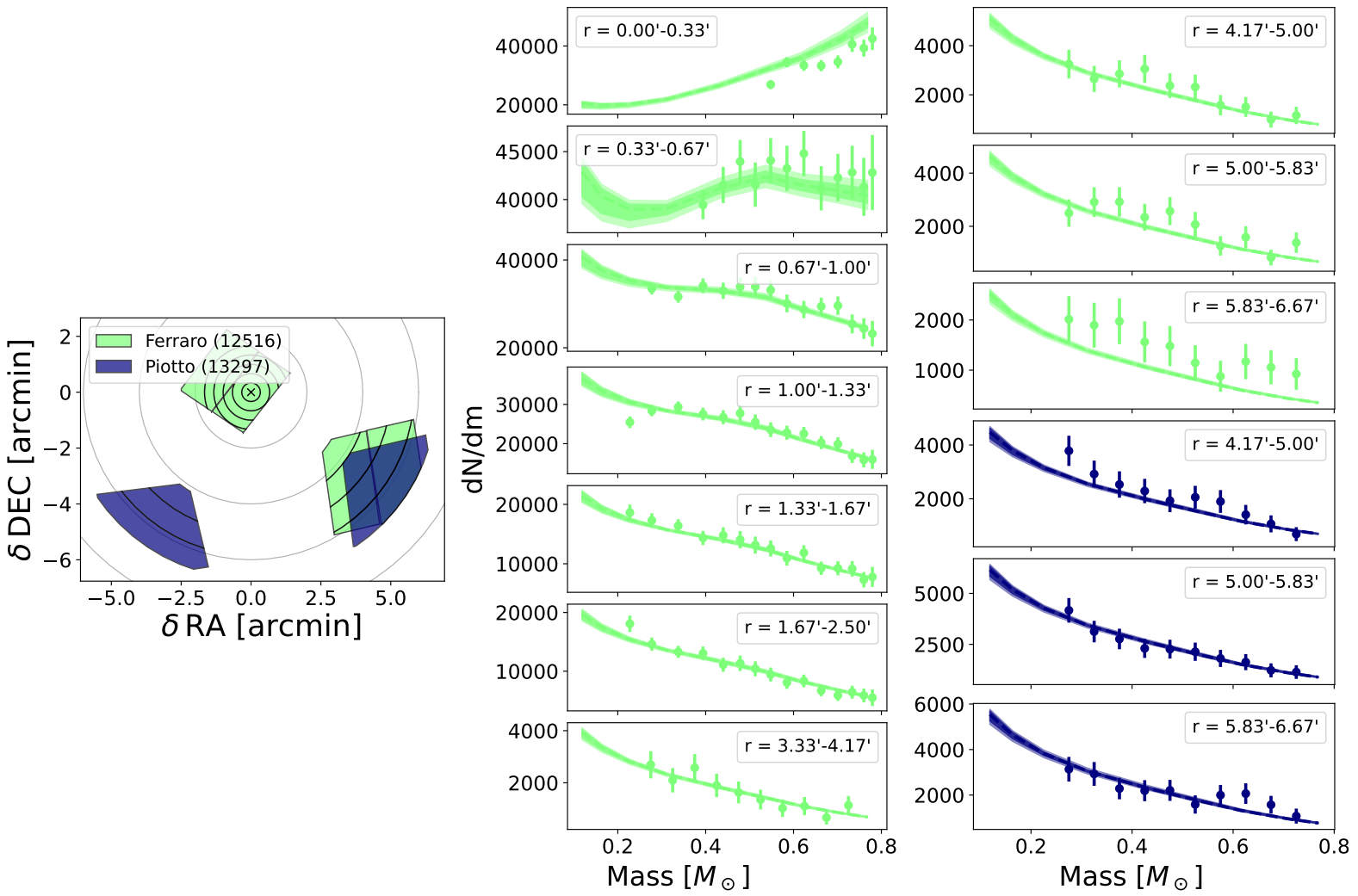

Figure A.72: Figure 5.3 repeated for NGC 6541, with the amount of black holes retained at the present day fixed to zero

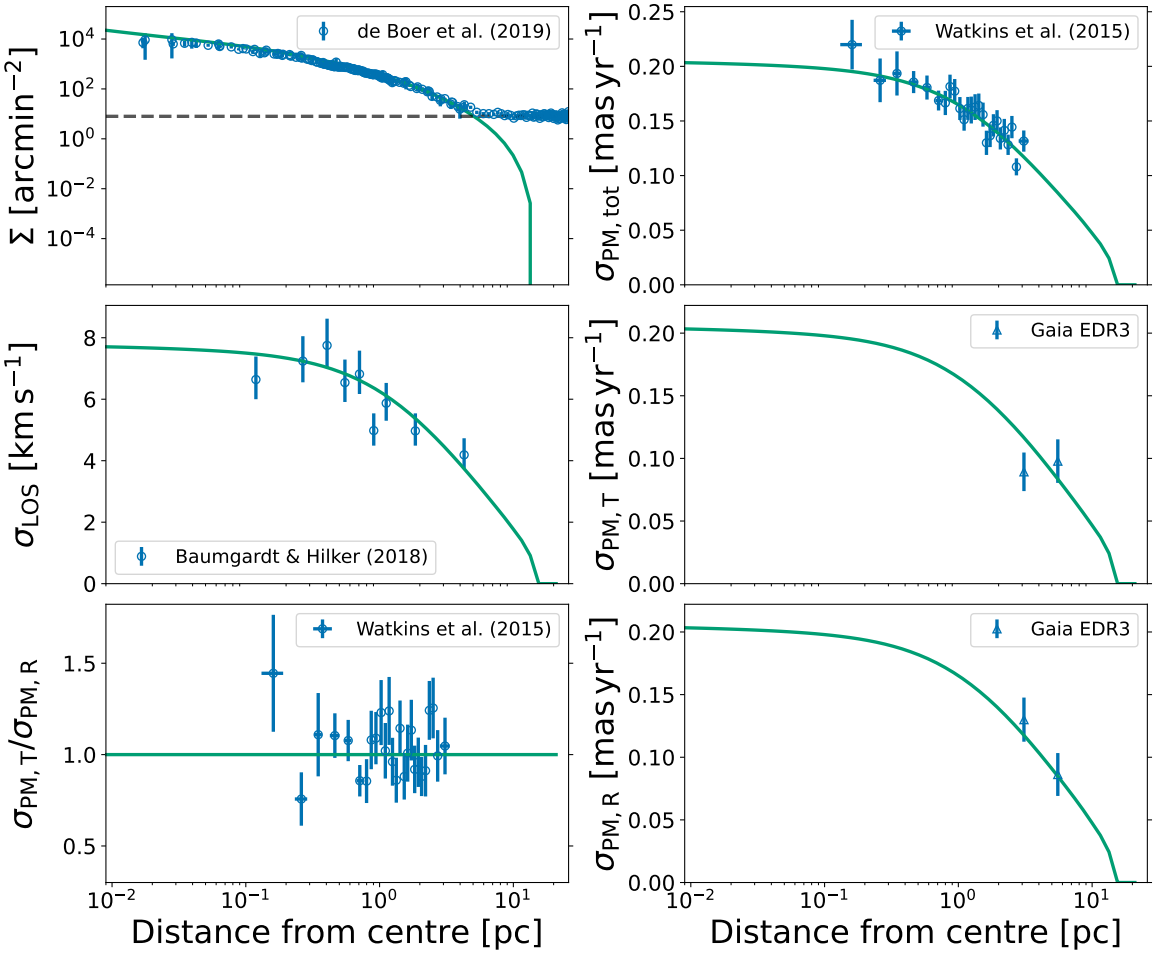

Figure A.73: Figure 5.2 repeated for NGC 6624, with the amount of black holes retained at the present day fixed to zero

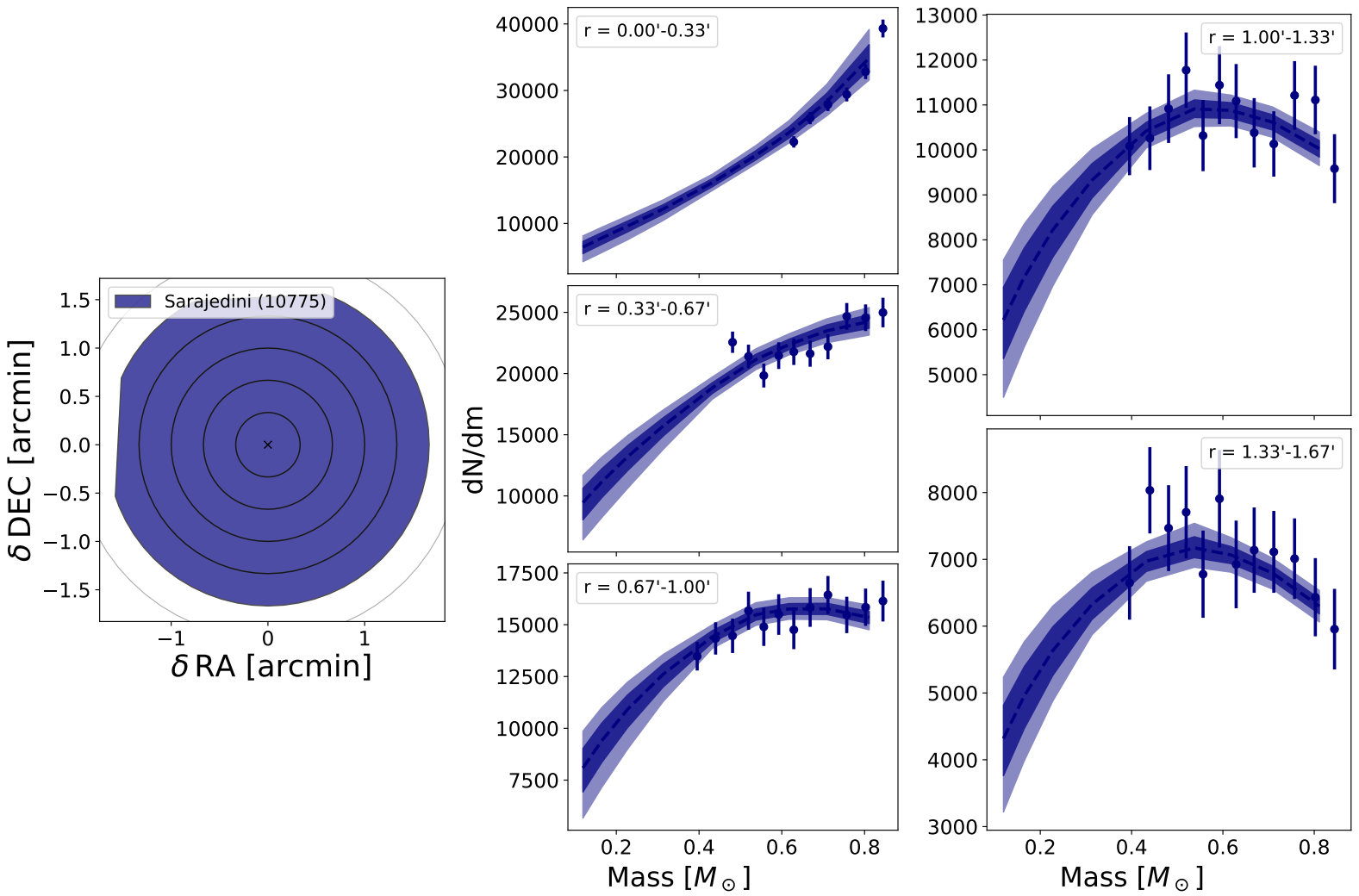

Figure A.74: Figure 5.3 repeated for NGC 6624, with the amount of black holes retained at the present day fixed to zero

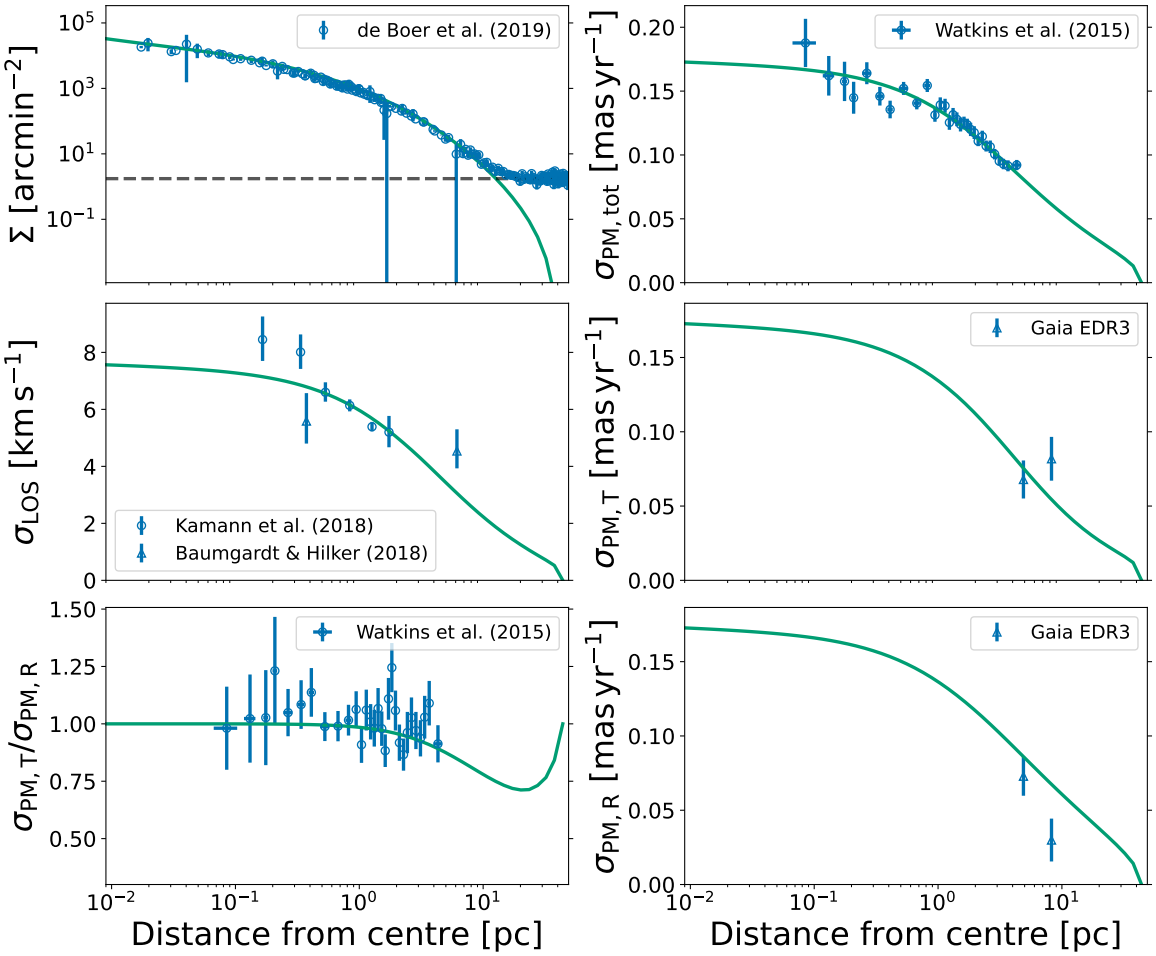

Figure A.75: Figure 5.2 repeated for NGC 6681, with the amount of black holes retained at the present day fixed to zero

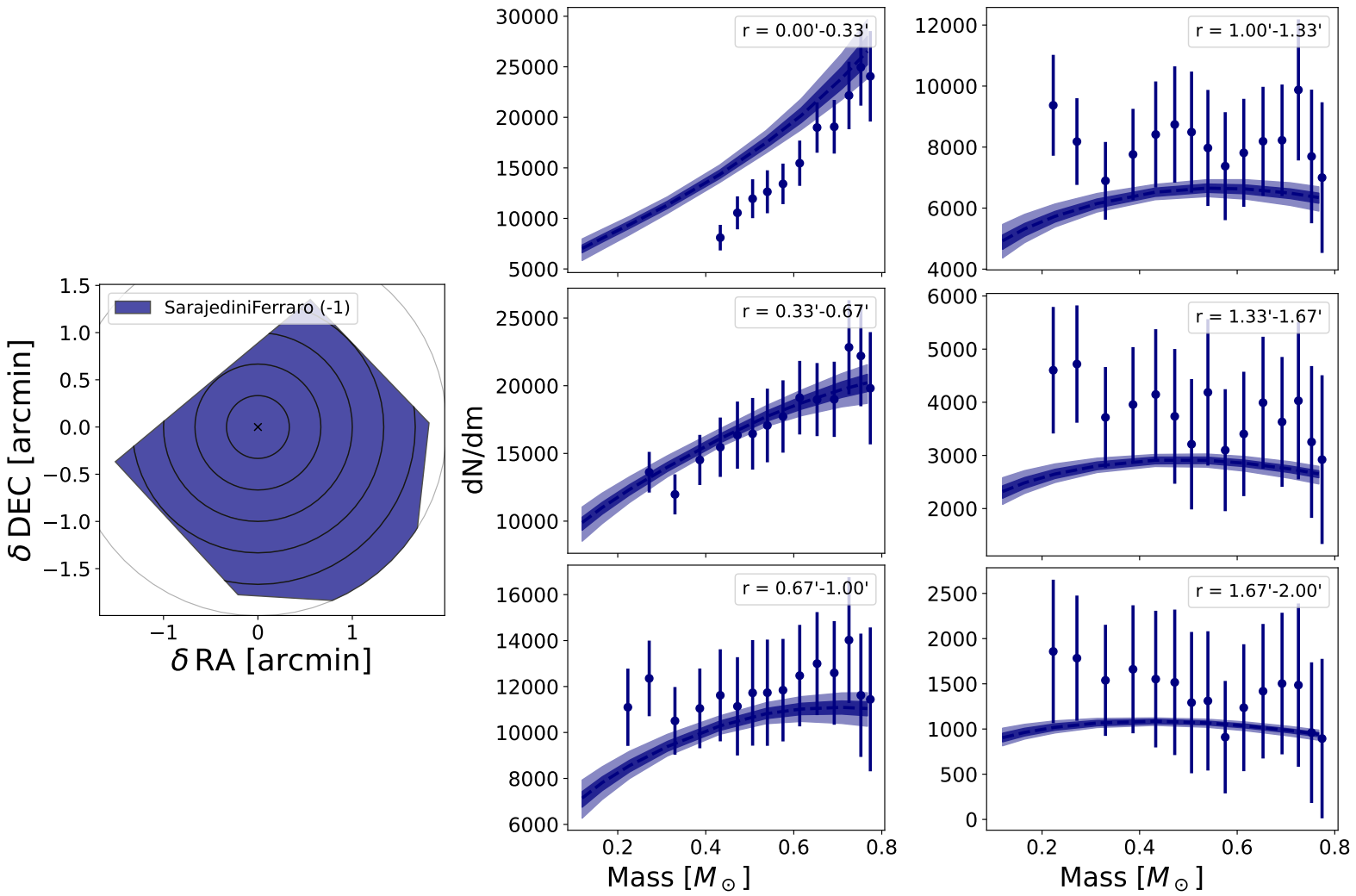

Figure A.76: Figure 5.3 repeated for NGC 6681, with the amount of black holes retained at the present day fixed to zero

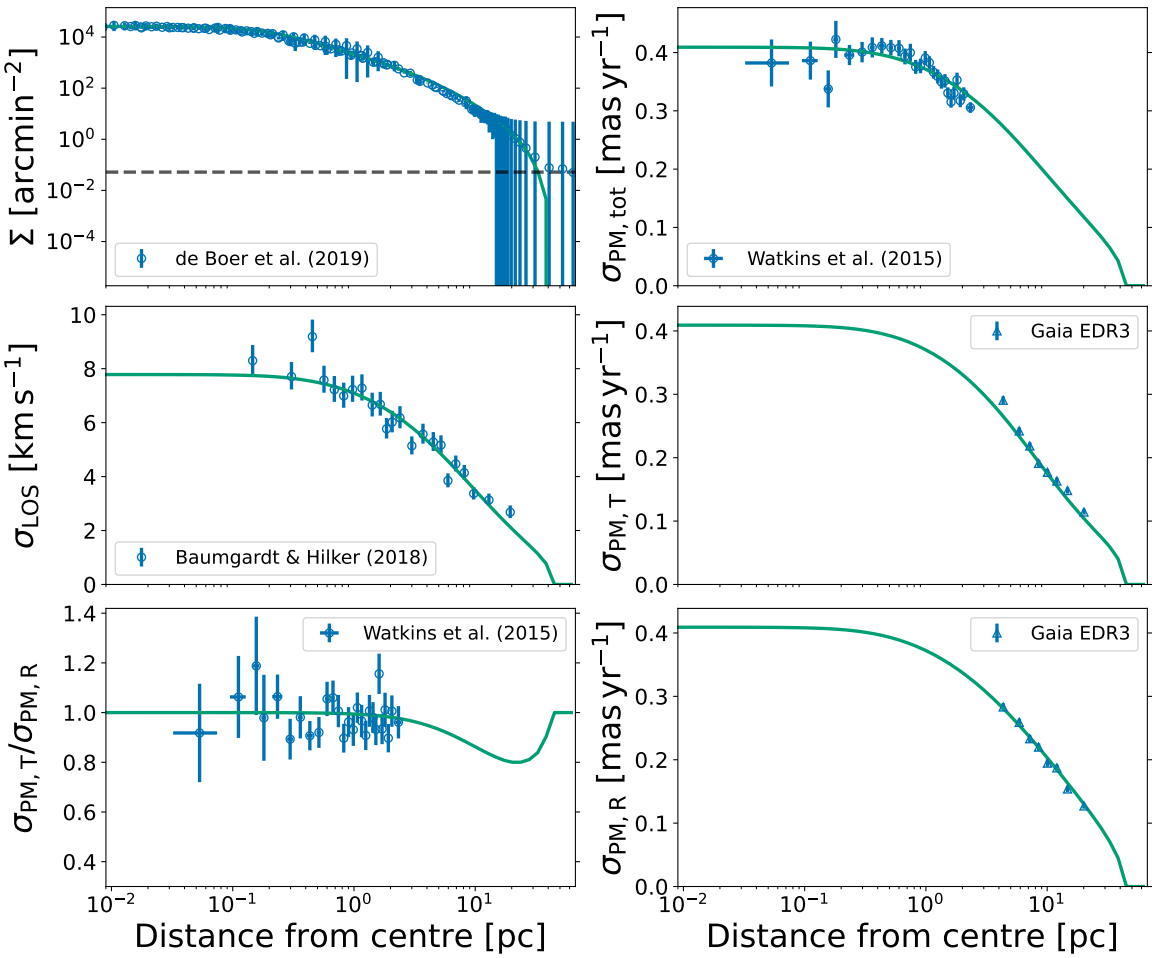

Figure A.77: Figure 5.2 repeated for NGC 6752, with the amount of black holes retained at the present day fixed to zero

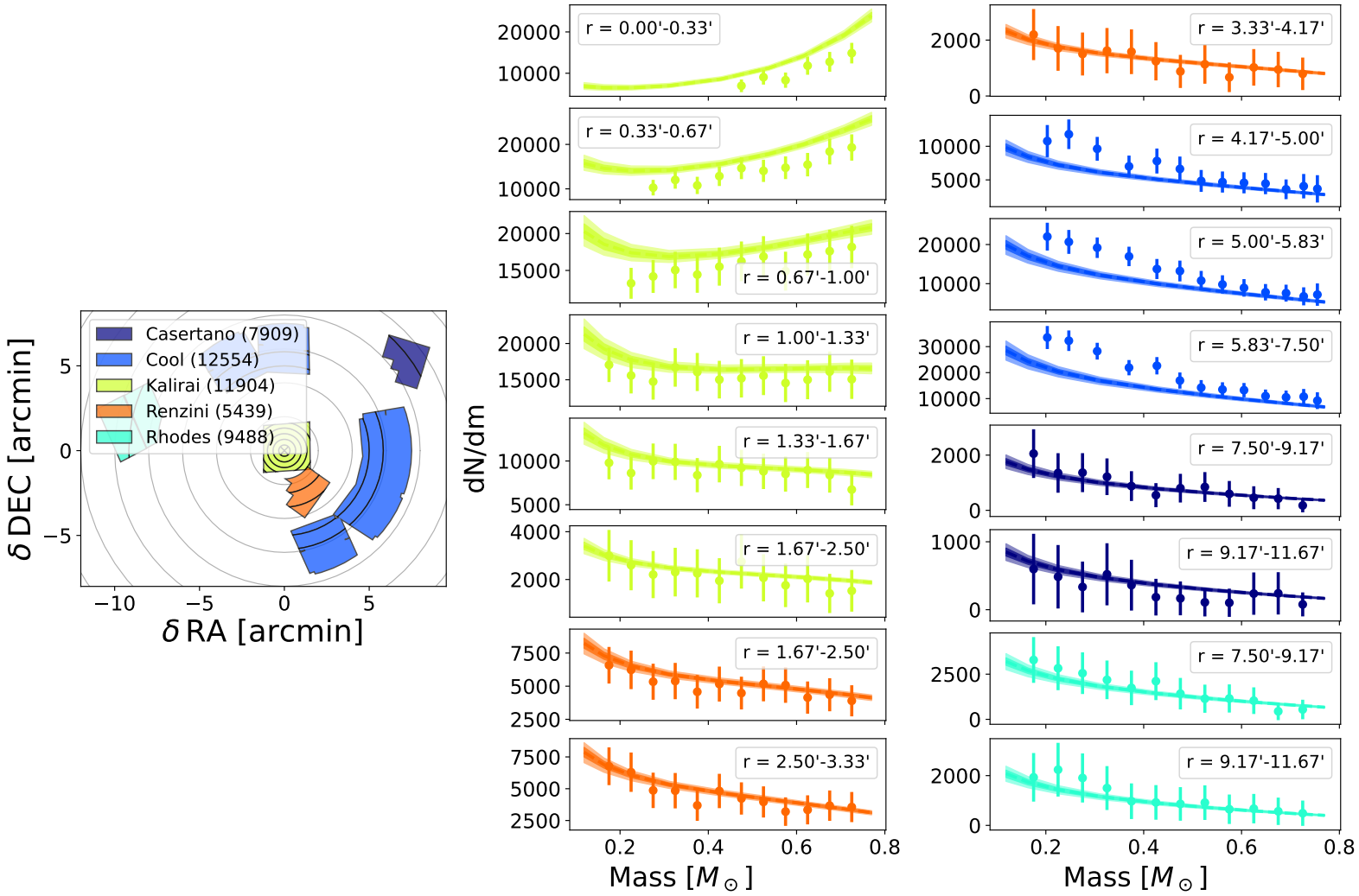

Figure A.78: Figure 5.3 repeated for NGC 6752, with the amount of black holes retained at the present day fixed to zero

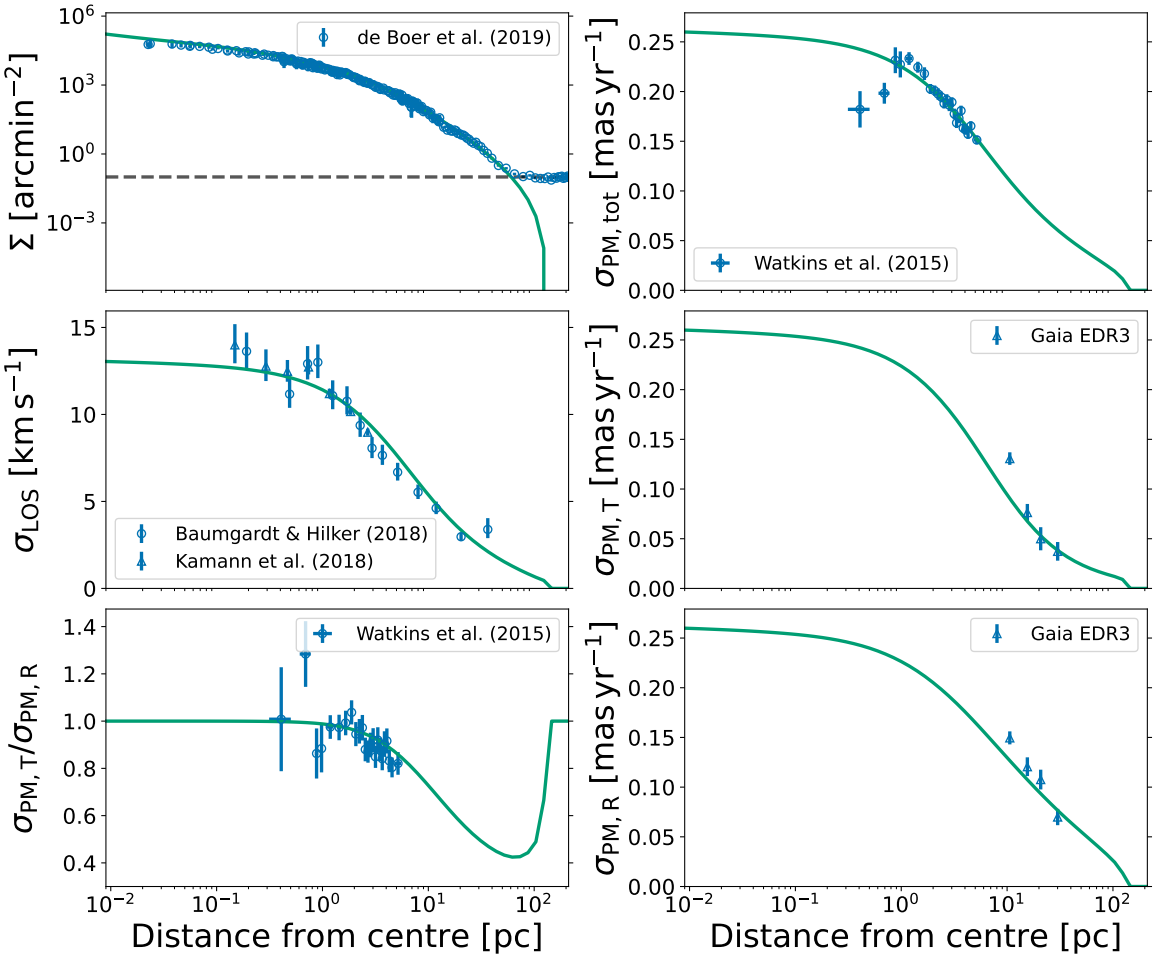

Figure A.79: Figure 5.2 repeated for NGC 7078, with the amount of black holes retained at the present day fixed to zero

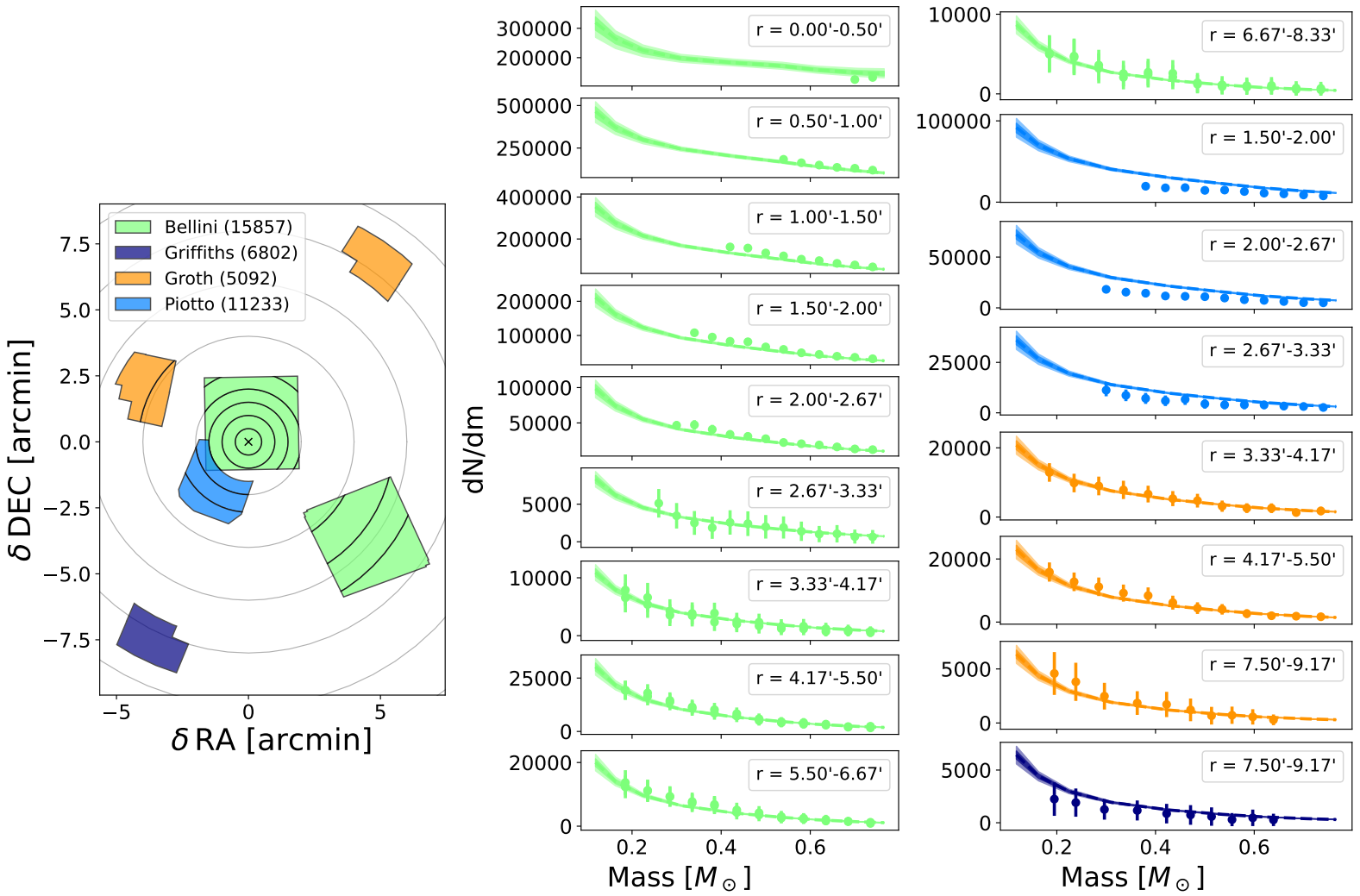

Figure A.80: Figure 5.3 repeated for NGC 7078, with the amount of black holes retained at the present day fixed to zero

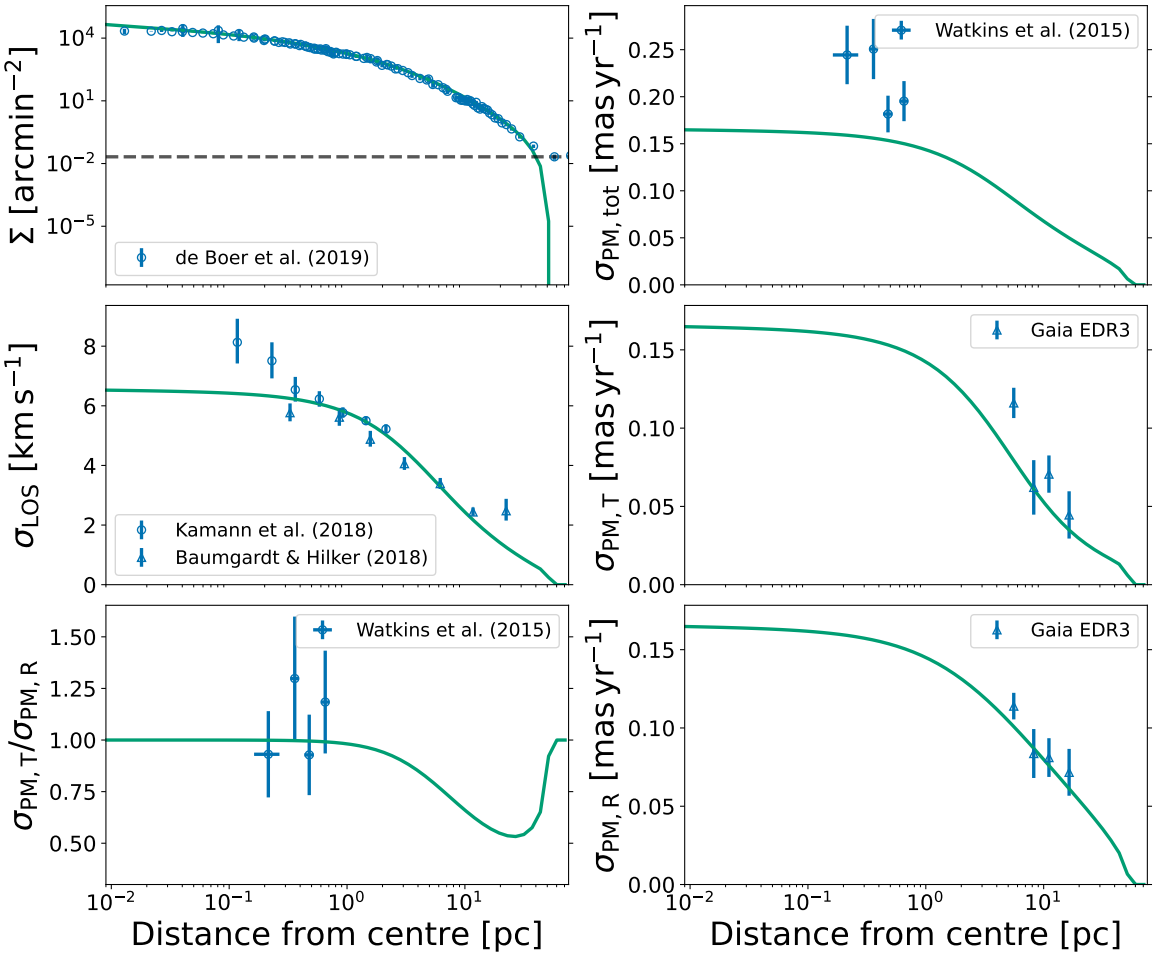

Figure A.81: Figure 5.2 repeated for NGC 7099, with the amount of black holes retained at the present day fixed to zero

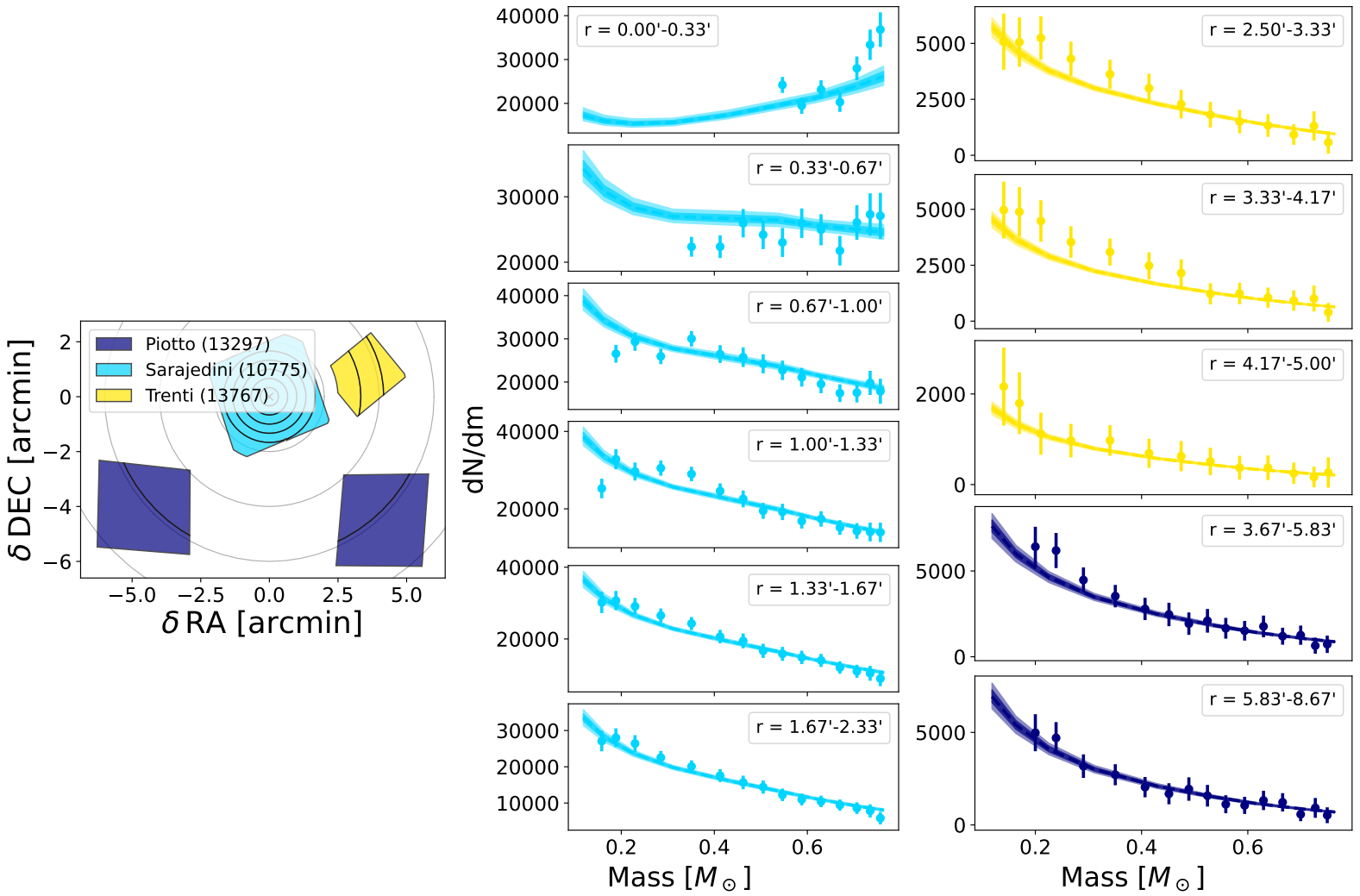

Figure A.82: Figure 5.3 repeated for NGC 7099, with the amount of black holes retained at the present day fixed to zero

Appendix B

`GCfit` Package Architecture

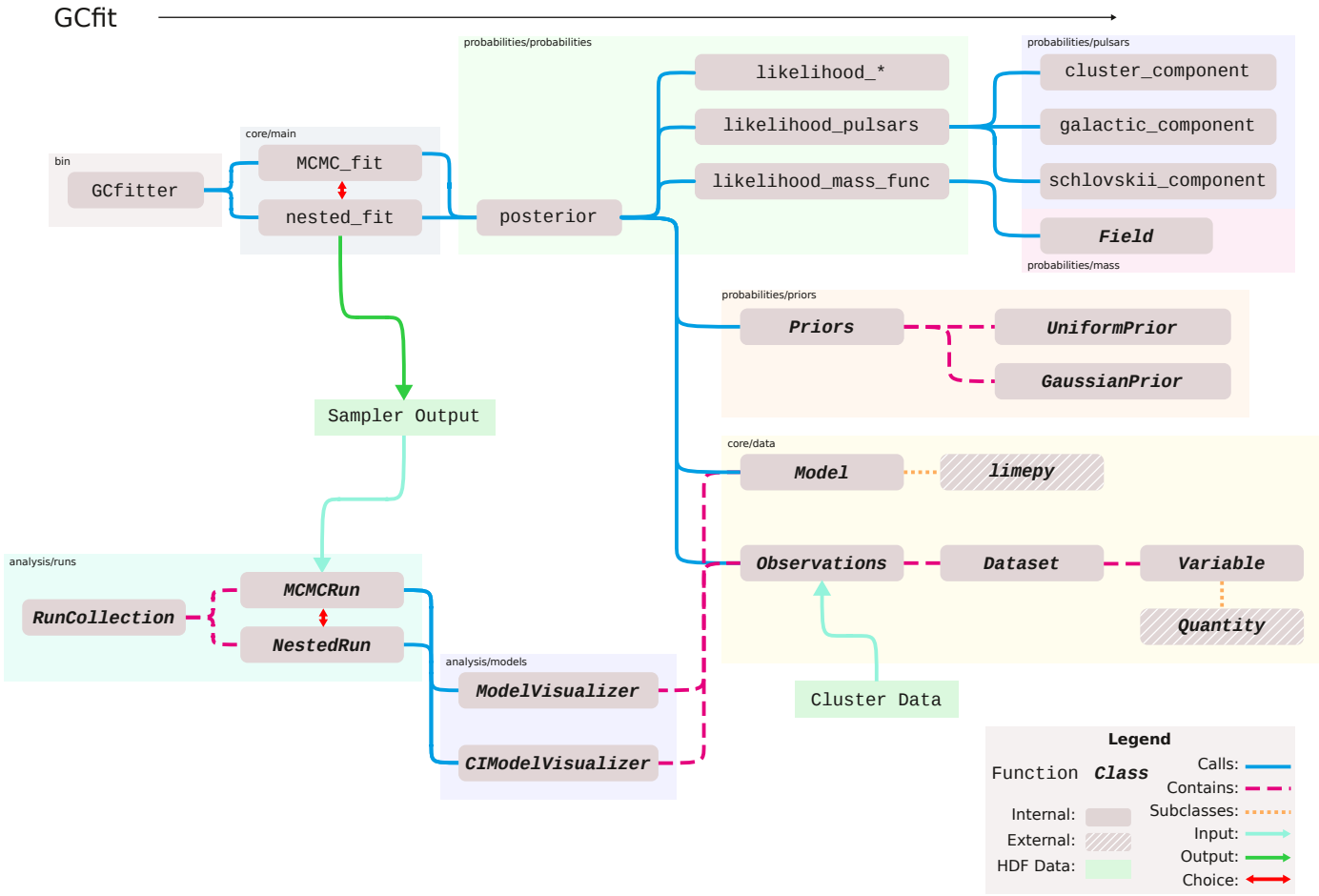

Figure B.1: Schematic representation of the architecture of the `GCfit` software package, showcasing the various Python modules, classes and functions and their relationships with one another. Fitting is handled, from the top-left, by the `GCfitter` script, using the likelihood and prior functions and data classes, to the right. Analysis and visualization of the results is handled by the `analysis` module (bottom-left).